Measurement of CKM-angle gamma with charmed BO meson decays

Baak, M.A.

2007

document version
Publisher's PDF, also known as Version of record

Measurement of CKM-angle γ with charmed B^0 meson decays

Cover: by Surya Bonam.

Printed by Ponsen & Looijen b.v., Wageningen.

VRIJE UNIVERSITEIT

Measurement of CKM-angle γ with charmed B^0 meson decays

ACADEMISCH PROEFSCHRIFT

ter verkrijging van de graad Doctor aan
de Vrije Universiteit Amsterdam,
op gezag van de rector magnificus
prof.dr. L.M. Bouter,
in het openbaar te verdedigen
ten overstaan van de promotiecommissie
van de faculteit der Exacte Wetenschappen
op maandag 5 februari 2007 om 13.45 uur
in de aula van de universiteit,
De Boelelaan 1105

door

Max Arjen Baak

geboren te Zaandam

promotor: prof.dr.ing. J.F.J. van den Brand
copromotor: dr. H.G. Raven

Half a bee, philosophically,
must, ipso facto, half not be.
But half the bee has got to be,
vis-à-vis its entity. D'you see?

But can a bee be said to be
or not to be an entire bee,
when half the bee is not a bee,
due to some ancient injury?

Monty Python,
Eric The Half A Bee

Contents

Chapter 1

Introduction

Violation of the symmetry of *CP* was first discovered in 1964 in the decays of 'neutral kaon' particles by a group of particle physicists lead by V. Fitch and J. Cronin [1]. The phenomenon of *CP* violation not only allows one to distinguish between matter and antimatter, but also, as shown by A. Sakharov in 1967 [2], it is one of the essential ingredients needed to explain the apparent abundance of matter over antimatter in the universe – one of the most puzzling questions in modern cosmology.

Following the discovery of *CP* violation, in 1973 M. Kobayashi and T. Maskawa proposed an explanation of this phenomenon [3] within the theoretical framework of the electroweak forces, which are part of the Standard Model of particle physics [4]. The Standard Model describes the hundreds of observed elementary particles in terms of three generations of quarks and leptons, as well as the weak, electromagnetic, and strong interactions between them.

The phenomenon of *CP* violation is incorporated in the Cabibbo-Kobayashi-Maskawa (CKM) matrix, which describes the weak interactions between the quarks. The weak interactions between quarks are described by coupling constants that are functions of three real parameters and one irreducible complex phase. The magnitude of all *CP* violating effects in the Standard Model is related to this complex phase.

The measurement of the *CP* violating phase of the CKM matrix [3, 5] is an important part of todays scientific program in particle physics. Certain relations between the coupling constants of the CKM matrix can be expressed graphically as triangles in the complex plane. One of these is referred to as 'the Unitarity Triangle'. Violation of the *CP* symmetry manifests itself as a non-zero area of the Unitarity Triangle. While it is sufficient to measure one of the triangles' internal angles α, β, and γ, to demonstrate the existence of *CP* violation, the Unitarity Triangle needs to be overconstrained by experimental measurements in order to demonstrate that the CKM mechanism is the correct explanation of this phenomenon. Several theoretically clean measurements of the CKM-angle β exist [6, 7], and over the last few years the CKM-angle α has been constrained quite successfully as well [8, 9]. However, today no stringent measurement of the CKM-angle γ is available.

In the previous decade two particle accelerators were built to study *CP* violation in the decays of a particle known as 'the B meson', which is an excellent probe of the Unitarity Triangle. One of these is the *BABAR* experiment at the Stanford Linear Accelerator Center in California. This accelerator provides abundant samples of B mesons, and makes it possible to perform a direct test of Kobayashi-Maskawa model and the origin of *CP* violation.

A measurement of $\sin(2\beta+\gamma)$ can be obtained from the study of the time evolution of the decays $B^0 \to D^{(*)\mp}\pi^{\pm}$ and $B^0 \to D^{\mp}\rho^{\pm}$ [10]. As the *CP*-violating effect to be measured is

small (at the level of 2% or smaller), the measurement is quite challenging experimentally. To extract γ from the *CP*-violating observables, some theoretical input parameters are needed. These parameters can be obtained from the decay rates of $B^0 \to \pi^- D_s^{(*)+}$ and $B^0 \to \rho^- D_s^+$ [11].

In this dissertation, data collected by the *BABAR* detector have been analyzed and measurements of the *CP* asymmetry amplitude $\sin(2\beta+\gamma)$ in the decays of B mesons are presented. Results based on 232M $B\overline{B}$ events are presented for the time-dependent analysis of the decays $B^0 \to D^{(*)\mp}\pi^\pm$ and $B^0 \to D^\mp \rho^\pm$. The measured *CP* asymmetries are converted into a constraint on the CKM-angle γ, and, as such, provide an important test of the Standard Model.

Outline

The remainder of this thesis is divided into the following chapters. In Chapter 2 we describe how *CP* violation is implemented in the Standard Model, and how B meson decays provide access to the angles of the Unitarity Triangle. We end with a description of the time-dependent evolution of the $B^0 \to D^{(*)\mp}\pi^\pm$ and $B^0 \to D^{(*)\mp}\rho^\pm$ system, and how these decays are sensitive to the CKM-angle γ. Chapter 3 provides a brief overview of the *BABAR* experiment, consisting of the e^+e^- PEP-II collider and the *BABAR* detector. In Chapter 4 we present the analysis technique of the measurement described in this thesis, consisting of three parts: B meson selection and reconstruction, B-flavor tagging, and the time difference measurement of two B decays. The phenomenon of 'tag-side interference' is dealt with in Chapter 5. An event of interest measured at the *BABAR* experiment contains two B mesons that evolve coherently in time. As a result, *CP* violation in one B^0 meson decay affects the time distribution of the other, an effect we need to account for in this measurement. Chapter 6 lists the ingredients of the fit to the time-dependent distributions of the reconstructed B samples. We present a validation of the fit procedure in Chapter 7. The results of the time-dependent fit are found in Chapter 8. The systematic uncertainties associated with this measurement are listed in Chapter 9. The conversion of our measurement into the CKM-angle γ requires several external input parameters, discussed in Chapter 10. Using these parameters, the extraction of γ is performed in Chapter 11. We conclude in Chapter 12 with a retrospective and discuss the prospects for the measurement of the CKM-angle γ.

Chapter 2

CP violation and B physics

Measurements of time-dependent CP asymmetries in B^0 decays provide information about the irreducible phase contained in the Cabibbo-Kobayashi-Maskawa (CKM) quark-mixing matrix [12], which describes CP violation in the Standard Model. This thesis reports measurements of the CP asymmetries in $B^0 \to D^{(*)\mp}\pi^{\pm}$ and $B^0 \to D^{\mp}\rho^{\pm}$ decays [13], as published in Ref. [14]. We denote these decays as $B \to D^{(*)\mp}h^{\pm}$, where $h^{\pm}$ is a charged pion or ρ meson. The time evolution of $B \to D^{(*)\mp}h^{\pm}$ decays is sensitive to the CP angle γ, because the CKM-favored decay amplitude $\overline{B}^0 \to D^{(*)+}h^-$ and the doubly-CKM-suppressed decay amplitude $B^0 \to D^{(*)+}h^-$ interfere due to $B^0\overline{B}^0$ mixing. The relative weak phase between these two amplitudes is γ. With $B^0\overline{B}^0$ mixing, the total weak phase difference between the interfering amplitudes is $2\beta+\gamma$.

In this Chapter we summarize all of the above in more detail, and conclude with a strategy for the measurement of time-dependent CP asymmetries. Extensive, excellent reviews of CP violation in general or time-dependent B decays in particular can be found in Refs. [15, 16].

2.1 CP violation in quantum field theory

Examples of discrete symmetry operators in particle physics are C, P, and T, where C stands for charge conjugation (swapping particles for their anti-particles), P for parity reflection (space reflection through the origin), and T for time reversal. The symmetry operators P and C are linear and unitary in nature, while T is anti-linear and anti-unitary. Time reversal, when applied to a field, takes the complex conjugate of any multiplicative constant or matrix.

The transformational properties of C, P, and T for the scalar fields $\phi(x)$, vector fields $V(x)$, and fermion fields $\psi(x)$ can be found in Ref. [15]. When applying the CP operator, every field is converted into its adjoint partner. Without derivation, for later comparison we give

$$\begin{aligned} CP\,\overline{\psi}'(x)\gamma^{\mu}\psi(x)(CP)^{\dagger} &= -\overline{\psi}(\tilde{x})\gamma_{\mu}\psi'(\tilde{x}) \\ CP\,\overline{\psi}'(x)\gamma^5\gamma^{\mu}\psi(x)(CP)^{\dagger} &= -\overline{\psi}(\tilde{x})\gamma^5\gamma_{\mu}\psi'(\tilde{x}) \\ CP\,V^{\mu}(x)(CP)^{\dagger} &= -V^{\dagger}_{\mu}(\tilde{x})\,, \end{aligned} \tag{2.1}$$

where $\tilde{x}^{\mu} = x_{\mu} = (t, -\vec{x})$.

Since the total Lagrangian $\mathcal{L}$ is required to be hermitian (like its Hamiltonian), each Lagrangian term is either self-adjoint, or contains a corresponding adjoint term. A CP transfor-

mation thus converts the fields in a Lagrangian term i into those of the adjoint's companion.

$$\mathcal{L}_i \quad \overset{CP}{\longleftrightarrow} \quad \mathcal{L}_i^\dagger$$

The *CP* symmetry is satisfied when the operator completely converts the two adjoint Lagrangian terms into each other. For a self-adjoint term this condition is obviously satisfied. In case of two adjoint terms *CP* invariance depends upon the *CP* properties of the coupling constants (or matrices).

From hermiticity the coupling constant of one adjoint term is the complex conjugated of the matching other. For *CP* invariance, the coupling constants need to be identical, *i.e.* real. Therefore, *CP* violation can be accommodated when complex coupling constants are present in the Lagrangian. (Looking back at the arrow, the imaginary parts of the coupling constants give a *CP*-odd transformation.)

It should be stressed that the *CP* symmetry can still be conserved in a theory with complex coupling constants. Since physical observables are invariant under global phase transformations, *e.g.*

$$\psi(x) \longrightarrow e^{i\phi}\psi(x)\,,$$

sometimes the phases of complex coupling constants can be absorbed through redefinitions of the quantum fields. A theory is not invariant under *CP* if, even after a number of phase redefinitions, one or more 'irreducible' phases still cannot be absorbed. In Section 2.3 irreducibility is discussed for the weak interactions of the Standard Model Lagrangian.

2.2 *CP* violation through interference

As demonstrated in Section 2.1, irreducible complex coupling constants are necessary for *CP* violation to occur. At the quantum level there are other requirements as well.

Let $|a\rangle$ be an initial state decaying to final state $|b\rangle$. The corresponding *CP*-conjugated states, *i.e.* (sets of) anti-particles, are defined as $|\bar{a}\rangle$ and $|\bar{b}\rangle$. The decay amplitude $\overline{A} = \langle\bar{b}|H|\bar{a}\rangle$ is related to $A = \langle b|H|a\rangle$ through the *CP* operation, or, effectively, by swapping each complex coupling constant in A with its conjugated counterpart. Irreducible complex coupling constants, when involved in particle interactions, thus lead to *CP*-odd phases in transition amplitudes. Several decay amplitudes $A_i = |A_i|\exp(i\varphi_i)$ may contribute to A. Each phase $\varphi_i = \phi_i + \delta_i$ consists of the *CP*-odd phase ϕ_i, induced by irreducible complex coupling constants, and a *CP*-even phase δ_i, *e.g.* generated by final state interactions or finite decay widths. One has $\overline{A}_i = |A_i|\exp i(-\phi_i + \delta_i)$.

In case of only one decay amplitude A_1 (or several amplitudes with identical *CP*-odd or identical *CP*-even phases), the decay rates $|A(a \to b)|^2$ and $|\overline{A}(\bar{a} \to \bar{b})|^2$ are equal, and no *CP* violation occurs. For two decay amplitudes, A_1 and A_2, *CP* violation can happen. Define $\Delta\delta = \delta_1 - \delta_2$ and $\Delta\phi = \phi_1 - \phi_2$. One has

$$\begin{aligned} |A|^2 &= |A_1 + A_2|^2 \\ &= |A_1|^2 + |A_2|^2 + 2\mathcal{R}e(A_2^* A_1) \\ &= |A_1|^2 + |A_2|^2 + 2|A_1 A_2|\cos(\Delta\phi + \Delta\delta)\,, \quad \text{and} \\ \\ |\overline{A}|^2 &= |A_1|^2 + |A_2|^2 + 2|A_1 A_2|\cos(\Delta\phi - \Delta\delta)\,. \end{aligned} \tag{2.2}$$

Clearly, the decay rates $|A(a\to b)|^2$ and $|\overline{A}(\bar{a}\to\bar{b})|^2$ are different when

1. $\phi_1 \neq \phi_2$, and

2. $\delta_1 \neq \delta_2$.

In conclusion, apart from a) the presence of one or more irreducible complex coupling constants, *CP* violation generally requires: b) interference of two or more transition amplitudes, c) with different *CP*-odd and *CP*-even phases.

2.3 *CP* violation in weak interactions

In the Standard Model, *CP* violation is accommodated in the weak quark currents, *i.e.* in the interactions between charged W vector bosons and quarks[1]. W bosons have the ability to mix different quark generations. Let us arrange the charge $\frac{2}{3}$ and the charge $-\frac{1}{3}$ quarks into up-type and down-type multiplets

$$U = \begin{pmatrix} u \\ c \\ t \end{pmatrix} \; ; \quad D = \begin{pmatrix} d \\ s \\ b \end{pmatrix} . \tag{2.3}$$

The charged weak current interactions can then be written as

$$\frac{g}{\sqrt{2}} \, (\, \overline{U}_L \gamma^\mu \, V_{CKM} \, D_L \, W^-_\mu + \overline{D}_L \gamma^\mu \, V^\dagger_{CKM} \, U_L \, W^+_\mu \,), \tag{2.4}$$

where W are the vector bosons. V_{CKM} is the unitary Cabibbo-Kobayashi-Maskawa (CKM) mixing matrix of the three quark generations. Note that in Eq. (2.1) the fields of the two terms get transformed into each other under the *CP* operation.

To show that the CKM mixing matrix contains an irreducible phase, we start with the quark mass terms of the Standard Model Lagrangian, which are given by

$$-(\, \overline{U} M_U U + \overline{D} M_D D \,) \, . \tag{2.5}$$

Using the quark mass eigenstates, by definition the mass matrices M_U and M_D are diagonal and real. As the quark weak eigenstates, interacting with the W boson in Eq. (2.4), are not necessarily equal to the mass eigenstates, V_{CKM} is non-trivial.

The CKM mixing matrix is written as

$$V_{CKM} = \begin{pmatrix} V_{ud} & V_{us} & V_{ub} \\ V_{cd} & V_{cs} & V_{cb} \\ V_{td} & V_{ts} & V_{tb} \end{pmatrix} . \tag{2.6}$$

Each matrix element $V_{q_i q_j}$ symbolizes the flavor-changing weak coupling between the quarks q_i and q_j.

There are $2n$ quark fields for n families of quarks. A unitary $n \times n$ matrix has a total of n^2 independent parameters. From orthogonality, $n(n-1)/2$ of these are real angles, and $n(n+1)/2$ are complex phases. Given that all up-type and down-type quark masses are different, one can

[1] In the Standard Model, *CP* violation is also likely to occur in neutrino mixing, but this has not yet been measured. There is a possible source of *CP* violation in the strong interactions as well, known as 'the strong *CP* problem'. This form of *CP* violation is not seen, however, and, if it exists at all, must be highly suppressed. See Ref. [15] for a discussion.

remove $(2n-1)$ of these phases by redefining the relative phases of the quark fields. From Eq. (2.5), this does not affect the real diagonal mass matrices M_Q. That leaves $(n-1)(n-2)/2$ complex phases. As a result, for $n \geq 3$ irreducible complex phases can be accomodated.

With three quark generations this allows for three real angles and one complex phase in the weak couplings. In the 'standard' parametrization [17], V_{CKM} is written as

$$V_{CKM} = \begin{pmatrix} c_{12}c_{13} & s_{12}c_{13} & s_{13}\,e^{-i\delta_{KM}} \\ -s_{12}c_{23} - c_{12}s_{23}s_{13}\,e^{i\delta_{KM}} & c_{12}c_{23} - s_{12}s_{23}s_{13}\,e^{i\delta_{KM}} & s_{23}c_{13} \\ s_{12}s_{23} - c_{12}c_{23}s_{13}\,e^{i\delta_{KM}} & -c_{12}s_{23} - s_{12}c_{23}s_{13}\,e^{i\delta_{KM}} & c_{23}c_{13} \end{pmatrix}, \qquad (2.7)$$

with $c_{ij} = \cos\theta_{ij}$ and $s_{ij} = \sin\theta_{ij}$, and the angles θ_{12}, θ_{23}, θ_{13} relate to the amount of mixing between generations i and j. The complex phase in the CKM mixing matrix is called the Kobayashi-Maskawa phase, δ_{KM}. Eight conditions must be satisfied for δ_{KM} to be irreducible [18], *i.e.* for having *CP* violation in the weak quark interactions. These are

$$\delta_{KM} \neq 0,\, \pi\,, \quad \theta_{ij} \neq 0,\, \pi/2\,, \text{ for } \qquad i \neq j \in \{1,2,3\}\,. \qquad (2.8)$$

Unless a specific representation is adopted for V_{CKM}, the *CP*-violating weak phase may appear in any of the elements $V_{q_iq_j}$. As such, by default $V_{q_iq_j}$ is treated as complex.

Using Eq. (2.2), one can construct a measure of the '*CP* non-conservation' of the weak interactions [18]. At least two weak amplitudes with different phases are required for *CP* violation. In case of quark-W interactions, the simplest case to consider is a transition involving four different quarks: two up-type quarks denoted by i and k, and two down-type quarks denoted by j and l. Define the transition amplitude as

$$A = (V_{ij}V_{kl})\,A_1\,e^{i\delta_1} + (V_{il}V_{kj})\,A_2\,e^{i\delta_2}\,, \qquad (2.9)$$

where $A_{1,2}$ are real, and $\Delta\delta = \delta_1 - \delta_2$ is the *CP*-even phase from final state interactions. The amplitude of the *CP*-conjugate process is

$$\overline{A} = (V_{ij}V_{kl})^*A_1\,e^{i\delta_1} + (V_{il}V_{kj})^*A_2\,e^{i\delta_2}\,, \qquad (2.10)$$

The *CP* asymmetry is then given by

$$\begin{aligned} \mathcal{A}_{CP} &\equiv \frac{|A|^2 - |\overline{A}|^2}{|A|^2 + |\overline{A}|^2} \\ &= \frac{2\,\mathcal{I}m(V_{ij}V_{kl}V_{kj}^*V_{il}^*)\,\sin(\Delta\delta)\,A_1A_2}{|V_{ij}V_{kl}|^2A_1^2 + |V_{kj}V_{il}|^2A_2^2 + 2\,\mathcal{R}e(V_{ij}V_{kl}V_{kj}^*V_{il}^*)\cos(\Delta\delta)A_1A_2}\,. \end{aligned} \qquad (2.11)$$

Thus, *CP* violation in weak decays is proportional to the Jacobian J, defined as

$$J = \mathcal{I}m(V_{ij}V_{kl}V_{il}^*V_{kj}^*)\,. \qquad (2.12)$$

It can be shown that the measure is phase-convention independent, and, because of unitarity, independent of the quarks involved [18]. (The constraints in Eq. (2.8) are equivalent to imposing $J \neq 0$.)

In summary – ignoring possible contributions from new physics – all *CP*-violating weak interaction processes involving quarks, be it kaon or B meson decays, probe the same source of *CP* violation. Any such *CP*-violating process necessarily involves mixing between the quark generations.

We discuss the unitarity of the CKM mixing matrix in Section 2.4.

2.4 The Unitarity Triangle

From experimental knowledge of the weak hadron interactions, and assuming unitarity and three generations [17], the current 90% confidence limits on the CKM matrix elements are

$$|V_{CKM}| = \begin{pmatrix} 0.9739\text{–}0.9751 & 0.221\text{–}0.227 & 0.0029\text{–}0.0045 \\ 0.221\text{–}0.227 & 0.9730\text{–}0.9744 & 0.039\text{–}0.044 \\ 0.0048\text{–}0.014 & 0.037\text{–}0.043 & 0.9990\text{–}0.9992 \end{pmatrix}. \tag{2.13}$$

The structure of V_{CKM} is found to be nearly diagonal, with only small off-diagonal elements (getting smaller for higher generations), meaning that generation mixing is generally suppressed – a phenomenon called Cabibbo suppression. For this reason, V_{CKM} is written in the Wolfenstein parametrization [19], which is an expansion in terms of $\lambda = |V_{us}| = 0.22$

$$V_{CKM} = \begin{pmatrix} 1 - \frac{\lambda^2}{2} & \lambda & A\lambda^3(\rho - i\eta) \\ -\lambda & 1 - \frac{\lambda^2}{2} & A\lambda^2 \\ A\lambda^3(1 - \rho - i\eta) & -A\lambda^2 & 1 \end{pmatrix} + \mathcal{O}(\lambda^4)\,, \tag{2.14}$$

where A, ρ, and η are real numbers of order unity.

As explained in Section 2.3, any *CP*-violating process involves mixing between the three quark generations, and therefore requires off-diagonal elements. Because of the smallness of the off-diagonal elements, experimentally *CP* violation turns out to be very small. In terms of the Wolfenstein parametrization, V_{td} or V_{ub} is required, both suppressed at the level of λ^3.

The unitarity of V_{CKM} implies nine constraints on its matrix elements. A review of these can be found in Ref. [20]. Six of them are orthogonality conditions, and require the sum of three complex terms to be zero. Graphically, they can be expressed as triangles in the complex plane – called 'unitarity triangles'. Three of the triangles, defined as

$$V_{ud}V_{us}^* + V_{cd}V_{cs}^* + V_{td}V_{ts}^* = 0\,, \tag{2.15}$$
$$V_{us}V_{ub}^* + V_{cs}V_{cb}^* + V_{ts}V_{tb}^* = 0\,, \tag{2.16}$$
$$V_{ud}V_{ub}^* + V_{cd}V_{cb}^* + V_{td}V_{tb}^* = 0\,, \tag{2.17}$$

are shown in Fig. 2.1.

All unitarity triangles have the same surface area $|J|/2$, as defined in Eq. (2.12), with

$$|J| = (3.05 \pm 0.18) \times 10^{-5}\ [21]\,. \tag{2.18}$$

As demonstrated in Section 2.3, *CP* violation in weak hadron decays is proportional to the Jacobian J. Therefore, the non-zero area of the triangles generally represents the *CP* violation of the weak interactions.

Specifically, the magnitude of *CP*-violating observables in B meson decays is a function of angles of the unitarity triangles. The squashed triangles in Figs. 2.1a,b cannot be resolved without high experimental precision. The third triangle, however, illustrated in Fig. 2.1c, has large angles (away from zero and not close to $\pi/2$ or π), resulting in large *CP*-violating effects. Eq. (2.17) is commonly referred to as 'The Unitarity Triangle'.

The Unitarity Triangle relates directly to *CP* violation in B decays (each term in Eq. (2.17) has a b in it), which is the topic of the remainder of this Chapter. Fig. 2.2 shows the rescaled

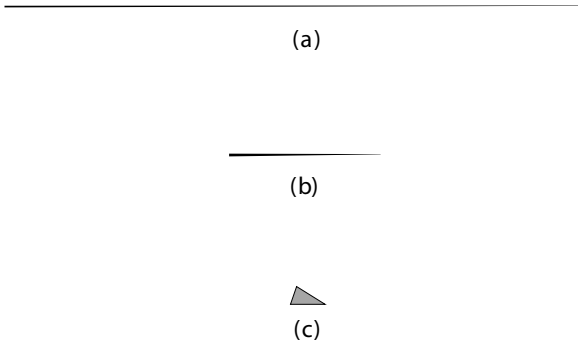

Figure 2.1: *The unitarity triangles defined by: a) Eq. (2.15), b) Eq. (2.16), and c) Eq. (2.17). All triangles use the same scale and have identical surface areas.*

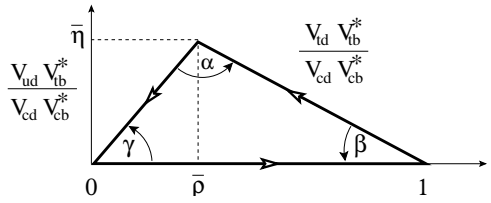

Figure 2.2: *Rescaled Unitarity Triangle, with all sides divided by* $V_{cb}^* V_{cd}$.

Unitary Triangle, with each term of Eq. (2.17) divided by $V_{cd}V_{cb}^*$. The two bottom corners are fixed at $(0,0)$ and $(1,0)$, and the apex lies at $(\bar{\rho},\bar{\eta})$, with

$$\bar{\rho} = \rho(1-\lambda^2/2)\,, \quad \bar{\eta} = \eta(1-\lambda^2/2)\,. \tag{2.19}$$

Both expressions are valid up to $\mathcal{O}(\lambda^6)$ compared with their exact expressions [22].

The three *CP* angles α, β, γ in Fig. 2.2 are defined by

$$\alpha \equiv \arg\left[-\frac{V_{td}V_{tb}^*}{V_{ud}V_{ub}^*}\right], \quad \beta \equiv \arg\left[-\frac{V_{cd}V_{cb}^*}{V_{td}V_{tb}^*}\right], \quad \gamma \equiv \arg\left[-\frac{V_{ud}V_{ub}^*}{V_{cd}V_{cb}^*}\right]\,. \tag{2.20}$$

The angles are related through $\alpha+\beta+\gamma=\pi$. The expressions are phase invariant, since every index appears twice: either once in V and once in V^*, or once in the numerator and once in the denominator.

Knowledge of the length of the sides of the Unitarity Triangle gives an indirect determination of the angles. The angles can also be measured directly through the observation of *CP* violation in certain *B* decay channels. The consistency of the (in-)dependent measurements provides an important test of the Standard Model.

The current constraints on the position of apex of the Unitarity Triangle from indirect and direct measurements of α, β, γ are shown in Fig. 2.3. The indirect and direct measurements of

α, β, and γ are summarized in Table 2.1 [21]. The two sets agree well. The indirect constraints come from measurements of the oscillation frequencies in B_d and B_s mesons (Δm_d and Δm_s), the ratio $|V_{ub}/V_{cb}|$, and the *CP* violation fraction in kaons (ϵ_K). The direct measurement of β is known best, and comes from the decays $B \to J/\psi K_S$. The angle α is (mostly) determined using the decays $B \to \rho^+\rho^-$. The angle γ is measured with the decays $B^+ \to D^{(*)0}K^{(*)+}$, and $B \to D^{(*)\mp}\pi^\pm$ and $B \to D^\mp\rho^\pm$. More about the direct angle measurements in Section 2.5.5.

The numbers in Table 2.1 make clear that γ is by far the least well-known *CP* angle, as determined from direct measurements. The direct constraint on the position of the apex of the Unitarity Triangle comes mostly from the measurements of β and α. A precise measurement of γ would thus help squeeze the uncertainty of the apex along the $\bar{\rho}$ axis. This thesis focuses on the direct measurement of γ using the decays $B \to D^{(*)\mp}\pi^\pm$ and $B \to D^\mp\rho^\pm$ – the theory of which is discussed in the following Sections.

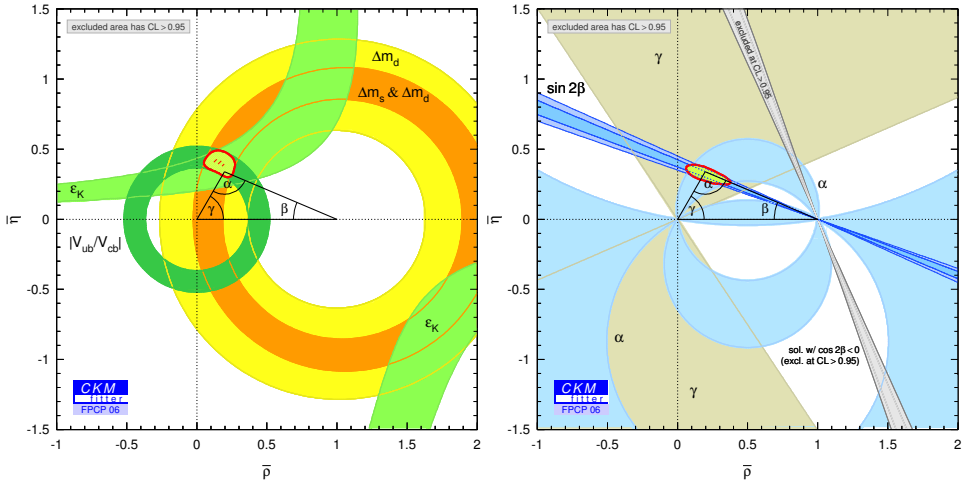

Figure 2.3: *Existing constraints on the Unitarity Triangle from (left) indirect measurements and (right) direct CP-angle measurements [21].*

CP angle	Indirect measurements (°)	Direct measurements (°)
β	$24.4^{+2.6}_{-1.5}$	$21.7^{+1.3}_{-1.2}$
α	97^{+5}_{-16}	100^{+15}_{-9}
γ	60^{+5}_{-4}	71^{+22}_{-30}

Table 2.1: *Current indirect and direct measurements of the CP angles α, β, and γ [21].*

2.5 *CP* violation in *B* decays

Decays of B mesons can provide theoretically clean information about the angles of the Unitarity Triangle. A $\overline{B}^0$ meson has a definite quark composition [13], and consists of a b quark and a $\bar{d}$ anti-quark. The $\overline{B}^0$ meson has the isospin partner B^-, containing a b and $\bar{u}$ quark. The b quark was first discovered in 1977 in the decays of the bound state $\Upsilon(1S) \equiv (b\bar{b})$ [23]. The average lifetime of hadrons containing a b quark was first measured in 1983 [24]. The properties B^0 and B^+ mesons have been summarized in Table 2.2. (Other B mesons exist, such as $\overline{B}^0_s$ $(b\bar{s})$ and B^-_c $(b\bar{c})$, but these are not accessible by the *BABAR* experiment because they are too heavy.)

Meson	Composition	Mass (MeV/c^2)	Lifetime (ps)	Spin
B^0	$\bar{b}d$	5279.4 ± 0.5	1.542 ± 0.016	0
B^+	$\bar{b}u$	5279.0 ± 0.5	1.674 ± 0.018	0

Table 2.2: *Properties of B mesons.*

In the following Sections the discussion is limited to the B^0 mesons. Weak interactions permit a phenomenon called '$B^0\overline{B}^0$ oscillation', which allows a B^0 to become $\overline{B}^0$ (and vice versa). Given a final state $|f\rangle$ accessible to both B^0 and $\overline{B}^0$ decays, $B^0\overline{B}^0$ oscillation thus provides two interfering amplitudes, which can lead to *CP* violation under the right conditions. We discuss how this feature is exploited to determine the *CP* angle γ.

2.5.1 $B^0\overline{B}^0$ oscillation

The flavor eigenstates $|B^0\rangle$ and $|\overline{B}^0\rangle$, produced in quark-level strong interactions, are not eigenstates of the weak interactions. Second-order weak interactions allow a $\overline{B}^0$ meson to become a B^0, as shown in Fig. 2.4. This process is called $B^0\overline{B}^0$ oscillation, and was first observed in 1987 [26, 27]. The eigenstates of the Hamiltonian, with definite mass and lifetime, are mixtures of the flavor eigenstates.

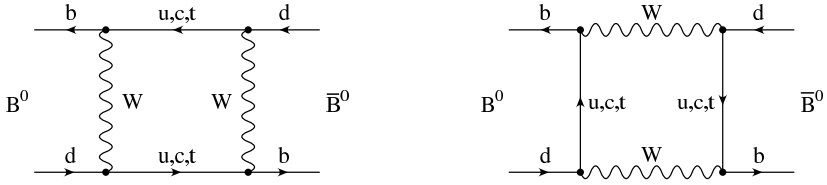

Figure 2.4: *Box diagrams inducing $B^0\overline{B}^0$ oscillation.*

In the Wigner-Weisskopf approximation [25], the time evolution and decay of the B^0 meson system is written in terms of only the flavor eigenstates, *i.e.*

$$|\psi(t)\rangle \equiv a(t)|B^0\rangle + b(t)|\overline{B}^0\rangle\,. \tag{2.21}$$

The wave function $\psi(t)$ evolves according to the Schrödinger equation

$$i\frac{d}{dt}\begin{pmatrix}a\\b\end{pmatrix} = \mathbf{H}\begin{pmatrix}a\\b\end{pmatrix} \equiv (\mathbf{M} - \frac{i}{2}\mathbf{\Gamma})\begin{pmatrix}a\\b\end{pmatrix} . \tag{2.22}$$

where the mass and lifetime matrices $\mathbf{M}$ and $\mathbf{\Gamma}$ are Hermitian. *CPT* invariance guarantees $H_{11} = H_{22}$. The matrices can be computed from the weak Hamiltonian H_W in second-order perturbation theory as

$$\begin{aligned} M_{ij} &= m_B\delta_{ij} + \langle i|H_W^{\Delta B=2}|j\rangle + \sum_n \frac{1}{m_B - E_n}\langle i|H_W^{\Delta B=1}|n\rangle\langle n|H_W^{\Delta B=1}|j\rangle \ , \\ \Gamma_{ij} &= 2\pi\sum_n \delta(E_n - m_B)\langle i|H_W^{\Delta B=1}|n\rangle\langle n|H_W^{\Delta B=1}|j\rangle \ . \end{aligned}$$

Physical states (on-shell), to which both B^0 and $\overline{B}^0$ decay, contribute to $\mathbf{\Gamma}$, whereas virtual (off-shell) intermediate states contribute to $\mathbf{M}$. The off-diagonal amplitudes M_{ij} and Γ_{ij} are called dispersive and absorptive, respectively.

The mass eigenstates of the Hamiltonian

$$|B_L\rangle = p|B^0\rangle + q|\bar{B}^0\rangle , \tag{2.23}$$

$$|B_H\rangle = p|B^0\rangle - q|\bar{B}^0\rangle , \tag{2.24}$$

have the complex eigenvalues

$$M - \frac{i}{2}\Gamma \pm \sqrt{\mathcal{H}_{12}\mathcal{H}_{21}} , \tag{2.25}$$

with $\Gamma \equiv \Gamma_{11} \equiv \Gamma_{22}$ and $M \equiv M_{11} \equiv M_{22}$. The mass and lifetime difference between the 'heavy' and 'light' eigenstates are

$$\Delta m_d - \frac{i}{2}\Delta\Gamma = (m_H - m_L) - \frac{i}{2}(\Gamma_H - \Gamma_L) = 2\sqrt{\mathcal{H}_{12}\mathcal{H}_{21}} , \tag{2.26}$$

where (m_H, m_L) and $(\Gamma_H^{-1}, \Gamma_L^{-1})$ are the masses and lifetimes of the heavy and light states. The ratio q/p is expressed as

$$\frac{q}{p} = \sqrt{\frac{M_{12}^* - \frac{i}{2}\Gamma_{12}^*}{M_{12} - \frac{i}{2}\Gamma_{12}}} . \tag{2.27}$$

The lifetime difference $\Delta\Gamma$ is sensitive to Γ_{12}, which is produced by decay channels common to B^0 and $\overline{B}^0$, *e.g.* $B \to D\bar{D}$. Typically, these decay modes are CKM-suppressed, with branching fractions at the level $\mathcal{O}(10^{-3})$ or below. More precisely, the Standard Model predicts $|q/p| - 1 = (2.5 - 6.5) \times 10^{-4}$ [16, 28]. For this reason $\Delta\Gamma$ is assumed to be negligible [16], and we assume $|q/p| \simeq 1$. On the other hand, the mass difference Δm_d is well-known to be [17]

$$\Delta m_d = 0.502 \pm 0.007 \text{ ps}^{-1} . \tag{2.28}$$

In conclusion, the two mass eigenstates have virtually equal lifetimes but noticeably different masses. This implies that Eqs. (2.26, 2.27) can be simplified to

$$\Delta m_d = 2|M_{12}|, \quad q/p = -|M_{12}|/M_{12}. \tag{2.29}$$

In terms of the CKM elements, q/p is given by

$$\frac{q}{p} = \frac{V_{tb}^* V_{td}}{V_{tb} V_{td}^*} = e^{-i2\beta}\,, \tag{2.30}$$

where β is the angle from the Unitarity Triangle in Eq. (2.20). Accordingly, β is also called the B^0 mixing phase. The significance of the magnitude $|q/p|$ is further discussed in Section 2.5.4.

Any state $|B\rangle$ can now be written as a linear combination of the states $|B_L\rangle$ and $|B_H\rangle$, whose coefficients evolve in time as

$$a_H(t) = a_H(0) e^{-iM_H} e^{-\frac{1}{2}\Gamma_H t}\,, \quad a_L(t) = a_L(0) e^{-iM_L} e^{-\frac{1}{2}\Gamma_L t}\,, \tag{2.31}$$

It can be easily shown that the evolution of a pure $|B^0\rangle$ or $|\overline{B}^0\rangle$ state at $t = 0$ is then given by

$$|B^0_{\rm phys}(t)\rangle = g_+(t)|B^0\rangle + (q/p) g_-(t)|\overline{B}^0\rangle, \tag{2.32}$$

$$|\bar{B}^0_{\rm phys}(t)\rangle = (p/q) g_-(t)|B^0\rangle + g_+(t)|\overline{B}^0\rangle, \tag{2.33}$$

where

$$g_+(t) = e^{-iMt} e^{-\Gamma t/2} \cos(\Delta m_d\, t/2), \tag{2.34}$$

$$g_-(t) = e^{-iMt} e^{-\Gamma t/2} i \sin(\Delta m_d\, t/2), \tag{2.35}$$

and we have applied $\Delta\Gamma = 0$, $\Gamma = 1/\tau_{B^0}$, $M = \frac{1}{2}(M_H + M_L)$. Eqs. (2.32, 2.33) demonstrate that the probability of a B^0 to become a $\overline{B}^0$ oscillates as a function of time and depends on the mass difference Δm_d.

We study the time-evolution of the $B^0\overline{B}^0$ system in more detail in the following Section.

2.5.2 Time-evolution of coherent $B^0\overline{B}^0$ states

At the *BABAR* experiment, B meson pairs are produced through the process $e^+e^- \to \Upsilon(4S) \to B\overline{B}$. To good approximation, equal amounts of B^+B^- and $B^0\overline{B}^0$ pairs are produced in the $\Upsilon(4S)$ decay.

A pair of neutral B mesons is produced coherently in a P-wave state. The time evolution of $|B^0_{\rm phys}\bar{B}^0_{\rm phys}\rangle$ is described as

$$|B^0_{\rm phys}\bar{B}^0_{\rm phys}; t_f, t_b\rangle = \left\{\, |B^0_{\rm phys}(t_f)\rangle|\bar{B}^0_{\rm phys}(t_b)\rangle - |\bar{B}^0_{\rm phys}(t_f)\rangle|B^0_{\rm phys}(t_b)\rangle \,\right\}/\sqrt{2}\,. \tag{2.36}$$

In the $\Upsilon(4S)$ frame the two B's have equal, back-to-back momenta. The forward and backward moving B mesons have the proper times t_f and t_b. Until one meson decays, necessarily at $t_f = t_b$, Eq. (2.36) contains one B^0 and one $\overline{B}^0$. Bose-Einstein statistics requires the total wave function to be symmetric; the relative minus sign between the terms reflects the anti-symmetry of the P-wave state.

We insert Eqs. (2.32–2.35) into Eq. (2.36) and introduce

$$A_i \equiv \langle f_i|H_W|B^0\rangle \quad , \quad \overline{A}_i \equiv \langle f_i|H_W|\overline{B}^0\rangle\,. \tag{2.37}$$

For the amplitude of the process where one B decays to final state f_1 at time t_1 and the other to f_2 at time t_2 we derive

$$\begin{aligned}\mathcal{A}(t_1,t_2) &= \{\,\langle f_1|H_W|B^0_{\rm phys}(t_1)\rangle\langle f_2|H_W|\bar{B}^0_{\rm phys}(t_2)\rangle - \langle f_1|H_W|\bar{B}^0_{\rm phys}(t_1)\rangle\langle f_2|H_W|B^0_{\rm phys}(t_2)\rangle\,\}/\sqrt{2}\\ &= \frac{1}{\sqrt{2}}e^{-(\Gamma/2+iM)(t_1+t_2)}\{\,\cos[\Delta m_d(t_1-t_2)](A_1\overline{A}_2 - \overline{A}_1A_2)\\ &\quad -i\sin[\Delta m_d(t_1-t_2)](\frac{p}{q}A_1A_2 - \frac{q}{p}\overline{A}_1\overline{A}_2)\,\}\,. \qquad (2.38)\end{aligned}$$

The time-dependent rate F for producing the combined final states f_1 and f_2 is then

$$\begin{aligned}F(T,\Delta t) &= Ce^{-\Gamma T}\{\,(|A_1|^2+|\overline{A}_1|^2)(|A_2|^2+|\overline{A}_2|^2) - 4\,\mathcal{R}e(\frac{q}{p}A_1^*\overline{A}_1)\,\mathcal{R}e(\frac{q}{p}A_2^*\overline{A}_2) \qquad (2.39)\\ &\quad -\cos(\Delta m_d\Delta t)[(|A_1|^2-|\overline{A}_1|^2)(|A_2|^2-|\overline{A}_2|^2) + 4\,\mathcal{I}m(\frac{q}{p}A_1^*\overline{A}_1)\,\mathcal{I}m(\frac{q}{p}A_2^*\overline{A}_2)]\\ &\quad +\sin(\Delta m_d\Delta t)[\mathcal{I}m(\frac{q}{p}A_1^*\overline{A}_1)\,(|A_2|^2-|\overline{A}_2|^2) - (|A_1|^2-|\overline{A}_1|^2)\,\mathcal{I}m(\frac{q}{p}A_2^*\overline{A}_2)]\,\}\,,\end{aligned}$$

where C is a normalization constant, and we have substituted $T = t_1+t_2$ and $\Delta t = t_1-t_2$.

The above expression can be integrated over the experimentally unobservable variable T, which for $t_1 \geq 0$ and $t_2 \geq 0$ takes values between $|\Delta t|$ and ∞. In Eq. (2.39) this changes the normalization, and converts $\exp(-\Gamma\,T)$ into $\exp(-\Gamma|\Delta t|)$. In the following text, T is ignored altogether.

The coherent production of $B^0\overline{B}^0$ leads to two important features, which are exploited experimentally in the following Chapters.

1. As a consequence of the coherent production of the two B states, one can fit the dependence on Δt without having to measure the $\Upsilon(4S)$ decay time. Experimentally, the variable Δt can be related directly to the distance between the two B decay vertices.

2. At the time of decay of one of the B mesons, say as a B^0, quantum coherence forces the other meson to be a $\overline{B}^0$. There are final states that directly identify the flavor of its parent B, called flavor eigenstates or 'tagging decays'. (In terms of Eq. (2.37), A_f or $\overline{A}_f = 0$; examples of tagging decays are $B^0 \to D^{*-}l^+\nu$.) Owing to quantum coherence, at $\Delta t = 0$ the flavor eigenstate of one B can thus be inferred from the flavor of the other – an experimental process called 'tagging'. So, if one of the B's produced by the $\Upsilon(4S)$ decays to a flavor eigenstate, and can be tagged as such, at that time ($\Delta t = 0$) the other B is identified to have the opposite flavor. This argument is valid regardless of the order of two B decays.

2.5.3 Two popular examples

This Section demonstrates two important applications of Eq. (2.39), common in the time-dependent studies of B decays. Both cases uses $|q/p| = 1$.

Flavor eigenstates

First, we discuss decays to flavor eigenstates, for which the final state identifies the flavor of the parent B. Examples are $B^0 \to D^{*-}l^+\nu$. One B meson produced in the $\Upsilon(4S)$ decay is (fully) reconstructed in a flavor eigenstate ($B_{\rm rec}$). The flavor of the other meson ($B_{\rm tag}$) is determined inclusively from its decay products.

Such events can be divided into two categories

- **Unmixed events**: $B_{\rm rec}$ and $B_{\rm tag}$ have different flavors, *i.e.* one B^0 and one $\overline{B}^0$. The unmixed amplitudes to be inserted into Eq. (2.39) are

$$\left\{ \begin{array}{rcl|rcl} A_1 & = & A_r & A_2 & = & 0 \\ \overline{A}_1 & = & 0 & \overline{A}_2 & = & A_t \end{array} \right\} \quad \text{and} \quad \left\{ \begin{array}{rcl|rcl} A_1 & = & 0 & A_2 & = & A_t \\ \overline{A}_1 & = & A_r & \overline{A}_2 & = & 0 \end{array} \right\},$$

  where $B_{\rm rec}$ is either a B^0 or a $\overline{B}^0$.

- **Mixed events**: $B_{\rm rec}$ and $B_{\rm tag}$ have the same flavor, *i.e.* a B^0B^0 or $\overline{B}^0\overline{B}^0$ pair. The mixed amplitudes for Eq. (2.39) are

$$\left\{ \begin{array}{rcl|rcl} A_1 & = & A_r & A_2 & = & A_t \\ \overline{A}_1 & = & 0 & \overline{A}_2 & = & 0 \end{array} \right\} \quad \text{and} \quad \left\{ \begin{array}{rcl|rcl} A_1 & = & 0 & A_2 & = & 0 \\ \overline{A}_1 & = & A_r & \overline{A}_2 & = & A_t \end{array} \right\}.$$

  The time-dependent rates for unmixed and mixed events are then

$$F_{\rm unmix}(\Delta t) \propto e^{-\Gamma|\Delta t|}\left(1+\cos\left(\Delta m_d \Delta t\right)\right), \tag{2.40}$$

$$F_{\rm mix}(\Delta t) \propto e^{-\Gamma|\Delta t|}\left(1-\cos\left(\Delta m_d \Delta t\right)\right). \tag{2.41}$$

A measurement of the $B^0\overline{B}^0$ oscillation frequency Δm_d can be extracted from the mixing asymmetry

$$\mathcal{A}_{\rm mix}(\Delta t) = \frac{F_{\rm unmix}(\Delta t) - F_{\rm mix}(\Delta t)}{F_{\rm unmix}(\Delta t) + F_{\rm mix}(\Delta t)} = \cos\left(\Delta m_d \Delta t\right). \tag{2.42}$$

Fig. 2.5 shows the Δt distributions of real unmixed and mixed events (including background events and resolution effects), together with the corresponding mixing asymmetry. The $B^0\overline{B}^0$ oscillation pattern is clearly visible. From Eq. (2.28), the mixing frequency is about 80 GHz.

CP **eigenstates**

Second, we discuss B decays to *CP* eigenstates. These events are used to measure *CP* violation. Here, $B_{\rm rec}$ is fully reconstructed in a *CP* eigenstate, f_{CP}, accessible to both B^0 and $\overline{B}^0$. A classic example is $B \to J/\psi K_{S,L}$. Again, at $\Delta t = 0$ the flavor of $B_{\rm rec}$ is inferred from the decay products of $B_{\rm tag}$.

Define the decay amplitudes

$$A_{f_{CP}} = \langle f_{CP}|H|B^0\rangle, \quad \overline{A}_{f_{CP}} = \langle f_{CP}|H|\overline{B}^0\rangle. \tag{2.43}$$

$B_{\rm tag}$ is either a B^0 or a $\overline{B}^0$, so the amplitudes inserted into Eq. (2.39) are

$$\left\{ \begin{array}{rcl|rcl} A_1 & = & A_{f_{CP}} & A_2 & = & A_t \\ \overline{A}_1 & = & \overline{A}_{f_{CP}} & \overline{A}_2 & = & 0 \end{array} \right\} \quad \text{and} \quad \left\{ \begin{array}{rcl|rcl} A_1 & = & A_{f_{CP}} & A_2 & = & 0 \\ \overline{A}_1 & = & \overline{A}_{f_{CP}} & \overline{A}_2 & = & A_t \end{array} \right\}.$$

The time-dependent probabilities are then

$$\begin{aligned} F(B_{\rm tag} = B^0, \Delta t) \propto\ & e^{-\Gamma|\Delta t|}\Big\{1 + \frac{1-|\lambda_{f_{CP}}|^2}{1+|\lambda_{f_{CP}}|^2}\cos(\Delta m_d \Delta t) \\ & - \frac{2\Im m \lambda_{f_{CP}}}{1+|\lambda_{f_{CP}}|^2}\sin(\Delta m_d \Delta t)\Big\} \end{aligned} \tag{2.44}$$

$$\begin{aligned} F(B_{\rm tag} = \overline{B}^0, \Delta t) \propto\ & e^{-\Gamma|\Delta t|}\Big\{1 - \frac{1-|\lambda_{f_{CP}}|^2}{1+|\lambda_{f_{CP}}|^2}\cos(\Delta m_d \Delta t) \\ & + \frac{2\Im m \lambda_{f_{CP}}}{1+|\lambda_{f_{CP}}|^2}\sin(\Delta m_d \Delta t)\Big\} \end{aligned} \tag{2.45}$$

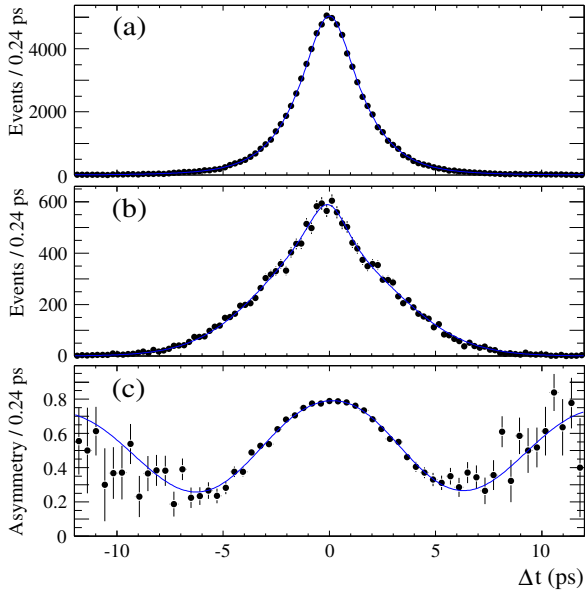

Figure 2.5: *Time evolution of: a) unmixed events, b) mixed events, and c) $\mathcal{A}_{\rm mix}(\Delta t)$ for di-lepton events measured at the BABAR experiment [29]. Likelihood fit projections are superimposed.*

using

$$\lambda_{f_{CP}} \equiv \frac{q}{p}\frac{\overline{A}_{f_{CP}}}{A_{f_{CP}}} = \eta_{f_{CP}}\frac{q}{p}\frac{\overline{A}_{\bar{f}_{CP}}}{A_{f_{CP}}} \ . \tag{2.46}$$

The second form of $\lambda_{f_{CP}}$ employs

$$\bar{A}_{f_{CP}} = \eta_{f_{CP}}\overline{A}_{\bar{f}_{CP}}, \tag{2.47}$$

where $\eta_{f_{CP}}$ is the *CP* eigenvalue of f_{CP}, and $\overline{A}_{\bar{f}_{CP}} = \langle \bar{f}_{CP}|H|\overline{B}^0\rangle$.

The time-dependent *CP* asymmetry is defined as

$$\mathcal{A}_{CP}(\Delta t) = \frac{F_{B_{\rm tag}=B^0} - F_{B_{\rm tag}=\overline{B}^0}}{F_{B_{\rm tag}=B^0} + F_{B_{\rm tag}=\overline{B}^0}} = \frac{1-|\lambda_{f_{CP}}|^2}{1+|\lambda_{f_{CP}}|^2}\cos\left(\Delta m_d \Delta t\right) - \frac{2\Im m\lambda_{f_{CP}}}{1+|\lambda_{f_{CP}}|^2}\sin\left(\Delta m_d \Delta t\right). \tag{2.48}$$

The amplitudes of the sine and cosine terms relate to different types of *CP* violation, as discussed in the following Section.

Using Eqs. (2.30, 2.46), for $B \to J/\psi K_{S,L}$ one has to good approximation [30]

$$\lambda_{f_{CP}} = \eta_{f_{CP}} e^{-2i\beta} \Rightarrow \quad |\lambda_{f_{CP}}| = 1, \quad \mathcal{I}m\lambda_{f_{CP}} = -\eta_{f_{CP}}\sin 2\beta\,, \tag{2.49}$$

giving the asymmetry

$$\mathcal{A}_{CP} = -\eta_{f_{CP}}\sin 2\beta \sin\left(\Delta m_d \Delta t\right). \tag{2.50}$$

The amplitude of the time-dependent asymmetry is the key to the *CP* angle β. In a time-integrated analysis the sine term vanishes. Therefore, in coherent $B^0\overline{B}^0$ production, the *CP* asymmetry can only be determined with an analysis of the Δt distributions.

The Δt distributions and asymmetries between B^0 tags and $\overline{B}^0$ tags for the samples $B \to J/\psi K_S$ ($\eta_f = -1$) and $B \to J/\psi K_L$ ($\eta_f = +1$) [6] are shown in Fig. 2.6. The time-dependent *CP* asymmetries are clearly visible. The world average value is measured to be [31]

$$\sin 2\beta = 0.687 \pm 0.032\,. \tag{2.51}$$

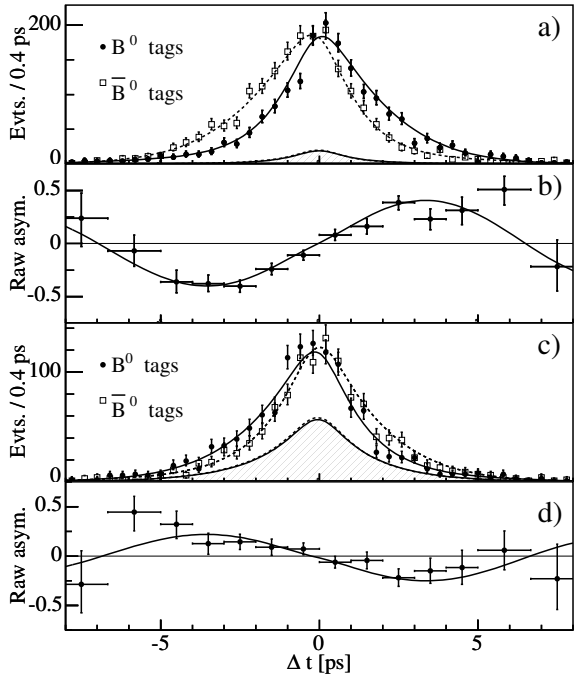

Figure 2.6: *a) Reconstructed $\eta_f = -1$ candidates (mostly $J/\psi K_S^0$) with a B^0 tag and with a $\overline{B}^0$ tag, and b) the CP asymmetry as functions of Δt. Figs. c) and d) are the corresponding plots for the $\eta_f = +1$ mode $J/\psi K_L^0$. The solid (dashed) curves represent the fit projections in Δt for B^0 ($\overline{B}^0$) tags. The shaded regions represent background contributions.*

2.5.4 Three types of *CP* violation in *B* decays

CP violation in the *B* system is generally classified into three categories. Each type of *CP* violation works along the principles laid out in Section 2.2, with two interfering decay amplitudes having different weak and strong phases.

Direct *CP* violation

Also known as '*CP* violation in decay', this type of *CP* violation occurs in both neutral and charged B meson decays. $B^0\overline{B}^0$ mixing is not involved. Given the processes $B \to f$ and $\overline{B} \to \bar{f}$, with decay amplitudes A_f and $\overline{A}_{\bar{f}}$, direct *CP* violation follows when

$$\left|\frac{\overline{A}_{\bar{f}}}{A_f}\right| \neq 1\,, \tag{2.52}$$

giving the *CP* asymmetry

$$\mathcal{A}_{CP} = \frac{1-|\overline{A}_{\bar{f}}/A_f|^2}{1+|\overline{A}_{\bar{f}}/A_f|^2} \neq 0\,. \tag{2.53}$$

Like in Section 2.2, A_f and $\overline{A}_{\bar{f}}$ consist of two (or more) decay paths having different weak and strong phases.

From Eq. (2.48) it is inferred that a non-zero coefficient in front of the cosine mixing term is a sign of direct *CP* violation.

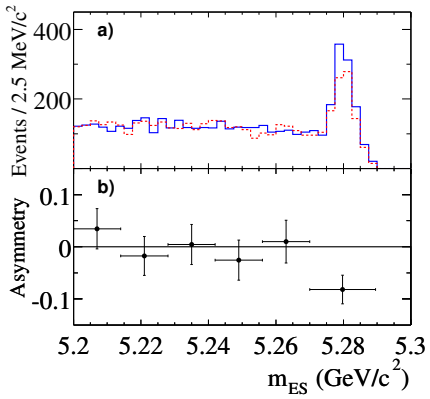

Figure 2.7: *a) B mass distribution of $B^0 \to K^+\pi^-$ (solid histogram) and $\overline{B}^0 \to K^-\pi^+$ (dashed histogram). b) CP asymmetry calculated for ranges of m_{ES}.*

Direct *CP* violation has been observed in the processes $B^0 \to K^+\pi^-$ and $\overline{B}^0 \to K^-\pi^+$, as shown in Fig. 2.7 [32]. There is a clear non-zero *CP* asymmetry in B signal window of $m_{ES} > 5.27$ GeV/c^2. For this decay channel $\mathcal{A}_{CP} = -10.8 \pm 1.7\%$ [31].

***CP* violation in mixing**

From Eqs. (2.32) and (2.33)

$$\begin{aligned} |\langle \overline{B}^0 | B^0_{\rm phys}(t)\rangle|^2 &= \left|\frac{q}{p}\right|^2 |g_-(t)|^2\,, \\ |\langle B^0 | \overline{B}^0_{\rm phys}(t)\rangle|^2 &= \left|\frac{p}{q}\right|^2 |g_-(t)|^2\,, \end{aligned} \tag{2.54}$$

and it follows that the oscillation probabilities of $B^0 \to \overline{B}^0$ and $\overline{B}^0 \to B^0$ are different when $|q/p| \neq 1$.

CP Violation in mixing is studied in semi-leptonic B^0 decays by measuring the asymmetry

$$\mathcal{A}_{SL} = \frac{\Gamma(B^0_{\text{phys}}(t) \to \ell^- \overline{\nu}_\ell X) - \Gamma(\overline{B}^0_{\text{phys}}(t) \to \ell^+ \nu_\ell X)}{\Gamma(B^0_{\text{phys}}(t) \to \ell^- \overline{\nu}_\ell X) + \Gamma(\overline{B}^0_{\text{phys}}(t) \to \ell^+ \nu_\ell X)} = \frac{1 - |q/p|^4}{1 + |q/p|^4} \tag{2.55}$$

The *CP* asymmetry is expected to be small, at the order of $\mathcal{O}(10^{-2})$, and to date has not been observed.

In Eq. (2.46), *CP* violation in mixing generally implies $|\lambda_f| \neq 1$, and again the cosine term in Eq. (2.48) is non-vanishing.

_CP_ violation in interference between mixing and decay

Consider the final state f, accessible by both B^0 and $\overline{B}^0$ decays. The third type of *CP* violation employs $B^0\overline{B}^0$ mixing to interfere the decay paths $B^0 \to f$ and $B^0 \to \overline{B}^0 \to f$. This is illustrated in Fig. 2.8. In path a) a B^0 decays directly to state f, with amplitude A_f. In path b) the B^0 first mixes to a $\overline{B}^0$, at which point it acquires the weak phase of q/p, and from there on decays to f, with amplitude $\overline{A}_f$. The analog paths for $\overline{B}^0 \to \bar{f}$ are shown in Figs. c) and d).

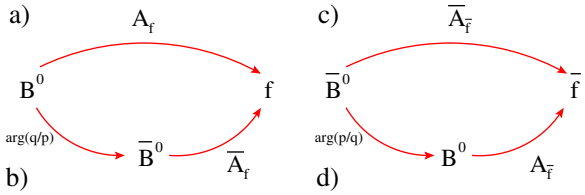

Figure 2.8: *The B^0 meson can decay a) directly to final state f, or b) first oscillate to a $\overline{B}^0$ and then decay to the same final state. For $\overline{B}^0$ mesons the analog paths are shown in c) and d).*

For f being a *CP* eigenstate, the interference between mixing and decay has been worked out in Section 2.5.3. In $B \to J/\psi K_S$, for example, the weak phase difference between decay paths a) and b) comes solely from q/p, acquired in the $B^0\overline{B}^0$ oscillation. Generally, an additional weak and strong phase difference can be induced by $\overline{A}_f$ over A_f. Due to the fact that, in Eqs. (2.34) and (2.35), $g_+(t)$ is real whereas $g_-(t)$ is purely imaginary, a *CP*-even phase of $\pi/2$ is picked up.

The case of non-*CP* eigenstates is similar, and is shown in Section 2.6. Like in Eq. (2.48), *CP* violation shows up as a sine (but not a cosine) mixing term in the time evolution of B^0 and $\overline{B}^0$ decays.

2.5.5 Measurements of α, β, γ using B decays

In this Section we discuss briefly how the CKM angles α, β, and γ can be obtained through the measurements of *CP* asymmetries in various B decay channels. A detailed discussion falls outside the scope of this thesis, and can be found in Refs. [16, 15].

In terms of the Wolfenstein parametrization, introduced in Eq. (2.14), the complex CKM phase is found in V_{td} and V_{ub}. As a rule of thumb only V_{td} and V_{ub} acquire a non-zero complex

phase

$$V_{td} = |V_{td}|e^{-i\beta}, \quad V_{ub} = |V_{ub}|e^{-i\gamma} \ , \tag{2.56}$$

and all other CKM couplings do not have complex phases, *i.e.* $V_{cb} = |V_{cb}|$

1. **Angle** β. In Section 2.5.3 it is shown that $\sin 2\beta$ is measured using $B \to J/\psi K_{S,L}$. The direct decays of $B^0 \to J/\psi K_{S,L}$ and $\overline{B}^0 \to J/\psi K_{S,L}$ both involve $\bar{b} \to \bar{c}$ and $b \to c$ transitions, which do not generate CKM phases. The phase 2β comes from $B^0\overline{B}^0$ mixing, due to the $\bar{t} \to \bar{d}$ and $t \to d$ transitions required.

2. **Angle** γ. As can be seen from Eq. (2.56), γ is obtained through the interference of a $b \to c$ and $b \to u$ quark transition. V_{cb} does not carry the CKM phase, whereas V_{ub} induces the weak phase γ. Example decays are $B^0 \to \bar{D}^0 K^+$, decaying through a $b \to c$ transition, and $B^0 \to D^0 K^+$, through a $b \to u$ transition, where $\bar{D}^0$ and D^0 must decay to same final state. In the next Section we study the interference of $B^0 \to D^{*-}\pi^+$ and $B^0 \to \overline{B}^0 \to D^{*-}\pi^+$, inducing the weak phase $2\beta+\gamma$.

3. **Angle** α. The weak phase α is the relative phase between V_{ub} and V_{td}. In the Wolfenstein parametrization α cannot be generated through a direct b transition. Instead, one uses the unitarity relation $\sin 2\alpha = -\sin(2\beta + 2\gamma)$. Therefore, α can only be studied using neutral B decays. Again, 2β is picked up through $B^0\overline{B}^0$ oscillation. The phase difference 2γ requires a $b \to u$ over $\bar{b} \to \bar{u}$ transition. Example decays are $B \to \rho^+\rho^-$ or $B \to \pi^+\pi^-$.

4. **New physics**. A popular place to look for new physics contributions is in $b \to s$ transitions. $b \to s$ has no tree level coupling in the Standard Model, and can only happen through suppressed loop diagrams. Loop diagrams are a natural place for new physics effects to show up in low energy phenomena. Popular decay channels are $B \to \phi K_S$ and $B \to \eta' K_S$.

2.6 The CKM-angle γ from $B^0 \to D^{(*)\mp}\pi^\pm$ and $B^0 \to D^\mp\rho^\pm$ decays

This thesis reports measurements of the *CP* asymmetries in $B^0 \to D^{(*)\mp}\pi^\pm$ and $B^0 \to D^\mp\rho^\pm$ decays [14]. We denote these decays as $B^0 \to D^{(*)\pm}h^\mp$, where $h^\mp$ is a charged pion or ρ meson. In this Section we discuss how the angle $2\beta+\gamma$ is obtained from the time-dependent distributions of $B^0 \to D^{(*)\mp}h^\pm$ [10].

Even though they are not *CP* eigenstates, the (six) final states $D^{(*)+}h^-$ and $D^{(*)-}h^+$ are accessible in both B^0 and $\overline{B}^0$ decays. The leading Feynman diagrams of $B \to D^+\pi^-$ are shown in Fig 2.9. There are no known penguin contributions, as can be inferred from the quark configuration of the final state. Because the Standard Model contributions are tree diagrams, it is unlikely that large new physics effects would be present.

In the following text we adopt the notation of Ref. [14]. Consider a $B^0\overline{B}^0$ pair produced at the $\Upsilon(4S)$ resonance. Again, one B is inferred to be a flavor eigenstate ($B_{\rm tag}$), say using $B^0 \to D^{*-}l^+\nu$ or $\overline{B}^0 \to D^{*+}l^-\bar{\nu}$, and the other is fully reconstructed ($B_{\rm rec}$) in the final state $D^{(*)+}h^-$ or $D^{(*)-}h^+$. From Eq. (2.39), the proper-time distributions of $B \to D^{(*)\pm}h^\mp$ decays

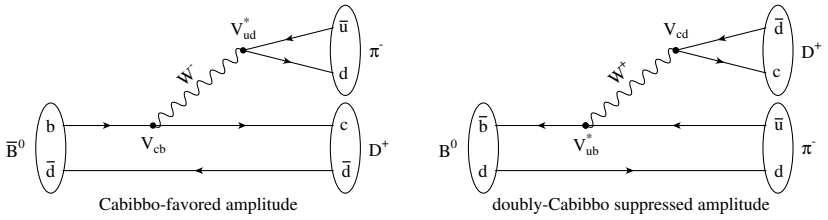

Figure 2.9: *The CKM-favored amplitude (left) and doubly-CKM-suppressed amplitude (right) for the final state* $D^+\pi^-$.

are

$$\begin{aligned}
F(B^0(\Delta t)\to D^{(*)-}h^+) &= Ne^{-|\Delta t|/\tau_{B^0}}\left(1+C\cos(\Delta m_d\Delta t)+(-1)^L S_+\sin(\Delta m_d\Delta t)\right),\\
F(\overline{B}^0(\Delta t)\to D^{(*)-}h^+) &= Ne^{-|\Delta t|/\tau_{B^0}}\left(1-C\cos(\Delta m_d\Delta t)-(-1)^L S_+\sin(\Delta m_d\Delta t)\right),\\
F(\overline{B}^0(\Delta t)\to D^{(*)+}h^-) &= Ne^{-|\Delta t|/\tau_{B^0}}\left(1+C\cos(\Delta m_d\Delta t)-(-1)^L S_-\sin(\Delta m_d\Delta t)\right),\\
F(B^0(\Delta t)\to D^{(*)+}h^-) &= Ne^{-|\Delta t|/\tau_{B^0}}\left(1-C\cos(\Delta m_d\Delta t)+(-1)^L S_-\sin(\Delta m_d\Delta t)\right),
\end{aligned} \tag{2.57}$$

where we neglect the decay width difference, and $\tau_{B^0}=1/\Gamma$ is the B^0 lifetime. The angular momentum of the decay is indicated with L. The cosine and sine terms are from interference between direct decay and decay after one or several $B^0\overline{B}^0$ oscillations. The S and C parameters are expressed as

$$S_\pm=-\frac{2\mathcal{I}m(\lambda_\pm)}{1+|\lambda_\pm|^2}, \quad \text{and} \quad C=\frac{1-r_\pm^2}{1+r_\pm^2}, \tag{2.58}$$

with $r_+\equiv|\lambda_+|$, $r_-\equiv 1/|\lambda_-|$, and

$$\lambda_\pm\equiv\lambda[D^{(*)\mp}h^\pm]\equiv\frac{q}{p}\frac{A(\overline{B}^0\to D^{(*)\mp}h^\pm)}{A(B^0\to D^{(*)\mp}h^\pm)}. \tag{2.59}$$

Note that $\lambda_\pm$ depends on the choice of final state.

Assuming no *CP* violation in mixing ($|q/p|=1$), as expected in the Standard Model, to good approximation q/p is given by Eq. (2.30)

$$\frac{q}{p}=\frac{V_{tb}^*V_{td}}{V_{tb}V_{td}^*}=e^{-i2\beta}.$$

For the final state $D^+\pi^-$, with help of Fig. 2.9 the ratio $\overline{A}_f/A_f$ is deduced as

$$\frac{A(\overline{B}^0\to D^+\pi^-)}{A(B^0\to D^+\pi^-)}=\frac{V_{cb}V_{ud}^*}{V_{cd}V_{ub}^*}\frac{\overline{M}(\overline{B}^0\to D^+\pi^-)}{M(B^0\to D^+\pi^-)}, \tag{2.60}$$

where $\overline{M}(\overline{B}^0\to D^+\pi^-)$ and $M(B^0\to D^+\pi^-)$ are hadronic decay amplitudes induced by strong interactions.

The combination of Eqs. (2.30) and (2.60) and the angle definitions in Eq. (2.20) leads to

$$\lambda_- = \lambda[D^+\pi^-] = e^{-i(2\beta+\gamma)} \left|\frac{V_{cb}V_{ud}^*}{V_{cd}V_{ub}^*}\right| \frac{\overline{M}(\overline{B}^0 \to D^+\pi^-)}{M(B^0 \to D^+\pi^-)}. \tag{2.61}$$

Extracting the strong phases results in

$$\lambda[D^+\pi^-] = e^{-i(2\beta+\gamma-\delta^{D\pi})} \left|\frac{V_{cb}V_{ud}^*}{V_{cd}V_{ub}^*}\right| \left|\frac{\overline{M}(\overline{B}^0 \to D^+\pi^-)}{M(B^0 \to D^+\pi^-)}\right|, \tag{2.62}$$

where $\delta^{D\pi}$ is the strong phase difference between $\overline{M}(\overline{B}^0 \to D^+\pi^-)$ and $M(B^0 \to D^+\pi^-)$.

In case of final state $D^-\pi^+$

$$\frac{A(\overline{B}^0 \to D^-\pi^+)}{A(B^0 \to D^-\pi^+)} = \frac{V_{ub}V_{cd}^*}{V_{ud}V_{cb}^*} \frac{\overline{M}(\overline{B}^0 \to D^-\pi^+)}{M(B^0 \to D^-\pi^+)}. \tag{2.63}$$

Conservation of CP in the strong interactions guarantees $\overline{M}_f = M_{\bar{f}}$ and $\overline{M}_{\bar{f}} = M_f$, so

$$\lambda_+ = \lambda[D^-\pi^+] = e^{-i(2\beta+\gamma+\delta^{D\pi})} \left|\frac{V_{cb}V_{ud}^*}{V_{cd}V_{ub}^*}\right| \left|\frac{M(B^0 \to D^+\pi^-)}{\overline{M}(\overline{B}^0 \to D^+\pi^-)}\right|, \tag{2.64}$$

or

$$|\lambda_+| = |1/\lambda_-|, \qquad r_+ = r_- \equiv r. \tag{2.65}$$

Similar expression holds for $\lambda[D^{(*)\pm}h^{\mp}]$, except that the hadronic matrix elements have different values.

Introducing the parameters r^j and δ^j, with $j = D\pi$, $D^*\pi$, $D\rho$, Eq. (2.58) simplifies to

$$S_{\pm}^j = \frac{2\,r^j}{1+[r^j]^2} \sin(2\beta+\gamma\pm\delta^j), \quad \text{and} \quad C^j = \frac{1-[r^j]^2}{1+[r^j]^2}. \tag{2.66}$$

The factor of $(-1)^L$ in Eqs. (2.57), first noted in Ref. [33], is absorbed in the strong phase, $\delta \to \delta + \pi$, without affecting the measurement. From Eq. (2.57) the CP asymmetry can then be defined as

$$\mathcal{A}_{CP}^j(\Delta t) = \frac{F_{B_{\rm tag}=B^0} - F_{B_{\rm tag}=\overline{B}^0}}{F_{B_{\rm tag}=B^0} + F_{B_{\rm tag}=\overline{B}^0}} \tag{2.67}$$

$$= \frac{2\,r^j}{1+[r^j]^2} \sin(2\beta+\gamma)\cos(\delta^j)\sin(\Delta m_d \Delta t). \tag{2.68}$$

Using this notation, the time-dependent decay distributions for the final state $D^-\pi^+$ are shown in Fig. 2.10.

In conclusion, the time evolution of $B^0 \to D^{(*)\pm}h^{\mp}$ decays is sensitive to the CP angle γ because the CKM-favored decay amplitude $\overline{B}^0 \to D^{(*)+}h^-$, which is proportional to the CKM matrix elements $V_{cb}V_{ud}^*$, and the doubly-CKM-suppressed decay amplitude $B^0 \to D^{(*)+}h^-$, proportional to $V_{cd}V_{ub}^*$, interfere due to $B^0\overline{B}^0$ mixing. The relative weak phase between these two amplitudes is γ. Including $B^0\overline{B}^0$ mixing, the total weak phase difference between the interfering amplitudes is $2\beta+\gamma$.

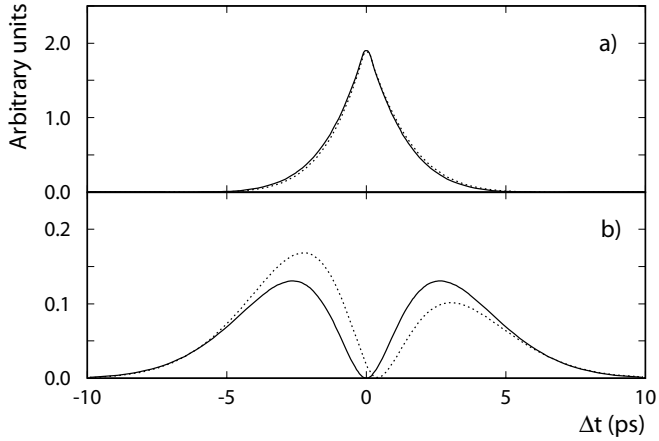

Figure 2.10: *Time-dependent decay distributions for the final state $D^{*-}\pi^+$, for a) a $\overline{B}^0$ tag, and b) a B^0 tag. The situation with no doubly-CKM-suppressed contribution on both the reconstruction-side is indicated with the solid line. The dotted line has $r = 0.1$, $\delta = 0$, and $2\beta + \gamma = 1.86$. In these examples, r is 5 times the expected value in order to clearly illustrate the difference with respect to the case with $r = 0$.*

2.6.1 Observations

From Table 2.1, current indirect measurements give: $\sin(2\beta+\gamma) = 0.94 \pm 0.03$, $\cos(2\beta+\gamma) = -0.34 \pm 0.10$. The angle β is well known from direct measurements, $\beta = 21.7^{+1.3}_{-1.2}{}^{\circ}$, so a measurement of $\sin(2\beta+\gamma)$ gives direct constraints on γ.

The angle $2\beta+\gamma$ can only be obtained from the amplitudes of the sine mixing terms, $S^j_\pm$. Assuming $\overline{M} \approx M$, r^j, with $j = D\pi$, $D^*\pi$, $D\rho$, equals $|V^*_{ub}V_{cd}/V_{cb}V^*_{ud}| \approx 0.02$ [17], or $|S^j_\pm| \lesssim 0.04$. The smallness of r^j greatly reduces the sensitivity to γ from $S^j_\pm$, making this measurement very challenging.

In theory, the time-dependent study of B decays to the final states $D^{(*)\pm}h^\mp$ allows one to extract the parameters r^j, $\sin(2\beta+\gamma+\delta^j)$, and $\sin(2\beta+\gamma-\delta^j)$ from the amplitudes of the mixing terms. The cosine amplitudes C^j depend quadratically on r^j, and, as a result, are very close to one. In practice, even at very high statistics there is no sensitivity to extract r^j. This implies that, to extract $2\beta+\gamma$, the parameters r^j are needed as external input parameters, and must be obtained through other means.

A naive method to get r^j is to measure the branching fractions $\mathcal{B}$ of the decays $B^0 \to D^{(*)+}h^-$ and $B^0 \to D^{(*)-}h^+$. The latter decays are Cabibbo allowed and have been measured [17], with branching fractions at the level of $\mathcal{O}(10^{-3})$ as shown in Table 2.3. Unfortunately, the former branching fractions are doubly Cabibbo suppressed, making their experimental measurements impossible. The expected branching ratios are too small, $\mathcal{O}(10^{-6})$, with an overwhelming background from the Cabibbo allowed decays. The only feasible way to obtain r^j is to measure $\mathcal{B}(B^0 \to D_s^{(*)+}h^-)$, as explained in Chapter 10.

Decay mode	Measured $\mathcal{B}$ ($\times 10^{-4}$)
$B^0 \to D^- \pi^+$	27.6 ± 2.5
$B^0 \to D^{*-} \pi^+$	27.6 ± 2.1
$B^0 \to D^- \rho^+$	77 ± 13

Table 2.3: *Measured branching fractions $\mathcal{B}$ of the Cabibbo allowed decays $B^0 \to D^{(*)-} h^+$.*

The strong phase differences are expected to be small, modulo π, but reliable estimates do not exist (see Chapter 10). Fixing the amplitude ratios r^j leaves six observables, $\sin(2\beta+\gamma \pm \delta^j)$, and four variables, $(2\beta+\gamma)$ and δ^j . There is a four-fold ambiguity in the extraction of $(2\beta+\gamma)$ from these parameters. Given the true solutions $(2\beta+\gamma)_0$ and $\delta(3)_0 = ({\delta^{D\pi}}_0, {\delta^{D^*\pi}}_0, {\delta^{D\rho}}_0)$, the algebraic relations of $S^j_\pm$ are invariant under the transformations

$$[2\beta+\gamma, \delta(3)] \;\to\; [-(2\beta+\gamma)_0, \pi - \delta(3)_0] \quad ; \quad \text{and} \tag{2.69}$$

$$\to\; [\pi - (2\beta+\gamma)_0, -\delta(3)_0]\,. \tag{2.70}$$

The presentation in terms of $|\sin(2\beta+\gamma)|$ is the same for all of these solutions.

For a single decay mode, another degeneracy in $(2\beta+\gamma)$ is the transformation

$$[2\beta+\gamma, \delta] \;\to\; [\pi/2 + \delta_0, \pi/2 - (2\beta+\gamma)_0]\,.$$

In our analysis with the modes $B \to D^\mp \pi^\pm$, $B \to D^{*\mp} \pi^\pm$, and $B \to D^\mp \rho^\pm$, this degeneracy is broken due to possibly different values of $\delta^{D\pi}$, $\delta^{D^*\pi}$, and $\delta^{D\rho}$.

Another difficulty in the *CP* measurement is the possible presence of a non-negligible *CP* asymmetries introduced in the decay of the tagging B. (The time evolutions discussed so far only considered the *CP* violation on the fully reconstructed side.) The modifications to the time-dependent evolution of our system are discussed in Chapter 5. They do not affect the ambiguity in the extraction of $2\beta+\gamma$.

It is interesting to consider what constraint can be made on the Standard Model from a measurement of $\sin(2\beta+\gamma)$. A typical measurement is shown in Fig. 2.11. Notice the four-fold ambiguity in the extraction γ. Unfortunately, a significant constraint can only be imposed on the apex position of the Unitarity triangle if the error on $\sin(2\beta+\gamma)$ is quite small. In part, this is due to $\sin(2\beta+\gamma) \approx 1$, with $d\sin(2\beta+\gamma)/d\gamma$ close to zero, so the variation of $\sin(2\beta+\gamma)$ has reduced impact on γ.

Other B decay channels to measure $\sin(2\beta+\gamma)$ and γ have been proposed. Each of these has advantages and disadvantages. Like our measurement, all are challenging experimentally. A comparison with existing measurements of γ is found in Section 12.3.

2.7 Analysis strategy

The Chapter culminates in an analysis strategy for the measurement of time-dependent *CP* asymmetries in $B^0 \to D^{(*)\mp} \pi^\pm$ and $B^0 \to D^\mp \rho^\pm$ decays.

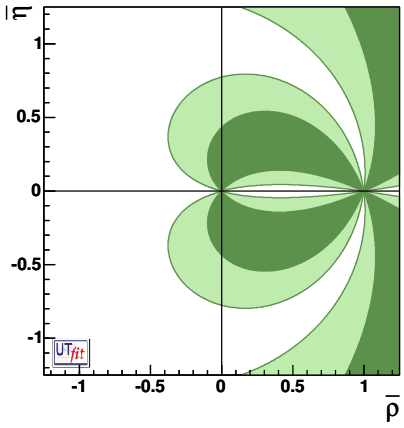

Figure 2.11: $\sin(2\beta+\gamma)$ *projected on the* $(\bar{\rho},\bar{\eta})$ *plane.*

2.7.1 Strategy for measurement of time-dependent *CP* asymmetries

The CKM angle γ can be obtained from the amplitude of the time-dependent *CP* asymmetry of Eq. (2.67)

$$\mathcal{A}^j_{CP}(\Delta t) = \frac{2\,r^j}{1+[r^j]^2}\sin(2\beta+\gamma)\cos(\delta^j)\sin(\Delta m_d \Delta t)\,,$$

which is measurable in the decays of $B \to D^{(*)\mp}\pi^{\pm}$ and $B \to D^{\mp}\rho^{\pm}$. Together, these occur in about one in hundred B decays. The amplitude ratios r^j equal about 0.02, the smallness of which greatly reduce the sensitivity to γ. Consequently, in order to have sufficient statistics for a sensitive *CP* analysis, it is necessary to produce a large number of B mesons.

Among other, B mesons are produced in the decay of the $\Upsilon(4S)$ meson, which decays exclusively to a $B\overline{B}$ pair. Half of these are $B^0\overline{B}^0$ pairs, which evolve coherently in time. Fig. 2.12 illustrates the topology of a boosted[2] $\Upsilon(4S)$ decay.

The measurement of $\mathcal{A}_{CP}$ requires knowledge of the time difference Δt between the decays of the two B mesons, as produced by the $\Upsilon(4S)$. The value of Δt can be computed from the spatial separation between the decay vertices of the B mesons. One B meson ($B_{\rm rec}$) is fully reconstructed in the final state $D^{(*)\pm}h^{\pm}$, and the decay vertex is computed from its decay products. The remaining particles in the event belong to the other B meson ($B_{\rm tag}$), and are combined inclusively to determine its decay vertex.

The next step is to determine whether $B_{\rm rec}$ is a B^0 or a $\overline{B}^0$ at $\Delta t = 0$. This cannot be deduced from the final state $D^{*\pm}h^{\mp}$, which is accessible to both B^0 and $\overline{B}^0$ mesons. Instead, one employs quantum coherence in the decay of the $\Upsilon(4S)$, which guarantees $B_{\rm rec}$ to be a B^0 ($\overline{B}^0$) if $B_{\rm tag}$ is a $\overline{B}^0$ (B^0) at the time of its decay.

When decaying to a flavor eigenstate, the flavor of $B_{\rm tag}$ can be determined from particle identification information and kinematic properties of reconstructed particles its the final state. The procedure is called b-flavor tagging.

[2]The boost of the $\Upsilon(4S)$ is explained in Section 3.2.

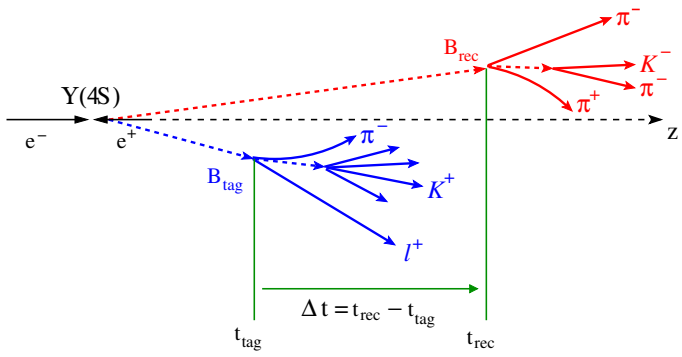

Figure 2.12: *The decay $\Upsilon(4S) \to B^0\overline{B}^0$, where one B decays to the final state $D^{*-}\pi^+$, $B_{\rm rec}$, and the other B decays in a flavor eigenstate, $B_{\rm tag}$.*

The constraint on the CKM-angle γ from measurements of the observables $S_{\pm}^{j}$ in Eq. (2.66) is set in Chapter 11. A motivation for the separation of the time-dependent analysis and the actual extraction of γ from the *CP* violation related parameters is found there as well. However, the extraction process first requires knowledge of the size of the amplitude ratios r^j, which are determined in Chapter 10.

2.7.2 Experimental requirements

The experimental requirements for the measurement of time-dependent *CP* asymmetries in B decays are described in the following Chapters. The analysis strategy is summarized as follows.

1. The main characteristics of the *BABAR* B factory are described in Chapter 3. This includes the PEP-II collider, needed to produce B mesons from the $\Upsilon(4S)$ resonance, followed by a brief description of the *BABAR* detector, used to detect the B decay products.

2. Chapter 4 discusses the analysis technique, consisting of

   (a) the selection criteria of $B\overline{B}$ events and B decay products, followed by the exclusive B reconstruction;

   (b) the inclusive b-flavor tagging algorithm;

   (c) the reconstruction procedure of B decay vertices and the measurement of Δt.

3. Chapter 6 describes the maximum-likelihood fit to the Δt distributions and the modeling of signal and background events.

Chapter 3

The *BABAR* experiment

The *BABAR* experiment consists of the PEP-II asymmetric-energy e^+e^- collider and the *BABAR* detector. Its general design considerations are discussed in Section 3.1.

A detailed description of the PEP-II collider can be found in Refs. [34, 35]. The main characteristics of the PEP-II collider are summarized in Section 3.2.

A detailed description of the *BABAR* detector is found in Ref. [36]. A brief overview of the components of the *BABAR* detector and their performance is given in Section 3.3. The *BABAR* data and Monte Carlo samples used in this analysis are found in Sections 3.4 and 3.5, respectively. Particle reconstruction and identification are summarized in Sections 3.6 and 3.7.

3.1 Design considerations

The design of the *BABAR* experiment has been optimized for the study of *CP* violation in the decays of neutral B mesons.

The $\Upsilon(4S)$ resonance is a clean source of B mesons, and decays to a B^+B^- or $B^0\overline{B}^0$ pair. The measurement of time-dependent *CP* violation requires knowledge of Δt, the time difference between the decays of the two B mesons. This can be computed from the distance between their decay vertices. The $\Upsilon(4S)$, with a mass of 10.58 GeV/c^2, is only slightly more massive than a $B\overline{B}$ pair. Consequently, with the $\Upsilon(4S)$ produced at rest, the low momenta of the mesons ($p^*_B \approx 340$ MeV/c) and the short B^0 lifetime ($\tau_{B^0} \approx 1.5$ ps) result in only a small separation between the decay vertices – too small to be measurable with sufficient precision.

The solution proposed by P. Oddone [37], applied at PEP-II, has been to produce the $\Upsilon(4S)$, and so the B mesons, with sufficient momentum in the lab frame. The boost of the B mesons leads to a greater displacement between the vertices, as demonstrated in Fig. 3.1, and allows the measurement of the spatial separation (about 260 μm average in *BABAR*).

The branching fractions and reconstruction efficiency of, and/or *CP* violation in interesting B decays are typically small. For this reason the PEP-II collider has high luminosity, yielding tens of millions of B decays per year.

The measurement of the decay-time distributions relies on good vertex reconstruction along the collision axis and in the transverse plane. The *BABAR* detector, designed to maximize the geometric acceptance for the boosted $\Upsilon(4S)$ decay products, possesses large and uniform coverage. High reconstruction efficiency and good momentum resolution for charged particles, together with reconstruction of the neutral particles, are important ingredients to fully reconstruct the B decays, and to separate signal events from background.

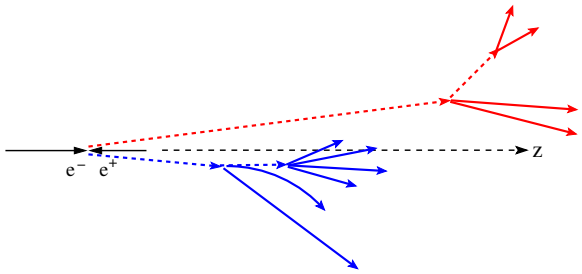

Figure 3.1: *The $\Upsilon(4S) \to B\bar{B}$ decay, boosted in the laboratory frame [37].*

Another requirement for time-dependent measurements is the determination of the flavor of one of the two decaying B mesons. As described in Chapter 4, this is done by using the B decay products like leptons, kaons and other flavor-sensitive features such as low momentum pions from D^* decays. For this purpose, *BABAR* has good particle identification (*i.e.* high efficiency and low mis-identification probability) and high tracking efficiency in a wide momentum range.

3.2 The asymmetric e^+e^- collider PEP-II

PEP-II is an asymmetric-energy e^+e^- collider, located at the Stanford Linear Accelerator Center (SLAC). SLAC's 3.6 km linear accelerator feeds 9.0 GeV electron bunches into a high energy ring (HER) and 3.1 GeV positron bunches into a low energy ring (LER). The rings have a circumference of 2.2 km. The particle bunches, kept in orbit by magnets and radio-frequency acceleration, are collided head-on at a unique interaction region inside the *BABAR* detector. At this point, the beams are brought together and separated by a pair of dipole magnets, and fine-tuning is provided by a series of quadrupole magnets.

High luminosity is achieved by maintaining several hundred bunches of electrons and positrons in each ring simultaneously. Maximum luminosity is maintained by continuously 'trickling' new bunches into the rings. Additionally, trickle injection makes fill-ups unnecessary, minimizing down-time from data taking.

The main technical design and operating parameters of PEP-II are listed in Table 3.1 [36]. PEP-II has significantly surpassed its design goals, both in terms of instantaneous and integrated daily luminosity.

PEP-II operates at a center-of-mass (CM) energy of 10.58 GeV, the mass of the $\Upsilon(4S)$ resonance. The $\Upsilon(4S)$ system is Lorentz boosted in the electron direction, with $\beta\gamma \approx 0.55$. The resulting B mesons travel an average distance of 260 μm along the electron beam before they decay. The cross sections for the main physics processes at the $\Upsilon(4S)$ energy are listed in Table 3.2 [16]. At about 1/nb, the production of $\Upsilon(4S) \to B\overline{B}$ accounts for a quarter of the total hadronic cross section.

The structure of the Υ resonances are shown in Fig 3.2 [38]. Most of the data are recorded at the peak of the $\Upsilon(4S)$ resonance (on-resonance data), right above the energy threshold of $B\overline{B}$ production. A small portion of the the data ($\approx 9\%$) is taken at a CM energy 40 MeV below the $\Upsilon(4S)$ peak (off-resonance data) in order to study only $e^+e^- \to u\bar{u}, d\bar{d}, s\bar{s}, c\bar{c}$ events. These are a source of background in many B decay analyses, commonly referred to as continuum

Parameters	Design	Best
Energy HER/LER (GeV)	9.0/3.1	9.0/3.1
Current HER/LER (A)	0.75/2.15	1.8/3.0
# of bunches	1658	1722
Bunch spacing (ns)	4.2	6.3–10.5
σ_{Lx} (μm)	110	90
σ_{Ly} (μm)	3.3	4
σ_{Lz} (mm)	9	9
Luminosity ($10^{33}\,\mathrm{cm}^{-2}\mathrm{s}^{-1}$)	3	11.2
Luminosity (pb^{-1}/d)	135	847

Table 3.1: *The design and best values of the PEP-II beam parameters, during the period of 1999–2006. HER and LER refer to the high energy e^- and low energy e^+ ring, respectively. The horizontal, vertical, and longitudinal RMS size of the luminous region are indicated with σ_{Lx}, σ_{Ly}, and σ_{Lz}, respectively.*

$e^+e^- \to X$	Cross section (nb)
$b\bar{b}$	1.1
$u\bar{u}, d\bar{d}, s\bar{s}, c\bar{c}$	3.4
$\tau^+\tau^-$	0.9
$\mu^+\mu^-$	1.2
e^+e^-	~ 53

Table 3.2: *Production cross sections at $\sqrt{s} = 10.58$ GeV. The e^+e^- cross section includes the detector acceptance.*

background.

The QED processes $e^+e^- \to e^+e^-, \mu^+\mu^-, \tau^+\tau^-$ are mostly used to study and calibrate the subsystems of the *BABAR* detector. Only a small fraction of these events is selected by the trigger, designed to maximize the number of selected hadronic events.

Knowledge of the beam energies is used to compute two important kinematic variables for selecting B meson candidates and rejecting combinatorial background (see Section 4.1.1). The energies are computed from the magnetic bending strength, and from the average deviations of the accelerating radio-frequencies from their central values. The relative energy setting for each beam is accurate and stable to about 1 MeV. The systematic uncertainty in the PEP-II calculation is estimated to be 5–10 MeV. The RMS energy spreads of the LER and HER beams are 2.3 MeV and 5.5 MeV, respectively.

The direction of the boost relative to the *BABAR* coordinate system is measured run-by-run using $e^+e^- \to e^+e^-$ and $e^+e^- \to \mu^+\mu^-$ events.

The size of the luminous region (or 'beam spot') affects the measurement of the distance between the B decay vertices (see Section 4.3). Events with only two tracks, mostly $e^+e^- \to e^+e^-$ and $e^+e^- \to \mu^+\mu^-$, are used to determine the parameters of the beam spot relative to the *BABAR* coordinate system. The size, position, and angles of the beam spot are determined every ten minutes from the collected ensemble of vertices of two-track events. The horizontal size is around 90 μm. The vertical size is too small to be measured directly, and is about 4 μm

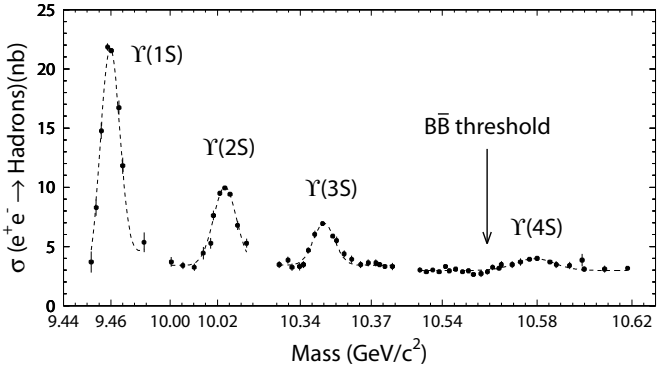

Figure 3.2: *Structure of the Υ resonances [38]. The mass of the $\Upsilon(4S)$ is above the threshold of $B\overline{B}$ production.*

from the measured luminosity. The uncertainties in the average position of the beam spot are less than a micron in the transverse plane, and about 100 μm along the beam axis. Between each determination, the random walk in the transverse plane is about 10 μm [39].

3.3 The *BABAR* detector

The design of the *BABAR* detector has been driven by the time-dependent study of B decays.

Fig. 3.3 shows a longitudinal Section through the *BABAR* detector. From the interaction point outward, its sub-detectors are

1. Silicon Vertex Tracker (SVT);
2. Drift CHamber (DCH);
3. Detector of Internally Reflected Čerenkov light (DIRC);
4. ElectroMagnetic Calorimeter (EMC);
5. Superconducting coil generating a magnetic field of 1.5 T; and
6. Instrumented Flux Return (IFR).

Next, we briefly describe the main features of each *BABAR* subsystem, focusing on those most relevant to this analysis.

The detector, designed for maximum acceptance of the boosted decay products, is offset relative to the beam-beam interaction point by 0.37m in the direction of the lower energy beam. Cylindrical symmetry is maintained around the beam direction. The polar angle $\theta_{\rm lab}$ coverage extends to 350 mrad in the forward direction and 400 mrad in the backward direction, defined relative to the high energy beam.

The right-handed coordinate system [40] is anchored on the drift chamber, with the z-axis coinciding with its principal axis. This axis is offset relative to the collision axis by about

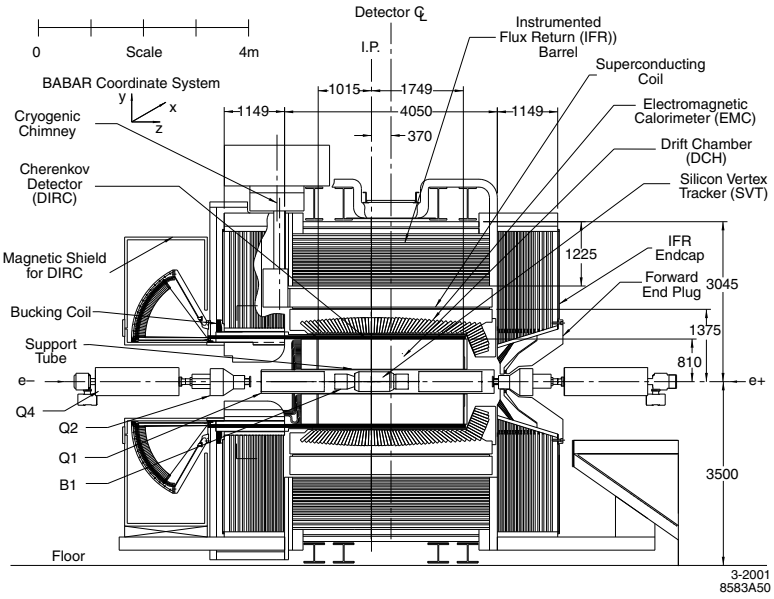

Figure 3.3: *Longitudinal section of the BABAR detector.*

20 mrad in the horizontal plane to minimize perturbations of the beams by the *BABAR* solenoid field [41]. The positive y-axis points upward, and the positive x-axis points away from the center of the PEP-II rings.

3.3.1 Silicon Vertex Tracker (SVT)

The silicon vertex tracker (SVT) is the crucial subdetector for the measurement of B^0-meson decay vertices. The SVT constitutes the inner part of the *BABAR* tracking system. The second tracking subsystem, the drift chamber, is discussed in the following Section.

The SVT has been designed to measure the angles and positions of charged particles just outside the beam pipe. Since the average momentum of charged particles produced in B decays is less than 1 GeV/c, multiple Coulomb scattering is a significant limitation on the resolution of the track parameters. Special care has been taken to reduce the volume and the amount of material in the tracking system.

The SVT is composed of five layers of double-sided silicon strip detectors, as schematically shown in Fig. 3.4. It is assembled from modules with readout at each end, thus reducing the inactive material in the acceptance volume. The tracker has a total of 340 silicon detectors ('wafers'), covering an area of about 1m^2, with a total of 150,000 readout channels. Each SVT strip has a typical hit resolution of 10 micron.

The inner three layers primarily are closest to the interaction point and provide the angular and vertex information for a track. They are mounted as close to the beam pipe as possible (radius of 3.2 cm) to minimize the impact of multiple scattering in the beam pipe on the extrapolation to the decay vertex. The outer two layers have much larger radii (14.4 cm) in

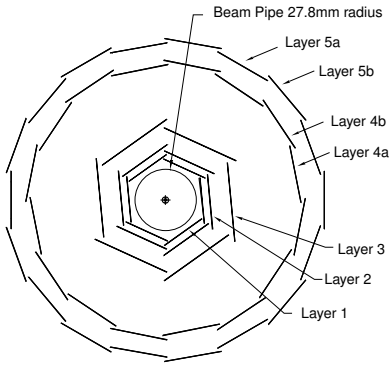

Figure 3.4: *Transverse view of a section of the SVT.*

order to provide the coordinate and the angle measurements needed to link SVT and drift chamber tracks.

Charged particles with transverse momenta between 60 MeV/c and 120 MeV/c, such as low momentum pions from D^* decays, do not reach or cannot be reconstructed by the DCH, for which the SVT provides all tracking information.

Since the SVT is not a rigid body, the relative positions of its wafers need to be aligned from time to time (called 'local alignment'). The alignment procedure is performed with cosmic rays, and e^+e^- and $\mu^+\mu^-$ events. The local alignment is relatively stable in time and the procedure is performed only after detector access or a magnet quench. The SVT local alignment is a source of systematic bias or distortion in the measurement of the distance of the two B decay vertices, and is accounted for in the CP asymmetry analysis.

3.3.2 Drift Chamber (DCH)

Combined with the SVT, the drift chamber forms the *BABAR* tracking system. The main purpose of the drift chamber is to determine the momentum measurement of charged particles. The DCH also supplies trigger information and a measurement of the energy loss $\mathrm{d}E/\mathrm{d}x$ used for particle identification.

A longitudinal cross view of the drift chamber is shown in Fig. 3.5. The readout electronics are mounted on the backward end-plate of the chamber, minimizing the amount of material in front of the calorimeter end-cap. The chamber is 280 cm long and occupies the radial region of $22 < r < 80$ cm. It consists of 7,104 small, approximately hexagonal cells, arranged in 40 cylindrical layers. The 40 layers are grouped into 10 super layers.

Each cell consists of a tungsten-rhenium sense wire surrounded by six aluminum field wires. The field wires are at ground potential. A positive high voltage of 1,930V applied to the sense wires. Two cell types exist with different geometry along the z direction: axial and stereo cells. The former run parallel to the z axis (forming axial layers), while the latter are tilted at a small stereo angle (stereo layers), which varies between 45 and 77 mrad. Stereo cells provide longitudinal information for the tracks, while both cell types provide curvature information. With 40 layers, the DCH can provide up to 40 measurements of space coordinates per track, ensuring high reconstruction efficiency for tracks with transverse momentum greater

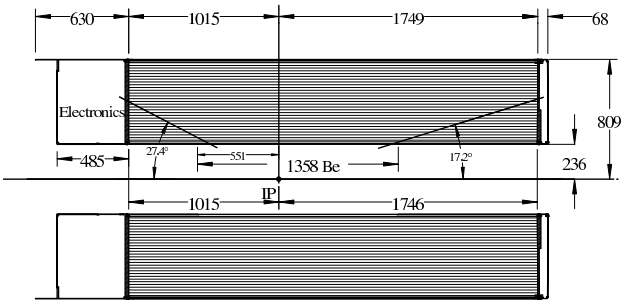

Figure 3.5: *Longitudinal view of a section of the DCH.*

than 100 MeV/c.

The DCH is filled with a 80 : 20 mixture of helium and isobutane. The gas mixture, wire material, and thickness, have been chosen to keep multiple scattering to a minimum. At normal incidence the DCH is only 1.08×10^{-2} radiation lengths long.

The DCH determines the global coordinate system for the *BABAR* detector. Because of seismic activity the SVT moves with respect to the drift chamber, and has to be aligned on a run-to-run basis ('global alignment'). The alignment procedure is performed with e^+e^- and $\mu^+\mu^-$ events. The global alignment procedure determines three translation and three rotation parameters by minimizing the difference between the track parameters obtained with the SVT-only and DCH-only track fits.

3.3.3 Detector of internally reflected Čerenkov light (DIRC)

The DIRC is a Čerenkov-based detector devoted to particle identification (PID), designed to provide separation of pions and kaons from momenta of about 500 MeV/c to 4.5 GeV/c. The DIRC is placed between the DCH and the calorimeter, and occupies only a small radial volume (10 cm). The detector is composed of 156 synthetic fused silica bars, 4.9m long, oriented parallel to the z axis, with a rectangular cross section, 1.7×3.5 cm.

The bar material has been chosen for its resistance to ionizing radiation, its long attenuation length, large index of refraction ($n = 1.473$), and low chromatic dispersion within the wavelength acceptance. A charged particle above the Čerenkov threshold emits Čerenkov photons, with an angle θ_c with respect to its track

$$\cos\theta_c = \frac{1}{n\beta}, \tag{3.1}$$

where $\beta = v/c$, v is the velocity of the particle, and c is the speed of light. For particles with β close to 1 some photons will always lie within the total internal reflection limit.

The Čerenkov light is transported to either one or both ends of the bars by total internal reflection, preserving θ_c at each reflection. To avoid instrumenting both ends of the bars, a perpendicular mirror is placed at the forward end. Photons emerge at the backward end into a toroidal water tank, called 'the standoff box', where they are detected by an array of photomultiplier tubes (PMTs). This array forms the backward wall of the tank, located beyond

the backward end of the magnet. Fig 3.6 shows a schematic view of the DIRC detector and illustrates the principles of light production, transport, and imaging.

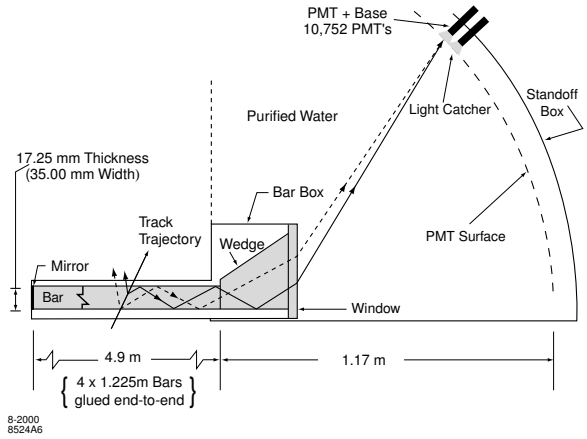

Figure 3.6: *Schematics of the DIRC fused silica radiator bars and imaging region.*

Images of the Čerenkov rings are reconstructed from the position and time of arrival of the signals in the PMTs. The Čerenkov light pattern is essentially a conic Section, where the cone opening-angle is the Čerenkov production angle, modified by refraction at the exit from the fused silica window. Time information is used to exclude other tracks in the same event as the source of the photon, and to reject beam-induced background hits.

The angular resolution on a single photon is about 10 mrad, while the time resolution is about 1.7 ns, close to the intrinsic time spread of a PMT. In absence of systematic errors, the resolution on θ_c is the single photon angle resolution divided by the square root of the number of photons detected. Measured on $\mu^+\mu^-$ events, this resolution is about 2.5 mrad.

3.3.4 Electromagnetic calorimeter (EMC)

The electromagnetic calorimeter (EMC) has been designed to detect electromagnetic showers with excellent energy and angular resolution, over an energy range from 20 MeV to 4 GeV. This allows the detection of low-energy π^0 and η^0 mesons from B decays, and higher energy photons and electrons from other radiative processes.

A longitudinal section of the EMC subdetector is shown in Fig. 3.7. The EMC is made of 6,580 thallium doped cesium iodide (Cs(Tl)) crystals. The crystals are arranged in modules that are supported individually from an external structure: a barrel and forward end-cap. The barrel is arranged in 48 distinct rings with 120 identical crystals each. The end-cap holds 820 crystals arranged in eight rings. The crystals, with radiation lengths between 16.0 and 17.5 X_0, are each read out with a pair of silicon photodiodes.

The amount of material in front and in-between the crystals is minimized in order to obtain the desired resolutions. At normal incidence there are in total 0.41 radiation lengths in front of the EMC.

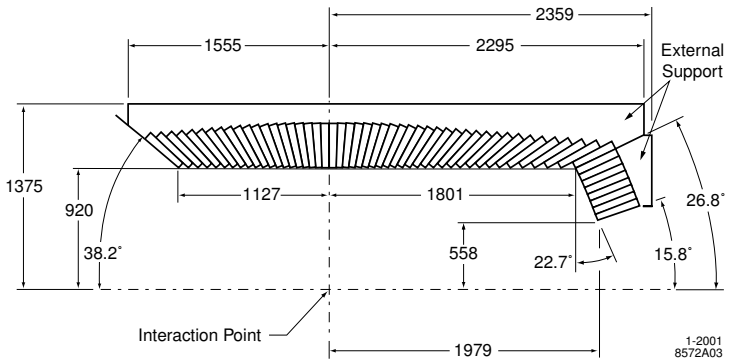

Figure 3.7: *EMC longitudinal section.*

3.3.5 Instrumented flux return (IFR)

The instrumented flux return (IFR) has been designed to identify muons and to detect neutral hadrons, such as K_L mesons.

Fig. 3.8 shows a 3D view of the IFR barrel and end-caps. The magnet flux return steel in the barrel and the two end doors (end-caps) is segmented into layers, increasing in thickness from 2 cm to 10 cm. Single gap resistive plate chambers (RPCs) are inserted between the absorbers to detect streamers from ionizing particles through external capacitive readout strips.

There are 19 layers of RPCs in the barrel and 18 in the end-caps. Additionally, two cylindrical layers of RPCs with four readout planes are placed in front of the magnet cryostat to detect particles exiting the EMC.

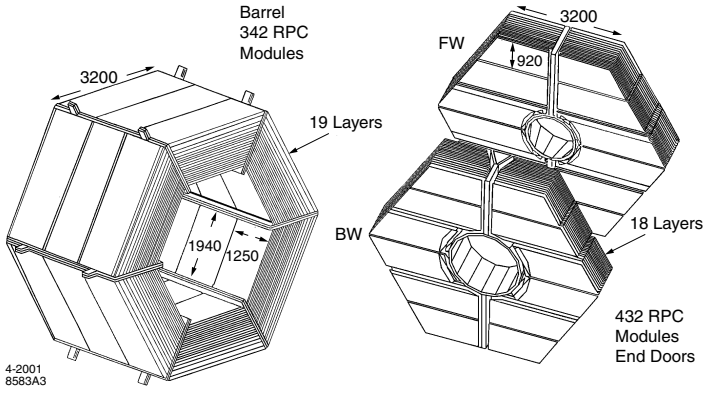

Figure 3.8: *View of IFR barrel and end-caps.*

The IFR reconstruction algorithm groups hits in the RPCs into clusters. A charged particle is associated to IFR clusters if the cluster is a predefined distance from the intersection of its

trajectory with the RPC planes.

3.3.6 Trigger system and data acquisition

The trigger system is designed to select events of interest with a high, stable, and well-understood efficiency, while rejecting background events and keeping the total event rate under 370 Hz.

Interesting events include $B\overline{B}$ and other $q\bar{q}$ events, as well as QED events needed for diagnostic and calibration purposes. The production rates of these events at the $\Upsilon(4S)$ resonance for a luminosity of 1×10^{34} cm^{-2} s^{-1} are shown in Table 3.3. Background events are due to interactions of the beams with residual gas or the beam pipe, with typical rates up to 70 kHz.

Event type	Cross Section (nb)	Production Rate (Hz)	Level 1 Trigger Rate (Hz)
$B\overline{B}$	1.1	10.7	10.7
$u\overline{u}$ +$d\overline{d}$ +$c\overline{c}$ +$s\overline{s}$	3.4	34.0	33.7
e^+e^-	∼53	530	520
$\mu^+\mu^-$	1.2	11.7	10.3
$\tau^+\tau^-$	0.9	9.3	8.0

Table 3.3: *Cross sections, production and trigger rates for the principal physics processes at 10.58* GeV/c^2 *for a luminosity of* $1 \times 10^{34}\,\mathrm{cm}^{-2}\mathrm{s}^{-1}$.

The trigger is implemented as a two-level hierarchy, the Level 1 (L1) in hardware, followed by the Level 3 (L3) in software. The trigger system is designed to accommodate up to ten times the expected PEP-II background rates at design luminosity.

The L1 trigger is responsible for interpreting incoming detector signals, and recognizing and removing beam-induced background to a level acceptable for the L3 software trigger. The L1 trigger decision is based on charged tracks in the DCH above a preset transverse momentum, showers in the EMC, and tracks detected in the IFR. During normal operation, the L1 is configured to have an output rate of typically 2.5 kHz.

The L3 responds to the L1 output, performs a rate reduction for the main physics sources, and identifies and flags special categories of events needed for luminosity determination, diagnostic, and calibration purposes. The L3 filter acceptance for physics is about 280 Hz, while 90 Hz contain the other special event categories. The selected events are then stored for offline processing.

At a luminosity of 1×10^{34} cm^{-2} s^{-1}, the trigger efficiency exceeds 98% for all $B\overline{B}$ events.

3.4 Data sample

The integrated luminosity delivered by PEP-II and recorded with *BABAR* between October 1999 and July 2004 is shown in Fig. 3.9. During that period, the luminosity recorded by *BABAR* has been about 244 fb^{-1}, including 22.7 fb^{-1} of off-peak data [42]. About 209 fb^{-1} of on-resonance data, corresponding to 230 million $B\overline{B}$ pairs, are used in the analysis presented in this thesis.

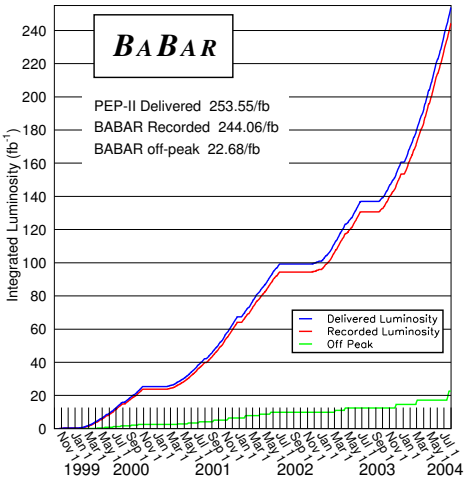

Figure 3.9: *The integrated luminosity delivered by PEP-II and recorded by BABAR between October 1999 and July 2004.*

The relative luminosity is monitored by PEP-II through the measurement of radiative Bhabha scattering. The absolute luminosity is measured offline by *BABAR* from e^+e^- and $\mu^+\mu^-$ production. The absolute luminosity has an estimated systematic error of about 1.5%, with negligible statistical uncertainty.

3.5 Monte Carlo sample

We use Monte Carlo simulation of the *BABAR* detector response based on GEANT4 software [43] to validate the analysis procedure and to estimate some of the background event levels. Particle production and decays are simulated in an event generator program, EvtGen [44], interfaced to LUND/JETSET [45]. Table 3.4 shows the fully-simulated Monte Carlo samples considered in this analysis, compared with the available data sample.

3.6 Particle reconstruction

This Section briefly discusses charged and neutral particle reconstruction in *BABAR*.

3.6.1 Charged particle reconstruction

A typical $B\overline{B}$ event has an average multiplicity of 11 charged tracks. Track reconstruction uses information from both the SVT and the DCH, as well as the L3 trigger.

Charged track finding is based on three different algorithms [46], and starts with pattern recognition in the DCH. The first algorithm uses the L3 trigger routine for finding and linking superlayer-based track segments from moderate-to-high p_t tracks, originating from the interaction point. Two other tracking algorithms are designed to find tracks with lower p_t, which did

Sample	Generated events (M)	Luminosity (fb^{-1})
On-resonance data	–	209
Signal cocktail	21.3	3133
Generic $B^0\overline{B}^0$	546	995
Generic B^+B^-	540	981
Continuum $c\bar{c}$	418	321
Continuum $u\bar{u}, d\bar{d}, s\bar{s}$	711	340

Table 3.4: *Fully-simulated Monte Carlo samples considered in this analysis. The 'signal cocktail' sample is a mixture of $B \to D^{(*)\mp}h^{\pm}$ ($h = \pi, \rho, a_1$) events, with branching fractions taken from the PDG.*

not pass through the entire DCH, or that did not originate from the interaction point. These algorithms use track segments not assigned to previously reconstructed tracks. All tracks found are refit with a Kalman filter [47], which takes into account the distribution of material in the detector and a detailed map of the magnetic field.

The tracks are extrapolated through the intervening material and field into the SVT, where silicon-strip hits are added if consistent within extrapolation errors. Among the possible SVT segments those with the smallest residuals and the largest number of SVT layers are kept, and a Kalman fit is performed to the full set of DCH and SVT hits. Any remaining SVT hits are passed to two complementary, standalone track finders. Finally, an attempt is made to match SVT- and DCH-only track segments to recover tracks scattered in the support tube.

Parameter	Description
ω	Curvature of the track, the inverse of the transverse momentum p_t
z_0	Distance along the z axis between the POCA and the origin
d_0	Distance in the x–y plane between the POCA and the origin
ϕ_0	Azimuth angle of POCA
$\tan\lambda$	Dip angle of the track relative to the transverse plane

Table 3.5: *Parameters describing the trajectory of a charged track. POCA stands for the point of closest approach of the trajectory to the z axis.*

The trajectory of a charged particle is defined by five parameters, listed in Table 3.5. The resolutions of the five track parameters are monitored with e^+e^- and $\mu^+\mu^-$ events and checked offline in multi-hadron events and cosmic ray muons. The measured resolutions depend on the transverse momentum p_t of the tracks. Using cosmic ray tracks with p_t of about $3\,\text{GeV}/c$, the resolutions are: $\sigma_{d_0} = 23\,\mu\text{m}$, $\sigma_{\phi_0} = 0.43\,\text{mrad}$, $\sigma_{z_0} = 29\,\mu\text{m}$, and $\sigma_{\tan\lambda} = 0.53 \times 10^{-3}$.

The left-hand side of Fig. 3.10 shows the the dependence of d_0 and z_0 resolutions on the transverse momentum p_t, measured with tracks from hadronic events. The right-hand side of Fig. 3.10 shows the resolution on the transverse momentum p_t as measured with cosmic muons traversing both the DCH and the SVT. The data are well represented by the linear function

$$\sigma_{p_t}/p_t = (0.13 \pm 0.01)\% \cdot p_t + (0.45 \pm 0.03)\%,$$

where p_t is measured in GeV/c. For a track with p_t of 1 GeV/c the resolution is about 5 MeV/c.

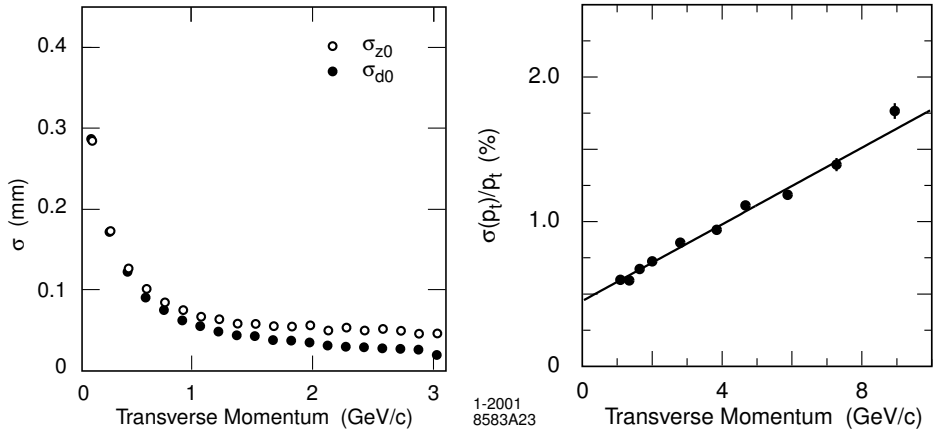

Figure 3.10: *Resolution as a function of the transverse momentum p_t for: (left) impact parameters d_0 and z_0, measured with multi-hadron events, and (right) the transverse momentum p_t, measured with cosmic muons traversing the DCH and the SVT.*

For later use, a good quality track, `GoodTrack`, consists of a charged track satisfying

1. $p < 10\,\text{GeV}/c$,
2. $d_0 < 1.5\,\text{cm}$,
3. $z_0 < 10\,\text{cm}$,
4. $p_t > 100\,\text{MeV}/c$, and
5. 12 or more DCH hits.

3.6.2 Reconstruction of neutral particles

Neutral particles, such as photons and π^0s, form electromagnetic showers in the EMC. A typical electromagnetic shower spreads over many adjacent crystals, forming a 'cluster' of energy deposits. Pattern recognition algorithms are used to identify these clusters, and to differentiate single clusters, having one energy maximum, from merged clusters, with more than one local energy maximum – also referred to as 'bumps'. Bumps occur, for example, when photons from high-energy π^0 or η decays are unresolved, resulting in two close showers.

Clusters are reconstructed around initial seed crystals, containing at least 10 MeV of deposited energy, E. Neighboring crystals are added to the cluster if $E > 1\,\text{MeV}$. If the newly added crystal has $E > 3\,\text{MeV}$, its neighbors are also considered for inclusion in the cluster. Local maxima within a cluster are defined as candidate crystals that have an energy exceeding each of its neighbors. The position of each bump is calculated with a center-of-gravity method [48].

The algorithms also check whether a bump is generated by a charged or a neutral particle. Neutral particles are required not to match to any charged track extrapolated from the tracking volume to the inner surface. The distance between a track impact point and the bump centroid is calculated, and compared with Monte Carlo expectations for different particle species. If the distance is consistent with the expectation, the bump is associated with the charged particle. Otherwise, it is assumed to originate from a photon.

The energy resolution of the calorimeter is measured from a radioactive source at low energies, and is derived from Bhabha scattering at high energies. At normal incidence, the energy resolution for photons is

$$\frac{\sigma_E}{E} = \frac{2.3\%}{E^{1/4}(\mathrm{GeV})} + 1.9\% \,. \tag{3.2}$$

The constant term, dominant at energies greater than 1 GeV, comes from leakage or absorption in the material between and in front of the crystals. The resolution worsens at smaller angles. The angular resolution is dominated by the transverse size of the crystals and by the distance from the interaction point

$$\sigma_\theta = \sigma_\phi = \frac{3\,\mathrm{mrad}}{\sqrt{E(\mathrm{GeV})}} + 2\,\mathrm{mrad} \,. \tag{3.3}$$

For energies below 2 GeV, the mass resolution of π^0 mesons is typically used to determine the energy resolution [49]. The π^0 mass resolution in hadronic events is $7\,\mathrm{MeV}/c^2$ (see Fig. 3.11).

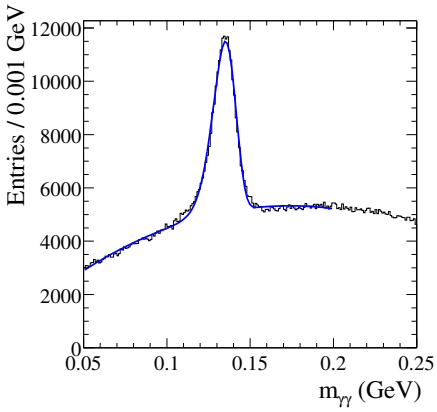

Figure 3.11: *Invariant mass of two photons in $B\overline{B}$ events. The energies of the photons and the π^0 are required to exceed 30* MeV *and 300* MeV*, respectively. The solid curve is a fit to the data.*

For use in Section 4.1.2, the label `GoodPhoton` is assigned to all energy bumps in the EMC not associated with a charged track, with

1. an energy $E > 30\,\mathrm{MeV}$,

2. a shower shape consistent with photon interactions (lateral shape $\lambda_{\rm lat}$ [50] less than 1.1), and

3. lab-frame polar angle $0.41 < \theta_{\rm lab} < 2.409\,{\rm rad}$ (*i.e.* withing the fiducial volume of the EMC).

3.7 Particle identification

The flavor determination of B mesons, described in Chapter 4, relies on efficient particle identification and low misidentification probability for kaons, electrons, and muons. Particle identification (PID) in *BABAR* is briefly discussed in the following Sections.

3.7.1 Kaon identification

The momenta of the kaons used for b-flavor tagging extend up to $2\,{\rm MeV}/c$, with most of them less than $1\,{\rm GeV}/c$ as they come from secondary decays of charmed mesons. In the full reconstruction of B decays kaon identification is also required in a high momentum range, *e.g.* $1.7 < p_K < 4.2\,{\rm GeV}/c$ in $B^0 \to K^+\pi^-$ decays.

Kaons are distinguished from pions and protons on the basis of specific energy-loss measurements ${\rm d}E/{\rm d}x$ in the SVT and DCH, and the number of Čerenkov photons and the Čerenkov angle in the DIRC [51, 52]. PID below $700\,{\rm MeV}/c$ exploits primarily ${\rm d}E/{\rm d}x$ measurements in the DCH and the SVT, while at higher momenta the dominant contribution comes from DIRC information.

The distribution of the measured ${\rm d}E/{\rm d}x$ in the DCH for selected control samples is shown in Fig. 3.12 as a function of momentum. The ${\rm d}E/{\rm d}x$ information of the DCH is able to separate pions from kaons at relatively low momenta.

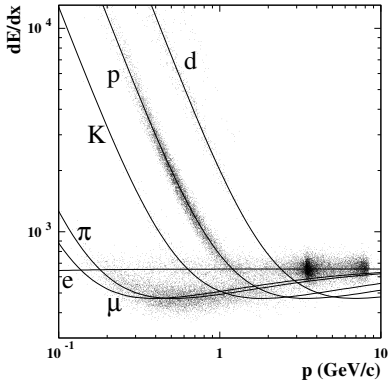

Figure 3.12: *Measurement of* ${\rm d}E/{\rm d}x$ *in the DCH as a function of track momentum. The curves show the Bethe-Bloch predictions derived from selected control samples of particles of different masses.*

The Čerenkov angle as a function of momentum for kaons and pions from a D^0 control

sample is shown Fig. 3.13. The K–π separation is greater than 8.0σ at 2.0 GeV/c, decreasing to 2.5σ at 4.2 GeV/c.

This analysis uses kaon selectors based on likelihood ratios computed from the DIRC, SVT and DCH information for different particle hypothesis (typically π, K and p). Different selectors exist, designed for different needs of efficiency and mis-identification level. Typically, loose kaon identification is used in exclusive B reconstruction, while the b-flavor tagging is based on tighter criteria. For example, the most loose kaon requirement, `NotAPion`, has a nearly constant kaon-identification efficiency of about 96% and a pion-misidentification probability of not larger than 30%, for tracks in the transverse momentum between 1.0 and 2.5 GeV/c. The `Tight` selector has values of 20% and 2%, respectively.

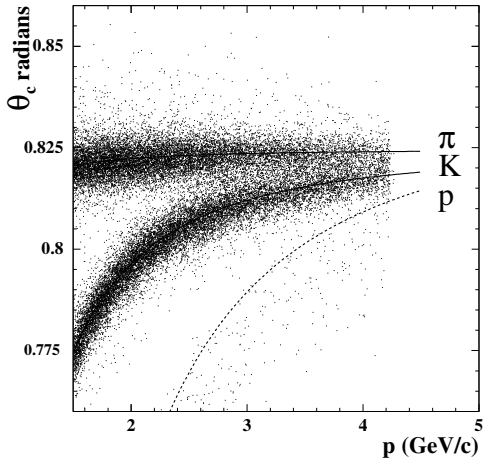

Figure 3.13: *The Čerenkov angle θ_c as a function of momentum for tracks from a control sample of $D^0 \to K^-\pi^+$ decays.*

3.7.2 Electron identification

The EMC is crucial for electron identification. Electrons are separated from charged hadrons primarily by the ratio of the energy deposited in the EMC to the track momentum, and by the lateral shape of the electromagnetic shower [50, 53]. In addition, $\mathrm{d}E/\mathrm{d}x$ energy loss in the DCH and the DIRC Čerenkov angle are required to be consistent with the electron hypothesis [54].

As for kaons, different electron selectors exist with different levels of efficiency and misidentification probability. The right-hand side of Fig. 3.14 shows the electron efficiency and pion mis-identification probability for two selector as a function of lab momentum. The electron efficiency is measured with $e^+e^- \to e^+e^-e^+e^-$ events, while the pion mis-identification probability is measured from selected charged pions from K_s and τ three-prong decays.

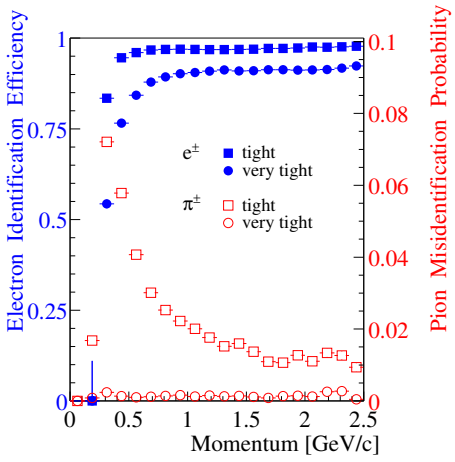

Figure 3.14: *The electron efficiency (left axis) and pion mis-identification probability (right axis) as a function of lab momentum for two selectors.*

3.7.3 Muon identification

Muons are identified by measuring the number of traversed interaction lenghts n, from the outside of the DCH through the iron of the IFR, and Δn, the difference between n and the predicted penetration depth for a muon of the same momentum and angle [55]. The projected intersections of a track with the RPC planes are computed, where for each readout lane all strip clusters detected within a predefined distance are associated with the track. The average number and RMS of the distribution of RPC strips per layer give additional μ/π discrimination power, as pions produce more hadronic interactions than muons.

The performance of the muon identification is assessed on kinematically selected samples of muons from $e^+e^- \to e^+e^-\mu^+\mu^-$, $\mu^+\mu^-\gamma$ events, and from charged pions from K_s and τ three-prong decays. Fig. 3.15 displays the muon efficiency and pion misidentification probability as a function of lab momentum. Again, different muon selectors exist, with different levels of efficiency and purity. For a `Tight` selection of muons, nearly 60% efficiency is achieved with a pion fake rate of $< 2.5\%$.

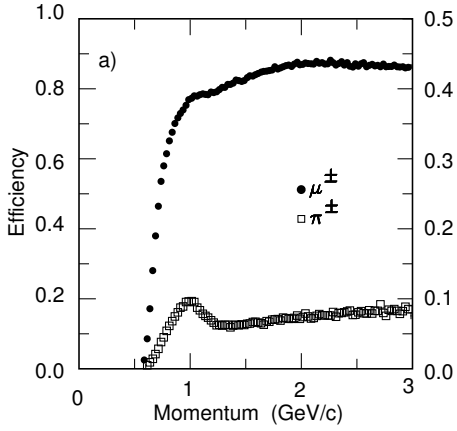

Figure 3.15: *Muon efficiency (left scale) and pion misidentification probability (right scale) as a function of laboratory track momentum.*

Chapter 4

Analysis technique

The data sample used in this analysis is a standard sample in the *BABAR* experiment [56]. The sample selection and B reconstruction process are summarized in Section 4.1. Although improvements to the sample selection have been studied (and can be made), for simplicity of reference and publication [14] it was decided to leave the selection, except for one minor alteration, unchanged.

The b-flavor tagging and Δt extraction procedure were used in the *BABAR* measurements of Δm_d and $\sin 2\beta$, prior to the analysis of the time-dependent CP-asymmetries in $B^0 \to D^{(*)\mp} h^{\pm}$. For this analysis the same techniques have been used. An excellent review of *BABAR*'s time-dependent analysis techniques is found in Ref. [56].

Since the efficiency for full reconstruction of B mesons is small, $\mathcal{O}(10^{-3})$, an inclusive method is used to infer the flavor and decay vertex from the decay products of the tagging B meson. This analysis employs the *BABAR* GeoKin vertexer [57] and Tag04 tagger [58].

The selected data sample, after Δt extraction and b-flavor tagging, is summarized in Section 4.4.

4.1 Selection and reconstruction of B mesons

This Section first discusses the selection and reconstruction of the $B \to D^{(*)\mp} h^{\pm}$ candidates used in our analysis, and ends with a signal and background description in terms of the mass variable m_{ES}, which will be described shortly.

4.1.1 Discriminating observables

For the the time-dependent CP analysis only $\Upsilon(4S) \to B\overline{B}$ events are needed. However, in addition to $B\overline{B}$ from $\Upsilon(4S)$ decays, the e^+e^- collisions at PEP-II produce many final states, as listed in Table 3.2. All are potential background sources to B decay analyses.

A collection of observables, exploited by most B analyses, is used to discriminate between the events of $\Upsilon(4S) \to B\overline{B}$, continuum events $e^+e^- \to q\bar{q}$ ($q = u, d, s, c$), and the QED events $e^+e^- \to e^+e^-, \mu^+\mu^-, \tau^+\tau^-$, and $\gamma\gamma$. Most of these variables discriminate signal events from continuum $q\bar{q}$ events on the basis of their different, characteristic topologies, and are thus called topological variables. In a signal event, the B mesons have low momenta in the $\Upsilon(4S)$ rest frame ($\approx 340\,\mathrm{MeV}/c$), and the decay of each B meson is nearly isotropic. In addition, in a signal event there is no correlation between the directions of the decay products coming from the two B mesons. In a $q\bar{q}$ event the event shape has a two-jet structure, and a direction exists

that characterizes the whole event (the 'jet axis'). Fake B candidates from such an event have less isotropic decay shapes in the $\Upsilon(4S)$ rest frame, and the directions of the decay products of the two B meson candidates tend to be correlated, as they lie within the two jets.

Finally, one can construct discriminating variables that exploit the kinematic constraints of the $\Upsilon(4S) \to B\overline{B}$ decay.

$B\overline{B}$ event selection

Most QED events produced by PEP-II have less than three tracks per event [16]. QED events are rejected by selecting events with at least three good tracks (see Section 3.6.1) and a visible energy greater than 4.5 GeV.

The visible energy $\mathcal{W}$ is defined as the sum over the energy of all good tracks and neutral particles (see Section 3.6.2)

$$\mathcal{W} = \sum_{i}^{\texttt{Tracks}} \sqrt{m_\pi^2 + p_i^2} + \sum_{j}^{\texttt{Neutrals}} E_j \tag{4.1}$$

The distribution of the visible energy $\mathcal{W}$ is shown in Fig. 4.1. The requirements above remove nearly all QED events and select the $B\overline{B}$ and continuum events.

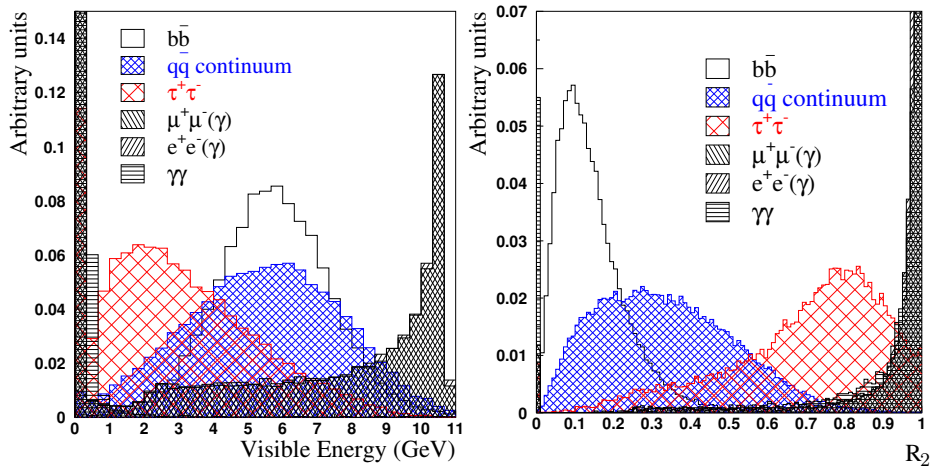

Figure 4.1: *For the main physics processes at the $\Upsilon(4S)$ energy: (left) the distribution of the visible energy $\mathcal{W}$, and (right) the distribution of R_2. The distributions are normalized to the same area.*

The l^{th} Fox-Wolfram moment [59], H_l, is the momentum-weighted sum of the l^{th} order Legendre polynomial, computed from the cosine of the angle between all pairs of particles

$$H_l = \sum_{i<j} \frac{|\vec{p}_i||\vec{p}_j| P_l(\cos\theta_{ij})}{E_T^2}\,, \tag{4.2}$$

where the sum runs over all good charged tracks and neutrals in the event, P_l is the l^{th} order Legendre polynomial, $\vec{p}_{i,j}$ are the particle momenta, θ_{ij} is the angle between particles

i and j, and E_T is the total energy of the event. Each moment H_l is a multipole moment of the momentum distribution in an event. For continuum events $H_l \sim 1$ when l even, and $H_l \sim 0$ when l odd. Neglecting the particle masses, energy-momentum conservation requires that $H_0 = 1$.

The quadrupole moment H_2 can discriminate between events with a jet-like structure of momentum (continuum background from $u\bar{u}$, $d\bar{d}$, $s\bar{s}$, and $c\bar{c}$ events) and those with a more spherically symmetric topology ($B\overline{B}$ events). The normalized ratio $R_2 = H_2/H_0$ is very close to unity for events with back-to-back tracks, such as QED events, and approaches zero for isotropic $B\overline{B}$ events. The R_2 distributions for the physics processes at the $\Upsilon(4S)$ energy are shown in Fig. 4.1. In order to reduce background from continuum events, R_2 is required to be less than 0.5.

The selection efficiency of $B\overline{B}$ events, using the criteria described above, is about 95%.

The B thrust axis

Additional rejection of continuum events is provided using the 'thrust axis' [60] of selected B candidates, $\vec{T}_B$. The thrust axis of a set of particles is defined as the direction that maximizes the sum of the longitudinal momenta of the set. The thrust axis for a reconstructed B candidate ($B_{\rm rec}$) is obtained[1] by maximizing the ratio R_T

$$R_T = \frac{\sum_i |\vec{T}_B \cdot \vec{p}_i^{\,*}|}{\sum_i \sqrt{\vec{p}_i^{\,*} \cdot \vec{p}_i^{\,*}}} \,, \tag{4.3}$$

where $\vec{p}_i^{\,*}$ is the three-momentum of particle i in the $\Upsilon(4S)$ rest frame, and the sum runs over the events' charged and neutral particles *not* used in the reconstruction of $B_{\rm rec}$.

The thrust angle θ_T is defined as the angle between the momentum of $B_{\rm rec}$, $\vec{p}_B^{\,*}$, and the thrust axis of the rest of the event. The cosine of θ_T is obtained as

$$\cos\theta_T = \frac{\vec{p}_B^{\,*} \cdot \vec{T}_B}{|\vec{p}_B^{\,*}||\vec{T}_B|} \,. \tag{4.4}$$

In a $q\bar{q}$ background event the decay particles of $B_{\rm rec}$, as well as the other particles in the event, lie in one of the two jets. Therefore, the $B_{\rm rec}$ decay axis is roughly co-linear with the thrust axis of the rest of the event, and $|\cos\theta_T|$ is peaked at one. For an isotropic $B\overline{B}$ event, the momentum of $B_{\rm rec}$ is uncorrelated with the thrust axis of the rest of the event (which comes from the decay of the other B meson), resulting in a uniform distribution of $|\cos\theta_T|$.

The selection cuts on $|\cos\theta_T|$ vary between the decay modes $B \to D^{(*)\mp}h^{\pm}$, and are described in the next Section.

Kinematic variables

The final B candidates are identified using a pair of nearly orthogonal kinematic variables, which exploit the kinematic constraints of the $\Upsilon(4S) \to B\overline{B}$ decay [61]. Both variables are Lorentz invariants.

1. In the $\Upsilon(4S)$ frame the 'energy difference', ΔE, is expressed as

$$\Delta E = E_B^* - E_{\rm beam}^*, \tag{4.5}$$

[1] The thrust axis is calculated after the B reconstruction in Section 4.1.2.

where E^*_B is the reconstructed energy of the B meson, and $E^*_{\rm beam}$ is half the $\Upsilon(4S)$ energy ($\sqrt{s}/2$), which represents the best estimate for the energy of the B meson. Hence, ΔE is simply the difference between the reconstructed and the expected B energy, and is around zero for signal candidates. The ΔE resolution, $\sigma_{\Delta E}$ is dominated by the momentum resolution. The size of $\sigma_{\Delta E}$ depends on the reconstructed B decay mode.

In the lab frame ΔE becomes

$$\Delta E = (2q_B \cdot q_0 - s)/2\sqrt{s}, \tag{4.6}$$

where $\sqrt{s}$ is the total energy in the e^+e^- center-of-mass (CM) frame, and q_B and q_0 are the laboratory four-momenta of the B candidate and the e^+e^- system, $q_0 = q_{e^+} + q_{e^-}$.

2. The second kinematic variable is the 'energy-substituted mass', m_{ES}, defined in the e^+e^- CM frame as

$$m_{ES} = \sqrt{E^{*2}_{\rm beam} - p^{*2}_B} \tag{4.7}$$

where p^*_B is the CM momentum of the B meson, obtained from the momenta of its decay products. Therefore, m_{ES} is the mass of the B, computed with E^*_B substituted by $E^*_{\rm beam}$. Given that $p^{*2}_B \ll E^{*2}_{\rm beam}$, the resolution in m_{ES} is dominated by the spread in $E^*_{\rm beam}$, and it is largely independent of the reconstructed B decay.

The standard implementation of m_{ES} is in the laboratory frame, using

$$m_{ES} = \sqrt{(s/2 + \vec{p}_0 \cdot \vec{p}_B)^2/E_0^2 - p_B^2}\,, \tag{4.8}$$

where $\vec{p}_B$ and $\vec{p}_0$ are the spatial momenta of the B candidate and the e^+e^- system, and E_0 is the total energy in the lab frame.

By definition, m_{ES} and ΔE are dependent variables. However, as their sources of experimental resolution are uncorrelated (beam energy for m_{ES} vs momentum resolution for ΔE), practically the two variables are uncorrelated as a result.

In the $(m_{ES}, \Delta E)$ plane signal candidates accumulate around $m_{ES} = m_B$ and $\Delta E = 0\,\text{MeV}$. Typically, the B 'signal region' is defined as

$$m_{ES} > 5.27\,\text{GeV}/c^2\,, \quad |\Delta E| < N\,\sigma_{\Delta E}\,, \tag{4.9}$$

where $\sigma_{\Delta E}$ is the decay-mode dependent ΔE resolution, and N is set to about 2.5 for our selected $B \to D^{(*)\mp}h^\pm$ candidates.

The exact selection cuts applied to ΔE are given in Section 4.1.2. The signal and background m_{ES} distributions are described in Section 4.1.3.

4.1.2 $B \to D^{(*)\mp}h^\pm$ Selection

The multi-hadron events considered for B selection are required to have at least 3 good tracks, a visible energy $\mathcal{W} > 4.5\,\text{GeV}$, and $R_2 < 0.5$. The B reconstruction process proceeds from the final state tracks and neutrals, to the light intermediate states, to the heavier $D^{(*)}$ mesons, and ends with the B mesons. Vertex and mass-constrained fits are applied to improve the resolution on the measured momenta and/or energy of intermediate mesons, and to reduce contributions from combinatorial background [62].

Particle	Reconstruced final state	PDG mass (MeV/c^2)	Measured width (MeV/c^2)	Mass cut (MeV/c^2) Low	High	Other requirements
π^+	–	140	–	–		`GoodTrack` (section 3.6.1)
K^+	–	494	–	–		`GoodTrack` (section 3.6.1)
π^0	$\gamma\gamma$	135	7	120	150	`GoodPhoton` (section 3.6.2), $E_{\pi^0} > 200\,\mathrm{MeV}$
K_S^0	$\pi^+\pi^-$	498	3.2	462	534	Vertex prob. $> 0.1\%$
ρ^+	$\pi^0\pi^+$	768	150	618	918	$E_\gamma > 50\,\mathrm{MeV}$, $\lambda_{\mathrm{lat}} < 0.8$, $E_{\pi^0} > 300\,\mathrm{MeV}$ $p^*_{\pi^0} > 400\,\mathrm{MeV}/c$, $p^*_{\rho^+} > 500\,\mathrm{MeV}/c$, $\lvert\cos\theta_{\pi\pi^0}\rvert > 0.4$

Table 4.1: *Particles containing u, d, s quarks used in the reconstruction of the B mesons. Composite particles in the list rely on the particles above them. The reconstructed width of the ρ^+ is simply its Breit-Wigner width.*

The lightest mesons are summarized in Table 4.1, together with their reconstructed decay modes and selection cuts.

The decay modes of the charmed mesons reconstructed in this analysis, $\overline{D}^0$ and D^-, are listed in Table 4.2. Loose PID is required for the charged kaons (`NotAPion`, see Section 3.7.1) to reduce combinatorial background. The vertex fit probability $P(\chi^2)$ is required to be larger than 0.1%. A D candidate is selected when its reconstructed mass m satisfies $|m-m_0|/\sigma_m < 3$, where m_0 is the nominal mass, and the uncertainty σ_m is calculated from the measured error matrices of the tracks involved. The momentum p^* in the $\Upsilon(4S)$ frame must lie between 1.3 and 2.5 GeV/c. The lower bound reduces combinatorial background, whereas the upper bound lowers charmed contributions from the process $e^+e^- \to c\bar{c}$.

For the decay $\overline{D}^0 \to K^+\rho^-$, a large component in $\overline{D}^0 \to K^+\pi^-\pi^0$, backgrounds are large due to the wide ρ mass. The decay has angular momentum one, and hence a $\cos^2\theta$ helicity distribution. For this mode the cut of $|\cos\theta_{D\pi}| > 0.4$, where $\theta_{D\pi}$ is the helicity angle between the D and π in the $\pi\pi^0$ rest frame, reduces background combinations by about 40%.

Meson	PDG mass (MeV/c^2)	Decay mode	$\mathcal{B}$ (%)
$\overline{D}^0$	1865	$K^+\ \pi^-$	3.80 ± 0.09
		$K^+\ \pi^-\ \pi^0$	13.0 ± 0.8
		$K^+\ \pi^-\ \pi^+\ \pi^-$	7.5 ± 0.3
		$K^0_S\ \pi^+\ \pi^-$	3.0 ± 0.2
D^-	1869	$K^+\ \pi^-\ \pi^+$	9.1 ± 0.6
		$K^0_S\ \pi^-$	1.4 ± 0.1

Table 4.2: *Selected decay modes of $\overline{D}^0$ and D^- mesons and their branching fractions $\mathcal{B}$.*

In the decay $D^{*+} \to D^0\pi^+$ the difference of the masses of the D^{*+} and D^0 is just above the π threshold ($\delta m_0 = 145.4\,\mathrm{MeV}/c^2$ [17]), and the resulting 'soft' pion carries very little momentum. The decay mode has a branching fraction of 67.7% [17]. D^{*-} candidates are constructed combining a $\overline{D}^0$ and a charged pion with a momentum between 70 and 450 MeV/c. The lower limit is the threshold for track reconstruction in the SVT, and the higher limit is the maximum possible soft pion momentum in the lab frame. The reconstructed mass difference $\delta m = m(\overline{D}^0\pi^-) - m(\overline{D}^0)$ is used to select the D^{*-} candidates. The resolution on δm is improved in the D^{*-} vertex fit by constraining the soft pion to originate from the beam spot. In the fit, the vertical size of the beam spot ($\approx 4\,\mu$m) is increased to $40\,\mu$m to account for the small transverse flight of a B meson.

The reconstructed δm value is required to be within $0.8\,\mathrm{MeV}/c^2$ of its nominal value for all $\overline{D}^0$ modes, and within $1.1\,\mathrm{MeV}/c^2$ for $\overline{D}^0 \to K^+\pi^-\pi^0$. The cut corresponds to about $2.5\sigma_{\delta m}$, with $\sigma_{\delta m}$ the RMS of the observed δm distribution in data.

The branching fractions for the reconstructed decay modes $B \to D^{(*)\mp}\pi^\pm$, $D^\mp\rho^\pm$ are at the level of $\mathcal{O}(10^{-3})$, and have been cited earlier in Table 2.3. The B candidates are formed from combinations of a $D^{(*)}$ candidate, constrained to its nominal mass, and a π^+/ρ^+ candidate. The hard pion is required not to qualify as a tight kaon (`!Tight`, see Section 3.7.1)) to reject background from $B \to D^{(*)\mp}K^\pm$ events. The selection cuts, which vary per B and D decay mode, are summarized in Table 4.3. The ΔE cut corresponds to roughly $2.5\sigma_{\Delta E}$, where $\sigma_{\Delta E}$ is the measured ΔE resolution, which varies between 18 and 32 MeV.

B Mode	D^-/D^0 mode	$\lvert\cos\theta_T\rvert$	$\lvert\Delta E\rvert$ (MeV)	Other requirements
$D^-\ \pi^+$	$K^0_S\ \pi^-$	< 0.9	< 42.5	$p_\pi, p_K > 200\,\mathrm{MeV}/c$
	$K^+\ \pi^-\ \pi^+$	< 0.9	< 45	$p_\pi, p_{K^0_S} > 200\,\mathrm{MeV}/c$
$D^-\ \rho^+$	$K^0_S\ \pi^-$	< 0.8	< 75	$p_\pi, p_K > 200\,\mathrm{MeV}/c$
	$K^+\ \pi^-\ \pi^+$	< 0.8	< 75	$p_\pi, p_{K^0_S} > 200\,\mathrm{MeV}/c$
$D^{*-}\ \pi^+$	$K^+\ \pi^-$	–	< 45	$p_\pi, p_K > 200\,\mathrm{MeV}/c$
	$K^+\ \pi^-\ \pi^0$	–	< 52.5	$p_\pi, p_K > 200\,\mathrm{MeV}/c$
	$K^+\ \pi^-\ \pi^+\ \pi^-$	–	< 45	$p_\pi, p_K > 200\,\mathrm{MeV}/c$
	$K^0_S\ \pi^-\ \pi^+$	–	< 37.5	$p_\pi, p_{K^0_S} > 200\,\mathrm{MeV}/c$

Table 4.3: *Selection criteria for $B^0 \to D^-\pi^+/\rho^+$ and $B^0 \to D^{*-}\pi^+$ decays.*

If more than one $B \to D^{\mp}h^{\pm}$ candidate passes the selection cuts per event, the best candidate is chosen based on the following criteria.

1. Select the charged D candidate with $|m - m_0|/\sigma_m$ closest to zero.
2. If the same D candidate is used in more than one B candidate, pick the candidate with the lowest $|\Delta E|$ value.

A similar algorithm is used for $B \to D^{*\mp}\pi^{\pm}$ candidates. The best candidate is chosen based on of lowest value of

$$\chi^2_D = \left(\frac{m - m_0}{\sigma_m}\right)^2 + \left(\frac{\delta m - \delta m_0)}{\sigma_{\delta m}}\right)^2 . \tag{4.10}$$

If this is not sufficient, the candidate is chosen with the best value of ΔE.

In the time-dependent fit we only use events with a successful flavor tag – see Section 4.2. Also, we select events with $\Delta t \in [-20, 20]$ ps and require the uncertainty $\sigma_{\Delta t}$ to be less than 2.5 ps – see Section 4.3. The final data sample, after these additional cuts, is presented in Section 4.4.

4.1.3 Signal and background m_{ES} description

Signal yields and sample purities are extracted from a fit to the m_{ES} distributions in data in Section 4.4. As discussed in Section 4.1.1, signal candidates accumulate around the nominal B mass, m_B, in the m_{ES} 'signal region' with $m_{ES} > 5.27$. The m_{ES} 'sideband region' is defined as $5.20 < m_{ES} < 5.27$, and is fully dominated by background events. Fig. 4.2 illustrates the composition of the candidates in the m_{ES} signal and sideband regions.

The signal component of B candidates is parameterized with a Gaussian, $\mathcal{G}(m_{ES})$, with mean m_B and width σ_m, centered at the B meson mass.

We distinguish between two types of background in the sample of selected B candidates. The first background is called combinatorial background and arises from random combinations of charged tracks and neutral showers from both B mesons in $B\overline{B}$ events or from continuum events. The second background is the so-called peaking background. Peaking background consists of mis-reconstructed B decays whose m_{ES} values concentrate near the nominal B mass.

The m_{ES} distribution of combinatorial background is by definition smoothly distributed, and does not peak near the B mass. It is parameterized with a threshold function, commonly

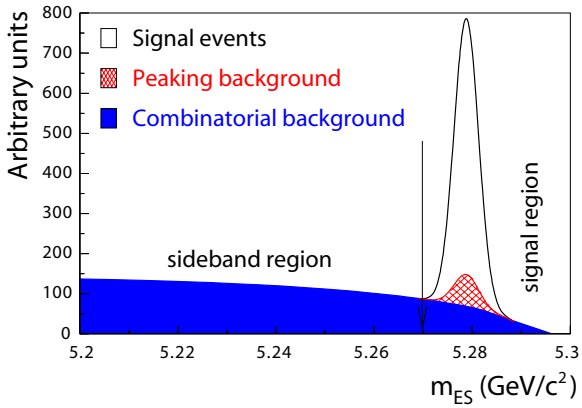

Figure 4.2: *Typical composition of the m_{ES} distribution.*

called the `Argus` function [63]

$$\mathcal{A}(m_{ES};m_0,\kappa) \;=\; m_{ES}\sqrt{1-(m_{ES}/m_0)^2}\,\exp\Big\{\kappa\left(1-(m_{ES}/m_0)^2\right)\Big\}, \tag{4.11}$$

where m_0 is the upper kinematic limit, fixed at the beam energy $E_{\rm beam}$ ($5.291\,{\rm GeV}/c^2$), and κ controls the slope of the function. The `Argus` shape parameter κ depends on the B decay mode.

Peaking background consists of events in which, for example, a true $B^+\to\overline{D}^{*0}\pi^+$ decay is mis-reconstructed as a $B^0\to D^{*-}\pi^+$ candidate. The slow π^0 from the $\overline{D}^{*0}$ candidate is replaced by a random charged track with a similar energy. The energy difference ΔE for this fake B candidate can be sufficiently close to zero, and the m_{ES} value of this candidate is near the nominal B mass, causing an enhancement not accounted for by the `Argus` shape.

We use the `Cruijff` function to describe peaking background events [64]

$$\mathcal{C}(m_{ES};\sigma(L,R),\alpha(L,R),m_B) \;=\; \exp\Big\{-\frac{(m_{ES}-m_B)^2}{2\sigma^2(L,R)+\alpha(L,R)(m_{ES}-m_B)^2}\Big\}. \tag{4.12}$$

The `Cruijff` function is simply a Gaussian with left- and right-handed widths, $\sigma(L,R)$, plus first order corrections to these widths, $\alpha(L,R)$.

In data, only a small fraction of the events in the m_{ES} signal region is due to the peaking background contribution. This fraction is determined using fully simulated Monte Carlo events in Section 4.1.4. The impact of the peaking background on the measured *CP* asymmetries is taken into account as a systematic uncertainty in Section 9.2.4.

The m_{ES} distributions in data are modeled with the sum of $\mathcal{G}(m_{ES})$, $\mathcal{C}(m_{ES})$, and $\mathcal{A}(m_{ES})$. For use in the Δt fit, each event is assigned a probability to be signal or background, f, on the basis of its energy-constrained mass m_{ES} and the fit to the m_{ES} distributions in data. The

probabilities are defined as

$$\begin{aligned} f^{\rm sig}(m_{ES}) &= \frac{\mathcal{G}(m_{ES})}{\mathcal{G}(m_{ES})+\mathcal{A}(m_{ES})+\mathcal{C}(m_{ES})}\,, \\ f^{\rm peak}(m_{ES}) &= \frac{\mathcal{C}(m_{ES})}{\mathcal{G}(m_{ES})+\mathcal{A}(m_{ES})+\mathcal{C}(m_{ES})}\,, \\ f^{\rm comb}(m_{ES}) &= \frac{\mathcal{A}(m_{ES})}{\mathcal{G}(m_{ES})+\mathcal{A}(m_{ES})+\mathcal{C}(m_{ES})}\,, \end{aligned} \tag{4.13}$$

and satisfy by construction $f^{\rm sig}+f^{\rm peak}+f^{\rm comb}=1$.

4.1.4 Peaking background composition

Peaking background consists of mis-reconstructed B decays whose m_{ES} values concentrate near the nominal B mass, and, as such, are recognized as signal events. An example is the decay $B^0 \to D^{(*)-}K^+$, where the hard kaon is mis-reconstructed as a pion. In general, the fraction of peaking background candidates is larger for final states with higher multiplicities. The fractions of peaking background in data are determined using the generic $B\overline{B}$ ($B^0\overline{B}^0$ and B^+B^-), fully-simulated Monte Carlo (MC) sample, described earlier in Section 3.5. After event selection and reconstruction – see Section 4.1.2 – this sample amounts to 165198 signal and 26674 background events, the equivalent of 4.5 times the number of $B\overline{B}$ events in data.

We split the reconstructed MC candidates into $B \to D^{*\mp}\pi^{\pm}$, $B \to D^{\mp}\pi^{\pm}$, and $B \to D^{\mp}\rho^{\pm}$ decays and, for each mode, determine the corresponding peaking background fraction as follows. First, we fit the m_{ES} distribution of the signal and $B\overline{B}$ background events with a Gaussian and `Argus` function, described in Eq. (4.11), respectively. Second, the `Argus` parameters are fixed, meaning the κ shape parameter and its normalization. We remove all signal MC events and redo the m_{ES} fit on the remaining $B\overline{B}$ background events with the `Argus` and a `Cruijff` function – the latter described in Eq. (4.12). For each B decay mode $\alpha(R)$ is set to zero. The peaking background fraction per B mode is determined as the ratio of the number of $B\overline{B}$ events in the `Cruijff` function, P, see Fig. 4.3, over the Gaussian yield from the first fit to the combined signal and $B\overline{B}$ background sample.

The same routine is applied to the signal events and $B^0\overline{B}^0$ background or B^+B^- background to find the corresponding B^0 or B^+ peaking background contributions. All fractions are listed in Table 4.4. The B^0 or B^+ peaking background fractions do not add up exactly to the combined $B\overline{B}$ contribution because, for the individual B^0 and B^+ fits, the `Argus` component sometimes accounts for more and sometimes accounts for less peaking background.

Decay mode	$B^{\pm}$ fraction (%)	B^0 fraction (%)	combined (%)	relative B^0 fraction
$B^0 \to D^-\pi^+$	1.2 ± 0.1	1.6 ± 0.1	2.8 ± 0.1	0.57
$B^0 \to D^{*-}\pi^+$	1.1 ± 0.2	1.0 ± 0.1	2.2 ± 0.1	0.47
$B^0 \to D^-\rho^+$	0.8 ± 0.2	0.8 ± 0.2	2.5 ± 0.2	0.50

Table 4.4: *Estimated peaking background contributions to the reconstructed B decay modes from: B^+B^- background, $B^0\overline{B}^0$ background, and (combined) $B\overline{B}$ background. The errors are statistical only. The last column shows the relative B^0 peaking background fraction used in the time-dependent fit to data.*

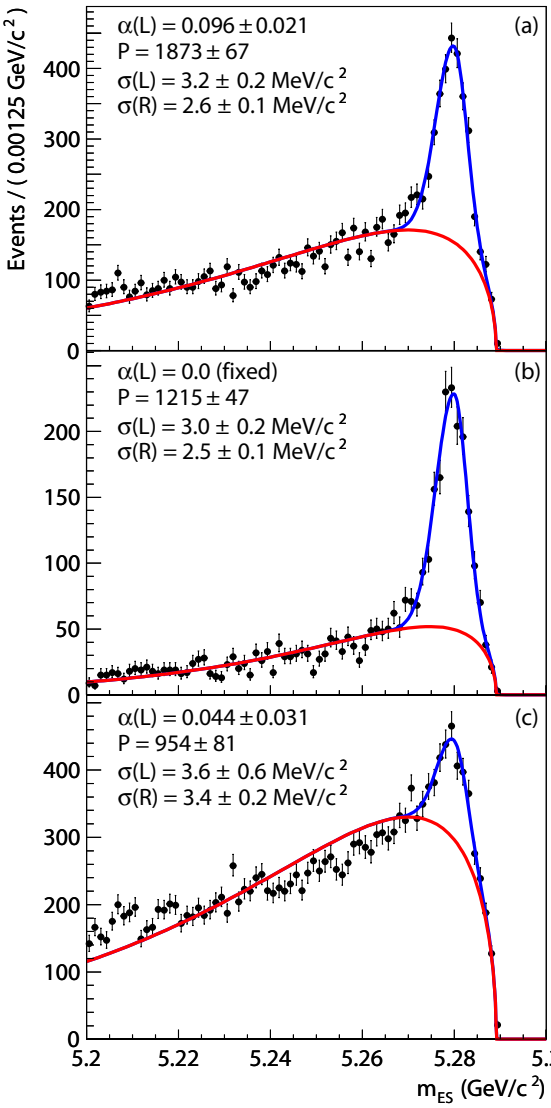

Figure 4.3: *Monte Carlo $B\overline{B}$ background contributing to the decays: a) $B \to D^{\mp}\pi^{\pm}$, b) $B \to D^{*\mp}\pi^{\pm}$, and c) $B \to D^{\mp}\rho^{\pm}$. The results of the m_{ES} fit described in the text are superimposed.*

In the m_{ES} fit to data, described in detail in Section 4.4, we fix the combined peaking background fractions relative to the overall signal yield, and fix the peaking background shapes to the `Cruijff` shapes in Fig. 4.3. In the time-dependent fit we split the combined peaking background into a B^0 mixing-component and a double-exponential B^+ component, as detailed in Section 6.3.2. The relative peaking background fractions used in the Δt fit to data are shown in the last column of Table 4.4.

In Table 4.5 one finds the dominant B decay modes contributing to the peaking background, determined by sorting all background B decay modes found in the signal box ($m_{ES} > 5.27\,\mathrm{GeV}/c^2$). Background from B^0 and B^+ decays that peaks in the m_{ES} signal region is nearly all due to charmed final states.

$B^0 \to D^- \pi^+$	%	$B^0 \to D^{*-} \pi^+$	%	$B^0 \to D^- \rho^+$	%
$B^+ \to D^{*0} \pi^+$	43	$B^+ \to D^{*0} \pi^+$	28	$B^+ \to D^0 \rho^+$	20
$B^0 \to D^{*-} \pi^+$	6	$B^0 \to D^{*-} \mu^+ \nu$	9	$B^+ \to D^{*0} \rho^+$	10
$B^+ \to D^0 \rho^+$	4	$B^+ \to D^0 \rho^+$	9	$B^0 \to D^{*-} \rho^+$	10
$B^+ \to D^0 K^+$	3	$B^0 \to D^{*-} \rho^+$	5	$B^0 \to D^{*-} a_1^+$	5

Table 4.5: *Decay modes with the largest contributions to the peaking background.*

In the previous $\sin(2\beta+\gamma)$ analyses [65] the main sources of peaking background ($\approx 35\%$) for the decay modes $B \to D^{\mp}\pi^{\pm}$ and $B \to D^{*\mp}\pi^{\pm}$ were $B^0 \to D^- K^+$ and $B^0 \to D^{*-} K^+$, respectively, with kaons mis-reconstructed as pions. In this analysis these background modes have been filtered out in the selection process by applying the `!Tight` kaon filter to the hard pion of $B \to D^{(*)\mp}\pi^{\pm}$ candidates (see Section 4.1.2).

4.2 The b-flavor tagging procedure

The procedure of identifying the flavor of the tagging B meson on the basis of its decay products is called b-flavor tagging, or B tagging. As discussed in Section 2.7, B tagging is a vital ingredient in the time-dependent CP analysis of $B^0 \to D^{(*)\mp} h^{\pm}$ decays. This analysis employs the so-called *BABAR* Tag04 algorithm [58].

The flavor tagging procedure analyzes an event after removing all tracks from the fully reconstructed B (B_{rec}). The tagging algorithm is split into two layers. The first layer consists of nine neural networks, called subnets or subtaggers. Each subnet is specialized in recognizing a 'tag signature', such as the presence of leptons from semi-leptonic B decays – discussed in the following Section. The second layer is a neural net that combines the output of these subnets, produces the combined 'flavor tag' for B_{tag}, and sorts events into 'tagging categories' – see Section 4.2.2

The performance of the *BABAR* tagging algorithm has been optimized and trained with large samples of fully simulated Monte Carlo events [58].

To quantify the discriminating power of each tagging category the tagging power $Q_i = \epsilon_i(1-2w_i)^2$ is used, where ϵ_i is the fraction of events associated to tagging category i and w_i is the mistag fraction, *i.e.* the probability of assigning the incorrect tag to an event in this category. The statistical errors of the CP asymmetries measured in this analysis are inversely proportional to $\sqrt{Q}$, with $Q = \sum_i Q_i$.

The mistag fractions and tagging performance are measured directly in data, and are therefore presented and discussed in Section 8.2. The impact of mistagging on the time-dependent distributions is presented in Section 6.2.2.

4.2.1 Tag signatures

The *BABAR* flavor tagging algorithm is based on the correlations between the flavor of neutral B mesons and the charge of particles in the final state, such as leptons, kaons, and soft pions. These correlations, or 'tag signatures', are summarized below.

Leptons from semi-leptonic B decays

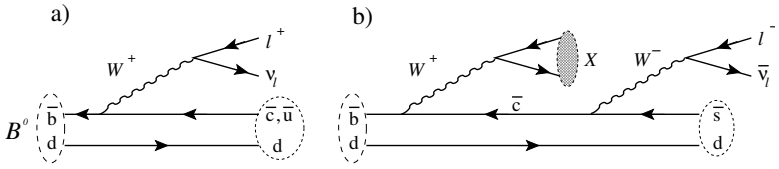

Figure 4.4: *a) Primary leptons from B decays, and b) secondary leptons with the opposite charge, produced by the cascade decay $\bar{b} \to \bar{c} \to \bar{s}$.*

Semi-leptonic $B \to X l \nu$ decays (see Fig. 4.4a) constitute roughly 20% of all B decays, and produce electrons or muons whose charge has the same sign as the b quark. Since these leptons are the 'primary' decay products of the virtual W boson, as emitted by the b quark, they carry large momenta p_l^* in the B center-of-mass frame. Thus, they can be distinguished from slower, 'secondary' leptons from $\bar{b} \to \bar{c} \to \bar{s}$ cascades, which exhibit the opposite b quark-lepton correlation (see Fig. 4.4b). Primary leptons are also faster than most pions and kaons produced by B decays. This permits discrimination of misidentified leptons and purely kinematic selection of semi-leptonic decays when no lepton PID is available. Last but not least, primary leptons do not suffer from so-called tag-side interference – an important feature for this analysis, discussed in detail in Chapter 5.

Three neural networks are used to recognize primary leptons: two examine identified electrons or muons, respectively, and the other only considers kinematics. Kinematics and strict lepton identification make the semi-leptonic B decays the cleanest – and hence most reliable – flavor tagging signature. As we shall see in Table 8.6, lepton tags are not very efficient ($\epsilon_l \approx 8.7\%$), but they are very accurate ($w_l \approx 3.8\%$), resulting in $Q_l \approx 7.4\%$.

Strangeness produced in B decays

Most kaons in B^0 decays come from the decay chain $\bar{b} \to \bar{c} \to \bar{s}$, as illustrated in Fig. 4.5. The kaons can have both the same and opposite charge sign as the b quark. The fractions of B^0 decays with a kaon are [66]

$$\begin{aligned} n(B^0 \to K^+ X) &= 0.58 \pm 0.01 \pm 0.08\,, \\ n(B^0 \to K^- X) &= 0.13 \pm 0.01 \pm 0.05\,. \end{aligned} \tag{4.14}$$

The majority of kaons in B^0 decays thus has a positive charge. Hence, an identified charged kaon provides a powerful flavor tag signature.

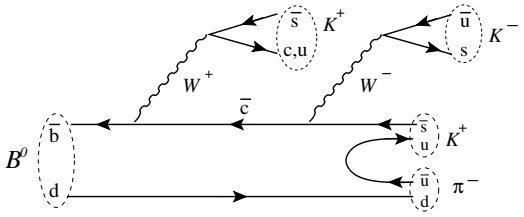

Figure 4.5: *Sources of charged kaons in the decay of a B^0 meson.*

Hadronization to a kaon of the $\bar{s}$ quark in the chain $\bar{b} \to \bar{c} \to \bar{s}$ is the primary source of 'right-sign' correlation between the b quark and the kaon charge. This cascade also emits two virtual W bosons that can hadronize to kaons, but this process is Cabibbo-suppressed compared with pion and D_s production ($|V_{us}|^2 \approx 0.04$). In Fig. 4.5 the W^+ produces a K^+, which is another source of right-sign correlation. Likewise, the W^- from the $\bar{c}$ decay can result in a wrong-sign kaon.

The tagging algorithm identifies kaons using one subnet. No kinematic separation between wrong and right-sign kaons is possible (unlike primary leptons), leaving kaon identification as the only tag signature. The three (or less) best kaon candidates determine the B flavor from the sum of products of each kaon's charge and kaon likelihood.

Based on the same line of reasoning, the tagging algorithm includes a Λ subtagger. Tagging information comes from the fact that the Λ baryon is most likely to contain an s quark produced in the decay $b \to c \to s$. Therefore, a Λ indicates a B^0 while a $\overline{\Lambda}$ indicates a $\overline{B}^0$.

Kaon tags are more efficient than leptons tags, but less accurate. From Table 8.6 'kaon' tags (including the Λ tagger) have a combined efficiency of about 28%, a mistag probability of roughly 11%, and result in $Q_k \approx 16.8\%$. The Λ subnet has an individual tagging power of only about $Q \approx 0.3\%$ [58].

Soft and hard pions

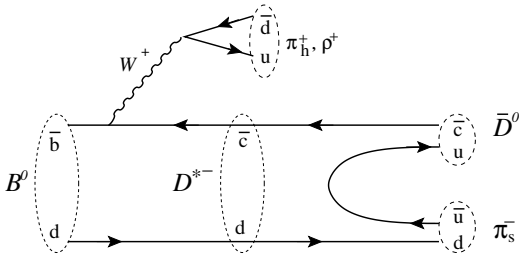

Figure 4.6: *The decay $B^0 \to D^{*-}\pi^+, \rho^+, a_1^+$. The charge of the soft pion π_s and that of the direct pion π_h are correlated with the charge of the b quark.*

As mentioned in Section 4.1.2, in the $D^{*+} \to D^0\pi^+$ decay the masses of the D^{*+} and D^0 are very close. The resulting pion carries very little momentum, and is called soft, or π_s. Viewed in the CM frame of the B, the soft pion flies in the nearly the same direction as the D^0. When the D^* originates from a B (see Fig. 4.6), the sign of its charge, and hence that of π_s, is opposite to that of the b quark.

The slow-pion subtagger examines pions with $p^*_{\pi_s} < 250\,\mathrm{MeV}/c$, and identifies slow pions using PID information, $p^*_{\pi_s}$, and the angle between its flight direction and the thrust axis of the remaining B decay products. The selection of soft pions suffers from high background, resulting in a large mistag fraction.

Another subnet exploits the correlation between the kaon and the slow pion from the D^*. This subnet studies all oppositely charged kaon and slow pion combinations, along with the kaon likelihood, the slow pion information, and the angle between the two tracks.

Even more tagging information is available when the W^+ in Fig. 4.6 hadronizes as a pion. The pion π_h has significant momentum, and its charge correlates directly to the flavor of the b quark. The same holds in the decay $B^0 \to D^-\pi^+$. The so-called maximum p^* subtagger attempts to determine the B flavor by selecting the track with the highest CM momentum that originates from less than 1 mm of the beam in the x–y plane.

The charge of π_h is opposite to that of π_s, which can also be used to determine the B flavor. This information is employed in the 'fast-slow-correlation' subnet, which examines all oppositely charged π_s and π_h combinations, using the available soft and hard pion information and the angle between the two tracks.

From Table 8.6 these tagging signatures have a combined efficiency of about 38%, $Q_\pi \approx 5.9\%$, and an average mistag probability as high as 30%.

4.2.2 Tagging categories

Each subtagger provides a continuous output whose sign and magnitude reflect the B flavor and confidence in its result. A set of charged particles belonging to B_{tag} can exhibit any of the tag signatures of Section 4.2.1. It may therefore be identified by several of the 9 subnets.

The second neural network combines the output of the subnets. The output is another continuous variable NN, with values between -1 and $+1$, where candidates with NN close to $+1$ (-1) are more likely to be a B^0 ($\overline{B}^0$). Based on NN, the most likely flavor tag is assigned to each event. The estimated mistag probability w for B_{tag} is obtained as $(1+NN)/2$. The output of the tagging algorithm is shown in Fig. 4.7.

Each event with an estimated mistag probability of less than 45% is assigned to one of six hierarchical, mutually exclusive tagging categories. The estimated mistag probability is not used elsewhere in this analysis. The selection criteria defining the tagging categories are described in Ref. [58]. The categories are named after the class(-es) of tag signature they (mostly) contain.

The `Lepton` tagging category contains events with an identified lepton, *i.e.* with semileptonic B decays. Other events are divided into categories based on their estimated mistag probability. Events dominated by kaon signatures tend to have a wide range of mistag probabilities, so two categories are defined: `Kaon I` and `Kaon II`. It also includes the lambda tags. The `K-Pi` category roughly contains the slow-pion/kaon tags.

The slow-pion and fast-slow-correlation tags, having similar mistag probabilities, are included in the `Pion` category. The last category, called `Other`, mostly collects events from the inclusive p^* tag.

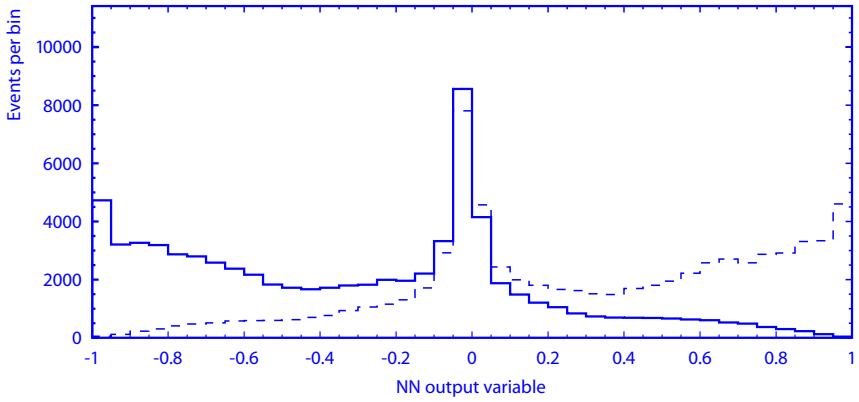

Figure 4.7: *Output of the BABAR tagger [58]. The dashed and solid histograms are the distributions obtained for true B^0 and $\overline{B}^0$ tags, respectively.*

As will become clear in Chapter 8, background levels and the Δt resolution depend upon the tagging category.

The motivation for having tagging categories, instead of a per-event mistag probability, is historical, and comes from the fact that earlier tagging algorithms in *BABAR* were split by tag signature. To optimize the tagging power Q, studies have been performed with per-event mistag probabilities and a larger number of categories, but with no significant improvements.

4.3 Time difference measurement

The time difference between the B decay times, $\Delta t \equiv t_{\rm rec} - t_{\rm tag}$, is determined from the measured separation Δz between the vertices of the reconstructed B meson ($B_{\rm rec}$) and the flavor-tagging B meson ($B_{\rm tag}$) and the Lorentz boost of the $\Upsilon(4S)$. The Δt resolution is dominated by the resolution of the $B_{\rm tag}$ vertex position.

4.3.1 Δz reconstruction

The decay vertex of the $B_{\rm rec}$ candidate is reconstructed using all its daughters' charged tracks. Daughter tracks from K^0_S or D candidates are first fit to a separate vertex, and the resulting momentum and position are used in the fit to the $B_{\rm rec}$ vertex. The typical resolution on the $z_{\rm rec}$ vertex position is about 65 μm.

The $B_{\rm tag}$ vertex is constructed with an inclusive technique, using all tracks in the event not associated to $B_{\rm rec}$. In order to reduce possible biases and tails from long-lived particles, K^0_S and Λ candidates are used in the fit instead of their daughters. Pairs of oppositely-charged tracks consistent with photon conversions ($\gamma \to e^+e^-$) are excluded. The remaining tracks and composite candidates serve as input in the geometrical fit to the $B_{\rm tag}$ vertex.

The three-momentum of the $B_{\rm tag}$ candidate and the estimated production point of the $B^0\overline{B}^0$ pair are included in the vertex fit. This so-called beam constraint helps in removing tracks that do not come directly from the $B_{\rm tag}$ candidate. The two are obtained as follows.

The three-momentum $\vec{p}_{\rm rec}$ and the decay vertex of the $B_{\rm rec}$ candidate are measured with good precision. The average beam spot ellipsoid has been determined in the rolling calibration, discussed in Section 3.2. Owing to the small size of the beam spot in y, the intersection of the two provides a good estimate of the production point of the $B^0\overline{B}^0$ pair. The three-momentum $\vec{p}_{\Upsilon(4S)}$ of the $\Upsilon(4S)$ is obtained from the beam energies. Momentum conservation then yields $\vec{p}_{\rm tag} = \vec{p}_{\Upsilon(4S)} - \vec{p}_{\rm rec}$. From the two a 'pseudo' track is formed, which is used along with the other tracks to find the $B_{\rm tag}$ vertex.

The $B_{\rm tag}$ vertex is determined with an iterative procedure, aimed at reducing biases from decay daughters of charmed mesons, which have a long decay length. For example, D^0 and D^+ mesons have a decay lengths $c\tau$ of about $130\,\mu$m and $300\,\mu$m, respectively, resulting in detached vertices from the B decay point. Since all particles are boosted forward, the resulting bias is always positive in $z_{\rm tag}$. After each iteration, tracks with a large χ^2 contribution to the fit ($\Delta\chi^2 > 6$) are removed, and the vertex is refit. This process is repeated until no track fails the χ^2 requirement, or only two tracks are left. The RMS resolution in z for the $B_{\rm tag}$ vertex is about $160\,\mu$m. Any remaining bias is modeled in the Δt resolution function; more about this in in Section 4.3.3.

The spatial separation between the $B_{\rm rec}$ and $B_{\rm tag}$ decay points is computed from the reconstructed decay vertices. Although the decay points are known in three dimensions, because of the boost along z only Δz is important. The algorithm that computes Δz also provides a per-event estimate $\sigma_{\Delta z}$ of the uncertainty on Δz, accounting for the correlation between $B_{\rm tag}$ and $B_{\rm rec}$ from the use of the pseudo track.

The overall Δz resolution of the *BABAR* detector is about $180\,\mu$m, and is dominated by the tag-side vertex reconstruction. The absolute scale of the measurement of Δz depends on the assumed positions of the silicon wafers in the SVT, the impact of which is treated in Sections 9.3.3 and 9.3.4.

4.3.2 Δt measurement

Neglecting the B momentum in the $\Upsilon(4S)$ rest frame ($\approx 340\,\mathrm{MeV}/c$), referred to as 'the boost approximation', the relation between Δz and Δt is simply given by

$$\Delta z = \beta\gamma\Delta t, \tag{4.15}$$

where $\beta\gamma$ is the average $\Upsilon(4S)$ boost factor ($\beta\gamma = 0.55$). The boost factor is calculated from the beam energies, monitored every 5 seconds, and has a precision of 0.1% [56].

Compared with the experimental resolution on Δz, the effect of the boost approximation on Δt is quite small. As the momentum of a fully reconstructed $B_{\rm rec}$ is measured to good precision, however, a correction is applied to account for the small B momentum in the $\Upsilon(4S)$ frame. A Lorentz transformation is applied to correct for the 20 mrad angle between the detector symmetry axis and the beam direction, *i.e.* the boost axis. The impact on the Δt measurement of the spread in the two beam energies, which results in a spread in the $\Upsilon(4S)$ momenta of about $6\,\mathrm{MeV}/c$, is negligible.

The exact relation between Δt and Δz is more complicated [67]

$$\Delta z = \beta\gamma\gamma^*_{\rm rec} c\Delta t + \gamma\beta^*_{\rm rec}\gamma^*_{\rm rec}\cos\theta^*_{\rm rec}\, c\,(t_{\rm rec} + t_{\rm tag})\,, \tag{4.16}$$

where $\theta^*_{\rm rec}$, $\beta^*_{\rm rec}$, and $\gamma^*_{\rm rec}$ are the polar angle with respect to the beam direction, the velocity, and the boost factor of $B_{\rm rec}$ in the $\Upsilon(4S)$ frame, and $t_{\rm rec} + t_{\rm tag}$ is the the sum of the decay

times. Instead of measuring $t_{\rm rec}+t_{\rm tag}$, which can only be determined with poor resolution, its expectation value is estimated by

$$\langle t_{\rm rec} + t_{\rm tag} \rangle = \tau_B + |\Delta t| \,. \tag{4.17}$$

The difference in Δt between Eqs. (4.15) and (4.16) is small because $\gamma^*_{\rm rec} = 1.002$ and $\beta^*_{\rm rec} = 0.064$. The event-by-event difference between Δt computed in the two ways has an RMS of 0.2ps. Eq. (4.16) improves the Δt resolution by about 5% [56], and removes a bias that increases when Δt increases.

As vertex quality cuts, in the final data sample we only include events with $\Delta t \in [-20, 20]$ ps. This is a very loose requirement considering the B^0 lifetime of 1.536 ps. Events outside this region are surely mis-reconstructed. Furthermore, we require the uncertainty $\sigma_{\Delta t}$ to be less than 2.5 ps.

4.3.3 Detector Δt resolution function

The measured and true values of Δt differ due to the finite detector resolution in the measurement of the decay vertices. The detector response for Δt, called the Δt resolution function $\mathcal{R}$, is approximated by three Gaussian distributions with different widths and means

$$\begin{aligned}
&\mathcal{R}_{\rm reso}(\delta t, \sigma_{\Delta t} | f_{\rm tail}, f_{\rm outlier}, S_{\rm core}, \delta_{\rm core}, S_{\rm tail}, \delta_{\rm tail}, \sigma_{\rm outlier}, \delta_{\rm outlier}) = \\
&\quad (1 - f_{\rm tail} - f_{\rm outlier}) \frac{\exp -\frac{1}{2}\left(\frac{\delta t - \delta_{\rm core}\cdot\sigma_{\Delta t}}{S_{\rm core}\sigma_{\Delta t}}\right)^2}{\sqrt{2\pi} S_{\rm core}\sigma_{\Delta t}} \\
&\quad + f_{\rm tail} \frac{\exp -\frac{1}{2}\left(\frac{\delta t - \delta_{\rm tail}\cdot\sigma_{\Delta t}}{S_{\rm tail}\sigma_{\Delta t}}\right)^2}{\sqrt{2\pi} S_{\rm tail}\sigma_{\Delta t}} \\
&\quad + f_{\rm outlier} \frac{\exp -\frac{1}{2}\left(\frac{\delta t - \delta_{\rm outlier}\cdot\sigma_{\Delta t}}{\sigma_{\rm outlier}}\right)^2}{\sqrt{2\pi}\sigma_{\rm outlier}} \,,
\end{aligned} \tag{4.18}$$

where $\delta t = \Delta t_{\rm meas} - \Delta t_{\rm true}$ is the measured value of Δt minus its true value, and $\sigma_{\Delta t}$ is the measured event-by-event error on Δt, computed by the vertex fit. The resolution function is assumed to be independent of $\Delta t_{\rm true}$.

For most events in data, the decay time difference Δt is well reconstructed ($f_{\rm core} = 1 - f_{\rm tail} - f_{\rm outlier} \approx 94\%$). Their distribution of $(\Delta t_{\rm meas} - \Delta t_{\rm true})/\sigma_{\Delta t}$ can be described by a single 'core' Gaussian with an RMS close to one. To account for a possible deviation from unit RMS, we allow for a global scale factor $S_{\rm core}$ to the error on Δt. In the fit to data, the scale factor $S_{\rm core}$ and is split by `Lepton` and non-lepton tagging categories. The distribution of the per-event errors $\sigma(\Delta t)$ for a sample of fully reconstructed $B \to D^{(*)\mp}\pi^\pm, \rho^\pm, a_1^\pm$ decays is shown in Fig. 4.8a.

For a small fraction of events the Δt error, $S_{\rm core}\sigma_{\Delta t}$, underestimates the true Δt uncertainty. These events are described by two other Gaussians in the resolution function: a 'tail' and an 'outlier'. The parametrization of the tail Gaussian is identical to the parametrization of the core Gaussian. The RMS ($\sigma_{\rm outlier} = 8$ ps) and the mean ($\delta_{\rm outlier} = 0$ ps) of the outlier Gaussian are fixed and do not use the calculated $\sigma_{\Delta t}$ values. The fractions of the outlier and the tail Gaussians, the means of the core and the tail Gaussian, and the sigma of the core Gaussian for the signal candidates are free fit parameters.

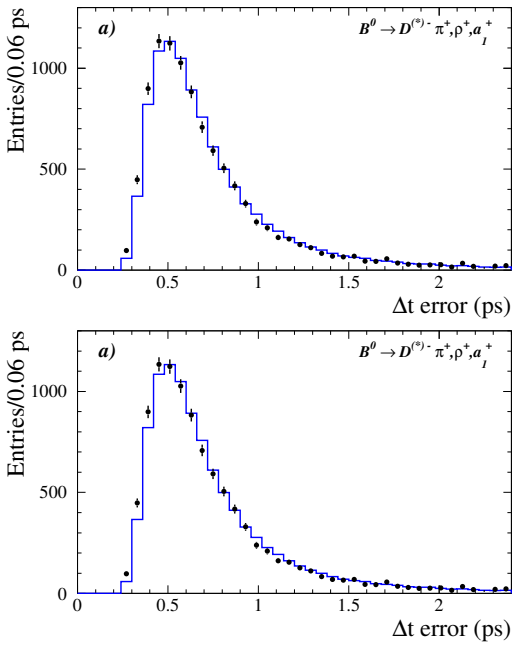

Figure 4.8: *a) Distribution of event-by-event uncertainty on Δt ($\sigma_{\Delta t}$) for the sample of neutral B decays to flavor eigenstates $D^{(*)-}\pi^+, \rho^+, a_1^+$. The histogram corresponds to Monte Carlo simulation and the points to data. The distributions have been normalized to the same area. b) Offset of the mean δt residual vs $\sigma_{\Delta t}$ from Monte Carlo simulation.*

The systematic uncertainties regarding the choice of the resolution function parameterization are discussed in Sections 9.1.1–9.1.4 and 9.2.3. For background candidates the fraction of events in the tail Gaussian is fixed to zero in order to reduce the number of parameters. In Section 9.2.3 we discuss the (small) systematic error from this simplification.

As mentioned earlier in Section 4.3.1, a bias in Δt is caused by tracks from secondary charmed particle decays in the $B_{\rm tag}$ vertex. The mean bias in $(\Delta t_{\rm meas} - \Delta t_{\rm true})$ is shown in Fig. 4.8b. Because $z_{\rm tag}$ is typically overestimated, the bias in Δt is negative. In general, the bias depends on the momenta and fraction of tracks from secondary charm decays used in the reconstruction of the tagging B vertex, and can be different per tagging category. We allow separate $\delta_{\rm core}$ parameters for the `Lepton` and non-lepton tagging categories.

In addition, it has been found that the bias is larger for events with larger $\sigma_{\Delta t}$ [68], as demonstrated in Fig. 4.8b. To model this, we scale the mean biases of the core and tail Gaussian, $\delta_{\rm core}$ and $\delta_{\rm tail}$, by $\sigma_{\Delta t}$. The correlation, illustrated in Fig. 4.9, can be explained as follows. The major axis of the $B_{\rm tag}$ vertex error ellipse comes from charm decay products, and is oriented along the charm meson flight direction. Thus, the z error of the vertex fit is correlated with the D flight length along the z axis. In particular, a D traveling in the forward direction tends to have both a larger flight length, introducing a larger bias on the vertex position estimate,

and a larger error along the z-axis.

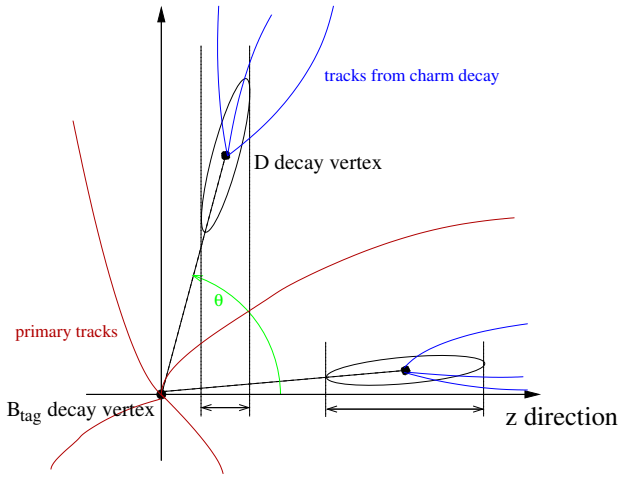

Figure 4.9: *The figure shows two flight directions of the D in the rest frame of the detector. In one case the D travels in the transverse plane, with angle θ, and in the other case in the forward direction, where the flight length in z tends to be larger. The projection of the error ellipse on the z axis is larger for the D meson flying in the forward direction.*

The time-evolutions for $B^0\overline{B}^0$ oscillations are convolved with the resolution function to take into account the uncertainties in Δt. The convolution is discussed in Section 6.2.3.

4.3.4 Correlations between mistag fraction w and $\sigma_{\Delta t}$

There is a known, linear correlation between $\sigma_{\Delta t}$ and the mistag fraction w. Namely, w increases as a function of $\sigma_{\Delta t}$ [69, 70]. This can be understood qualitatively through the parameters' mutual dependence on $(\sum_i p_{t_i}^2)^{-\frac{1}{2}}$, where the sum runs over the transverse momenta of all tracks in the B_{tag} vertex.Intuitively, this vertex is constructed with smaller uncertainty when using high-momentum tracks with good-precision trajectories. Second, due to the hard spectrum of right-sign tagged kaons, the flavor-tagging algorithm has a smaller mistag rate for high-energy particles.

The correlation is negligible for events in the lepton category, having the smallest mistag fraction. Furthermore, for these events the B_{tag} vertex-determination is dominated by high-momentum tracks. The correlation is stronger for the hadronic tagging categories, which have higher mistag fractions and rely mainly on identified kaons in the final state for flavor tagging. In Section 4.2 it has been discussed that a K^+ (right-sign), or a total positive charge of all kaons, indicates a B^0, while a K^- (wrong-sign), or a total negative charge for all kaons, indicates a $\overline{B}^0$. The probability of assigning the wrong flavor tag, based on the charge of the kaons, is higher because of wrong-sign kaons present in many B decays. And usually, wrong-sign kaons are present in events with higher multiplicity due to charge conservation, which results in a softer momentum spectrum.

The effect of the correlation between w and $\sigma_{\Delta t}$ on the measured CP asymmetries is small [71, 72]. In our nominal fit the mistagging correlation is accounted for, and the average dilutions ($D = 1-2w$) and dilution differences (ΔD) for B^0 and $\overline{B}^0$ tags – introduced in Section 6.2.2 – are parametrized as

$$\begin{aligned} D &= D_0 + D_S\,\sigma_{\Delta t}, \\ \Delta D &= \Delta D_0 + \Delta D_S\,\sigma_{\Delta t}. \end{aligned} \tag{4.19}$$

The description holds up well to the cut $\sigma_{\Delta t} < 2.5$ ps. The slopes of the average dilutions $\sigma_{\Delta t}$ for each tagging category are left free in the likelihood fit. The slopes for the dilution differences for B^0 and $\overline{B}^0$ tags $S_{\Delta D}$ are fixed to zero.

4.4 Data sample summary

The Section presents a summary of the data sample used in the time-dependent analysis in Chapter 8.

In the maximum-likelihood fit to the Δt distributions of the samples $B \to D^{(*)\mp}\pi^{\pm}$ and $B \to D^{\mp}\rho^{\pm}$, the probability of an event to be signal (or background) used the measured value of m_{ES}, and is based on the (fitted) distribution of m_{ES} for signal and background. as indicated in Eq. (4.13). The result of the m_{ES} fit to data is presented in this Section.

The m_{ES} fit is performed to all samples simultaneously, with a subset of the parameters split by tagging category and B and $D^{(*)}$ decay mode. The amount of background varies within the B decay modes and tagging categories, and also slightly for each $D^{(*)}$ decay mode. For example, $B \to D^{*\mp}\pi^{\pm}$ decays have a higher signal purity than $B \to D^{\mp}\pi^{\pm}/\rho^{\pm}$ decays, and, likewise, the `Lepton` tagging category has less background events than the non-lepton (‘`N-Lept.`’) tagging categories. Hence, the m_{ES} fit with certain parameters split per category provides a better estimate of the signal probability.

As described in Section 4.1.3, each distribution is fit to the sum of a Gaussian (for signal events), an `Argus` function (for combinatorial background events), and a `Cruijff` function (for background events that peak in m_{ES}, not described by the `Argus` function). The peaking background functions in m_{ES} are fixed to the shapes obtained in Section 4.1.4 from the reconstructed sample of generic, fully-simulated $\Upsilon(4S) \to B\overline{B}$ events.

The results of the m_{ES} fit are summarized Table 4.6. The signal yields from the m_{ES} fit for the various tagging categories and $B{\otimes}D$ modes are shown in Table 4.7. The combinatorial background yields are shown in Table 4.8. The $B{\otimes}D$ modes have been labeled `Dst`, `D`, `R` for the $B \to D^{*\mp}\pi^{\pm}$, $B \to D^{\mp}\pi^{\pm}$, $B \to D^{\mp}\rho^{\pm}$ decays respectively, and these names are concatenated with a description of the D decay, *e.g.* making ‘`DstKpi`’ for $B^0 \to D^{*-}\pi^{+}$ with $\bar{D}^0 \to K^{+}\pi^{-}$ following the D^{*-} decay. From Tables 4.6-4.8 there are 118 free parameters, of which 96 determine signal and background yields, and 16 fixed parameters, mostly related to the peaking background description.

Distributions of m_{ES} for $B \to D^{(*)\mp}h^{\pm}$, where the tagging categories and corresponding D decay modes have been summed, are shown in Fig. 4.10. The result of the fit, used to determine the event-by-event signal probability, is overlaid on the data. Fig. 7.17 in Section 7.6 shows the corresponding residual plots.

In Table 4.6 the signal purity $\mathcal{P}$ – defined as the fraction of signal yield over total number of events – and combinatorial background fraction have been calculated for events in the signal box, *i.e.* for events with $m_{ES} > 5.27$ GeV/c^2. The signal, combinatorial and peaking background

Parameter	$B \to D^{\mp}\pi^{\pm}$		$B \to D^{*\mp}\pi^{\pm}$		$B \to D^{\mp}\rho^{\pm}$	
Signal yield	14617 ± 129		13694 ± 120		8517 ± 99	
Peak. bkg. yield	421.1 ± 3.7		308.0 ± 2.7		218 ± 2.5	
Comb. bkg. yield	13996 ± 131		5950 ± 84		9823 ± 107	
$\mathcal{P}$ (%)	84.5 ± 0.3		91.1 ± 0.2		79.7 ± 0.4	
Comb. bkg. fraction (%)	13.0 ± 0.3		6.8 ± 0.2		18.3 ± 0.4	
m_B (MeV/c^2)	5280.01 ± 0.02		5279.98 ± 0.02		5279.97 ± 0.04	
σ_m (MeV/c^2)	2.46 ± 0.02		2.52 ± 0.02		2.80 ± 0.03	
End point (MeV/c^2)	5290.5 (fixed)					
`Argus` parameter κ	`Lepton`	`N-Lept.`	`Lepton`	`N-Lept.`	`Lepton`	`N-Lept.`
κ[`DKpipi`]	-109 ± 40	-19 ± 4	–		–	
κ[`DKspi`]	-40 ± 11	-27 ± 1	–		–	
κ[`DstKpi`]	–		-80 ± 27	-28 ± 3	–	
κ[`DstKpipi0`]	–		-75 ± 32	-37 ± 3	–	
κ[`DstKspipi`]	–		-115 ± 65	-7 ± 4	–	
κ[`DstK3pi`]	–		-118 ± 83	-21 ± 6	–	
κ[`RKpipi`]	–		–		-87 ± 10	-40 ± 1
κ[`RKspi`]	–		–		-31 ± 29	-38 ± 5
Peak. bkg. fraction (%)	2.9 (fixed)		2.2 (fixed)		2.6 (fixed)	
`Cruijff` p.b. parameters	Left	Right	Left	Right	Left	Right
σ_{pb} (MeV/c^2) (fixed)	3.2	2.6	3.0	2.5	3.6	3.4
α_{pb} (fixed)	0.096	0.0	0.0	0.0	0.044	0.0

Table 4.6: *Summary of results of the m_{ES} fit to the data sample.*

Signal yield	`Lepton`	`Kaon I`	`Kaon II`	`K-Pi`	`Pion`	`Other`
`DKpipi`	1464 ± 39	1952 ± 46	2925 ± 58	2504 ± 53	2463 ± 54	1711 ± 45
`DKspi`	181 ± 14	223 ± 16	356 ± 20	311 ± 19	311 ± 19	217 ± 16
`DstKpi`	566 ± 24	685 ± 27	1080 ± 33	865 ± 30	945 ± 31	607 ± 25
`DstKpipi0`	359 ± 19	440 ± 22	673 ± 27	559 ± 25	622 ± 26	400 ± 21
`DstK3pi`	544 ± 24	689 ± 27	1058 ± 34	873 ± 31	934 ± 32	610 ± 26
`DstKspipi`	130 ± 11	180 ± 14	294 ± 17	185 ± 14	233 ± 16	167 ± 13
`RKpipi`	934 ± 31	1130 ± 35	1804 ± 46	1320 ± 40	1447 ± 41	1003 ± 35
`RKspi`	111 ± 11	133 ± 12	220 ± 16	147 ± 13	157 ± 13	112 ± 11
Total	4288 ± 66	5430 ± 77	8408 ± 97	6763 ± 87	7113 ± 90	4825 ± 74

Table 4.7: *Signal yields from the m_{ES} fit to data, split by tagging category (row) and $B \otimes D$ mode (column).*

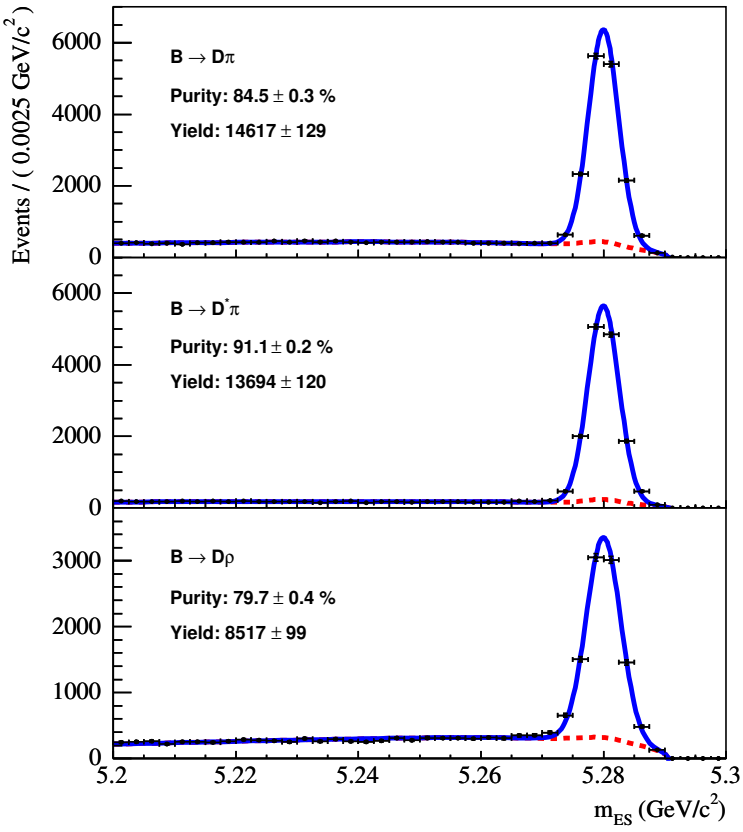

Figure 4.10: *The m_{ES} distributions in the signal region for, from top to bottom, the $B \to D^{\mp}\pi^{\pm}$, $B \to D^{*\mp}\pi^{\pm}$, and $B \to D^{\mp}\rho^{\pm}$ sample for the events that satisfy the selection criteria, fit with the function described in the text. The dashed curves indicate the sum of the combinatorial and peaking background contributions.*

yields are measured over the entire m_{ES} range. The fractions of peaking background are defined relative to the signal yields of B decay modes.

As seen in Fig. 4.10, the likelihood to find signal events in the m_{ES} sideband, with $5.20 < m_{ES} < 5.27$ GeV/c^2, is practically zero. Notice in Table 4.6 that the average signal purity varies from 80% to over 90% between the three B decay modes. In total, $36,828 \pm 202$ signal events are available in the Δt fit to determine CP violation related parameters.

Comb. bkg. yield	Lepton	Kaon I	Kaon II	K-Pi	Pion	Other
DKpipi	149 ± 14	1402 ± 42	3161 ± 62	2611 ± 56	3043 ± 61	2511 ± 55
DKspi	17 ± 5	160 ± 14	283 ± 19	211 ± 16	248 ± 18	201 ± 16
DstKpi	7 ± 4	173 ± 14	345 ± 20	265 ± 18	290 ± 18	208 ± 15
DstKpipi0	24 ± 6	267 ± 18	541 ± 25	392 ± 22	411 ± 22	312 ± 19
DstK3pi	25 ± 6	355 ± 21	644 ± 27	433 ± 22	470 ± 24	375 ± 21
DstKspipi	3 ± 3	56 ± 8	107 ± 11	92 ± 10	82 ± 10	72 ± 9
RKpipi	220 ± 17	878 ± 32	2135 ± 49	1902 ± 46	2161 ± 49	1724 ± 44
RKspi	18 ± 5	85 ± 10	204 ± 15	179 ± 14	184 ± 14	134 ± 12

Table 4.8: *Combinatorial background yields from the m_{ES} fit to data, split by tagging category (row) and $B \otimes D$ mode (column).*

Chapter 5

Tag-side interference

Interference between CKM-favored $b \to c\overline{u}d$ and doubly-CKM-suppressed $\overline{b} \to \overline{u}c\overline{d}$ amplitudes in final states used for B flavor tagging gives deviations from the standard time evolution assumed in CP-violation measurements at B factories producing coherent $B^0\overline{B}^0$ pairs. The time-dependent analysis of $B \to D^{(*)\mp}h^{\pm}$ decays ($h = \pi, \rho$), used for measuring $\sin(2\beta+\gamma)$, must incorporate this possible tag-side interference, which could produce asymmetries as large as the expected signal asymmetry.

5.1 Introduction

An essential ingredient in CP violation measurements in B^0 decays is flavor tagging. In this Chapter, we point out a subtlety of flavor tagging previously overlooked in many CP violation analyses, describe its impact on the measurement of $\sin(2\beta+\gamma)$, and show how to address it.

In the PEP-II asymmetric B-factory $B^0\overline{B}^0$ meson pairs are produced in e^+e^- interactions at the $\Upsilon(4S)$ resonance, where the pair evolves coherently in a P-wave state until one of the B mesons decays. Typically, as in this measurement, one B decay is fully reconstructed and the flavor (whether it's a B^0 or $\overline{B}^0$) of this B, at the time of the other B's decay, is inferred from the decay products of the other B (the tag B). At the time the first of the two B mesons decays, the B mesons are known to be in opposite flavor states. In terms of the time difference between the two B decays, $\Delta t \equiv t_{\rm rec} - t_{\rm tag}$, the time-dependent CP asymmetry is defined as

$$\mathcal{A}_{CP}(\Delta t) \equiv \frac{N\left(\text{tag } B^0, \Delta t\right) - N\left(\text{tag } \overline{B}^0, \Delta t\right)}{N\left(\text{tag } B^0, \Delta t\right) + N\left(\text{tag } \overline{B}^0, \Delta t\right)}\,, \tag{5.1}$$

where N is the number of events at Δt with a B^0 or $\overline{B}^0$ as the tag B.

As described in Section 4.2.1, charged leptons and kaons are often used to infer the flavor of the tag B meson. The charge of a lepton from a semi-leptonic B decay has the same sign as the charge of the b quark that produced it. For example, a high-momentum e^+ (e^-) would indicate that the tag B was a B^0 ($\overline{B}^0$) at the time of its decay. Similarly, a $K^+(K^-)$ more often than not comes from a B^0 ($\overline{B}^0$). This works because the most likely b decay is $b \to c$ and the most likely c decay is $c \to s$; thus the s quark usually has the same charge as the b quark. However, the lepton or kaon charge does not always correctly indicate the tag-B flavor: mistags can arise from either incorrect particle identification or from other B decay chains that produce wrong-sign leptons or kaons. As a result, the mistag fraction must be measured from data in order to determine the true CP asymmetry from the measured one.

It is usually assumed that the measured *CP* asymmetry is entirely due to the interfering amplitudes contributing to the fully reconstructed B decay mode, and that the individual tagging states, such as $\overline{B}^0 \to D^+\pi^-$, are dominated by a single B decay amplitude. In other words, if only one B decay amplitude contributes to the tagging final state, it is safe to assume that all interference effects, such as *CP* violation, are due to the evolution of the fully reconstructed B. This assumption, which is valid for semi-leptonic B decays, ignores the possibility of suppressed contributions to the tag-side final state with different weak phases, such as happens for non-leptonic decays.

These suppressed contributions may be important for kaon tags. For example, the $D^+\pi^-$ final state with $D^+ \to K^-\pi^+\pi^+$, which is usually associated with a $\overline{B}^0$ decay, can also be reached from a B^0 through a $\overline{b} \to \overline{u}c\overline{d}$ decay. Its amplitude is suppressed relative to the dominant $\overline{B}^0$ decay amplitude ($b \to c\overline{u}d$) by a factor of roughly $|(V^*_{ub}V_{cd})/(V_{cb}V^*_{ud})| \approx 0.02$, and has a relative weak phase difference of γ. Both Feynman diagrams have been shown in Fig. 2.9 in Section 2.6. The tag-side $b \to c\overline{u}d$ and $\overline{b} \to \overline{u}c\overline{d}$ amplitudes interfere, and, through the coherent evolution of the $B^0\overline{B}^0$ pair, alter the time evolution of $A_{CP}(\Delta t)$. In the following Sections we investigate the consequences of this (small) 'tag-side interference' effect on the time-dependent *CP*-asymmetry measurement of $B \to D^{(*)\mp}h^{\pm}$ decays ($h = \pi, \rho$), at B factories that use coherent B decays.

In Sections 5.2–5.6, we review the general formalism for describing the coherent evolution of the $B^0\overline{B}^0$ system, define our notation for describing the tag-side amplitude, and state the assumptions we employ in our analysis. In Section 5.7, we evaluate how tag-side interference affects the mistag fraction measured from the amplitude of the time-dependent mixing (not *CP*) asymmetry. We find that the tag-side interference effects are not simply absorbed into the mistag fractions and that, to first order, the mistag fractions are unchanged by tag-side interference. In Section 5.8 we evaluate how tag-side interference affects the decay time-dependent techniques used for measuring $\sin(2\beta+\gamma)$ (*e.g.* the time-dependent analysis of $B \to D^{(*)\mp}h^{\pm}$). We find that tag-side interference effects can be as large as the signal asymmetry. We show a technique for performing the analysis in a general way, which does not require assumptions about the size of tag-side interference effects and maximizes the statistical sensitivity to $(2\beta + \gamma)$. We summarize our conclusions in Section 5.9. The impact of tag-side interference on the standard mixing-induced *CP* asymmetry measurements – *e.g.* $\sin 2\beta$ from $B \to J/\psi K_S$ and the *CP* asymmetry in $B \to \pi^+\pi^-$ – can be found in Ref. [73].

5.2 General coherent formalism

In Section 2.5.2 we have defined the formalism for describing the time evolution of a pair of neutral B mesons that are coherently produced in an $\Upsilon(4S)$ decay and then subsequently decay to final states $f_{\rm t}$ and $f_{\rm r}$ at times $t_{\rm t}$ and $t_{\rm r}$, respectively, measured in the parent B meson's rest frame. For completeness, we summarize it here.

Given the B^0 ($\overline{B}^0$) decay amplitude to f_k, A_k ($\overline{A}_k$), the complex parameters $a_{\pm}$ can be defined as

$$a_+ = \overline{A}_{\rm t}\, A_{\rm r} - A_{\rm t}\, \overline{A}_{\rm r} \quad , \quad a_- = \frac{p}{q} A_{\rm t}\, A_{\rm r} - \frac{q}{p}\overline{A}_{\rm t}\, \overline{A}_{\rm r}\,, \tag{5.2}$$

where the 't' ('r') subscript refers to the tag (reconstructed) B meson or its final state.

Assuming *CPT* invariance, $\Delta\Gamma/\Gamma \ll 1$, and $|q/p| \simeq 1$ (see Section 2.5.1), the resulting time

dependence of Eq. (2.39), when the tagged meson is a B^0, can be expressed as

$$F(\Delta t) = e^{-\Gamma|\Delta t|}\,\left[R + C\cos(\Delta m\Delta t) + S\sin(\Delta m\Delta t)\right]\,, \tag{5.3}$$

and correspondingly when the tagged meson is a $\overline{B}^0$

$$\overline{F}(\Delta t) = e^{-\Gamma|\Delta t|}\,\left[\overline{R} + \overline{C}\cos(\Delta m\Delta t) + \overline{S}\sin(\Delta m\Delta t)\right]\,, \tag{5.4}$$

where $\Delta t \equiv t_{\rm r} - t_{\rm t}$. The coefficients satisfy the constraint $C^2 + S^2 = R^2$, and are given by

$$R \equiv \frac{1}{2}\left(|a_+|^2 + |a_-|^2\right), \qquad C \equiv \frac{1}{2}\left(|a_+|^2 - |a_-|^2\right), \qquad S \equiv +{\rm Im}(a_+^* a_-)\,. \tag{5.5}$$

5.3 Characterization of tagging amplitude

The strength of the doubly-CKM-suppressed (DCS) decays has been expressed in Eq. (2.46) as

$$\lambda_f = \frac{q}{p}\frac{\overline{A}_f}{A_f}\,. \tag{5.6}$$

This combination is independent of the choice of phases for the B^0 and $\overline{B}^0$ states. Suppose $|f\rangle$ is a final state that is the result of a B^0 decay. For example, if $|f\rangle$ represents the tag B, a K^+ would indicate that the tag B decayed as a B^0, assuming the dominant $\overline{b} \to \overline{c}u\overline{d}$ transition occurred. Then, like in Section 2.6,

$$\lambda_f = r_f e^{-2i\beta - i\gamma} e^{i\delta_f}\,, \tag{5.7}$$

where the relative amplitude r_f is a real number of order 0.02, and δ_f is the strong phase difference of the $\overline{B}^0$ decay relative to that of the B^0 decay, assuming $\overline{b} \to \overline{c}u\overline{d}$ and $b \to u\overline{c}d$ transitions for the B^0 and $\overline{B}^0$ decays respectively. If, for this final state, there is only one mechanism contributing to the B^0 decay and to the $\overline{B}^0$ decay, then for the CP conjugate state $|\overline{f}\rangle$ we have

$$\lambda_f = \frac{1}{r_f} e^{-2i\beta - i\gamma} e^{-i\delta_f}\,. \tag{5.8}$$

We shall make the assumption of a single contributing amplitude except as noted below.

Because the DCS amplitudes are only about 2% of the allowed amplitudes, in what follows we shall drop all terms that are quadratic or higher in this suppression. In practice we combine many final states f in a single tagging category, $f \in T$. For the tagging category we then have effective values of r' and δ' defined by

$$r' e^{i\delta'} = \frac{\sum_{f\in T}\,\epsilon_f |A_f|^2\, r_f e^{i\delta_f}}{\sum_{f\in T}\,\epsilon_f |A_f|^2}\,, \tag{5.9}$$

where ϵ_f is the relative tagging efficiency for the state f. Notice that

$$|r'| \le \frac{\sum_{f\in T}\,\epsilon_f |A_f|^2 |r_f|}{\sum_{f\in T}\,\epsilon_f |A_f|^2}\,, \tag{5.10}$$

so there is a tendency for contributions from different tagging states to cancel, unless all contributions have nearly the same strong phase. More about this in Section 5.5. Eq. (5.9) holds only if terms of order r_f^2 can be ignored, as we are assuming.

5.4 Time-dependent asymmetry coefficients

In this Section, we evaluate the coefficients $R\,(\overline{R})$, $C\,(\overline{C})$, and $S\,(\overline{S})$ of Eqs. (5.3) ((5.4)). Here we consider the 'mixing' case, where the reconstructed B meson decays in an apparent flavor eigenstate (*e.g.* $D^{*+}\pi^-$, normally assumed to originate from $\overline{B}^0$ decay). The '*CP*' case, where the reconstructed B has decayed into a *CP* eigenstate, can be found in Ref. [73]. Dropping the common factor $A_{\rm t}\,A_{\rm r}\,(p/q)$, we can write a_+ and a_- in terms of the λ parameters for the tag and reconstructed B mesons as

$$\begin{aligned} a_+ &= \lambda_{\rm t} - \lambda_{\rm r} \\ a_- &= 1 - \lambda_{\rm t}\,\lambda_{\rm r}. \end{aligned} \tag{5.11}$$

Quite generally then,

$$\begin{aligned} |a_+|^2 &= |\lambda_{\rm t}|^2 - 2\,{\rm Re}\,\lambda_{\rm t}\,\lambda_{\rm r}^* + |\lambda_{\rm r}|^2 \\ |a_-|^2 &= 1 - 2\,{\rm Re}\,\lambda_{\rm t}\,\lambda_{\rm r} + |\lambda_{\rm t}|^2\,|\lambda_{\rm r}|^2 \\ {\rm Im}\,a_+^* a_- &= {\rm Im}\,\lambda_{\rm r}\,(1-|\lambda_{\rm t}|^2) \;-\; {\rm Im}\,\lambda_{\rm t}\,(1-|\lambda_{\rm r}|^2)\,. \end{aligned} \tag{5.12}$$

The coefficients for the mixing case are given in Table 5.1, where for the reconstructed B meson final state we have dropped the subscript f from the amplitude ratio r and from the strong phase difference δ in $\lambda_{\rm r}$, defined by Eq. (5.7). The only deviation from the familiar case with no DCS contributions, to first order in r and r', is the presence of a small $S(\overline{S})$ coefficient. Fig. 5.1 shows an illustration of the time evolution for when the flavor of the two B mesons at the time of decay was opposite (unmixed) or the same (mixed). The nominal ($r = r' = 0$) case is contrasted with an example of a non-zero DCS contribution in the reconstructed B amplitude and with an example of non-zero DCS contributions to both the tag and reconstructed B amplitudes. The amplitude ratios r and r' have been enlarged by a factor of five with respect to the expected value (0.02) so that the DCS contributions are more clear.

5.5 Completely inclusive tagging categories

We can relate the effective r' and δ' to the 2×2 matrix Γ that generalizes the decay rate for the $B^0\overline{B}^0$ system. Let T be the class of states DX, where X represents non-charmed hadrons. Neglecting the relative tagging efficiency ϵ_f for the moment, we have

$$\sum_{f\in T}\frac{q}{p}A_f^*\overline{A}_f = \sum_{f\in T}|A_f|^2\lambda_f = \sum_{f\in T}\langle B^0|\mathcal{H}|f\rangle\langle f|\mathcal{H}|B^0\rangle r_f e^{-2i\beta-i\gamma+i\delta_f} = \Gamma_{DX}\,r' e^{-2i\beta-i\gamma+i\delta'}\,, \tag{5.13}$$

where Γ_{DX} is, up to a trivial normalization, the partial width of B^0 into the class of states of the form DX. On the other hand, we can write

$$\sum_{F\in T}\frac{q}{p}A_f^*\overline{A}_f = \sum_{F\in T}\frac{q}{p}\langle B^0|\mathcal{H}|f\rangle\langle f|\mathcal{H}|\overline{B}^0\rangle = \frac{q}{p}\Gamma_{DX\,12}\,, \tag{5.14}$$

where $\Gamma_{DX\,12}$ is the contribution of states of the form DX to the off-diagonal part of the Γ matrix. So

$$r' e^{-2i\beta-i\gamma+i\delta'} = \frac{q}{p}\Gamma_{DX\;12}/\Gamma_{DX}\,. \tag{5.15}$$

Parameter	[tag=$B^0(K^+)$, rec=B^0]	[tag=$B^0(K^+)$, rec=$\overline{B}^0$]	[tag=$\overline{B}^0(K^-)$, rec=B^0]	[tag=$\overline{B}^0(K^-)$, rec=$\overline{B}^0$]
$\lambda_{\rm t}$	$r'e^{-2i\beta-i\gamma+i\delta'}$	$r'e^{-2i\beta-i\gamma+i\delta'}$	$\frac{1}{r'}e^{-2i\beta-i\gamma-i\delta'}$	$\frac{1}{r'}e^{-2i\beta-i\gamma-i\delta'}$
$\lambda_{\rm r}$	$re^{-2i\beta-i\gamma+i\delta}$	$\frac{1}{r}e^{-2i\beta-i\gamma-i\delta}$	$re^{-2i\beta-i\gamma+i\delta}$	$\frac{1}{r}e^{-2i\beta-i\gamma-i\delta}$
$\lvert a_+\rvert^2$	0	$\frac{1}{r^2}$	$\frac{1}{r'^2}$	0
$\lvert a_-\rvert^2$	1	0	0	$\frac{1}{+r^2r'^2}$
Im $a_+^*a_-$	$-r\sin(2\beta+\gamma-\delta)$ $+r'\sin(2\beta+\gamma-\delta')$	$-\frac{r'}{r^2}\sin(2\beta+\gamma-\delta')$ $-\frac{1}{r}\sin(2\beta+\gamma+\delta)$	$\frac{r}{r'^2}\sin(2\beta+\gamma-\delta)$ $+\frac{1}{r'}\sin(2\beta+\gamma+\delta')$	$-\frac{1}{r^2r'}\sin(2\beta+\gamma+\delta')$ $+\frac{1}{rr'^2}\sin(2\beta+\gamma+\delta)$
R	1	1	1	1
C	-1	1	1	-1
S	$-2r\sin(2\beta+\gamma-\delta)$ $+2r'\sin(2\beta+\gamma-\delta')$	$-2r'\sin(2\beta+\gamma-\delta')$ $-2r\sin(2\beta+\gamma+\delta)$	$2r\sin(2\beta+\gamma-\delta)$ $+2r'\sin(2\beta+\gamma+\delta')$	$-2r'\sin(2\beta+\gamma+\delta')$ $+2r\sin(2\beta+\gamma+\delta)$

Table 5.1: *Contributions to the time dependence of tagged decays when the reconstructed decay is an apparent flavor eigenstate, with doubly-CKM-suppressed decays considered only to first order. The dependences proportional to* 1 *and to* $\cos(\Delta m\Delta t)$ *are unaffected. A small* $\sin(\Delta m\Delta t)$ *term is induced. Appropriate factors of* r *and* r' *have been removed to scale* R *to unity.*

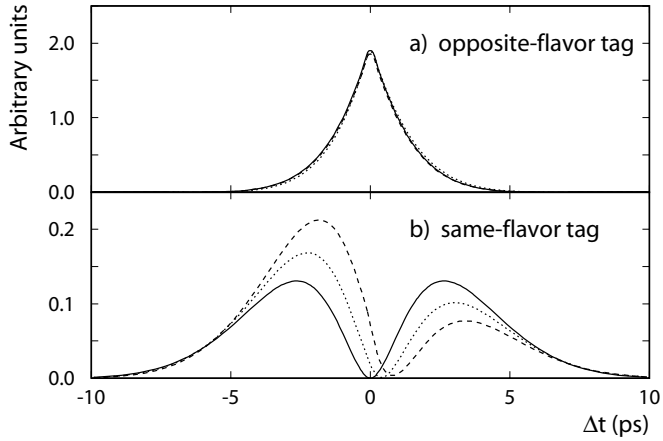

Figure 5.1: *Time-dependent decay distributions for the final state $D^{*-}\pi^+$, for a) a $\overline{B}^0$ tag, and b) a B^0 tag. The angle $(2\beta+\gamma)$ is set to the value* 1.86*. The situation with no doubly-CKM-suppressed contribution on both the tag-side and reconstruction-side is indicated with the solid curve. The dotted curve has $r = 0.1$ and $\delta = 0$, but no tag-side interference. The dashed curve represents the example with $r = r' = 0.1$, $\delta = 0$, and $\delta' = \pi$. In these examples, the r and r' values are $\times 5$ the expected values in order to clearly illustrate the differences with respect to the case with $r = r' = 0$.*

If sum over states in Eq. (5.14) were complete, then δ' would vanish. To see this, imagine using as a basis of states f_S not the physical states that are observed but instead a basis of states that are eigenstates of the S matrix, that is, a basis of states that each scatter into themselves. Because we are summing over all states in a collection connected by strong interactions, there is such a basis. Then the final state interaction phases associated with A_{f_S} and $\overline{A}_{f_S}$ would both be $e^{i\delta_{f_S}}$. These would cancel in the product $A^*_{f_S}\overline{A}_{f_S}$.

In general, however, because tagging does not capture every state, one should think of Γ_{12} and Γ as effective quantities, limited by the partial sum over states. Therefore one cannot assume that δ' vanishes. Also, in reality, the relative tagging efficiency ϵ_f, set to one in Eq. (5.13), is not the same for all of the states in T, so the tagging category representing the class of states DX is not completely inclusive either.

5.6 Estimated size of doubly-CKM suppressed amplitude

In the introduction of this Chapter we have given an estimate for the size of the DCS amplitude (r), relative to the favored amplitude, to be approximately 0.02, which is simply the ratio of the CKM elements involved, $|(V^*_{ub}V_{cd})/(V_{cb}V^*_{ud})|$. Here, we discuss the uncertainty of r' as well as what can be assumed, if anything, about the average strong phase difference (δ') between the DCS and favored tagging amplitudes.

The decay $B^0 \to D^+\pi^-$ is doubly-CKM suppressed, but its branching fraction has not been

measured. We can estimate its branching fraction from the related decay mode $B^0 \to D_s^+\pi^-$, using Eq. (10.2)

$$r^{D\pi} \approx \sqrt{\frac{\mathcal{B}(B^0 \to D_s^+\pi^-)}{\mathcal{B}(B^0 \to D^-\pi^+)}} \left|\frac{V_{cd}}{V_{cs}}\right| \frac{f_D}{f_{D_s}} \ .$$

In Chapter 10 we obtain

$$\begin{aligned} r^{D\pi} &= (1.53 \pm 0.33\,(\text{exp.}) \pm 0.08\,(\text{theo.})) \times 10^{-2}\,, \\ r^{D^*\pi} &= (2.10 \pm 0.47\,(\text{exp.}) \pm 0.11\,(\text{theo.})) \times 10^{-2}\,, \\ r^{D\rho} &= (0.31 \pm 0.59\,(\text{exp.}) \pm 0.02\,(\text{theo.})) \times 10^{-2}\,. \end{aligned}$$

For $D^{(*)}\pi$ is in good agreement with the naive estimate of 0.02, albeit with large uncertainties.

There are some theoretical arguments for expecting the strong phase difference δ to be small [89] (modulo π), but we know of at least one case where a non-trivial strong phase has been observed in B decay[1]. The size of the effective amplitude ratio, r', given by Eq. (5.9), depends on the values of δ the final states included in the tagging category. As Eq. (5.10) shows, varying over many values of δ between the states will tend to reduce r'.

Given the large uncertainty on the DCS amplitude ratio r for individual final states and the general lack of knowledge concerning strong phase differences, we conclude that the most conservative assumptions regarding the effective parameters r' and δ' would be to allow r' values from 0 (full cancellation in the sum) up to 0.04 (no cancellation, with an enhancement of a factor of two over our estimate of 0.02) and to allow for any value of δ'.

5.7 Mistag calibration with flavor oscillation amplitude

As mentioned earlier, the sign of the tagging kaon charge does not always give the correct flavor tag. For example, CKM-suppressed D decays, such as $D^+ \to K^+\overline{K}^0$, can produce wrong-sign kaons. Pions, incorrectly identified as kaons, can also produce wrong-sign kaons. The amplitude of any measured asymmetry using kaon tags will be reduced by a factor of $(1 - 2\omega)$, called the dilution factor, where ω is the fraction of tagging kaons that have the wrong sign (mistag fraction). The mistag fraction ω is usually measured from the amplitude of time-dependent flavor oscillations in a sample of reconstructed B^0 decays to flavor-specific final states [56]. The measured value of the asymmetry C/R will be a direct measurement of $(1 - 2\omega)$, which can then be used to interpret measured CP asymmetry coefficients.

Contrary to what one may guess, the corrections due to DCS amplitude contributions are not simply absorbed into the mistag fractions. However, to first order in r and r', the R and C coefficients are the expected ones, as can be seen in Table 5.1. This means that the measured mistag fractions will be unaffected by DCS amplitude contributions, either on the tag side or the reconstructed side.

Using Monte Carlo pseudo-experiments, we find that Δm_d is unaffected to the level of 0.001 ps^{-1} if allowed to float in the fit. The only effect is in the S coefficient, which is usually assumed to be zero in the analysis of mixing data. We discuss the impact on the measurement of $2\beta + \gamma$ in Section 5.8.

[1] The strong phase difference between the longitudinal and parallel polarization amplitudes of the transversity basis in $B \to J/\psi K^*(892)$ has been measured [74] to be 2.50 ± 0.22, which is about 3σ from π, in contradiction with the factorization prediction of 0 or π.

Remember that the statements above apply to measurements that only use kaon tags. In practice, all useful sources of flavor information from the tag side B are employed in order to maximize the sensitivity of the measurement. The statistical error on the measured asymmetry scales as $1/\sqrt{\sum_i Q_i}$, where each flavor tagging category contributes $Q_i = \epsilon_i(1-2\omega_i)^2$ and ϵ_i is efficiency for category i. Lepton flavor tags do not have the problem of a suppressed amplitude contribution with a different weak phase, so one can assume that $r' = 0$ for lepton tags. If a measurement uses both lepton and non-lepton tags, the magnitude of the tag-side interference uncertainty will be scaled down by a factor of $Q_{\rm non-lep}/(Q_{\rm lep} + Q_{\rm non-lep})$. For example, the *BABAR* flavor tagging algorithm (see Section 8.2) has roughly $Q_{\rm lep} \approx 0.1$ and $Q_{\rm non-lep} \approx 0.2$. This gives a reduction of the tag-side interference uncertainty of about a factor of 2/3.

5.8 Impact on measurement of γ with $B \to D^{(*)\mp}h^{\pm}$ decays

As laid out in Section 2.6, one technique for measuring or constraining γ is to perform a time-dependent analysis of a decay mode that is known to have a non-zero DCS contribution, such as $B \to D^{(*)\mp}h^{\pm}$ decays ($h = \pi, \rho$). For illustration purposes, here we focus on the final state $D^{*+}\pi^-$. The time-dependent asymmetry coefficients are those given in Table 5.1. In the usual case, tag-side interference is ignored ($r' = 0$) and the amplitude of the $\sin(\Delta m\Delta t)$ term is $2r\sin(2\beta+\gamma\pm\delta)$, where r is the ratio of the DCS to CKM-favored amplitude contributions for the reconstructed, or non-flavor-tag, B and δ is the strong phase difference between the two amplitudes. Measuring r and $\sin(2\beta+\gamma\pm\delta)$ simultaneously is very challenging due to the small value of r, so r will have to be constrained from other measurements (see Chapter 10).

Symbol	Reco	Tag	$\sin(\Delta m\Delta t)$ coefficient	
$S1$	B^0 $(D^{*-}\pi^+)$	B^0 (K^+)	$-2\,r\sin(2\beta+\gamma-\delta)$	$+\,2\,r'\sin(2\beta+\gamma-\delta')$
$S2$	B^0 $(D^{*-}\pi^+)$	$\overline{B}^0$ (K^-)	$2\,r\sin(2\beta+\gamma-\delta)$	$+\,2\,r'\sin(2\beta+\gamma+\delta')$
$S3$	$\overline{B}^0$ $(D^{*+}\pi^-)$	B^0 (K^+)	$-2\,r\sin(2\beta+\gamma+\delta)$	$-\,2\,r'\sin(2\beta+\gamma-\delta')$
$S4$	$\overline{B}^0$ $(D^{*+}\pi^-)$	$\overline{B}^0$ (K^-)	$2\,r\sin(2\beta+\gamma+\delta)$	$-\,2\,r'\sin(2\beta+\gamma+\delta')$

Table 5.2: *The 4 coefficients of the* $\sin(\Delta m\Delta t)$ *term in the time-dependence of* $D^*\pi$*. The 2nd and 3rd columns give the interpretation of the observed final state (given in parentheses) in terms of the dominant amplitude.*

Since both r and r' are expected to be of the same order (≈ 0.02), it is clear that tag-side DCS interference can not be treated as a perturbation on the usual case. This effect is illustrated in Fig. 5.1. The time dependent analysis should be performed in a way that is general enough to accommodate $r' \approx r$ and any value of δ'.

Table 5.2 gives the $\sin(\Delta m\Delta t)$ coefficients, taken from Table 5.1, for the four combinations of reconstructed and flavor tag B final states, where we have neglected r^2, rr', and r'^2 contributions. The minimum number of independent parameters in which the S coefficients can be written is three. It is useful to rewrite the relations for the S coefficients in the following way

$$S1 = -a + b + c \tag{5.16}$$
$$S2 = +a + b - c \tag{5.17}$$
$$S3 = -a - b - c \tag{5.18}$$
$$S4 = +a - b + c\,, \tag{5.19}$$

where the three variables to be determined in the time-dependent analysis are

$$a \equiv 2\, r \sin(2\beta+\gamma) \cos\delta \tag{5.20}$$

$$b \equiv 2\, r' \sin(2\beta+\gamma) \cos\delta' \tag{5.21}$$

$$c \equiv 2\cos(2\beta+\gamma)\left(r\sin\delta - r'\sin\delta'\right) . \tag{5.22}$$

This parameterization makes no assumptions about the magnitude of r' or δ', and is attractive for several reasons. First, a does not depend at all on the tag-side parameters r' and δ'. In the case where $\delta = 0$, which is favored by some [89], a is exactly what one wants to know ($\sin(2\beta+\gamma)$). Secondly, this parameterization cleanly separates the flavor-tag symmetric and antisymmetric components; the a and c coefficients are diluted by a factor of $(1-2\omega)$, while the b coefficient is not, since it has the same sign for tag-side B^0 and tag-side $\overline{B}^0$ events. In the following Chapters we use the a, b, and c coefficients as the experimental observables to be determined in the time-dependent asymmetry analysis.

The set of kaon tagging final states that yields correct tags is in general quite different from the set of final states that yields incorrect tags. This means that within a tagging category, the effective r' and δ' values for correct tags are different from those for incorrect tags. In the sum over correct and incorrect tags, the terms linear in r' that appear in the observables of the asymmetry are

$$(1-2\omega) r' e^{i\delta'} = (1-\omega) r'_c e^{i\delta'_c} - \omega r'_i e^{i\delta'_i} . \tag{5.23}$$

This equation gives effective r' and δ' parameters in terms of the mistag fraction ω, effective parameters for correct tags (r'_c and δ'_c) and incorrect tags (r'_i and δ'_i). This implies that, in order to have a completely general parameterization in the data analysis, each tagging category (kaon, lepton, slow pion, etc.) must have different effective r' and δ' parameters, and thus different b and c parameters, due to the dependence on the mistag fraction ω. One particular case that is relevant for a kaon tag category is when $r'_i = 0$. In this case $r' = r'_c(1-\omega)/(1-2\omega)$, which means that the effective r' is enhanced by a factor of $(1-\omega)/(1-2\omega)$.

The experimental knowledge of δ depends on c, so even though the a parameter does not depend on r' and δ', one does not avoid uncertainties due to r' and δ' in the analysis. The best way to reduce this uncertainty is to take advantage of the fact that lepton tags are immune to the problem ($r' = 0$). If the fit is performed with an independent c coefficient for lepton tags, $c_{\rm lep}$, then, when combined with the a parameter measured by all flavor tagging categories, it will help resolve to δ and thus $(2\beta+\gamma)$.

If r' and δ' are not constrained from other measurements, one must allow for values of r' and δ' that are consistent with the measured values of b and c. Since it is possible to have a measured set of a, b, and c parameters that are consistent with $r' = 0$ when $r' \neq 0$, one must always consider all r' values between 0 and $r'_{\rm max}$ consistent with b and c, where $r'_{\rm max}$ is the largest allowed single-final-state value. This point is illustrated in Fig. 5.2. The uncertainty on $(2\beta+\gamma)$ due to r' and δ' is maximal when a is small. In this case, the sensitivity to $(2\beta+\gamma)$ is mostly from the c coefficient and one must rely on flavor tag categories that are known to have $r' = 0$, such as lepton tags.

Using Monte Carlo pseudo-experiments, we perform a simplified study of the impact of DCS tag-side interference on a system with only two tagging categories: one for unaffected lepton tags, and the other containing kaon tags. The significance ratio of both categories is set to $Q_{\rm lep}/Q_{\rm non-lep} = 0.6$. All tests use the realistic value of 0.02 for r and r'. Each category shares the same a parameter. The lepton category constrains $c_{\rm lep}$, and the kaon category fits b and c. All fit parameters are unbiased, and consistent with Gaussian distributions. Compared

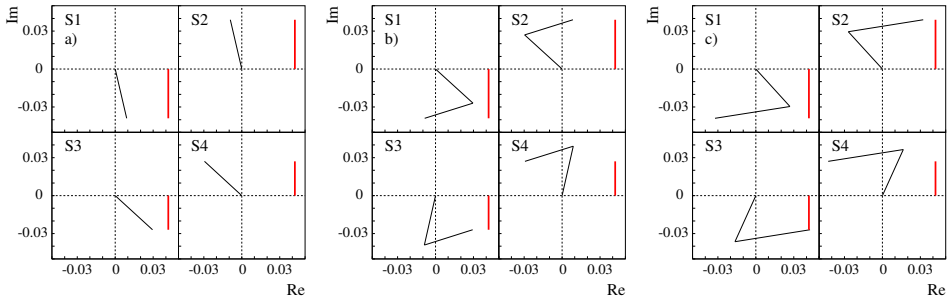

Figure 5.2: *An example of three amplitude configurations that all give the same set of S coefficients (see Table 5.2). For each set (a, b, or c) the S coefficients are consistent with no tag-side interference ($r' = 0$), while this is only true in the first case. Each configuration is represented by four diagrams showing the addition of the reconstructed and tag-side amplitude vectors in the complex plane. The observable coefficient (S) is the imaginary part, represented by the vertical band on the right side of each diagram. The parameters for the three configurations are:* $r = 0.02$*;* $(2\beta+\gamma) = 2.10,\ 1.87,\ 1.73$*;* $r' = 0.00,\ 0.02,\ 0.03$*;* $\delta = 0.30,\ -0.53,\ -0.58$*; and* $\delta' = \mathrm{NA},\ 1.57,\ 1.57$.

to the situation with no DCS contribution, having one tagging category and identical errors for its two parameters a and c, the statistical error on a is unchanged, and that on $c_{\rm lep}$ has increased by a ratio compatible with $((Q_{\rm non-lep} + Q_{\rm lep})/Q_{\rm lep})^{1/2} = 1.6$. The parameters a and b show a 20% correlation, while all other correlations are smaller than 1%.

One experimental strategy for reducing the uncertainties due to r' and δ' would be to constrain them by performing a time-dependent analysis of a flavor-specific final state that has no DCS contribution ($r = 0$), such as $D^{*+}l^-\overline{\nu}$. For such a final state, the undiluted b coefficient is the same as for $D^{*+}\pi^-$ and c now has $r = 0$. This information can be used to recover the $(2\beta + \gamma)$ sensitivity in the c coefficients in the signal sample that was lost due to the lack of knowledge of r' and δ'.

The measured a, b, and c coefficients for the various tagging categories and samples can be combined by forming a χ^2 using the measured parameters and the corresponding, inverted covariance matrix. This assumes that the measurement uncertainties on the a, b, and c parameters are Gaussian. A constraint on $(2\beta + \gamma)$ can be derived from the χ^2 by scanning the χ^2 vs $(2\beta + \gamma)$ where for each $(2\beta + \gamma)$ value the χ^2 is minimized with respect to the unknown parameters δ, δ', and r'. If there are no external constraints on r' and δ', such as from the analysis of $D^{*+}l^-\overline{\nu}$ suggested above, the b and c parameters from non-lepton tags do not provide much information, since r' must be varied from its minimum value compatible with b to its maximum possible value (for example, see Fig. 5.2). The non-lepton-tag b and c parameters still must be included in the time-dependent fit, but they are not very useful in the χ^2 analysis to extract $(2\beta + \gamma)$.

An example of the χ^2 procedure for a hypothetical measurement where $(2\beta + \gamma) = 1.86$, $r = 0.02$, and $\delta = 0.9$ is shown in Fig. 5.3. The measured values of the a, b, and c coefficients were set to the correct values, so the χ^2 is zero at the correct and degenerate solutions. The

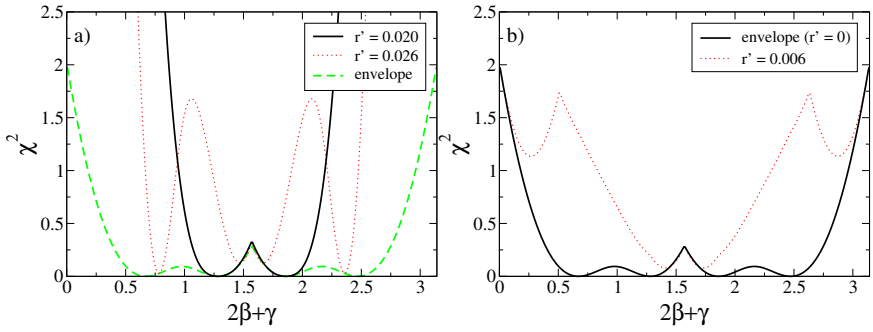

Figure 5.3: *Scans of χ^2 from measured a, b, and c coefficients as a function of $(2\beta+\gamma)$ illustrating two cases: a) one with non-zero tag-side DCS interference, and b) one without tag-side interference. The solid curve in both a) and b) was made with the true value of r'. The dashed curve labeled 'envelope' in figure a) encloses from below all χ^2 curves made with r' ranging from zero to arbitrarily large values. The envelope curve in b) coincides with the χ^2 curve made with the true r' value of zero. The dotted curves in both a) and b) illustrate χ^2 curves with incorrect values of r'. The input values were $(2\beta+\gamma) = 1.86$, $r = 0.02$, and $\delta = 0.9$. The tag-side parameters for a) were $r' = 0.02$ and $\delta' = 0.3$. The measured values of the a, b, and c coefficients were set to the correct values. The statistics of the hypothetical measurement correspond to roughly 450 fb^{-1} of B factory data from one experiment, including a constraint from $D^* l\nu$. There is a discreet ambiguity that gives exactly the same curves after adding π to the horizontal axis $(2\beta+\gamma)$.*

two plots in Fig. 5.3 illustrate two cases: a) one with non-zero tag-side DCS interference, and b) one without tag-side interference. In addition to the curve which allows for any value of r', labeled 'envelope', additional curves with fixed values of r' are included. The statistical errors correspond to a measurement from $D^*\pi$ in roughly 450 fb^{-1} of B-factory data from one experiment including a constraint from $D^* l\nu$.

Three important conclusions can be drawn from Fig. 5.3. First, comparing envelope curves for the $r' = 0.02$ case a) to the $r' = 0$ case b), the measurements give nearly identical constraints on $(2\beta+\gamma)$. This means that the uncertainty on r' and δ' does not affect the measurement. The only degradation with respect to the situation with no tag-side interference is that, when not including $D^{*+} l^- \overline{\nu}$ in the analysis, the non-lepton-tag c parapeters no longer contain useful information.

The second conclusion is that if r' is non-zero, the constraint on $(2\beta+\gamma)$ can be better than the case where r' is zero. If so, the b and c parameters in the $D^* l\nu$ sample will in general be non-zero, and one effectively adds a measurement of $(2\beta+\gamma)$ from the tag-side B. This can be seen most clearly from the symmetry between the tag-side and reconstruction-side within the definitions of a, b, and c in Eqs. (5.20–5.22). An extreme, unrealistic example is given by the solid curve in case a) of Fig. 5.3. It shows what the constraint looks like if r' would equal 0.02, and if that information were known precisely and were included in the analysis.

Thirdly, the result for $D^*\pi$ alone, after varying r' to arbitrarily large values, is equivalent to the χ^2 curve constructed from only a and $c_{\rm lep}$. In other words, when not including the $D^*l\nu$ sample in the analysis, the b and non-lepton-tag c parameters do not contribute to the sensitivity to $(2\beta+\gamma)$. Again, however, these degrees of freedom must still be included in the time-dependent analysis of the data.

5.9 Conclusions

Interference effects between CKM-favored $b \to c\overline{u}d$ and doubly-CKM-suppressed $\overline{b} \to \overline{u}c\overline{d}$ amplitudes in final states used for flavor tagging in coherent $B^0\overline{B}^0$ pairs from $\Upsilon(4S)$ decays introduce deviations from the standard time evolution assumed in *CP* violation measurements at the asymmetric-energy B factories.

In measurements of $\sin(2\beta+\gamma)$ which explicitly use interference between CKM-favored and doubly-CKM-suppressed amplitude contributions in the final state that is reconstructed, such as $B \to D^{(*)\mp}h^{\pm}$ decays ($h = \pi, \rho$), tag-side interference effects can be as large as the interference effects of interest one is trying to measure. In any such analysis, the data must be analyzed in a way that is general enough to allow for tag-side interference effects. We have shown a general framework for dealing with tag-side interference effects in $\sin(2\beta+\gamma)$ measurements. It is possible to achieve an experimental sensitivity to $(2\beta+\gamma)$ similar to the originally proposed measurements, which ignored this effect.

Chapter 6

Ingredients of Δt likelihood fit

The *CP* violation related parameters containing γ are determined with an unbinned maximum likelihood fit to the Δt distributions of the flavor tagged $B \to D^{(*)\mp}\pi^{\pm}$, $D^{\mp}\rho^{\pm}$ samples. This Chapter describes the Δt likelihood functions for the events in the full data sample.

The likelihood function is summarized in Section 6.1. In Section 6.2 the parametrization for signal events is obtained from the theoretical distributions by incorporating the mistag fractions and the Δt resolution function. Functions for the background components follow in Section 6.3. The free fit parameters are summarized in Section 6.5.

The likelihood sum and functions described below are implemented in the maximum likelihood fitting package `RooFit` [75].

6.1 Likelihood function

The to-be-maximized likelihood sum over the events in our data sample is given by

$$\begin{aligned} \ln\mathcal{L} &= \sum_{i,j,k}\Bigg[\ln\Big\{\mathcal{H}^{+}_{i,j,k}(\eta{=}+,\Delta t)\Big\}+\ln\Big\{\mathcal{H}^{-}_{i,j,k}(\eta{=}+,\Delta t)\Big\}+ \\ &\quad \ln\Big\{\mathcal{H}^{+}_{i,j,k}(\eta{=}-,\Delta t)\Big\}+\ln\Big\{\mathcal{H}^{-}_{i,j,k}(\eta{=}-,\Delta t)\Big\}\Bigg], \end{aligned} \tag{6.1}$$

where, in the likelihood function $\mathcal{H}^{\pm}_{i,j,k}$, the upper + (−) sign refers to the flavor of $B_{\rm tag}$ as a B^0 ($\overline{B}^0$), i refers to the tagging category, j refers to the reconstructed B mode, and k refers to the reconstructed D mode. There are 3 reconstructed modes ($D\pi, D^*\pi, D\rho$) and 6 tagging categories. We have $\eta = +1$ (-1) for the final state $D^{(*)-}h^{+}$ ($D^{(*)+}h^{-}$).

The probability density function $\mathcal{H}^{\pm}_{i,j,k}(\eta,\Delta t)$ is made up of three contributions

$$\mathcal{H}^{\pm}_{i,j,k}(\eta,\Delta t) = f^{\rm sig}_{i,j,k}\mathcal{F}^{\pm}_{i,j}(\eta,\Delta t)+f^{\rm peak}_{i,j,k}\mathcal{P}^{\pm}_{i,j}(\eta,\Delta t)+f^{\rm comb}_{i,j,k}\mathcal{B}^{\pm}_{i,j}(\eta,\Delta t)\,, \tag{6.2}$$

where $\mathcal{F}(\eta,\Delta t)^{\pm}_{i,j}$ is the likelihood function for the signal component, and $\mathcal{P}(\eta,\Delta t)^{\pm}_{i,j}$ and $\mathcal{B}(\eta,\Delta t)^{\pm}_{i,j}$ are the likelihood functions for the peaking and combinatorial background components, respectively.

Each event is assigned a probability to be signal or background, $f_{i,j,k}$, on the basis of its energy-constrained mass m_{ES} and the fit to the m_{ES} distributions in data, as described in Sections 4.1.3 and 4.4. The m_{ES} distribution is modeled with a Gaussian distribution $\mathcal{G}(m_{ES})$

for signal events, an ARGUS parameterization $\mathcal{A}(m_{ES})$ for combinatorial background, and a Cruijff function $\mathcal{C}(m_{ES})$ for peaking background. The probabilities are defined as

$$\begin{aligned} f^{\rm sig}_{i,j,k}(m_{ES}) &= \frac{\mathcal{G}_{i,j,k}(m_{ES})}{\mathcal{G}_{i,j,k}(m_{ES})+\mathcal{A}_{i,j,k}(m_{ES})+\mathcal{C}_{i,j,k}(m_{ES})}\,, \\ f^{\rm peak}_{i,j,k}(m_{ES}) &= \frac{\mathcal{C}_{i,j,k}(m_{ES})}{\mathcal{G}_{i,j,k}(m_{ES})+\mathcal{A}_{i,j,k}(m_{ES})+\mathcal{C}_{i,j,k}(m_{ES})}\,, \\ f^{\rm comb}_{i,j,k}(m_{ES}) &= \frac{\mathcal{A}_{i,j,k}(m_{ES})}{\mathcal{G}_{i,j,k}(m_{ES})+\mathcal{A}_{i,j,k}(m_{ES})+\mathcal{C}_{i,j,k}(m_{ES})}\,. \end{aligned} \tag{6.3}$$

and are assigned per tagging category and $B\otimes D$ mode.

The three fractions satisfy $f^{\rm sig}_{i,j,k}+f^{\rm peak}_{i,j,k}+f^{\rm comb}_{i,j,k}=1$.

6.2 Signal Δt description

The Δt distributions for signal events are summarized in Section 6.2.1. These do not account for the mistag probability introduced in Section 4.2, w, and the effect of the finite Δt resolution of Section 4.3.3. The modifications to the Δt distribution from these effects are described in Sections 6.2.2 and 6.2.3.

6.2.1 The a, b, c parametrization

The Δt distributions for $B\to D^{(*)\mp}h^{\pm}$ events with no mistagging and perfect Δt resolution have been introduced in Eqs. (2.57–2.57) and 5.16–5.19. They can be summarized as

$$\begin{aligned} F^{\pm}_{i,j}(\eta,\Delta t) &= \frac{e^{-|\Delta t|/\tau}}{4\tau}\times[1\mp(a^j\mp\eta b_i-\eta c^j_i) \\ &\quad \sin(\Delta m_d\Delta t)\mp\eta\cos(\Delta m_d\Delta t)]\,, \end{aligned} \tag{6.4}$$

where, again, the upper (lower) sign refers to the flavor of $B_{\rm tag}$ as a B^0 ($\overline{B}^0$), i refers to the tagging category, j to the reconstructed B mode, and $\eta=+1$ (-1) for the final state $D^{(*)-}h^+$ ($D^{(*)+}h^-$).

The parameters a^j, b_i, and c^j_i are left free in the fit to the data (except for $b_{\rm lep}=0$, see below). From Eqs. (5.20–5.22) in Chapter 5 the *CP* violation related parameters are

$$\begin{aligned} a^j &= 2r^j\sin(2\beta+\gamma)\cos\delta^j\,, \\ b_i &= 2r'_i\sin(2\beta+\gamma)\cos\delta'_i\,, \\ c^j_i &= 2\cos(2\beta+\gamma)(r^j\sin\delta^j-r'_i\sin\delta'_i)\,. \end{aligned} \tag{6.5}$$

The primed parameters relate to tagside interference, which is absent in semi-leptonic decays – hence $r'_{\rm lep}=0$. The parameters a^j, common to all the tagging categories, and $c^j_{\rm lep}$ do not depend on the tagside *CP* parameters and as a result are sensitive to $(2\beta+\gamma)$.

The a, b, c parametrization is completely general since it accounts for different r'_i and δ'_i in different tagging categories. The parametrization neglects the terms $\mathcal{O}([r^j]^2)$, $\mathcal{O}(r'^2_i)$, and $\mathcal{O}(r^j r'_i)$. This assumption is safe given the expected values of the parameters involved: r^j is at the level of of 0.02, and $r'_i\lesssim r^j$. Consequently, in Eq. (6.4) the amplitude of the cosine mixing terms is one, which we employ in the following Section.

To remove any a-priori assumption on *CP* violation on the reconstruction side, three sets of a and c parameters are used for the final states $D\pi$, $D^*\pi$, $D\rho$. In total, we have 26 a, b, c parameters

1. $a^{D\pi}$, $a^{D^*\pi}$, $a^{D\rho}$;
2. $c_{\rm lep}^{D\pi}$, $c_{\rm lep}^{D^*\pi}$, $c_{\rm lep}^{D\rho}$;
3. $b_{\rm ki}$, $b_{\rm kii}$, $b_{\rm kpi}$, $b_{\rm pi}$, $b_{\rm oth}$;
4. $c_{\rm ki}^{D\pi}$, $c_{\rm kii}^{D\pi}$, $c_{\rm kpi}^{D\pi}$, $c_{\rm pi}^{D\pi}$, $c_{\rm oth}^{D\pi}$;
5. $c_{\rm ki}^{D^*\pi}$, $c_{\rm kii}^{D^*\pi}$, $c_{\rm kpi}^{D^*\pi}$, $c_{\rm pi}^{D^*\pi}$, $c_{\rm oth}^{D^*\pi}$; and
6. $c_{\rm ki}^{D\rho}$, $c_{\rm kii}^{D\rho}$, $c_{\rm kpi}^{D\rho}$, $c_{\rm pi}^{D\rho}$, $c_{\rm oth}^{D\rho}$.

After fitting for these parameters, a second analysis step is necessary to obtain γ. This process is described in Chapter 11.

6.2.2 Mistag probability

The mistag probability for each tagging category, w_i, is approximately the same for B^0 and $\overline{B}^0$ tagged events, but not exactly equal. For example, the detector response to positive kaons differs from that to negative kaons due to differences in the total and charge-exchange cross sections. As a result, two mistag probabilities are defined for each tagging category

1. w_i : fraction of true B^0 mesons, tagged as a $\overline{B}^0$,
2. $\bar{w}_i$: fraction of true $\overline{B}^0$ mesons, tagged as a B^0.

The Δt distributions change due to mistagging

$$\begin{aligned} F_{i,j}'^{+}(\eta,\Delta t) &= (1-w)\ F_{i,j}^{+}(\eta,\Delta t) + \bar{w}\ F_{i,j}^{-}(\eta,\Delta t)\,, \\ F_{i,j}'^{-}(\eta,\Delta t) &= w\ F_{i,j}^{+}(\eta,\Delta t) + (1-\bar{w})\ F_{i,j}^{-}(\eta,\Delta t)\,, \end{aligned} \tag{6.6}$$

where $F_{i,j}'^{+}(\eta,\Delta t)$ ($F_{i,j}'^{-}(\eta,\Delta t)$) is the distribution of B^0 ($\overline{B}^0$) tagged events, using realistic flavor tagging. More compactly, in presence of non-zero mistag probabilities the Δt distributions are written in terms of dilution factors D_i, related to the mistag probabilities as $D_i = 1 - 2w_i$. After some algebra Eq. (6.4) can be expressed as

$$\begin{aligned} F_{i,j}'^{\pm}(\eta,\Delta t) &= \frac{e^{-|\Delta t|/\tau}}{4\tau} \times [(1 \pm \frac{\Delta D_i}{2}) \mp (\langle D\rangle_i \times a^j \mp \eta b_i - \langle D\rangle_i \times \eta c_i^j) \\ &\quad \sin(\Delta m_d \Delta t) \mp \eta \langle D\rangle_i \cos(\Delta m_d \Delta t)]\,, \end{aligned} \tag{6.7}$$

with the dilution differences $\Delta D_i = D_i - \bar{D}_i$ and the average dilutions $\langle D\rangle_i = \frac{1}{2}(D_i + \bar{D}_i)$. It can be observed from Eq. (6.7) that the average dilutions can be extracted from coefficients of the cosine mixing terms of the $D\pi$, $D^*\pi$, and $D\rho$ samples, and the dilution differences from the unit terms.

Compared with Eq. (6.4) the *CP* asymmetries of interest get diluted because of mistagging. Assuming one tagging category and $w = \bar{w}$, a *CP* asymmetry $\mathcal{A}$ is reduced by

$$\mathcal{A}_{\rm meas} = (1-2w)\mathcal{A}_{\rm true}. \tag{6.8}$$

The expression clarifies why untagged events ($w = \bar{w} = 0.5$) cannot be used for the measurement of *CP* asymmetries. Note, however, that the b parameters are unaffected by mistagging as they have the same sign for B^0 and $\overline{B}^0$ tagged events.

The correlation between the average dilutions and $\sigma_{\Delta t}$ for hadronic tagging categories, see Eq. (4.19), is modeled as

$$\langle D \rangle_i = \langle D \rangle_{0i} + \langle D \rangle_{Si}\, \sigma_{\Delta t}\,. \tag{6.9}$$

There are 18 additional free parameters in the likelihood fit to account for mistagging in signal events: $\langle D \rangle_0$, ΔD, and the $\langle D \rangle_S$ parameters, split by tagging category. As the process of B tagging is independent of $B_{\rm rec}$, no distinction is made between the mistag probabilities of the three reconstructed B modes. The possible systematic uncertainty from this assumption is expected to be small, and is determined in Section 9.1.5.

6.2.3 The Δt resolution model

The Δt resolution function $R(\delta t; \hat{p})$ has been described in detail in Section 4.3.3, and is a function of the residuals $\delta t = \Delta t_{\rm meas} - \Delta t_{\rm true}$ and the parameter set $\hat{p}$. As a reminder, it is modeled as the sum of three Gaussians

$$\begin{aligned} \mathcal{R}(\delta t; \hat{p}) \;=\; & \sum_{n=1}^{2} \frac{f_n}{S_n \sigma_{\Delta t}\sqrt{2\pi}} \exp\left(-\frac{(\delta t - \delta_n \sigma_{\Delta t})^2}{2 S_n^2 \sigma_{\Delta t}^2} \right) \;+ \\ & \frac{f_{\rm outlier}}{\sigma_{\rm outlier}\sqrt{2\pi}} \exp\left(-\frac{\delta t^2}{2\sigma_{\rm outlier}^2} \right), \end{aligned} \tag{6.10}$$

where the index n runs over the core and tail components, and the parameters f are the fractions of events in each component.

The final expression for the signal Δt distribution is obtained by convolving Eq. (6.7), understood to hold for $\Delta t_{\rm true}$, with $R(\delta t; \hat{p})$. The likelihood functions for signal events, $\mathcal{F}^{\pm}_{i,j}(\eta, \Delta t)$ in Eq 6.2, become

$$\mathcal{F}^{\pm}_{i,j}(\eta, \Delta t) = F'^{\pm}_{i,j}(\eta, \Delta t_{\rm true}) \otimes \mathcal{R}(\delta t; \hat{p})\,. \tag{6.11}$$

The Δt distributions described by Eqs. (6.4) and (6.11), for a realistic choice of mistag fractions and Δt resolution function, are illustrated in Fig. 6.1. The fit to data is most sensitive to the resolution function parameters at $\Delta t_{\rm true} \approx 0$, where the distribution corresponding to Eq. (6.4) shows a clear, sharp peak.

The normalization of these distributions is given by

$$\begin{aligned} \int_{-\infty}^{+\infty} \big(& \mathcal{F}^{+}_{i,j}(\eta{=}+, \Delta t) + \mathcal{F}^{-}_{i,j}(\eta{=}+, \Delta t) + \\ & \mathcal{F}^{+}_{i,j}(\eta{=}-, \Delta t) + \mathcal{F}^{-}_{i,j}(\eta{=}-, \Delta t) \big)\, d\Delta t = 1\,. \end{aligned} \tag{6.12}$$

Eq. (6.12) does not account for the possibility to fit over a finite Δt range. For the measurement described here we only include the Δt range from -20 to $+20$ ps, see Section 4.1.2. However, the likelihood fit implementation in `RooFit` implements this in its normalization.

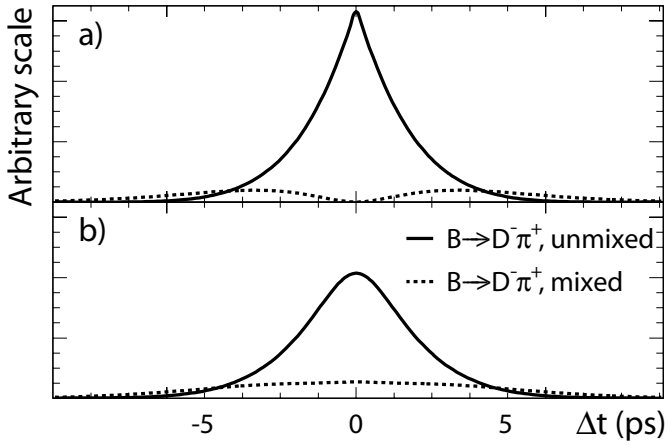

Figure 6.1: *The Δt distribution for mixed and unmixed events a) with perfect tagging and Δt resolution, and b) with typical mistag fractions and Δt resolution. The scale is arbitrary and common to the two plots.*

6.3 Background Δt description

The background composition of the selected $B \to D^{(*)\mp}h^{\pm}$ candidates has been described in Section 4.1.3. In the Δt likelihood fit, we distinguish between combinatorial and peaking background.

Modeling the background time evolution correctly is important in order to avoid biases on the measured *CP* parameters. Rather than a description of each physical decay mode, see Table 4.5, an empirical parametrization has been adopted, which decomposes the Δt distributions into several components.

The combinatorial and peaking background functions, $\mathcal{B}^{\pm}_{i,j}(\eta, \Delta t)$ and $\mathcal{P}^{\pm}_{i,j}(\eta, \Delta t)$ respectively, consist of various components, sub-indexed with l. The background PDFs are normalized similar to signal. For example, for the combinatorial background component

$$\int_{-\infty}^{+\infty} \big(\mathcal{B}^{+}_{i,j,l}(\eta{=}+, \Delta t) + \mathcal{B}^{-}_{i,j,l}(\eta{=}+, \Delta t) + \mathcal{B}^{+}_{i,j,l}(\eta{=}-, \Delta t) + \mathcal{B}^{-}_{i,j,l}(\eta{=}-, \Delta t)\big)\, d\Delta t = 1 \; . \tag{6.13}$$

The same holds for the peaking background normalization.

The following Sections describe the Δt parametrization of each source of background.

6.3.1 Combinatorial background

Combinatorial backgrounds arise from many different sources and the true time-dependence cannot be derived from first principles. We approximate the physical shapes with analytical functions. The goal is to provide an empirical description of the background Δt distribution, and not to perform a measurement of the 'physical' parameters of the background candidates.

This general approach allows for more fit parameters then may be absolutely necessary to describe the background Δt distributions. Since the background levels in the signal region are low, the background and signal fit parameters are largely uncorrelated. This makes the final result relatively insensitive to the quality of the fit to the background candidates or to the details of the parametrization of their Δt dependence.

For the combinatorial background, the Δt distribution is modeled with a sum of three components

$$\begin{aligned}\mathcal{B}^{\pm}_{i,j}(\eta,\Delta t) &= p_{i,j,1}\mathcal{B}^{\pm}_{i,j,1}(\eta,\Delta t;\hat{b}) + \\ &\quad (1-p_{i,j,1})\left((1-p_{i,j,3})\mathcal{B}^{\pm}_{i,j,2}(\eta,\Delta t;\hat{b}) + p_{i,j,3}\mathcal{B}^{\pm}_{i,j,3}(\eta,\Delta t;\hat{b})\right), \end{aligned} \quad (6.14)$$

where $p_{i,j,l}$ is the fraction of the background component l, which can differ per reconstructed B mode and `Lepton` and non-lepton tagging category.

Each component $\mathcal{B}^{\pm}_{i,j,l}(\Delta t;\hat{b})$ uses the Δt resolution function $\mathcal{R}(\delta_t;\hat{b})$, with a common set of background parameters $\hat{b}$. The resolution function is the same for each type of combinatorial background, and consists of a core and outlier Gaussian that take into account a small fraction of 'badly reconstructed' background events. The width and bias of the outlier component are the same as for signal events, *i.e.* 8 ps and 0 ps, respectively. The other resolution parameters are left free in the fit.

The three background components are listed below.

1. **Zero lifetime component**
   This term accounts for combinatorial background from continuum $q\bar{q}$ events, as the tracks used to create the B candidate tend to be selected from two hadronic jets, which is not expected to have a significant lifetime component, even for $c\bar{c}$ events. We have

   $$\mathcal{B}^{\pm}_{i,j,1}(\eta,\Delta t;\hat{b}) = \frac{1}{2}\big(1\mp\eta D'_{i,j,1}\big)\delta(\delta t_{\rm true})\otimes\mathcal{R}(\delta t;\hat{b}), \quad (6.15)$$

   where $D'_{i,j,1}$ are effective dilution factors, floated in the fit to the data.

2. **Non-zero lifetime component (non-mixing)**
   An effective lifetime is expected from combinatorial background from $B\bar{B}$ events, when tracks from two different B mesons are selected. We have

   $$\mathcal{B}^{\pm}_{i,j,2}(\eta,\Delta t;\hat{b}) = \frac{1}{4}\Gamma_2\big(1\mp\eta D'_{i,j,2}\big)e^{-\Gamma_2|\delta t_{\rm true}|}\otimes\mathcal{R}(\delta t;\hat{b}), \quad (6.16)$$

   where Γ_2 and $D'_{i,j,2}$ are effective dilutions, floated in the fit to the data.

3. **Non-zero lifetime component (mixing)**
   A systematic error is assigned in Section 9.2.5 for the possible presence of mixing background or a *CP* asymmetric background. The events are modeled with a modified copy of the signal event function of Eq. (6.11)

   $$\begin{aligned}\mathcal{B}^{\pm}_{i,j,3}(\eta,\Delta t;\hat{b}) &= \frac{1}{4}\Gamma_3\big(1\mp\eta D'_{i,j,2}\big)e^{-\Gamma_3|\delta t_{\rm true}|}\big(1\mp\eta D'_{i,j,3}\cos\Delta m_d\Delta t_{\rm true} \\ &\quad \mp(D'_{i,j,3}\times a\mp\eta b - D'_{i,j,3}\times\eta c)\sin(\Delta m_d\Delta t_{\rm true})\big)\otimes\mathcal{R}(\delta t;\hat{b}), \end{aligned} \quad (6.17)$$

   where $D'_{i,j,3}$ are effective dilutions, and the a, b, c parameters are varied over reasonable ranges.

The background parameters are mostly extracted from the m_{ES} sideband region.

The background lifetimes $\tau_l = 1/\Gamma_l$ are not expected to be the exact lifetimes of decaying particles such as B or D mesons. Due to mis-reconstruction, the background lifetimes can be smaller or larger. Based on the same argument, we do not expect the mixing frequency of the background to equal Δm_d. And likewise, the 'dilutions' $D'_{i,j,l}$ should not be interpreted as dilutions due to mistag rates. They contain the effects due to production asymmetry and flavor mis-assignment: in this sense dilutions are also meaningful for non-signal events.

In the nominal likelihood fit, the fraction of mixing combinatorial background, $p_{i,j,3}$, is fixed to zero. We fit for the fraction of background with zero lifetime, split by B mode and `Lepton` and non-lepton tagging categories. The generic lifetime of the B background, Γ_2, is also fit for. Separate background dilutions are floated for the zero-lifetime background, non-mixing background with lifetime, and per B mode and tagging category.

The systematic uncertainty from the parametrization of the combinatorial background is described in Section 9.2.

6.3.2 Peaking background

The composition of the peaking background of the $B \to D^{(*)\mp}h^{\pm}$ data sample has been analyzed in Section 4.1.4. For the Δt description we distinguish between contributions from B^0 and B^+ decays. Their relative fractions have been summarized in Table 4.4 and are fixed in the fit to data. The corresponding systematic uncertainty on the a and $c_{\rm lep}$ parameters is evaluated in Sections 9.2.4.

Mis-reconstructed B^0 decays have a Δt distribution similar to signal events. Therefore, the events are modeled with (a copy of) Eq. (6.11). In the likelihood fit, the same Δt resolution function are dilution parameters are used as for the signal events. The peaking background related a, b, c parameters are likely to be tiny and have been fixed to zero. In Section 9.2.6, their values are varied over reasonable ranges.

The time-dependence of the background from B^+ decays can be described by

$$\mathcal{P}^{\pm}_{i,j,1}(\eta, \Delta t; \hat{p}) = \frac{1}{4}\Gamma_{B^+} e^{-\Gamma_{B^+}|\Delta t_{\rm true}|}\left(1 \mp \eta D_i^+\right) \otimes \mathcal{R}(\delta t; \hat{p})\,, \tag{6.18}$$

where $\Gamma_+ = 1/\tau_{B^+}$ is the B^+ width and the dilutions D_i^+ are different from the dilutions for B^0 decays. We fix the B^+ lifetime to the PDG value [17], and the dilution factors D_i^+ are measured with a large sample of fully reconstructed $B^{\pm}$ mesons [76]. Again, the Δt resolution function is the same as for signal events.

6.4 Reconstruction and tagging efficiencies

The efficiency of tagging a B^0 could potentially be different from the efficiency of tagging a $\overline{B}^0$. Likewise, a potential difference between the reconstruction efficiencies of the final states $D^{(*)-}h^+$ and $D^{(*)+}h^-$ could exist.

In the likelihood fit, we do not account for such potential differences[1]. The impact of relative tagging and reconstruction efficiency differences is tested in Section 9.1.6.

[1] The required modifications to the likelihood functions for $B^0\overline{B}^0$ oscillations are described in Refs. [56, 77].

6.5 Summary of fit parameters

The signal and peaking-background parameters are determined from the Δt distribution of the events in the signal region, while the parameters of the combinatorial background components are dominated by the events in the m_{ES} sideband. There are 99 free parameters in the Δt likelihood fit. These include the a, b, c parameters, Δt resolution function parameters, mistag fractions, and the parameters of the empirical Δt spectrum of the background events. They are summarized in Table 6.1.

Description	Number of parameters
a, b, c Parameters	26
Signal Δt resolution function	9
Signal dilutions	18
Background Δt resolution function	3
Background composition	43
Total	99

Table 6.1: *Summary of the free parameters in the maximum-likelihood fit.*

In the Δt fit 29 additional parameters are fixed (not considering the parameters from the m_{ES} fit, which are also fixed, together making a total of 262 fit parameters). These include the $B^0\overline{B}^0$ oscillation frequency Δm_d, the B^0 lifetime τ_{B^0}, and the peaking background fractions and dilutions.

Chapter 7

Validation studies

Various validation tests have been performed to verify the quality of the fit procedure, the selection criteria and reconstruction chain, and the consistency of the measurement in Chapter 8.

1. The performance of the time-dependent fit algorithm for the $D^{(*)}\pi$ and $D\rho$ samples has been studied with parametrized, fast Monte Carlo experiments ('fast-parameterized Monte Carlo studies') in Section 7.1.

2. The fit model for signal and background and the reconstruction, vertexing, and flavor tagging chain have been evaluated in Sections 7.2 and 7.3 with large samples of fully simulated, Geant 4 Monte Carlo events ('full Monte Carlo studies'), described earlier in Section 3.5.

3. Agreement between the data and full Monte Carlo samples is tested for the Δt resolution function and dilution parameters in Section 7.4.

4. The goodness of fit for data is evaluated in Sections 7.5 and 7.6.

5. Also, the data sample has been split into various subsamples, and the nominal fit has been performed on a control sample of charged B mesons. See Sections 7.8 and 7.9.

For simplicity, the fit to data is referred to as 'the nominal fit'.

7.1 Parameterized Monte Carlo studies

To validate the fit procedure and determine possible biases in the *CP* parameters introduced by the fit algorithm, a study has been performed with samples of fast parameterized simulated events. For the $D\pi$, $D^*\pi$, and $D\rho$ modes, $1,296$ samples have been generated with the same number of signal and background events as in data, summarized in Tables 4.6–4.8. Each generated D decay mode has the m_{ES} signal and background shapes values found in data. Also, Δt resolution function parameters, dilutions, and background parameters of the fast Monte Carlo samples have been copied from the nominal fit results, see Tables 8.2–8.4. The study uses identical $\sigma_{\Delta t}$ distributions to the ones in data, split by signal, background, and tagging categories. The nominal data fit is performed on each generated Monte Carlo sample.

As described in Section 6.2.1, the following *CP* parameters are floated in the nominal fit:

Parameter	Mean	Pull	Width
	Pseudo configuration 1		
$a^{D\pi}$	0.0410 ± 0.0007	0.04 ± 0.03	1.06 ± 0.02
$a^{D^*\pi}$	0.0400 ± 0.0007	0.00 ± 0.03	1.06 ± 0.02
$a^{D\rho}$	0.0392 ± 0.0009	-0.03 ± 0.03	1.02 ± 0.02
$c_{\rm lep}^{D\pi}$	0.0007 ± 0.0011	0.02 ± 0.03	1.01 ± 0.02
$c_{\rm lep}^{D^*\pi}$	-0.0003 ± 0.0012	-0.01 ± 0.03	1.04 ± 0.02
$c_{\rm lep}^{D\rho}$	0.0007 ± 0.0016	0.01 ± 0.03	1.01 ± 0.02
	Pseudo configuration 2		
$a^{D\pi}$	-0.0003 ± 0.0008	-0.01 ± 0.03	0.98 ± 0.02
$a^{D^*\pi}$	-0.0006 ± 0.0008	-0.02 ± 0.04	1.04 ± 0.03
$a^{D\rho}$	-0.0010 ± 0.0011	-0.03 ± 0.03	1.01 ± 0.03
$c_{\rm lep}^{D\pi}$	0.0423 ± 0.0014	0.06 ± 0.04	1.04 ± 0.02
$c_{\rm lep}^{D^*\pi}$	0.0399 ± 0.0015	0.00 ± 0.04	1.04 ± 0.03
$c_{\rm lep}^{D\rho}$	0.0419 ± 0.0020	0.03 ± 0.04	1.04 ± 0.03

Table 7.1: *Fit values and pull distributions for the a and $c_{\rm lep}$ parameters in the modes $B \to D^{\mp}\pi^{\pm}$, $B \to D^{(*)\mp}\pi^{\pm}$, and $B \to D^{\mp}\rho^{\pm}$ from two fast Monte Carlo studies described in the text.*

1. Three a^j signal parameters, one for each B decay mode $j = D\pi$, $D^*\pi$, $D\rho$.

2. Three $c_{\rm lep}^j$ signal parameters, for the lepton tagging category of each final state.

3. Five b_i parameters account for tag-side interference, common amongst the tagging categories i of $D^{(*)}\pi$ and $D\rho$. For the lepton tagging category, $b_{\rm lep} \equiv 0$.

4. Fifteen c_i^j parameters, like $c_{\rm lep}^j$, but including tag-side interference, one for each B decay mode and non-lepton tagging category.

Two particular configurations of *CP* parameters are considered to validate the a, b, c parametrization. In the first scenario of pseudo-experiments, for each B mode and tagging category, the a^j parameters equal 0.04, and b_i and c_i^j equal 0. This corresponds to $r^j = 0.02$, $\sin(2\beta+\gamma) = 1$, $\delta^j = 0$, and $r_i' = 0$. In the second scenario, $a^j = 0$, $b_i = 0$, and $c_i^j = 0.04$, corresponding to $r^j = 0.02$, $\cos(2\beta+\gamma) = 1$, $\delta^j = 0$, and $r_i' = 0$.

Once the samples have been fit, the resulting a^j and $c_{\rm lep}^j$ distributions – the parameters most sensitive parameters to $\sin(2\beta+\gamma)$ – are fit with single Gaussians. Table 7.1 lists the distributions of the fit values, the errors, and the pulls for a^j and $c_{\rm lep}^j$ in the two configurations. The mean values of the pull distributions are all consistent with zero, and the widths are consistent with one. The error distributions obtained for the a^j and $c_{\rm lep}^j$ parameters are discussed in Section 7.6.

The fit algorithm gives consistent, unambiguous results. No artificial biases are introduced in the *CP* parameters by the algorithm, and the errors are neither over- nor underestimated.

More fast parameterized Monte Carlo studies are performed in Section 7.3.

7.2 Geant 4 Monte Carlo studies

As a consistency check of the fit models used for signal and background events, discussed in Chapter 6, and the reconstruction, vertexing, and flavor tagging chain, see Chapter 4, fits have been performed to all fully simulated, Geant 4 Monte Carlo events ('the full Monte Carlo sample'), listed in Section 3.5. The studies have been split in two. To start, we only test the signal component of the fit model. Then, in the second part, we add the background component.

First the signal model. The signal Monte Carlo sample amounts to 18.4 times the number of signal events estimated in data. No *CP* asymmetry has been generated, *i.e.* the true values of a, b, c equal zero. After the event selection, 249,059 $D^*\pi$, 297,962 $D\pi$, and 152,979 $D\rho$ fully simulated events remain. Only signal events with $m_{ES} > 5.27$ GeV/c^2 are considered. No background pdf's are included in this Δt fit.

The fit result is projected on Δt in Figs. 7.1–7.3, split by final state and flavor tag. Tables 7.2 and 7.3 list the fit results split by *CP* parameters and other signal parameters. All a, b, c parameters are consistent with zero within 2.3σ. The *CP* parameters most sensitive to $\sin(2\beta+\gamma)$, a and $c_{\rm lep}$, are consistent with zero within their errors, except for $c_{\rm lep}^{D^*\pi}$, which is 1.8σ from zero.

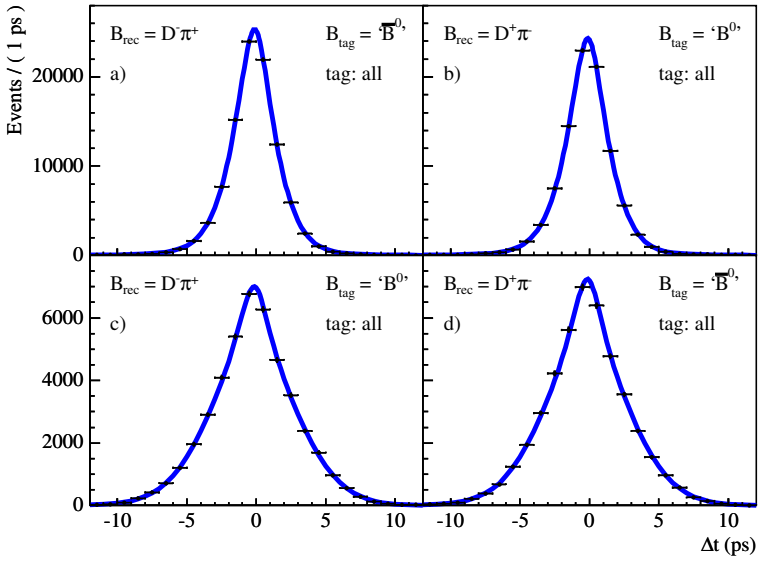

Figure 7.1: *Distributions of Δt for $B \to D^{\mp}\pi^{\pm}$ signal Monte Carlo candidates, split by B tagging flavor and reconstructed final state. The four plots show candidates of all tagging categories; the solid curves are fit projections.*

We split the signal Monte Carlo sample into 18 independent sets, equal in size, and fit each one separately. The average results of these fits are shown in the middle column of Table 7.4. The combined numbers agree with with the fit result of the combined sample.

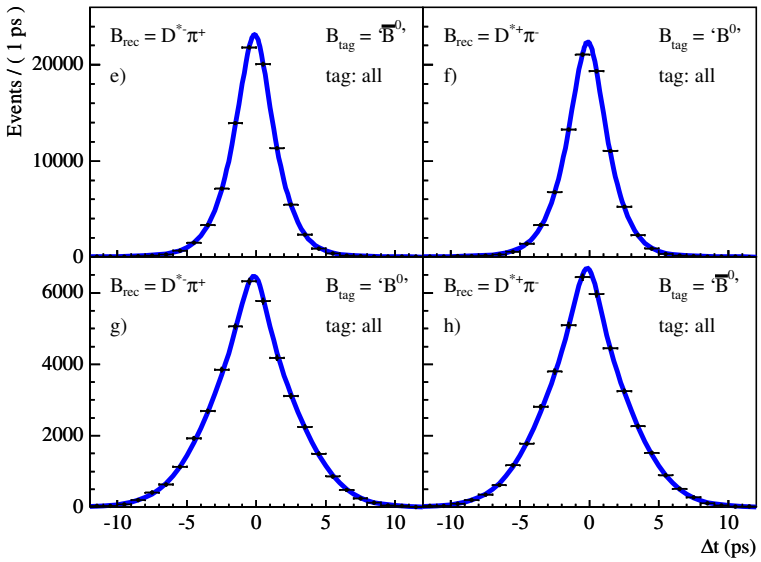

Figure 7.2: *Distributions of Δt for $B \to D^{*\mp}\pi^{\pm}$ signal Monte Carlo candidates, split by B tagging flavor and reconstructed final state. The four plots show candidates of all tagging categories; the solid curves are fit projections.*

In Fig. 7.4 one can find the pull distributions of the 18 fits for, respectively, the *CP* parameters a, b, $c_{\rm lep}$, and the c parameters belonging to non-lepton tagging categories. The a, b parameters are unbiased within 1.3σ, and the $c_{\rm lep}$ pull distribution is unbiased within 1.5σ. A 2.8σ bias is seen in the non-lepton c pull distribution. For completeness, the pull distribution of all a, b, c parameters combined is also given. The mean is consistent with zero within 1.8σ. The widths of all distributions agree with one.

The c parameters for the lepton and non-lepton categories are shown separately for two reasons. First, the lepton category is fit with only fit 2 *CP* parameters per B mode ($b_{\rm lep} \equiv 0$), while the other categories are fit with three (the b parameters float). Second, the lepton tagging category is fit using a separate set of Δt resolution function parameters. As discussed in Section 4.3.1 non-lepton tagging categories show a slight bias in the reconstruction of Δt, coming from short-lived D decays. The c parameters strongly correlate with the bias parameter in the core Gaussian of the Δt resolution function (Eq. (4.18)). This parameter, along with the core and tail Gaussian scale-factor parameters, has thus been split by lepton and non-lepton tagging category.

Next, the background fit model is validated. We reuse the 18 independent signal event sets created earlier.

BABAR has not enough generated Geant 4 uds, $c\bar{c}$, and $B\overline{B}$ background events to create 18 statistically independent, data-like Monte Carlo samples. We retain, respectively, 1.8, 1.7, and 4.5 times the corresponding number of background events observed in data, see Table 3.4. The data-size, fully simulated Monte Carlo samples used below therefore contain statistically

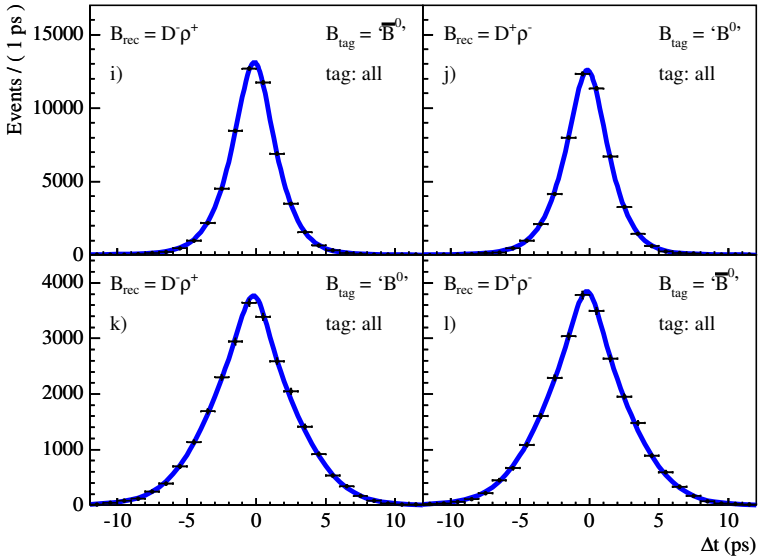

Figure 7.3: *Distributions of Δt for $B \to D^{\mp}\rho^{\pm}$ signal Monte Carlo candidates, split by B tagging flavor and reconstructed final state. The four plots show candidates of all tagging categories; the solid curves are fit projections.*

dependent $c\bar{c}$, uds, and $B\overline{B}$ background samples. The latter have been pulled randomly from the available background sets. Table 7.5 presents the numbers of events employed in each sample. The fit strategy applied to each sample is identical to the one to data.

The right-hand column of Table 9.19 summarizes the results of the a, b, c parameters, averaged over the 18 fits. Because of the common background events, the fit parameters of each sample are correlated. However, given the high purities of the $D\pi$, $D^*\pi$, and $D\rho$ samples, the correlation between the a, b, c and background parameters, and given that the a, b, c parameters are determined from independent signal events, that correlation is small. We ignore it for the errors on the averaged fit parameters.

The *CP* parameter results agree with the other columns in Table 9.19. Most are statistically zero within one sigma, and nearly all within two sigma – consistent with the hypothesis of no bias.

The average minimal log(likelihood) value ('goodness of fit') for the 18 data-size Monte Carlo samples turns out to be $-25,166$, with a spread of about $1,100$. This value is consistent with the minimal log(likelihood) seen in data, being $-25,213$.

In conclusion, the fit models for reconstructed, vertexed, and flavor-tagged signal and background events perform as desired. Within the statistics of the available Geant 4 Monte Carlo sample, no biases are observed in the signal parameters used for the extraction of $\sin(2\beta+\gamma)$, a and $c_{\rm lep}$.

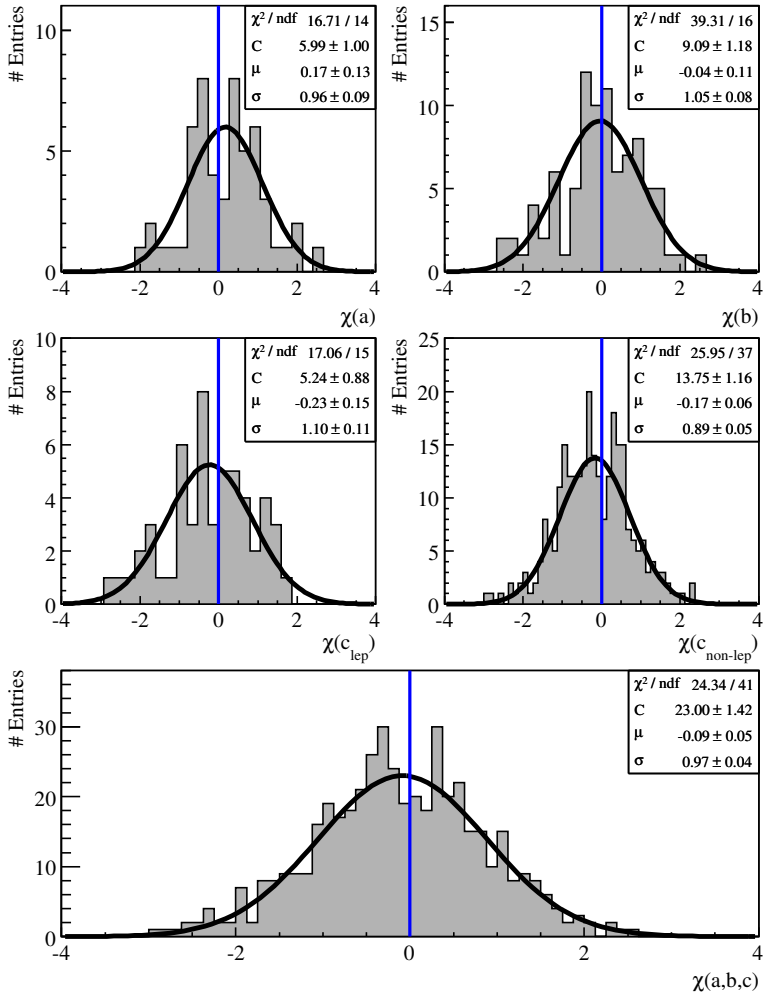

Figure 7.4: *Pull distribution of the combined CP parameters a, b, c_{lep}, and c parameters of non-lepton tagging categories of the* 18 *signal Monte Carlo fits. For the lepton tagging category $b_{\mathrm{lep}} \equiv 0$, while for the non-lepton tagging categories the corresponding b parameters are left to vary in the fit.*

Parameter	Result	Corrl. $a^{D\pi}$	Corrl. $a^{D^*\pi}$	Corrl. $a^{D\rho}$	Corrl. $c_{\rm lep}^{D\pi}$	Corrl. $c_{\rm lep}^{D^*\pi}$	Corrl. $c_{\rm lep}^{D\rho}$
CP Parameters							
$a^{D\pi}$	0.0002 ± 0.0047	1.000	0.033	0.024	0.006	0.000	0.000
$a^{D^*\pi}$	0.0042 ± 0.0049	0.033	1.000	0.023	0.001	−0.001	0.001
$a^{D\rho}$	0.0067 ± 0.0067	0.024	0.023	1.000	0.000	0.000	0.017
$c_{\rm lep}^{D\pi}$	-0.0051 ± 0.0086	0.006	0.001	0.000	1.000	0.086	0.082
$c_{\rm lep}^{D^*\pi}$	-0.0156 ± 0.0089	0.000	−0.001	0.000	0.086	1.000	0.079
$c_{\rm lep}^{D\rho}$	-0.0080 ± 0.0121	0.000	0.001	0.017	0.082	0.079	1.000
Tag-side interference parameters							
$b_{\rm lep}$	0.0 (fixed)	–	–	–	–	–	–
$b_{\rm ki}$	-0.0017 ± 0.0046	0.162	0.152	0.108	0.001	0.000	0.002
$b_{\rm kii}$	0.0001 ± 0.0045	0.092	0.088	0.065	0.001	0.000	0.001
$b_{\rm kpi}$	0.0008 ± 0.0052	0.040	0.037	0.029	0.000	0.000	0.001
$b_{\rm pi}$	0.0006 ± 0.0066	0.016	0.014	0.010	0.000	0.000	0.000
$b_{\rm oth}$	-0.0030 ± 0.0052	0.004	0.004	0.003	0.000	0.000	0.000
$c_{\rm ki}^{D\pi}$	-0.0069 ± 0.0079	0.008	0.000	−0.001	0.001	0.001	0.001
$c_{\rm kii}^{D\pi}$	0.0041 ± 0.0103	0.003	0.000	0.000	0.001	0.001	0.001
$c_{\rm kpi}^{D\pi}$	0.0014 ± 0.0156	−0.002	0.000	0.000	0.000	0.001	0.001
$c_{\rm pi}^{D\pi}$	-0.0045 ± 0.0232	0.005	0.000	0.000	0.000	0.000	0.000
$c_{\rm oth}^{D\pi}$	-0.0370 ± 0.0607	0.001	0.000	0.000	0.000	0.000	0.000
$c_{\rm ki}^{D^*\pi}$	-0.0207 ± 0.0083	−0.001	0.008	−0.001	0.001	0.001	0.001
$c_{\rm kii}^{D^*\pi}$	0.0038 ± 0.0107	0.000	0.001	0.000	0.001	0.001	0.001
$c_{\rm kpi}^{D^*\pi}$	-0.0121 ± 0.0162	0.000	−0.005	0.000	0.000	0.001	0.001
$c_{\rm pi}^{D^*\pi}$	-0.0499 ± 0.0238	0.000	0.003	0.000	0.000	0.000	0.000
$c_{\rm oth}^{D^*\pi}$	-0.1102 ± 0.0627	0.000	0.001	0.000	0.000	0.000	0.000
$c_{\rm ki}^{D\rho}$	-0.0273 ± 0.0116	−0.001	−0.001	0.012	0.000	0.000	0.001
$c_{\rm kii}^{D\rho}$	0.0036 ± 0.0145	0.000	0.000	0.003	0.000	0.000	0.001
$c_{\rm kpi}^{D\rho}$	-0.0491 ± 0.0219	0.000	0.000	−0.001	0.000	0.000	0.000
$c_{\rm pi}^{D\rho}$	0.0001 ± 0.0339	0.000	0.000	0.007	0.000	0.000	0.000
$c_{\rm oth}^{D\rho}$	0.0173 ± 0.0881	0.000	0.000	0.002	0.000	0.000	0.000

Table 7.2: *Results of the simultaneous likelihood fit to the $B \to D^{\mp}\pi^{\pm}$, $B \to D^{(*)\mp}\pi^{\pm}$, and $B \to D^{\mp}\rho^{\pm}$ fully simulated signal Monte Carlo samples (a, b, c parameters).*

7.3 Fast Monte Carlo studies continued

The fit model test in Section 7.2, performed with 18 times the amount of signal in data, gives statistical errors at the level of about 30%, compared to the expected sizes of the *CP* asymmetries. Here, we use the available Geant 4 signal sample as a template for generating fast Monte Carlo signal samples, giving a precise handle on possible biases from using an incorrect fit model.

In Section 7.1, the dilutions and Δt resolution parameters have been generated from the values obtained from the fit to data. In this test, the tagging state, tagging category, and

Parameter	Result	Corrl. $a^{D\pi}$	Corrl. $a^{D^*\pi}$	Corrl. $a^{D\rho}$	Corrl. $c_{\text{lep}}^{D\pi}$	Corrl. $c_{\text{lep}}^{D^*\pi}$	Corrl. $c_{\text{lep}}^{D\rho}$
Signal resolution function parameters							
Scale (c), `Lepton`	1.05 ± 0.02	-0.001	0.004	0.007	0.017	0.012	0.021
Scale (c), `N-Lept.`	1.14 ± 0.01	-0.005	0.002	-0.005	0.001	0.004	0.007
Scale (t), `Lepton`	2.7 ± 0.3	-0.005	0.002	-0.009	-0.025	-0.019	-0.004
Scale (t), `N-Lept.`	3.9 ± 0.2	-0.008	0.001	-0.007	0.002	0.006	0.009
Width (o)	8.0 (fixed)	–	–	–	–	–	–
$\delta(\Delta t)$ (c), `Lepton`	-0.087 ± 0.015	0.004	0.000	0.005	0.238	0.228	0.211
$\delta(\Delta t)$ (c), `N-Lept.`	-0.266 ± 0.007	0.005	-0.002	0.005	-0.006	-0.009	-0.010
$\delta(\Delta t)$ (t)	-1.7 ± 0.1	0.003	-0.001	0.002	0.010	0.008	0.003
$\delta(\Delta t)$ (o)	0.0 (fixed)	–	–	–	–	–	–
f (t)	0.058 ± 0.007	0.007	-0.001	0.006	-0.001	-0.004	-0.008
f (o)	0.0037±0.0003	0.005	-0.001	0.005	0.001	-0.002	-0.005
Signal dilution parameters							
$\langle D_0 \rangle$, `Lepton`	0.956 ± 0.008	0.015	-0.012	0.007	-0.012	0.008	0.019
$\langle D_0 \rangle$, `Kaon I`	0.933 ± 0.008	-0.007	-0.003	-0.002	0.000	0.000	0.000
$\langle D_0 \rangle$, `Kaon II`	0.736 ± 0.007	0.000	0.002	-0.006	0.000	0.000	0.000
$\langle D_0 \rangle$, `K-Pi`	0.538 ± 0.008	-0.003	-0.001	-0.002	0.000	0.000	0.000
$\langle D_0 \rangle$, `Pi`	0.328 ± 0.008	-0.002	-0.003	0.001	0.000	0.000	0.000
$\langle D_0 \rangle$, `Other`	0.171 ± 0.010	0.000	0.002	-0.002	0.000	0.000	0.000
ΔD, `Lepton`	0.002 ± 0.004	0.001	0.005	-0.007	0.014	-0.018	-0.010
ΔD, `Kaon I`	-0.001 ± 0.004	-0.002	0.004	0.010	0.000	0.000	0.000
ΔD, `Kaon II`	0.013 ± 0.004	-0.008	-0.007	0.001	0.000	0.000	0.000
ΔD, `K-Pi`	0.039 ± 0.005	-0.003	-0.002	0.001	0.000	0.000	0.000
ΔD, `Pi`	-0.118 ± 0.005	-0.002	-0.001	0.000	0.000	0.000	0.000
ΔD, `Other`	-0.093 ± 0.007	-0.001	0.000	0.000	0.000	0.000	0.000
D slope, `Lepton`	-0.005 ± 0.015	-0.014	0.009	-0.010	0.008	-0.008	-0.026
D slope, `Kaon I`	-0.101 ± 0.015	0.003	0.003	0.003	0.000	0.000	0.000
D slope, `Kaon II`	-0.085 ± 0.011	-0.001	-0.003	0.004	0.000	0.000	0.000
D slope, `K-Pi`	-0.059 ± 0.011	0.000	0.001	0.002	0.000	0.000	0.000
D slope, `Pi`	-0.024 ± 0.010	0.002	0.002	-0.002	0.000	0.000	0.000
D slope, `Other`	-0.002 ± 0.013	0.000	-0.001	0.002	0.000	0.000	0.000
ΔD slope	0.0 (fixed)	–	–	–	–	–	–
External parameters							
Δm_d (ps^{-1})	0.489 (fixed)	–	–	–	–	–	–
$\tau_{B^0_d}$ (ps)	1.541 (fixed)	–	–	–	–	–	–
$\Delta\Gamma_d$ (ps^{-1})	0.0 (fixed)	–	–	–	–	–	–

Table 7.3: *Results of the simultaneous likelihood fit to the $B \to D^{\mp}\pi^{\pm}$, $B \to D^{(*)\mp}\pi^{\pm}$, and $B \to D^{\mp}\rho^{\pm}$ data samples (signal parameters).*

CP	Combined signal	Split signal	Signal and background	Glob. corr.
$a^{D\pi}$	$+0.0002 \pm 0.0047$	$+0.0001 \pm 0.0049$	$+0.0017 \pm 0.0051$	0.049
$a^{D^*\pi}$	$+0.0042 \pm 0.0049$	$+0.0050 \pm 0.0052$	$+0.0026 \pm 0.0052$	0.045
$a^{D\rho}$	$+0.0067 \pm 0.0067$	$+0.0074 \pm 0.0069$	$+0.0034 \pm 0.0075$	0.038
$c_{\rm lep}^{D\pi}$	-0.0051 ± 0.0086	-0.0048 ± 0.0087	-0.014 ± 0.0088	0.202
$c_{\rm lep}^{D^*\pi}$	-0.0156 ± 0.0089	-0.0173 ± 0.0090	-0.018 ± 0.0093	0.191
$c_{\rm lep}^{D\rho}$	-0.0080 ± 0.0121	-0.0065 ± 0.0122	-0.011 ± 0.0129	0.181
$b_{\rm KI}$	-0.0017 ± 0.0046	-0.0017 ± 0.0050	$+0.0041 \pm 0.0052$	0.049
$b_{\rm KII}$	-0.0001 ± 0.0045	-0.0000 ± 0.0046	$+0.0003 \pm 0.0048$	0.043
$b_{\rm KPi}$	-0.0008 ± 0.0052	-0.0011 ± 0.0054	-0.0066 ± 0.0056	0.015
$b_{\rm Oth}$	$+0.0006 \pm 0.0066$	$+0.0012 \pm 0.0068$	$+0.0020 \pm 0.0072$	0.004
$b_{\rm Pi}$	-0.0030 ± 0.0052	-0.0027 ± 0.0054	-0.0039 ± 0.0057	0.020
$c_{\rm KI}^{D\pi}$	-0.0069 ± 0.0079	-0.0075 ± 0.0084	-0.008 ± 0.009	0.092
$c_{\rm KII}^{D\pi}$	$+0.0041 \pm 0.0103$	$+0.0029 \pm 0.0102$	-0.011 ± 0.011	0.087
$c_{\rm KPi}^{D\pi}$	$+0.0014 \pm 0.0156$	$+0.0014 \pm 0.0166$	-0.023 ± 0.018	0.065
$c_{\rm Pi}^{D\pi}$	-0.0045 ± 0.0232	-0.0057 ± 0.0267	-0.014 ± 0.029	0.134
$c_{\rm Oth}^{D\pi}$	-0.0370 ± 0.0607	-0.0337 ± 0.0619	$+0.056 \pm 0.066$	0.022
$c_{\rm KI}^{D^*\pi}$	-0.0207 ± 0.0083	-0.0217 ± 0.0089	-0.018 ± 0.009	0.099
$c_{\rm KII}^{D^*\pi}$	$+0.0038 \pm 0.0107$	$+0.0022 \pm 0.0106$	-0.007 ± 0.011	0.087
$c_{\rm KPi}^{D^*\pi}$	-0.0121 ± 0.0162	-0.0134 ± 0.0173	-0.012 ± 0.018	0.061
$c_{\rm Pi}^{D^*\pi}$	-0.0499 ± 0.0238	-0.0505 ± 0.0278	-0.060 ± 0.029	0.095
$c_{\rm Oth}^{D^*\pi}$	-0.1102 ± 0.0627	-0.1214 ± 0.0644	-0.121 ± 0.066	0.026
$c_{\rm KI}^{D\rho}$	-0.0273 ± 0.0116	-0.0289 ± 0.0125	-0.015 ± 0.013	0.096
$c_{\rm KII}^{D\rho}$	$+0.0036 \pm 0.0145$	$+0.0021 \pm 0.0146$	$+0.003 \pm 0.016$	0.074
$c_{\rm KPi}^{D\rho}$	-0.0491 ± 0.0219	-0.0529 ± 0.0235	-0.053 ± 0.026	0.062
$c_{\rm Pi}^{D\rho}$	$+0.0001 \pm 0.0339$	-0.0005 ± 0.0383	$+0.008 \pm 0.042$	0.158
$c_{\rm Oth}^{D\rho}$	$+0.0173 \pm 0.0881$	-0.0040 ± 0.0872	-0.047 ± 0.094	0.023

Table 7.4: *Results for the CP parameters from the fit to the Δt distribution on a signal Monte Carlo sample (*18.4 *times the data).* `Dst` $= B \to D^{\mp}\pi^{\pm}$, `D` $= B \to D^{(*)\mp}\pi^{\pm}$, *and* `R` $= B \to D^{\mp}\rho^{\pm}$. *The left column shows the results of the single fit to the entire dataset. The right column shows the fit to the same sample split into 18 different pieces.*

Sample	Events reconstructed	Expected in data	Ratio
Data	67,544	–	–
Signal MC	674.0k	36,828	18.3
$B\overline{B}$ bkg MC	26.7k	5,946	4.5
$c\overline{c}$ MC	24.9k	14,431	1.7
uds MC	18.9k	10,339	1.8

Table 7.5: *Numbers of fully simulated Monte Carlo events used in each test sample.*

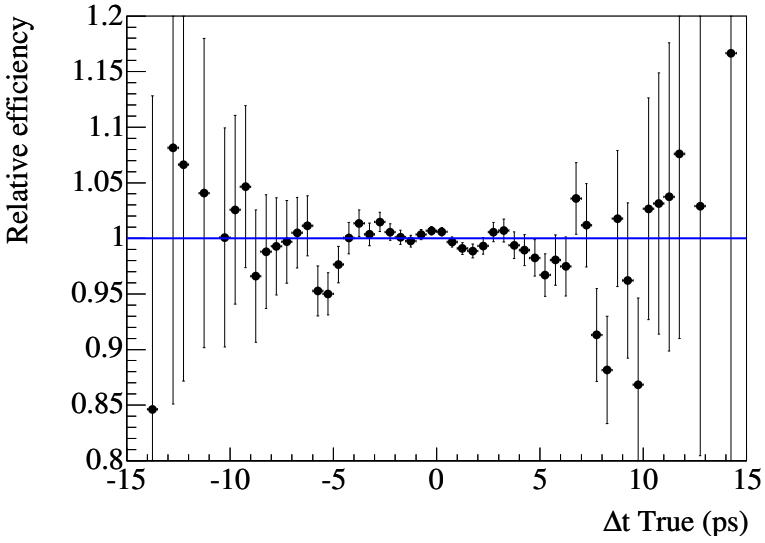

Figure 7.5: *Efficiency correction applied to the $\Delta t_{\rm true}$ spectrum as obtained from the full-simulated Monte Carlo sample, after selection and reconstruction.*

mixing state are taken at random from the template full Monte Carlo set.

The reconstructed decay-time difference, $\Delta t_{\rm meas}$, is obtained from the true time, $\Delta t_{\rm true}$, as follows. Define the difference in Δt as $\delta\Delta t = \Delta t_{\rm meas} - \Delta t_{\rm true}$. A generated event in a fast Monte Carlo sample, with a certain value of $\Delta t_{\rm true}$, is linked with the event in the full Monte Carlo set – with the decay-time difference $\delta\Delta t_{\rm full}$ (see Fig. 7.15) and the error $\sigma_{(\Delta t;\,\rm full)}$ – that has the closest value of $\Delta t_{\rm true}$ in the same tagging category. For that event we set $\Delta t_{\rm meas} = \Delta t_{\rm true} + \delta\Delta t_{\rm full}$, and assign as error $\sigma_{(\Delta t;\,\rm full)}$. The copied event is removed from the full Monte Carlo sample to avoid possible correlations between generated events in the fast Monte Carlo sample. The procedure is repeated for the remaining events in the fast Monte Carlo sample.

Finally, we apply an efficiency correction to the $\Delta t_{\rm true}$ spectrum, obtained from the full Monte Carlo sample (after selection and reconstruction), as shown in Fig. 7.5.

This routine for generating realistic fast Monte Carlo samples has several advantages. We properly reconstruct all (possible) correlations between $\Delta t_{\rm true}$, $\delta\Delta t$, $\sigma_{\Delta t}$, and the tagging categories. One can generate any *CP* asymmetry for the fast MC samples, using as template the full MC set with no *CP* asymmetry. (Compared with a re-weighting routine, where this is not generally possible, this method does not run into phase-space problems.) Also, the algorithm is far more efficient than re-weighting, which typically keeps only a fraction of all full MC events. But most importantly, because the *CP* asymmetries in data are expected to be small, these fast MC samples allow us to perform a precise, realistic fit bias test.

We generate fast MC samples with $36,828$ events each – the number of signal events in the data sample – in three configurations for the *CP* parameters. The first configuration has no generated *CP* asymmetry, *i.e.* $a, b, c = 0$. In the second configuration, for each B decay mode,

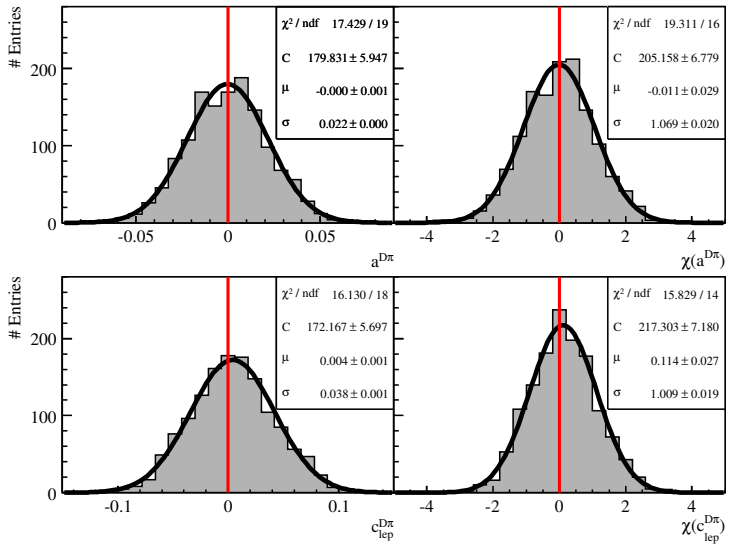

Figure 7.6: *Fitted a and c_{lep} parameters of $B \to D\pi$ sample. No CP asymmetry has been generated.*

the a parameters are generated equal to 0.10, the c parameters are generated equal to 0, and also all the other *CP* parameters, b, equals zero. In the third configuration, the a parameters are generated equal to 0, the c parameters are generated equal to 0.10, and the b parameters are again zero.

The fit results of these three tests are shown in Figs. 7.6–7.14. In all figures, the top row shows the fitted a parameters, and the bottom row shows the fitted c_{lep} parameters; the right-handed column shows the a and c_{lep} pull distributions. As can be seen, for all three configurations and all three B modes, the a parameters are statistically unbiased. In addition, but not shown, biases are neither observed in the b parameters. The c_{lep} parameters are positively biased, though, at the level of 10% compared to the statistical error. This opposed to the statistically limited, negative biases in the c_{lep} parameters, seen in Section 7.2.

The biases are correlated with vertex biases of Δt, as mentioned at the end of the previous Section, which – apparently – are not fully accounted for in the resolution function, described in Eq. (4.18).

The average biases in a and c_{lep} over the three fit configurations are listed in Table 7.6. We account for these systematical fit biases in Section 9.5.

7.4 Resolution function and dilutions in Geant 4 Monte Carlo events

The agreement between the data and the Monte Carlo samples has been verified by studying the Δt resolution function and dilution parameters.

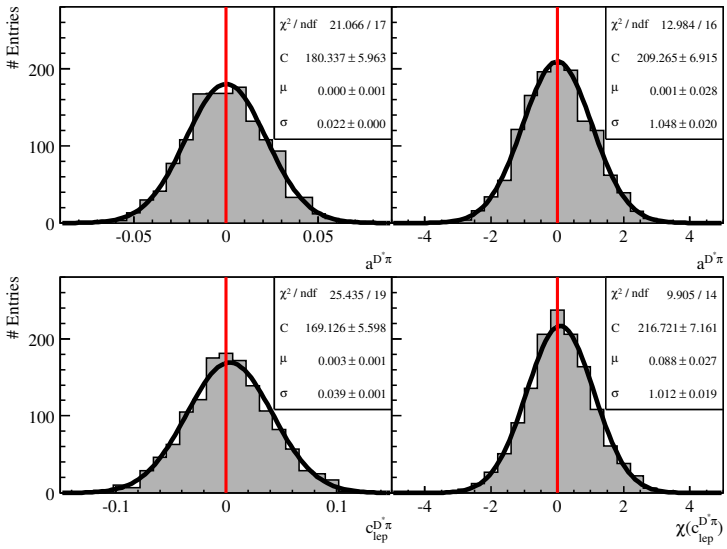

Figure 7.7: *Fitted a and* c_{lep} *parameters of* $B \to D^*\pi$ *sample. No CP asymmetry has been generated.*

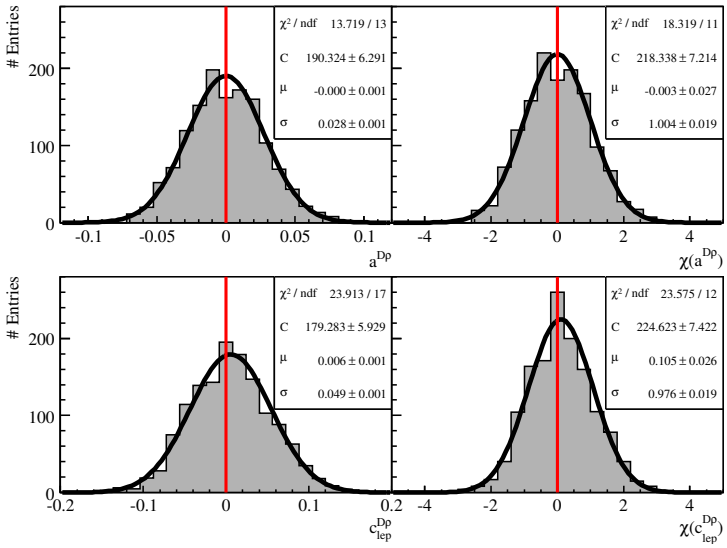

Figure 7.8: *Fitted a and* c_{lep} *parameters of* $B \to D\rho$ *sample. No CP asymmetry has been generated.*

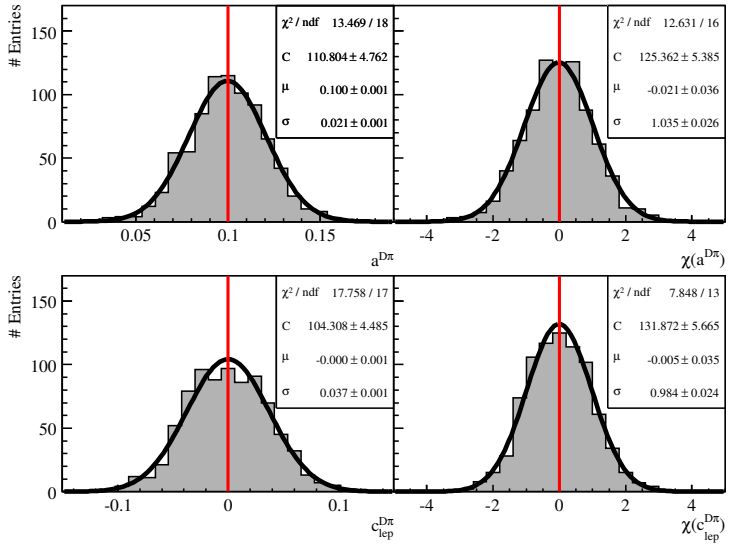

Figure 7.9: *Fitted a and c_{lep} parameters of $B \to D\pi$ sample. The generated CP asymmetry: $a = 0.10$, and $c_{\mathrm{lep}} = 0$.*

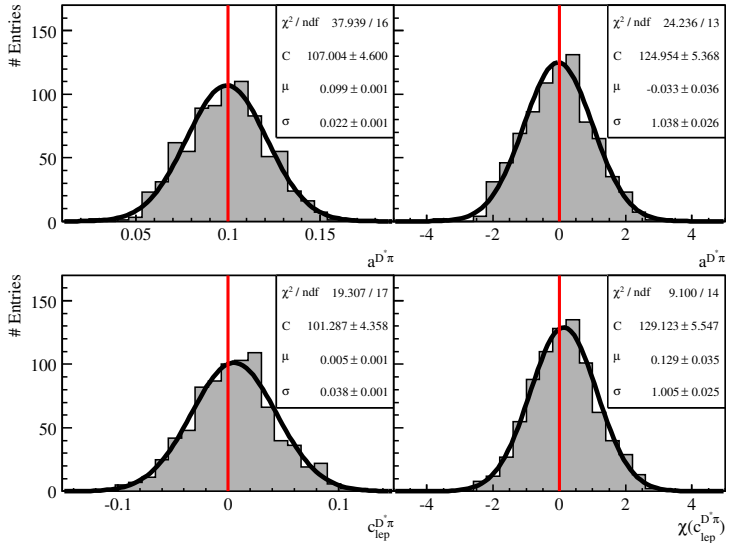

Figure 7.10: *Fitted a and c_{lep} parameters of $B \to D^*\pi$ sample. The generated CP asymmetry: $a = 0.10$, and $c_{\mathrm{lep}} = 0$.*

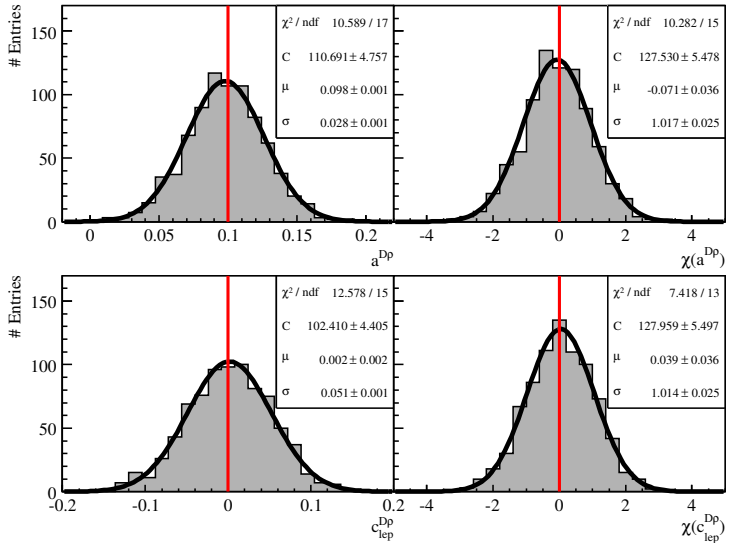

Figure 7.11: *Fitted a and c_{lep} parameters of $B \to D\rho$ sample. The generated CP asymmetry: $a = 0.10$, and $c_{\mathrm{lep}} = 0$.*

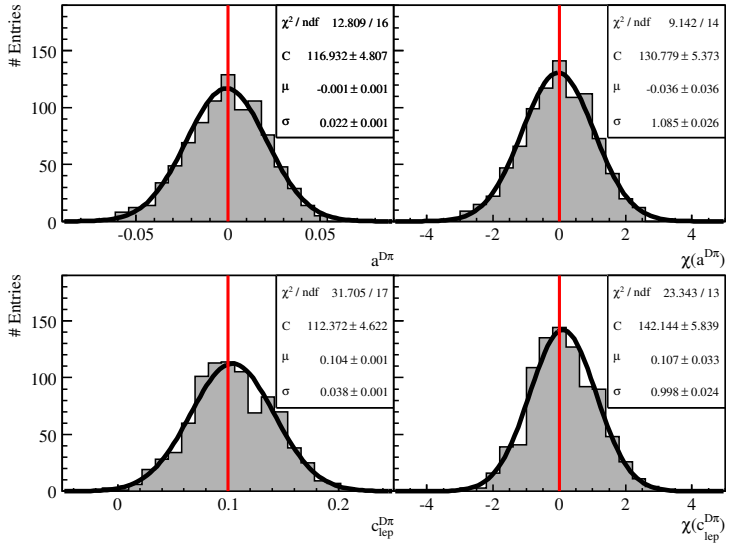

Figure 7.12: *Fitted a and c_{lep} parameters of $B \to D\pi$ sample. The generated CP asymmetry: $a = 0$, and $c_{\mathrm{lep}} = 0.10$.*

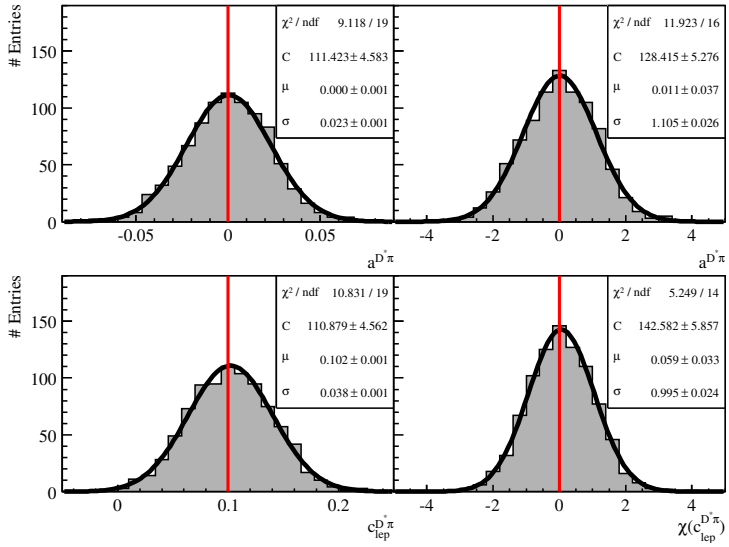

Figure 7.13: *Fitted a and c_{lep} parameters of $B \to D^*\pi$ sample. The generated CP asymmetry: $a = 0$, and $c_{\mathrm{lep}} = 0.10$.*

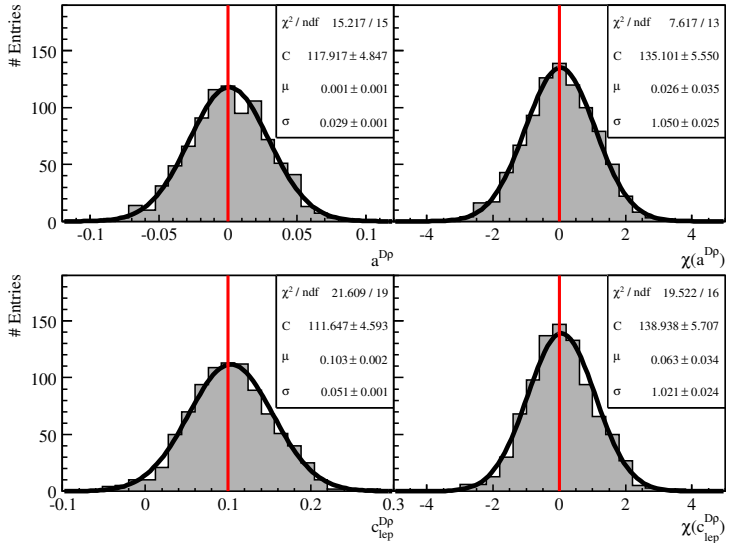

Figure 7.14: *Fitted a and c_{lep} parameters of $B \to D\rho$ sample. The generated CP asymmetry: $a = 0$, and $c_{\mathrm{lep}} = 0.10$.*

CP parameter	$a^{D\pi}$	$a^{D^*\pi}$	$a^{D\rho}$
Fit bias	-0.0004 ± 0.0004	-0.0001 ± 0.0004	-0.0004 ± 0.0005

CP parameter	$c_{\rm lep}^{D\pi}$	$c_{\rm lep}^{D^*\pi}$	$c_{\rm lep}^{D\rho}$
Fit bias	$+0.0034 \pm 0.0007$	$+0.0034 \pm 0.0007$	$+0.0037 \pm 0.0009$

Table 7.6: *Average fit biases of the parameters a^j and $c_{\rm lep}^j$ over three fast MC configurations given in the text.*

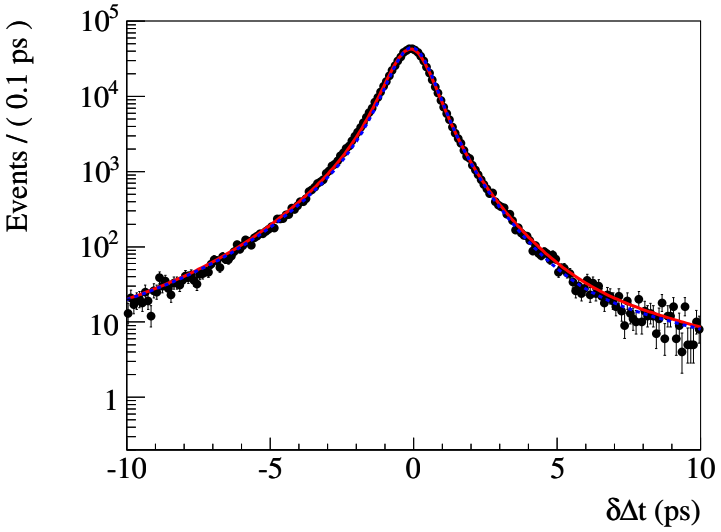

Figure 7.15: *The $\delta\Delta t$ residual distribution, as obtained from fully-simulated signal Monte Carlo events, with the Δt resolution functions obtained from the fit to data (dotted) and signal Monte Carlo events (solid) overlaid.*

Using Monte Carlo truth information, the signal Δt resolution function has been extracted from a fit to the Δt residuals, $\delta_t \equiv \Delta t_{\rm meas} - \Delta t_{\rm true}$, of the full Monte Carlo sample of signal events. The resulting distribution can be compared to the resolution function found in data and in the fit to signal Monte Carlo events. Results are listed in Table 7.7 and they are overlaid in Fig. 7.15. The Δt resolution function parameters agree well for data and the full Monte Carlo.

The dilution parameters, dilution differences, and dilutions slope parameters, as found in the fits to the full signal Monte Carlo and data samples, are compared in Table 7.7. The parameter values are found to agree well.

Parameter	Data	Signal MC
Signal resolution function parameters		
Scale (c), `Lepton`	0.95 ± 0.08	1.05 ± 0.02
Scale (c), `N-Lept.`	1.10 ± 0.04	1.14 ± 0.01
Scale (t), `Lepton`	2.1 ± 1.0	2.7 ± 0.3
Scale (t), `N-Lept.`	3.6 ± 0.4	3.9 ± 0.2
Width (o)	8.0 (fixed)	8.0 (fixed)
$\delta(\Delta t)$ (c), `Lepton`	-0.01 ± 0.06	-0.08 ± 0.02
$\delta(\Delta t)$ (c), `N-Lept.`	-0.19 ± 0.03	-0.266 ± 0.007
$\delta(\Delta t)$ (t)	-1.9 ± 0.5	-1.7 ± 0.1
$\delta(\Delta t)$ (o)	0.0 (fixed)	0.0 (fixed)
f (t)	0.06 ± 0.02	0.058 ± 0.007
f (o)	0.004 ± 0.001	0.0037 ± 0.0003
Signal dilution parameters		
$\langle D_0 \rangle$, `Lepton`	0.94 ± 0.03	0.956 ± 0.008
$\langle D_0 \rangle$, `Kaon I`	0.93 ± 0.03	0.933 ± 0.008
$\langle D_0 \rangle$, `Kaon II`	0.68 ± 0.03	0.736 ± 0.007
$\langle D_0 \rangle$, `K-Pi`	0.54 ± 0.04	0.538 ± 0.008
$\langle D_0 \rangle$, `Pi`	0.37 ± 0.04	0.328 ± 0.008
$\langle D_0 \rangle$, `Other`	0.22 ± 0.04	0.171 ± 0.010
ΔD, `Lepton`	0.03 ± 0.02	0.002 ± 0.004
ΔD, `Kaon I`	0.02 ± 0.02	-0.001 ± 0.004
ΔD, `Kaon II`	0.01 ± 0.02	0.013 ± 0.004
ΔD, `K-Pi`	0.02 ± 0.02	0.039 ± 0.005
ΔD, `Pi`	-0.13 ± 0.02	-0.118 ± 0.005
ΔD, `Other`	-0.08 ± 0.03	-0.093 ± 0.007

Table 7.7: *Signal resolution and dilution parameters as found on data and on fully simulated signal Monte Carlo.*

7.5 Expected statistical errors

To evaluate the goodness of the nominal fit to data, we compare the statistical errors on a and $c_{\rm lep}$, with the results found from the fast Monte Carlo studies in Section 7.1.

The distributions of statistical errors of a and $c_{\rm lep}$ for each B decay are given in Fig. 7.16. The values from the data fit are indicated with vertical arrows. The errors obtained with data are in agreement with the error distributions from the fast-parameterized Monte Carlo samples.

7.6 χ Test

The χ distributions of the m_{ES} fit to data are shown in Fig. 7.17, with the corresponding projections on the χ-axis in the right-hand column. For all three B decay modes, the normalized χ^2 values are relatively large. The pulls of the projected distributions are consistent with zero, but the widths of the Gaussians are slightly larger than one. The spread in χ increases for

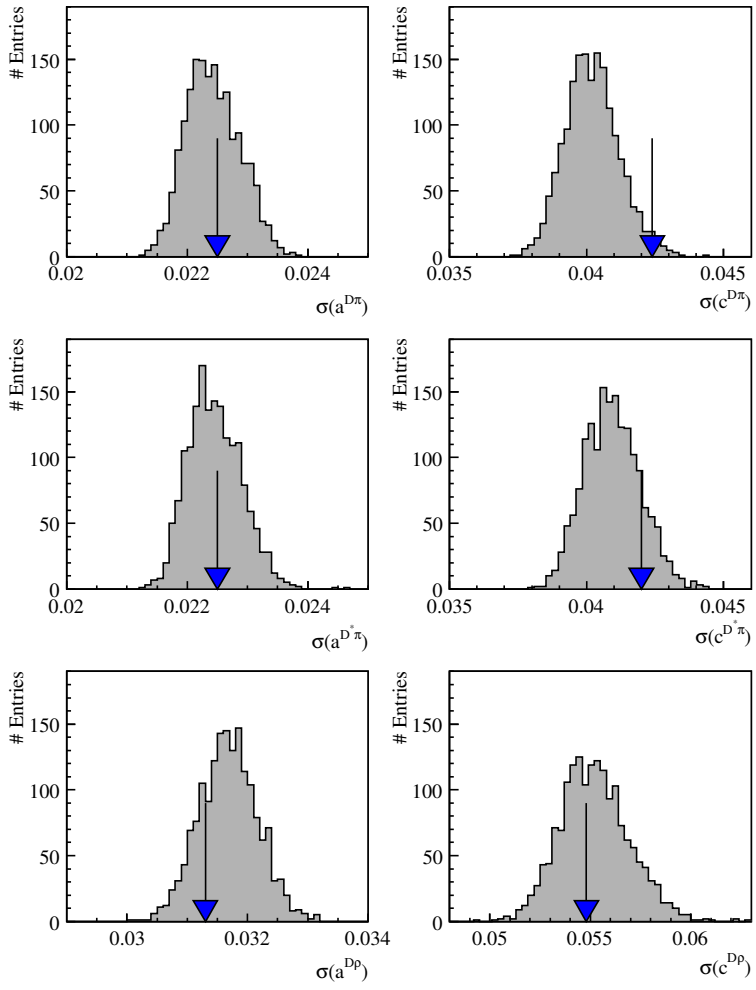

Figure 7.16: *Distributions errors on the fitted values of the a and c_{lep} parameters in the modes $B \to D^{-}\pi^{+}$, $B \to D^{*-}\pi^{+}$, and $B \to D^{-}\rho^{+}$, obtained from the fast Monte Carlo studies described in the text. The vertical arrows indicate the corresponding values obtained with data.*

$m_{ES} > 5.28$ GeV/c^2, with an apparent overestimate of events close to the kinematic endpoint of the m_{ES} spectrum. To account for the latter dip in χ, the endpoint of the `Argus` function in Eq. (4.11) is varied by 2 MeV/c^2 in Section 9.2.2.

The $B \to D^{\mp}\rho^{\pm}$ signal events tend to leak out into the m_{ES} sideband, and are perhaps better described using a `Crystal Ball` function [78]. (For practical bookkeeping issues, this is not done in the m_{ES} fit to data.) Second, as also seen in Fig. 4.3 in Section 4.1.4, for $B \to D\rho$ the peaking background shape used in the m_{ES} sideband is not perfect. This explains the structure seen in the χ vs m_{ES} graph of $B \to D\rho$ events. However, these two effects should not affect the description of the $B \to D\rho$ events in the m_{ES} signal box.

The goodness of the fit results presented at the end of Section 7.2 can be supported by constructing χ distributions of the time-dependent fit to data. To do so, events categorized by final state and as mixed or unmixed, have been summed up in Δt bins of 0.2 ps. The resulting bins obey Poissonian statistics, which is accounted for when calculating χ (see [79], Eq. (31.12)). The left-hand sides of Figs. 7.18–7.20 show χ versus Δt for the 12 sets of data.

The right-hand sides of Figs. 7.18–7.20 show the corresponding χ distributions of all bins with $|\Delta t| < 7$ ps. Bins for which $|\Delta t| > 7$ ps have been excluded from these projections, as they do not contain enough statistics to justify binning[1]. All χ distributions show pulls consistent with zero and agree with Gaussians of unit width.

7.7 Results of τ_{B^0} and Δm_d from data

In the fit to data, the mixing frequency Δm_d and the B^0 lifetime τ_{B^0} have been fixed to their world averages of $\Delta m_d = 0.502 \pm 0.007$ ps^{-1} and $\tau_B^0 = 1.536 \pm 0.014$ ps [17]. We check whether the Δt distributions are consistent with these values by allowing the corresponding parameters to vary individually in the fit. Note that the analysis has not been optimized for these measurements. The fits give $\Delta m_d = 0.515 \pm 0.006$ ps^{-1} and $\tau_{B^0} = 1.496 \pm 0.013$ ps.

The quoted errors on these numbers are merely statistical. No systematic uncertainties or Monte Carlo biases have been evaluated. Naive estimates of the systematic errors could be at the level of 0.009 ps^{-1} and 0.020 ps [17]. Including these, the fit values agree with the world average values, as far as a comparison is valid. The value of Δm_d is also consistent with *BABAR*'s last measurement of hadronic B decays, $0.516 \pm 0.016\,(\text{stat.}) \pm 0.010\,(\text{syst.})$, using $30\,\text{fb}^{-1}$ of data [29]. Similarly, on $20\,\text{fb}^{-1}$ of data, τ_{B^0} was found to be $1.546 \pm 0.032 \pm 0.022$ [29]. The differences observed are accounted for in the systematic error evalutation of a and c_{lep} (see Section 9.4).

As a cross-check, we have also determined the mixing frequency Δm_d and the B^0 lifetime τ_{B^0} simultaneously on the sample of fully simulated Monte Carlo events, which has generated values of 0.489ps^{-1} and 1.541ps respectively. The fit to Monte Carlo events finds the values 0.4935 ± 0.0014 ps^{-1} and 1.528 ± 0.003 ps. The correlation between the two parameters is -34%.

The correlations between Δm_d and τ_{B^0} on the one hand and the a and c_{lep} parameters on the other hand are found to be small, as shown in Table 7.8. So even though the fit values of Δm_d and τ_{B^0} are slightly biased, they have little to no impact on the measured *CP* parameters.

[1] Bins with (too) small statistics show up as the correlated points in the graphs 'χ vs Δt'. In the range $\Delta t \in [-7, 7]$, they have the tendency to pull the mean of the χ distribution towards negative values.

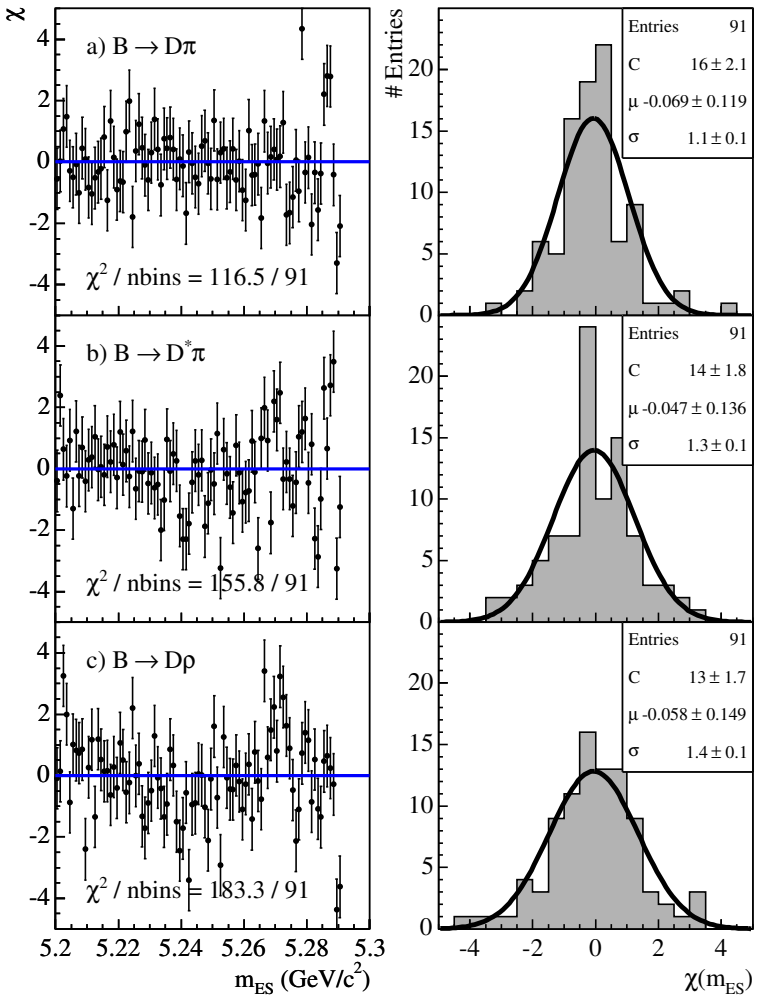

Figure 7.17: *Plot of χ vs m_{ES} for, from top to bottom, $B \to D^{\mp}\pi^{\pm}$, $B \to D^{*\mp}\pi^{\pm}$, and $B \to D^{\mp}\rho^{\pm}$ events.*

7.8 Fit by tagging category and data taking period

The a parameters have been split by tagging category in the fit to data. The results, including the projections of the fit, are plotted in Fig. 7.21. The parameters show no significant disagreements.

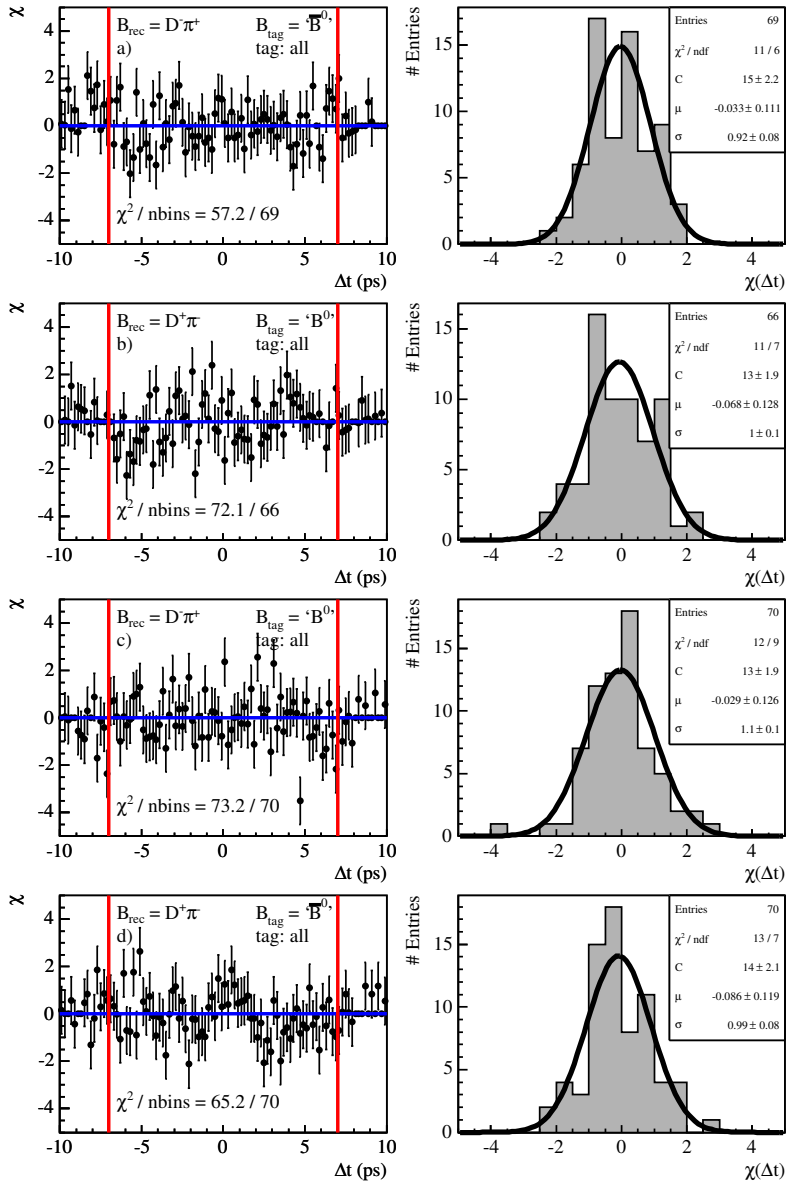

Figure 7.18: *Plot of χ vs Δt (left) and the χ distributions (right) for $B \to D\pi$ events categorized as $D^-\pi^+$ or $D^+\pi^-$ and as unmixed or mixed.*

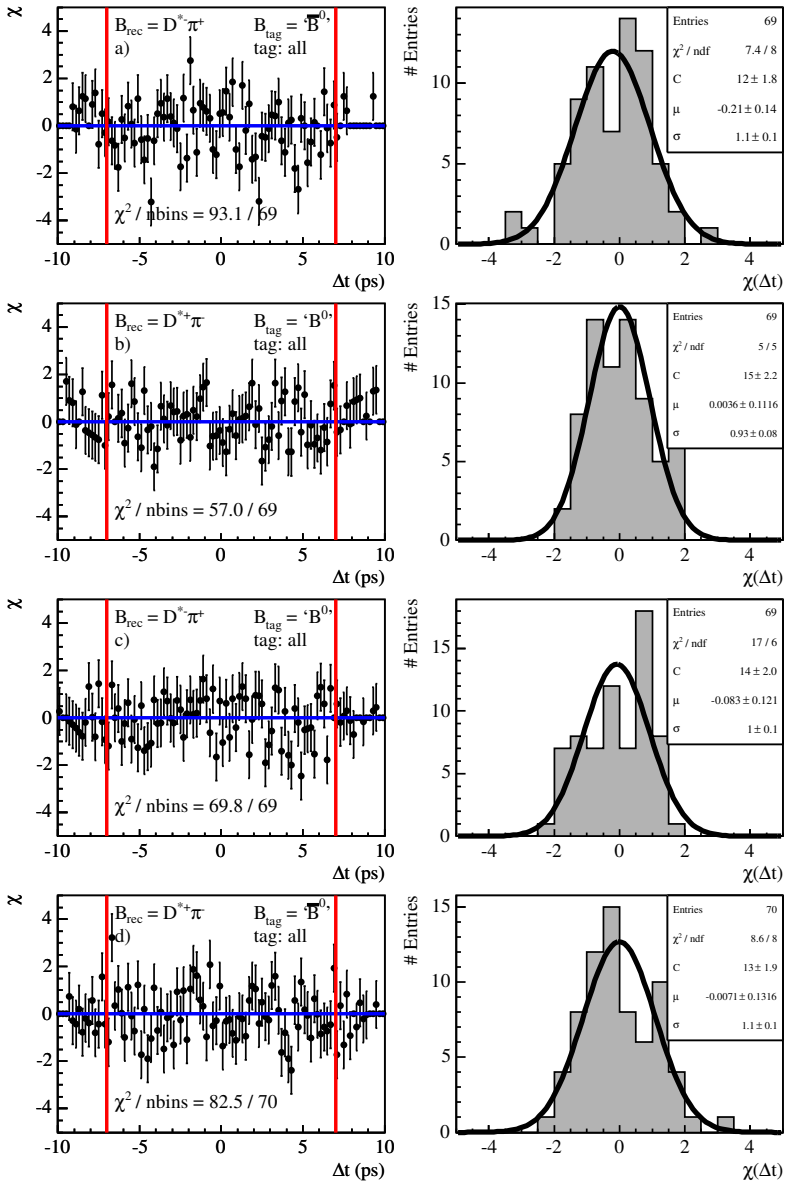

Figure 7.19: *Plot of χ vs Δt (left) and the χ distributions (right) for $B \to D^*\pi$ events categorized as $D^{*-}\pi^+$ or $D^{*+}\pi^-$ and as unmixed or mixed.*

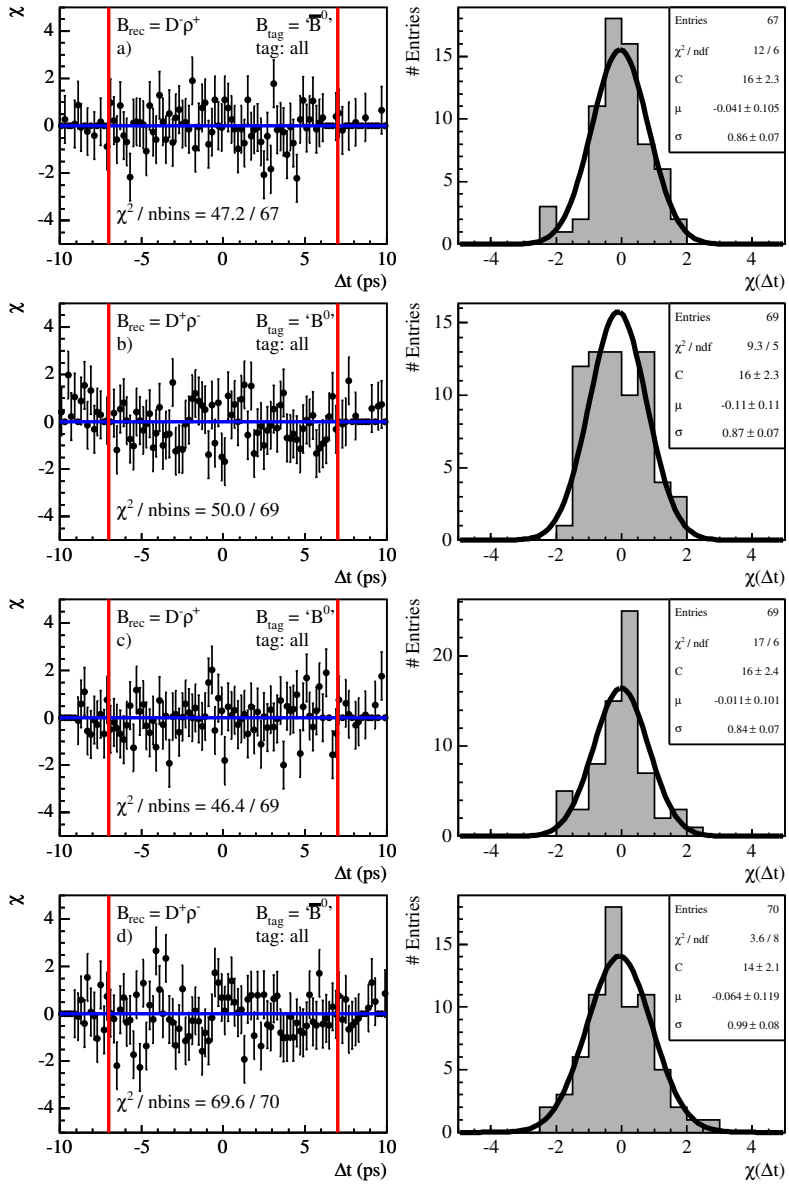

Figure 7.20: *Plot of χ vs Δt (left) and the χ distributions (right) for $B \to D\rho$ events categorized as $D^-\rho^+$ or $D^+\rho^-$ and as unmixed or mixed.*

Correlation	$a^{D\pi}$	$a^{D^*\pi}$	$a^{D\rho}$	$c_{\rm lep}^{D\pi}$	$c_{\rm lep}^{D^*\pi}$	$c_{\rm lep}^{D\rho}$
Δm_d	-0.0028	-0.0024	-0.0034	-0.0130	-0.0106	-0.0071
τ_{B^0}	-0.0024	-0.0035	-0.0025	$+0.0086$	$+0.0088$	$+0.0019$

Table 7.8: *Correlations of a and $c_{\rm lep}$ with Δm_d and τ_{B^0}.*

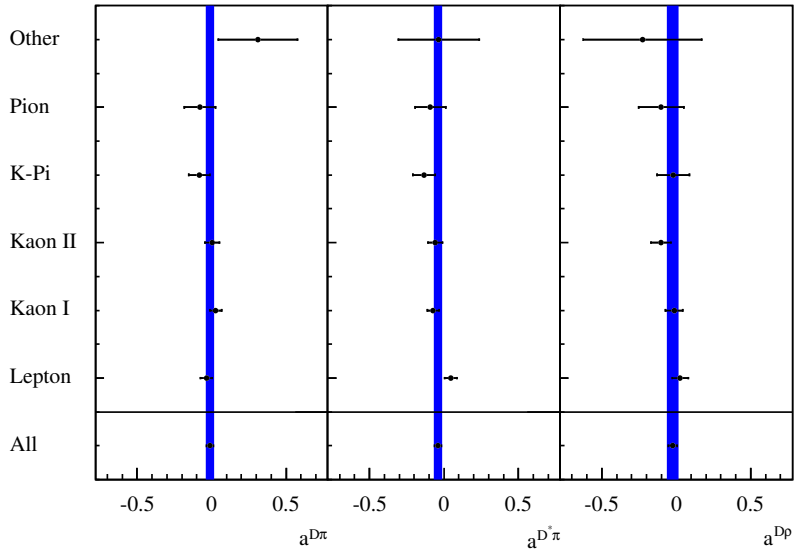

Figure 7.21: *The a CP parameters split by tagging category for the modes $B \to D\pi$, $B \to D^*\pi$, and $B \to D\rho$.*

7.9 Fit to charged B control sample

As another cross-check, we have performed the fit to the charged B data sample $B^- \to D^{(*)0}\pi^-$, obtained from Ref. [76] For charged B mesons there are two states to study: B^- and B^+ decays, so one can test only one $\sin(\Delta m_d \Delta t)$ 'mixing' term, with one corresponding CP amplitude, S. As sine terms we choose $+S\sin(\Delta m_d \Delta t)$ for B^+ decays, and $-S\sin(\Delta m_d \Delta t)$ for B^- decays. Compared with the the a, b, c parametrization used for the B^0 sample, this corresponds to the sine term with the a coefficient.

The available data sample has about 6.8k signal candidates of $B^- \to D^{(*)0}\pi^-$. We obtain the sine amplitudes given in Table 7.9. Both amplitudes are consistent with zero, as expected. The results indicate that the fit procedure and model do not create a fake CP asymmetry where there is none.

Coefficient	Observed asymmetry
$S^{D\pi}$	$+0.072 \pm 0.136$
$S^{D^*\pi}$	-0.112 ± 0.105

Table 7.9: *Observed sine asymmetries in* $B^- \to D^{0(*)}\pi^-$.

7.10 Fit to the m_{ES} sideband region

As shown in Fig. 4.10, the likelihood to find signal events in the m_{ES} sideband, with $m_{ES} < 5.27$ GeV/c^2, is practically zero. Events in that mass region are used to determine the properties of background events in the Δt fit.

To verify the validity of the description of background events in the Δt fit, detailed in Section 6.3, we have made Δt projections for the m_{ES} sideband. They can be seen in Figs. 7.22–7.24. The background model used does not show any discrepancies.

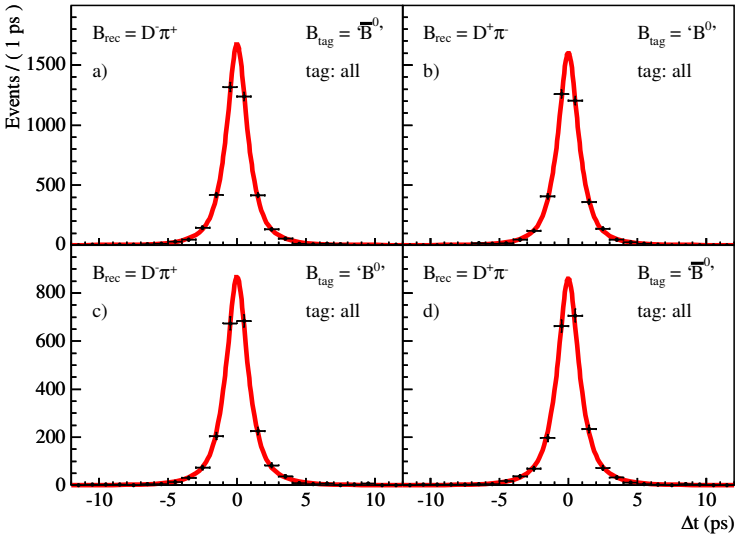

Figure 7.22: *Distributions of* Δt *for* $B \to D^{\mp}\pi^{\pm}$ *background candidates, split by* B *tagging flavor and reconstructed final state. The four plots show candidates of all tagging categories; the solid curves are fit projections.*

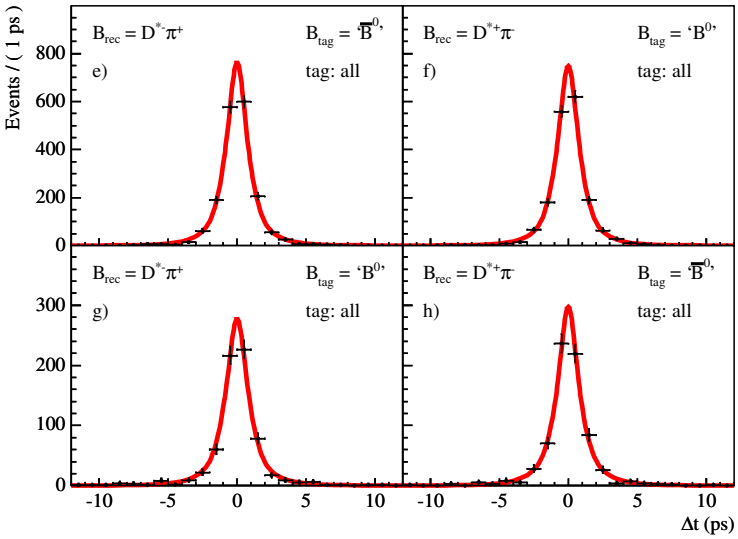

Figure 7.23: *Distributions of Δt for $B \to D^{*\mp}\pi^{\pm}$ background candidates, split by B tagging flavor and reconstructed final state. The four plots show candidates of all tagging categories; the solid curves are fit projections.*

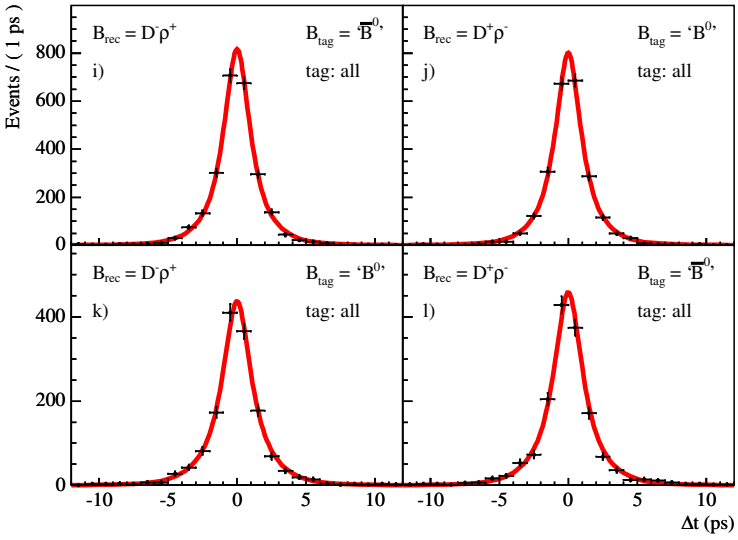

Figure 7.24: *Distributions of Δt for $B \to D^{\mp}\rho^{\pm}$ background candidates, split by B tagging flavor and reconstructed final state. The four plots show candidates of all tagging categories; the solid curves are fit projections.*

Chapter 8

Result of the fit to data

In this Chapter results of the maximum-likelihood fit, described in Chapter 6, to the Δt distributions of the $B \to D^{(*)\mp}\pi^{\pm}$ and $B \to D^{\mp}\rho^{\pm}$ sample are presented.

The sample of events used in the fit has been selected in Section 4.1.2. As explained in Section 4.1.3, the fit to the data sample is performed in two steps. The m_{ES} distributions of all selected events in various sub-categories have been fit in Section 4.4 to determine the event-by-event signal probability. Now, with this information, the fit to the Δt distributions is performed in Section 8.1. The Chapter concludes with a description of the performance of the B-flavor tagging algorithm in Section 8.2.

The validation of the fit results and a comparison to the results from fully simulated (Geant 4) Monte Carlo events is found in Chapter 7. Finally, the extraction of $\sin(2\beta+\gamma)$ from the measured *CP* parameters is performed in Chapter 11.

8.1 Δt Fit results

This Section presents the results of the Δt fit to data.

The maximum-likelihood fit to the Δt distributions of events in the $B \to D^{(*)\mp}\pi^{\pm}$ and $B \to D^{\mp}\rho^{\pm}$ samples is performed using the event-by-event signal and background probability, assigned on the basis of the measured values of m_{ES}, using the m_{ES} fit results obtained in the Section 4.4. The Δt fit is performed to all samples simultaneously, with the floating fit parameters split by tagging category and/or B decay mode. The function used to describe signal and background events has been presented in Chapter 6.

The results of the overall Δt fit to the $B \to D\pi$, $B \to D^*\pi$, and $B \to D\rho$ data sample can be found in Tables 8.1-8.4. Tables 8.1 and 8.2 list consecutively: the determined *CP* and tag-side interference parameters, and parameters related to the signal PDFs. Tables 8.3 and 8.4 list the background parameters: first those for the combinatorial background, then the peaking background parameters. Each table shows the correlations with the *CP* parameters of interest: $a^{D\pi}$, $a^{D^*\pi}$, $a^{D\rho}$, $c_{\rm lep}^{D\pi}$, $c_{\rm lep}^{D^*\pi}$, and $c_{\rm lep}^{D\rho}$. There are 99 free parameters in the Δt fit, while 29 additional parameters have been kept fixed (not considering the parameters obtained from the separate m_{ES} fit, which are also fixed, for a grand total of 262 fit parameters).

A summary of the values used in the extraction of $\sin(2\beta+\gamma)$ is given in Table 8.5. The largest correlation between (one of) the *CP* parameters and any linear combination of the other free parameters is listed in the right-handed column.

Figs. 8.1–8.3 show the Δt distribution for data events in signal box, with $m_{ES} > 5.27$ GeV/c^2,

for the final states $D\pi$, $D^*\pi$, and $D\rho$ with the likelihood projection superimposed, for all events together and separated by tagging category. Remember that *CP* violation, if present, can best be observed between the mixed events of *CP*-conjugated final states as the difference in uneven behavior in Δt. See Section 7.2 for a comparison with fully simulated Monte Carlo fit results. In Section 7.10 one can find the Δt distributions of the m_{ES} sideband region, $m_{ES} < 5.27$ GeV/c^2, again with all events summed and split by tagging category.

The mixing asymmetries can be defined as

$$\mathcal{A}^f_{\rm mix} = \frac{N^f(\Delta t; \text{unmixed}) - N^f(\Delta t; \text{mixed})}{N^f(\Delta t; \text{unmixed}) + N^f(\Delta t; \text{mixed})}\,, \tag{8.1}$$

with $N^f(\Delta t; \text{(un-)mixed})$ being the observed number of (un-)mixed events in intervals of Δt and final state f. These are shown in Figs. 8.4 and 8.5 for events in the signal box. Ignoring the Δt resolution, $\mathcal{A}^f_{\rm mix} = D\cos(\Delta m \Delta t)$. Including resolution effects, the cosine term is shifted slightly upwards and the asymmetry fades out at larger (mis-reconstructed) values of $|\Delta t|$. The first set of plots shows the mixing asymmetries for all tagging categories combined, and the second set for only the `Lepton` tagging category. Notice how the mixing asymmetries can clearly be seen. Each asymmetry is diluted in amplitude because of B-flavor mistagging, hence the larger amplitudes for the `Lepton` category.

Fig. 8.6 shows the tagging asymmetries for each final B decay mode $j = D\pi$, $D^*\pi$, $D\rho$, defined by

$$\mathcal{A}^j_{\rm tag} = \frac{N^j(\Delta t; B^0_{\rm tag}) - N^j(\Delta t; \overline{B}^0_{\rm tag})}{N^j(\Delta t; B^0_{\rm tag}) + N^j(\Delta t; \overline{B}^0_{\rm tag})}\,, \tag{8.2}$$

where $N^j(\Delta t; B^0_{\rm tag})$ and $N^j(\Delta t; \overline{B}^0_{\rm tag})$ are, consecutively, the observed number of B^0-tagged and $\overline{B}^0$-tagged events in intervals of Δt and B decay mode μ. In case of perfect Δt resolution, $\mathcal{A}^j_{\rm tag} = D\,a^j\,\sin(\Delta m \Delta t)$. Each tagging asymmetry is proportional to a^j, and, again, is diluted because of B-flavor mistagging. The fit projections are shifted slightly downwards. This is merely a sign of non-zero dilution differences between B^0 and $\overline{B}^0$ tags (ΔD) induced by the tagging algorithm.

It should be noted, as can be seen in Fig. 8.4, that the bias in the resolution function gives rise to a slightly uneven Δt behavior in the asymmetry distributions. In relation to this, the large global correlation ($\approx 25\%$) of any of the $c_{\rm lep}$ parameters comes from the `Lepton` bias parameter of the core Gaussian of the Δt resolution function. The a parameters are mostly correlated to the tag-side interference b parameters and to themselves.

The tag-side interference parameter $b_{\rm lep}$ has been fixed to zero, as no tag-side interference effect is expected in the `Lepton` tagging category. No significant *CP* asymmetry is observed in any of the a, b, c parameters.

8.2 Performance of the B-flavor tagging algorithm

The performance of the tagging algorithm is expressed in terms of the effective tagging power, defined as $Q = \sum_i \epsilon_i (1 - 2\langle w \rangle_i)^2$, where ϵ_i and $\langle w \rangle_i$ are the efficiency and the average mistag probability, respectively, for tagging category i.

The figure of merit Q can be interpreted as follows. A tagging power of, for example, 25% is the equivalent to an effective tagging efficiency of that same value (so 75% of the signal events cannot be flavor-tagged, called 'untagged' events) with perfect flavor-tagging for the B-tagged sample (that is, no mis-tagging).

Parameter	Result	Corrl. $a^{D\pi}$	Corrl. $a^{D^*\pi}$	Corrl. $a^{D\rho}$	Corrl. $c_{\rm lep}^{D\pi}$	Corrl. $c_{\rm lep}^{D^*\pi}$	Corrl. $c_{\rm lep}^{D\rho}$
CP Parameters							
$a^{D\pi}$	-0.0095 ± 0.0225	1.000	0.038	0.018	0.002	-0.003	0
$a^{D^*\pi}$	-0.0400 ± 0.0225	0.038	1.000	0.023	0.001	-0.055	0.002
$a^{D\rho}$	-0.0235 ± 0.0313	0.018	0.023	1.000	0	-0.003	-0.048
$c_{\rm lep}^{D\pi}$	-0.0331 ± 0.0424	0.002	0.001	0	1.000	0.080	0.081
$c_{\rm lep}^{D^*\pi}$	0.0488 ± 0.0420	-0.003	-0.055	-0.003	0.080	1.000	0.066
$c_{\rm lep}^{D\rho}$	-0.0978 ± 0.0548	0	0.002	-0.048	0.081	0.066	1.000
Tag-side interference parameters							
$b_{\rm lep}$	0.0 (fixed)	–	–	–	–	–	–
$b_{\rm ki}$	-0.00431 ± 0.0226	0.141	0.179	0.086	0	-0.010	-0.003
$b_{\rm kii}$	0.00313 ± 0.0203	0.101	0.103	0.059	0	-0.006	-0.002
$b_{\rm kpi}$	0.0580 ± 0.0238	0.041	0.048	0.034	0	-0.003	-0.002
$b_{\rm pi}$	0.00782 ± 0.0240	0.022	0.020	0.013	0	-0.001	-0.001
$b_{\rm oth}$	-0.0263 ± 0.0298	0.006	0.003	0.003	0	0	0
$c_{\rm ki}^{D\pi}$	0.0405 ± 0.0385	0.010	0.002	-0.001	0	0	0
$c_{\rm kii}^{D\pi}$	0.0695 ± 0.0475	0.010	0	-0.001	0	0	0
$c_{\rm kpi}^{D\pi}$	-0.134 ± 0.0711	0.007	-0.002	-0.001	0	0	0
$c_{\rm pi}^{D\pi}$	0.072 ± 0.260	0.010	-0.001	-0.002	0	0	0
$c_{\rm oth}^{D\pi}$	-0.053 ± 0.104	-0.002	0	0.003	0	0	0
$c_{\rm ki}^{D^*\pi}$	-0.0831 ± 0.0381	0.005	-0.008	0	0	0.001	0
$c_{\rm kii}^{D^*\pi}$	-0.0231 ± 0.0468	-0.001	0	-0.002	0	0	0
$c_{\rm kpi}^{D^*\pi}$	0.0663 ± 0.0732	0	-0.007	-0.003	0	0.001	0
$c_{\rm pi}^{D^*\pi}$	0.210 ± 0.273	0	0.003	-0.001	0	0	0
$c_{\rm oth}^{D^*\pi}$	0.065 ± 0.104	-0.002	0.001	0.002	0	0	0
$c_{\rm ki}^{D\rho}$	-0.0501 ± 0.0568	0	-0.001	-0.012	0	0	0
$c_{\rm kii}^{D\rho}$	-0.0991 ± 0.0670	0.002	0.001	0.006	0	0	0
$c_{\rm kpi}^{D\rho}$	0.047 ± 0.106	0.001	0	-0.009	0	0	0
$c_{\rm pi}^{D\rho}$	0.114 ± 0.151	0.001	0.001	0.012	0	0	-0.001
$c_{\rm oth}^{D\rho}$	0.749 ± 0.394	-0.004	-0.001	0.010	0	0	0

Table 8.1: *Results of the simultaneous likelihood fit to the $B \to D^{\mp}\pi^{\pm}$, $B \to D^{*\mp}\pi^{\pm}$, and $B \to D^{\mp}\rho^{\pm}$ data samples (a, b, c parameters).*

As already mentioned in Section 4.2, the errors on the *CP* parameters of interest, a and $c_{\rm lep}$, are proportional to $1/\sqrt{Q}$. Untagged events do not contribute to the sensitivity to a and $c_{\rm lep}$, as can be seen from Eqs. (5.16–5.19). They do contribute to the sensitivity to the tag-side interference parameters b.

The tagging efficiency ϵ_i is defined as

$$\epsilon_i = \frac{N_i^{\rm sig}}{N_{\rm untag}^{\rm sig} + \sum_{j=1}^{6} N_j^{\rm sig}}\,, \tag{8.3}$$

where $N_i^{\rm sig}$ is the number of signal events in category i, and $N_{\rm untag}^{\rm sig}$ is the number of untagged

Parameter	Result	Corrl. $a^{D\pi}$	Corrl. $a^{D^*\pi}$	Corrl. $a^{D\rho}$	Corrl. $c_{\rm lep}^{D\pi}$	Corrl. $c_{\rm lep}^{D^*\pi}$	Corrl. $c_{\rm lep}^{D\rho}$
Signal resolution function parameters							
Scale (c), `Lepton`	0.95 ± 0.08	-0.012	-0.019	0.027	-0.003	0.031	-0.020
Scale (c), `N-Lept.`	1.10 ± 0.04	-0.003	0	-0.003	0.006	0.008	0.006
Scale (t), `Lepton`	2.1 ± 1.0	0.022	0.016	-0.042	-0.068	-0.047	-0.048
Scale (t), `N-Lept.`	3.6 ± 0.4	0.012	0.001	-0.013	-0.002	0.006	0.001
Width (o)	8.0 (fixed)	–	–	–	–	–	–
$\delta(\Delta t)$ (c), `Lepton`	-0.01 ± 0.06	-0.011	-0.005	0.006	0.266	0.233	0.230
$\delta(\Delta t)$ (c), `N-Lept.`	-0.19 ± 0.03	-0.011	-0.004	0.007	0.003	-0.003	0.001
$\delta(\Delta t)$ (t)	-1.9 ± 0.5	0.013	0.005	-0.014	-0.013	-0.008	-0.011
$\delta(\Delta t)$ (o)	0.0 (fixed)	–	–	–	–	–	–
f (t)	0.06 ± 0.02	-0.002	0	0.002	-0.008	-0.011	-0.009
f (o)	0.004 ± 0.001	-0.006	-0.003	0.008	0.014	0.002	0.007
Signal dilution parameters							
$\langle D_0 \rangle$, `Lepton`	0.94 ± 0.03	0.009	0.028	0.021	0.017	-0.040	0.022
$\langle D_0 \rangle$, `Kaon I`	0.93 ± 0.03	0.037	-0.004	-0.008	0	0	0.001
$\langle D_0 \rangle$, `Kaon II`	0.68 ± 0.03	0.004	-0.004	-0.011	0	0	0.001
$\langle D_0 \rangle$, `K-Pi`	0.54 ± 0.04	0.004	-0.003	0.016	0	0	-0.001
$\langle D_0 \rangle$, `Pi`	0.37 ± 0.04	-0.011	-0.014	-0.012	0	0.001	0.001
$\langle D_0 \rangle$, `Other`	0.22 ± 0.04	0.001	0.003	0.017	0	0	-0.001
ΔD, `Lepton`	0.03 ± 0.02	0.016	-0.052	0.018	0.039	0.101	0.017
ΔD, `Kaon I`	0.02 ± 0.02	-0.001	0.033	0.017	0	-0.002	-0.001
ΔD, `Kaon II`	0.01 ± 0.02	-0.014	0.002	-0.001	0	0	0
ΔD, `K-Pi`	0.02 ± 0.02	0.002	-0.012	0.002	0	0.001	0
ΔD, `Pi`	-0.13 ± 0.02	-0.001	-0.003	-0.005	0	0	0
ΔD, `Other`	-0.08 ± 0.03	0	-0.002	-0.001	0	0	0
D slope, `Lepton`	-0.02 ± 0.05	0	0	-0.015	-0.004	0.002	-0.002
D slope, `Kaon I`	-0.05 ± 0.06	-0.027	0.001	0.009	0	0	-0.001
D slope, `Kaon II`	0.00 ± 0.05	-0.001	0.006	0.008	0	0	-0.001
D slope, `K-Pi`	-0.04 ± 0.05	-0.009	0	-0.014	0	0	0.001
D slope, `Pi`	-0.01 ± 0.05	0.008	0.013	0.014	0	-0.001	-0.001
D slope, `Other`	-0.07 ± 0.06	0.006	-0.002	-0.022	0	0	0.001
ΔD slope	0.0 (fixed)	–	–	–	–	–	–
External parameters							
Δm_d ($\rm ps^{-1}$)	0.502 (fixed)	–	–	–	–	–	–
$\tau_{B^0_d}$ (ps)	1.536 (fixed)	–	–	–	–	–	–
$\Delta\Gamma_d$ ($\rm ps^{-1}$)	0.0 (fixed)	–	–	–	–	–	–

Table 8.2: *Results of the simultaneous likelihood fit to the $B \to D^{\mp}\pi^{\pm}$, $B \to D^{*\mp}\pi^{\pm}$, and $B \to D^{\mp}\rho^{\pm}$ data samples (signal parameters).*

Parameter	Result	Corrl. $a^{D\pi}$	Corrl. $a^{D^*\pi}$	Corrl. $a^{D\rho}$	Corrl. $c_{\rm lep}^{D\pi}$	Corrl. $c_{\rm lep}^{D^*\pi}$	Corrl. $c_{\rm lep}^{D\rho}$
Combinatorial background resolution function							
Scale (c)	1.37 ± 0.01	-0.002	0	0.002	0	0	0.002
$\delta(\Delta t)$ (c)	-0.016 ± 0.011	0.001	0.001	0	-0.002	0.002	-0.001
Width (o)	8.0 (fixed)	–	–	–	–	–	–
$\delta(\Delta t)$ (o)	0.0 (fixed)	–	–	–	–	–	–
f (o)	0.020 ± 0.002	-0.001	0	-0.003	-0.001	0	-0.003
Combinatorial background dilutions (1)							
$\langle D \rangle_{\rm lep}^{D\pi}$, $\tau = 0$	0.62 ± 0.28	0.003	-0.002	-0.001	0.007	0.003	-0.002
$\langle D \rangle_{\rm ki}^{D\pi}$, $\tau = 0$	0.56 ± 0.03	0	0	0	0	0	0
$\langle D \rangle_{\rm kii}^{D\pi}$, $\tau = 0$	0.45 ± 0.02	0.001	0	0.001	0	0	0
$\langle D \rangle_{\rm kpi}^{D\pi}$, $\tau = 0$	0.31 ± 0.03	0	0	0	0	0	0
$\langle D \rangle_{\rm pi}^{D\pi}$, $\tau = 0$	0.15 ± 0.03	0	0	0	0	0	0
$\langle D \rangle_{\rm oth}^{D\pi}$, $\tau = 0$	0.08 ± 0.03	-0.001	0	0	0	0	0
$\langle D \rangle_{\rm lep}^{D^*\pi}$, $\tau = 0$	0.64 ± 0.60	0	0.005	0	-0.002	0.002	-0.003
$\langle D \rangle_{\rm ki}^{D^*\pi}$, $\tau = 0$	0.88 ± 0.04	-0.002	0.001	0	0	0	0
$\langle D \rangle_{\rm kii}^{D^*\pi}$, $\tau = 0$	0.69 ± 0.03	0	0	0	0	0	0
$\langle D \rangle_{\rm kpi}^{D^*\pi}$, $\tau = 0$	0.48 ± 0.04	0	0.001	0	0	0	0
$\langle D \rangle_{\rm pi}^{D^*\pi}$, $\tau = 0$	0.14 ± 0.05	0	0	0	0	0	0
$\langle D \rangle_{\rm oth}^{D^*\pi}$, $\tau = 0$	0.08 ± 0.05	-0.001	0	0	0	0	0
$\langle D \rangle_{\rm lep}^{D\rho}$, $\tau = 0$	1.26 ± 0.46	-0.001	-0.002	-0.013	-0.001	0.002	-0.016
$\langle D \rangle_{\rm ki}^{D\rho}$, $\tau = 0$	0.59 ± 0.06	-0.002	0	0.005	0	0	0
$\langle D \rangle_{\rm kii}^{D\rho}$, $\tau = 0$	0.58 ± 0.05	-0.001	0	0.001	0	0	0
$\langle D \rangle_{\rm kpi}^{D\rho}$, $\tau = 0$	0.35 ± 0.05	0	0	-0.002	0	0	0
$\langle D \rangle_{\rm pi}^{D\rho}$, $\tau = 0$	0.13 ± 0.05	0	0	0	0	0	0
$\langle D \rangle_{\rm oth}^{D\rho}$, $\tau = 0$	0.07 ± 0.06	-0.001	0	0.001	0	0	0
Combinatorial background lifetimes and fractions							
τ, comb. bkg. (ps)	1.39 ± 0.05	0.001	0	0.004	0	0	0.005
$f^{D\pi}(\tau = 0)$, `Lepton`	0.33 ± 0.10	-0.003	0	0.001	-0.004	0	0.001
$f^{D\pi}(\tau = 0)$, `N-Lept.`	0.81 ± 0.01	-0.002	0	0.002	0	0	0.003
$f^{D^*\pi}(\tau = 0)$, `Lepton`	0.28 ± 0.18	0	-0.005	0	-0.001	0	0
$f^{D^*\pi}(\tau = 0)$, `N-Lept.`	0.78 ± 0.02	0	0	0.002	0	0	0.003
$f^{D\rho}(\tau = 0)$, `Lepton`	0.23 ± 0.12	0.001	0	0.012	0	0.001	0.009
$f^{D\rho}(\tau = 0)$, `N-Lept.`	0.60 ± 0.02	0	0	0.001	0	0	0.004
$f(\tau > 0,$ mix)	0.0 (fixed)	–	–	–	–	–	–

Table 8.3: *Results of the simultaneous likelihood fit to the $B \to D^{\mp}\pi^{\pm}$, $B \to D^{*\mp}\pi^{\pm}$, and $B \to D^{\mp}\rho^{\pm}$ data samples (background parameters).*

Parameter	Result	Corrl. $a^{D\pi}$	Corrl. $a^{D^*\pi}$	Corrl. $a^{D\rho}$	Corrl. $c_{\rm lep}^{D\pi}$	Corrl. $c_{\rm lep}^{D^*\pi}$	Corrl. $c_{\rm lep}^{D\rho}$
Combinatorial background dilutions (2)							
$\langle D\rangle_{\rm lep}^{D\pi}$, $\tau>0$	0.40 ± 0.16	-0.001	0	0	-0.006	0	0
$\langle D\rangle_{\rm ki}^{D\pi}$, $\tau>0$	0.48 ± 0.10	0.002	0	0	0	0	0
$\langle D\rangle_{\rm kii}^{D\pi}$, $\tau>0$	0.45 ± 0.07	-0.001	0	0	0	0	0
$\langle D\rangle_{\rm kpi}^{D\pi}$, $\tau>0$	0.38 ± 0.10	0.001	0	0	0	0	0
$\langle D\rangle_{\rm pi}^{D\pi}$, $\tau>0$	0.01 ± 0.09	0	0	0	0	0	0
$\langle D\rangle_{\rm oth}^{D\pi}$, $\tau>0$	0.09 ± 0.11	0	0	0	0	0	0
$\langle D\rangle_{\rm lep}^{D^*\pi}$, $\tau>0$	0.08 ± 0.29	0	-0.003	0	0.001	-0.007	0.001
$\langle D\rangle_{\rm ki}^{D^*\pi}$, $\tau>0$	0.41 ± 0.11	0	-0.002	0	0		0
$\langle D\rangle_{\rm kii}^{D^*\pi}$, $\tau>0$	0.57 ± 0.10	0	0.002	0	0		0
$\langle D\rangle_{\rm kpi}^{D^*\pi}$, $\tau>0$	0.47 ± 0.13	0	-0.001	0	0		0
$\langle D\rangle_{\rm pi}^{D^*\pi}$, $\tau>0$	0.12 ± 0.14	0	0.001	0	0		0
$\langle D\rangle_{\rm oth}^{D^*\pi}$, $\tau>0$	0.09 ± 0.15	0	0	0	0		0
$\langle D\rangle_{\rm lep}^{D\rho}$, $\tau>0$	0.35 ± 0.12	0	0	0.005	0.001	0.001	0.018
$\langle D\rangle_{\rm ki}^{D\rho}$, $\tau>0$	0.39 ± 0.09	0.001	0	-0.005	0		0
$\langle D\rangle_{\rm kii}^{D\rho}$, $\tau>0$	0.10 ± 0.07	0	0	-0.001	0		0
$\langle D\rangle_{\rm kpi}^{D\rho}$, $\tau>0$	0.09 ± 0.08	0	0	0.003	0		0
$\langle D\rangle_{\rm pi}^{D\rho}$, $\tau>0$	0.14 ± 0.08	0	0	0	0		0
$\langle D\rangle_{\rm oth}^{D\rho}$, $\tau>0$	0.04 ± 0.09	0	0	0	0		0
Peaking background lifetimes and fractions							
τ, peak. bkg. (ps)	1.668 (fixed)	–	–	–	–	–	–
$f_{pb}^{D\pi}$ bkg. (%)	2.9 (fixed)	–	–	–	–	–	–
$f_{pb}^{D^*\pi}$ bkg. (%)	2.2 (fixed)	–	–	–	–	–	–
$f_{pb}^{D\rho}$ bkg. (%)	2.6 (fixed)	–	–	–	–	–	–
$f_{pb}^{D\pi}(B^0)$ (%)	57.0 (fixed)	–	–	–	–	–	–
$f_{pb}^{D^*\pi}(B^0)$ (%)	47.0 (fixed)	–	–	–	–	–	–
$f_{pb}^{D\rho}(B^0)$ (%)	50.0 (fixed)	–	–	–	–	–	–
B^+ Peaking background dilutions (B^0 p.b. dilutions have been fixed to signal values)							
$\langle D_0\rangle$, `Lepton`	0.9708 (fixed)	–	–	–	–	–	–
$\langle D_0\rangle$, `Kaon I`	0.9018 (fixed)	–	–	–	–	–	–
$\langle D_0\rangle$, `Kaon II`	0.7666 (fixed)	–	–	–	–	–	–
$\langle D_0\rangle$, `K-Pi`	0.6179 (fixed)	–	–	–	–	–	–
$\langle D_0\rangle$, `Pi`	0.3621 (fixed)	–	–	–	–	–	–
$\langle D_0\rangle$, `Other`	0.1724 (fixed)	–	–	–	–	–	–
ΔD, `Lepton`	-0.0116 (fixed)	–	–	–	–	–	–
ΔD, `Kaon I`	0.0305 (fixed)	–	–	–	–	–	–
ΔD, `Kaon II`	-0.0028 (fixed)	–	–	–	–	–	–
ΔD, `K-Pi`	0.0250 (fixed)	–	–	–	–	–	–
ΔD, `Pi`	-0.0985 (fixed)	–	–	–	–	–	–
ΔD, `Other`	-0.1047 (fixed)	–	–	–	–	–	–
D slope	0.0 (fixed)	–	–	–	–	–	–
Peaking background resolution parameters have been fixed to signal values							

Table 8.4: *Results of the simultaneous likelihood fit to the $B\to D^{\mp}\pi^{\pm}$, $B\to D^{*\mp}\pi^{\pm}$, and $B\to D^{\mp}\rho^{\pm}$ data samples (background parameters).*

Parameter	Fit (stat. error)	Global correlation (%)
$a^{D\pi}$	-0.010 ± 0.023	19
$a^{D^*\pi}$	-0.040 ± 0.023	23
$a^{D\rho}$	-0.024 ± 0.031	14
$c_{\rm lep}^{D\pi}$	-0.033 ± 0.042	30
$c_{\rm lep}^{D^*\pi}$	$+0.049 \pm 0.042$	31
$c_{\rm lep}^{D\rho}$	-0.098 ± 0.055	27

Table 8.5: *Summary of fit variables used for the extraction of* $\sin(2\beta+\gamma)$.

Category	$N^{\rm sig}$	ϵ (%)	$\langle w \rangle$ (%)	Δw (%)	Q (%)
`Lepton`	4288 ± 66	8.7 ± 0.1	3.8 ± 0.5	-1.1 ± 0.9	7.4 ± 0.2
`Kaon I`	5430 ± 77	11.0 ± 0.1	4.7 ± 0.6	-0.5 ± 1.0	9.0 ± 0.2
`Kaon II`	8408 ± 97	17.0 ± 0.2	16.1 ± 0.6	-0.8 ± 1.2	7.8 ± 0.3
`K-Pi`	6763 ± 87	13.7 ± 0.2	24.1 ± 0.8	-1.3 ± 0.9	3.7 ± 0.2
`Pion`	7113 ± 90	14.4 ± 0.2	31.9 ± 0.8	4.2 ± 1.5	1.9 ± 0.2
`Other`	4825 ± 74	9.8 ± 0.1	41.3 ± 1.0	6.7 ± 1.2	0.3 ± 0.1
Total	49368 ± 220	74.6 ± 0.2			30.1 ± 0.5

Table 8.6: *Tagging performance on data signal events.*

signal events. The signal yields per tagging category have been repeated in Table 8.6. With the m_{ES} fit like in Section 4.4, the nominal data set, this time including the untagged events, is determined to contain $49,368 \pm 220$ signal events (which equals the denominator of Eq. (8.3)), resulting in the tagging efficiencies listed in Table 8.6.

The average mistag fraction $\langle w \rangle_i$ and difference Δw_i for B^0 and $\overline{B}^0$ tags are related to the dilution parameters $\langle D \rangle_i$ and ΔD_i in Section 6.2.2. The numbers listed in Table 8.6 have not been converted from the dilutions found in Table 8.2. They are obtained from the nominal fit to data with the dilution slope parameters, D slope, fixed to zero. This to make sure that the dilution parameter are averaged over $\sigma_{\Delta t}$, as in the historical definition of Q. (See Section 4.3.4 for the dependence of $\langle D \rangle_i$ on $\sigma_{\Delta t}$.)

Using the numbers in Table 8.6, the effective tagging power Q is found to be $30.1 \pm 0.5\%$ for this analysis. The mistag probabilities, efficiencies, and performance are consistent with those found using fully simulated Monte Carlo events.

Notice that about 75% percent of all selected B candidates is assigned a flavor tag. The `Lepton` tag category has the smallest mistag fraction, as expected. The kaon categories have the highest tagging efficiencies and, as a consequence, the highest Q values. The remaining categories show a difference in the mistag fractions for B^0 and $\overline{B}^0$ mesons. This can be explained due to the different interaction cross sections of K^+ and K^- mesons with the detector material, or different reconstruction efficiencies for negative and positive soft pions.

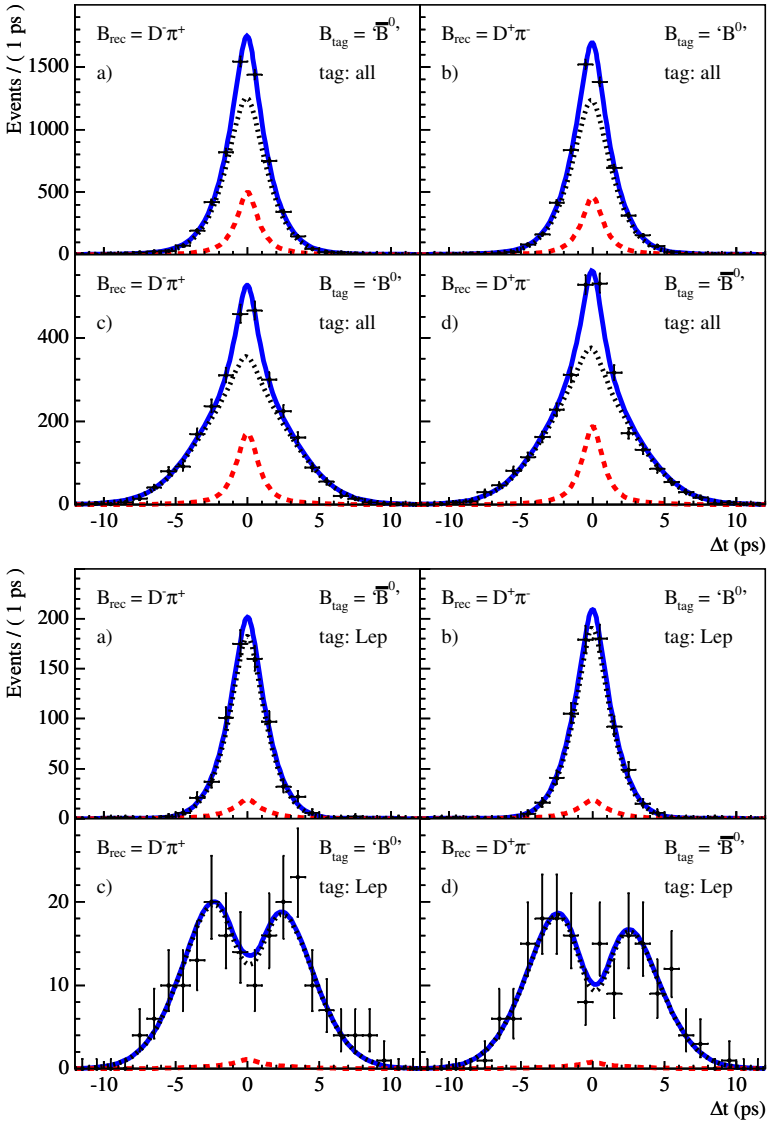

Figure 8.1: *Distributions of Δt for $B^0 \to D^{\pm}\pi^{\mp}$ candidates split by B tagging flavor and reconstructed final state. The top four plots show candidates in all tagging categories, and the bottom four plots show candidates tagged with leptons only. The solid curves are fit projections. The background contributions are represented by the dashed curves, and the signal contributions by the dotted curves.*

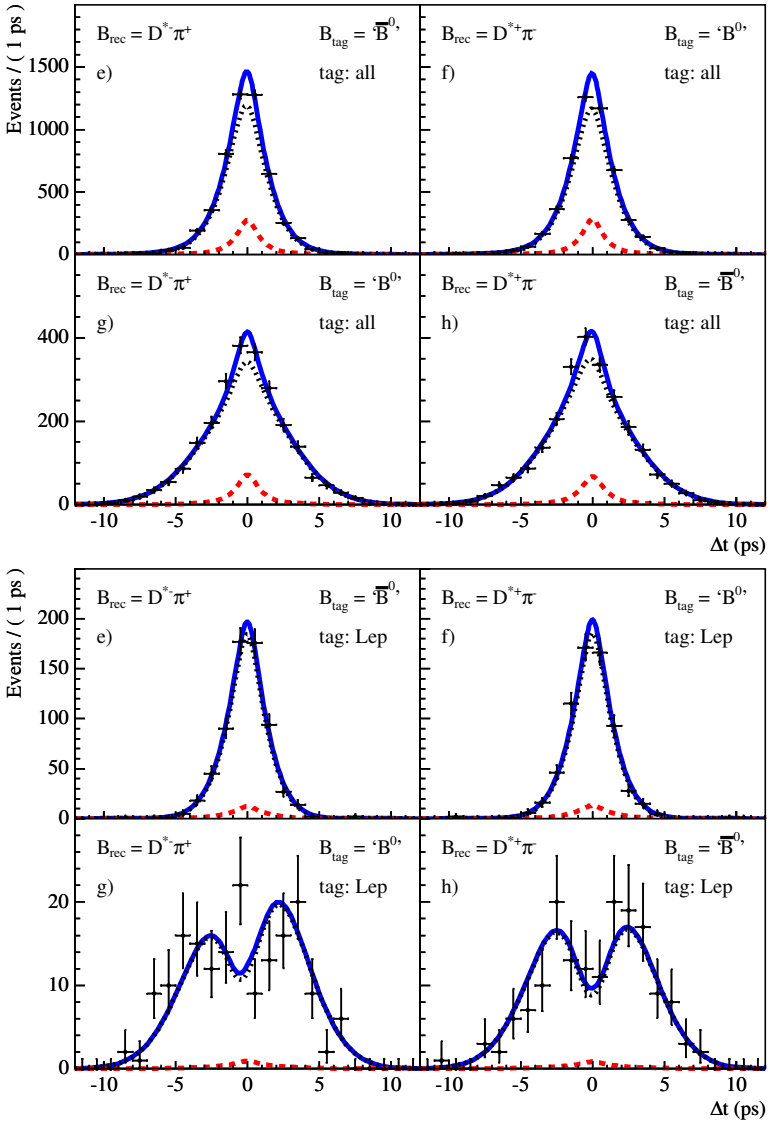

Figure 8.2: *Distributions of Δt for $B^0 \to D^{*\pm}\pi^{\mp}$ candidates split by B tagging flavor and reconstructed final state. The top four plots show candidates in all tagging categories, and the bot-tow four plots show candidates tagged with leptons only. The solid curves are fit projections. The background contributions are represented by the dashed curves, and the signal contributions by the dotted curves.*

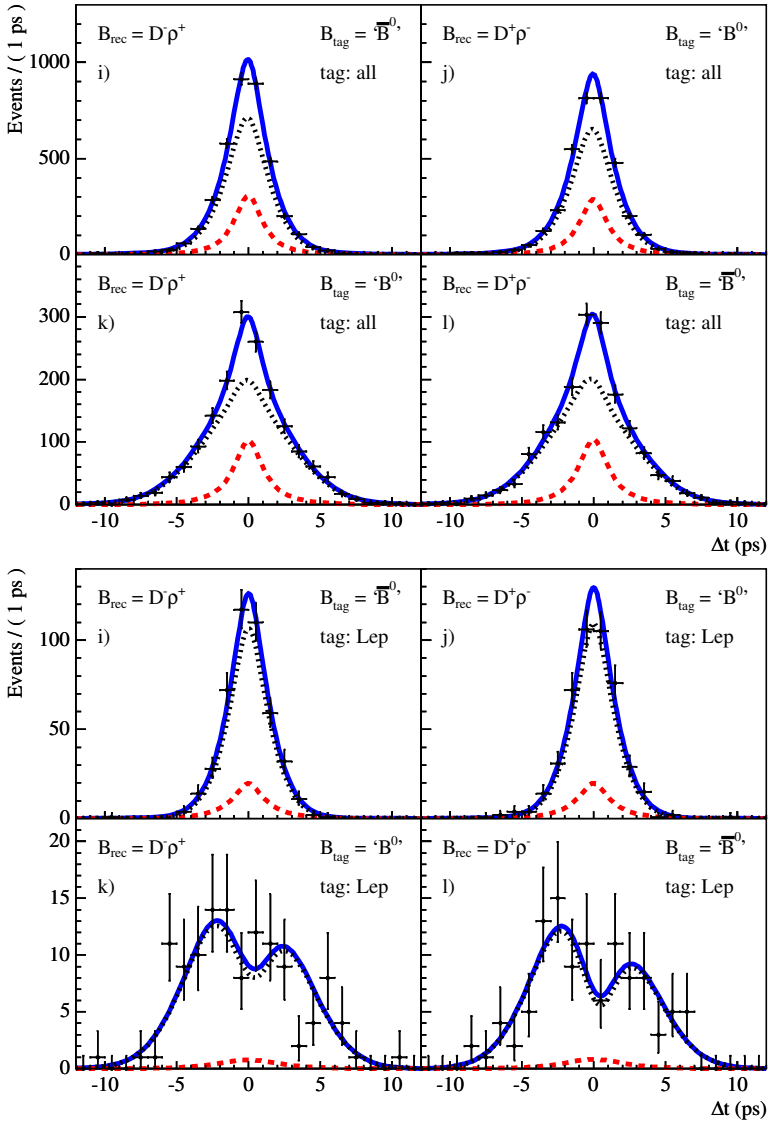

Figure 8.3: *Distributions of Δt for $B^0 \to D^{\pm}\rho^{\mp}$ candidates split by B tagging flavor and reconstructed final state. The top four plots show candidates in all tagging categories, and the bot-tow four plots show candidates tagged with leptons only. The solid curves are fit projections. The background contributions are represented by the dashed curves, and the signal contributions by the dotted curves.*

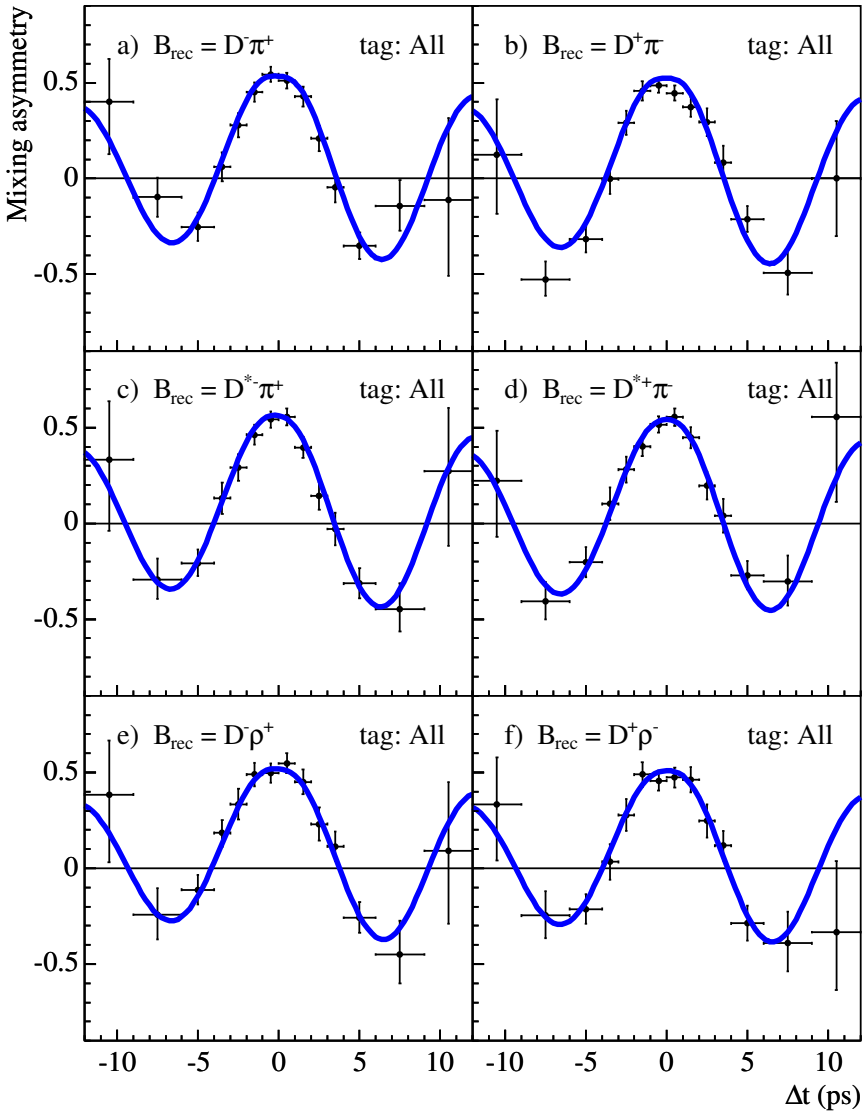

Figure 8.4: *The Δt mixing asymmetries for, from top to bottom, $B^0 \to D^{\pm}\pi^{\mp}$, $B^0 \to D^{*\pm}\pi^{\mp}$, and $B^0 \to D^{\pm}\rho^{\mp}$ events in the signal box, split by reconstructed final state. The solid curves are fit projections. All tagging categories have been lumped together.*

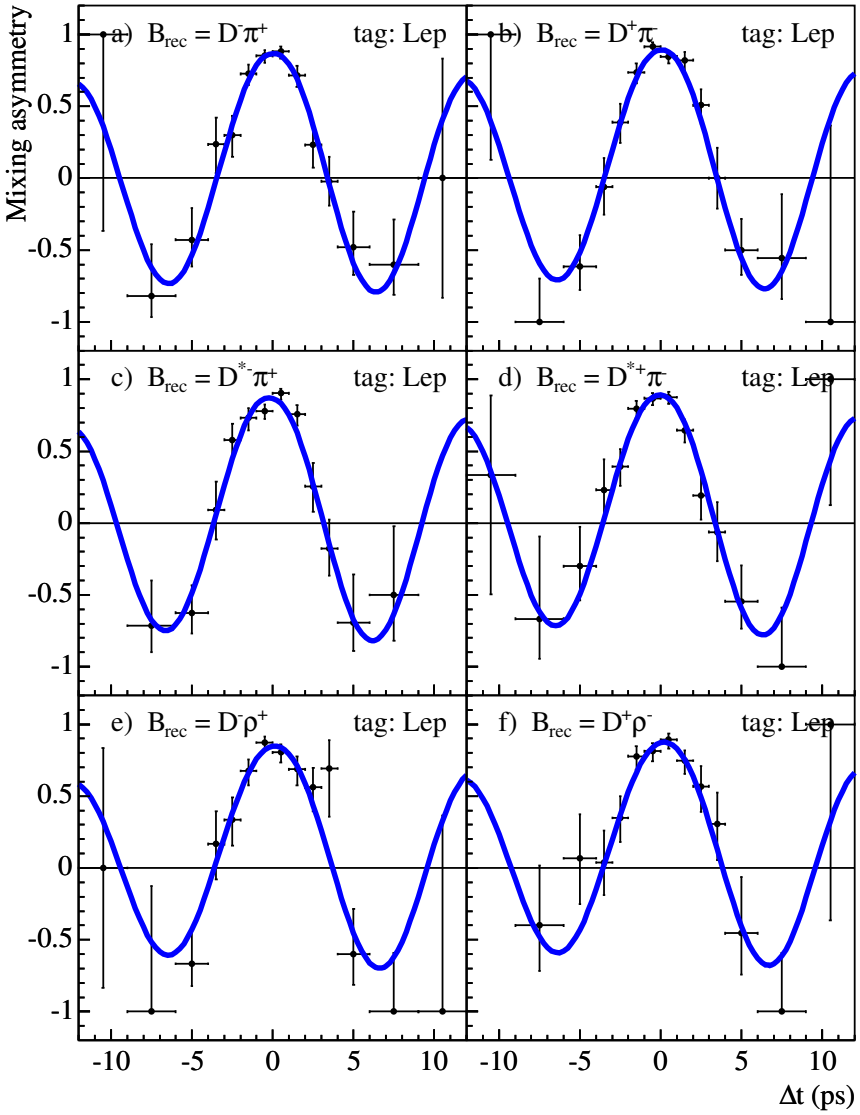

Figure 8.5: *The Δt mixing asymmetries for, from top to bottom, $B^0 \to D^{\pm}\pi^{\mp}$, $B^0 \to D^{*\pm}\pi^{\mp}$, and $B^0 \to D^{\pm}\rho^{\mp}$ signal events in the tagging category, split by reconstructed final state. The solid curves are fit projections.*

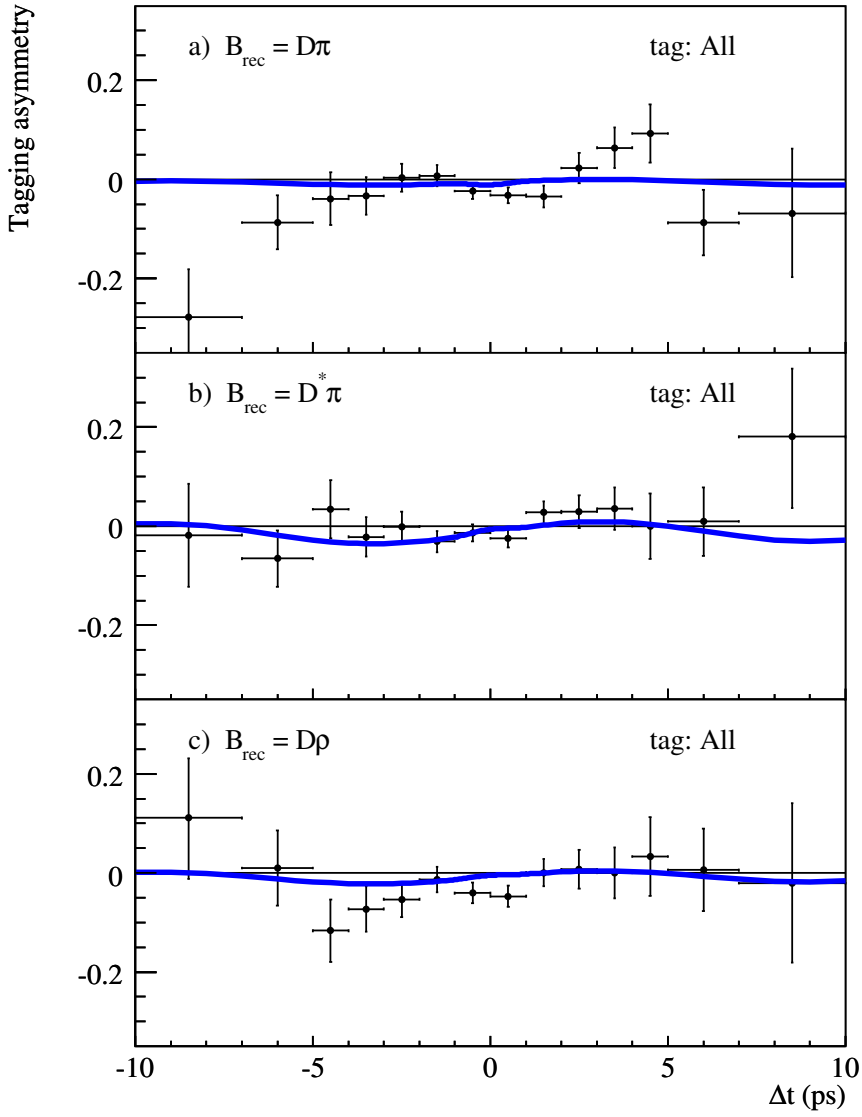

Figure 8.6: *The Δt tagging asymmetries for, from top to bottom, $B^0 \to D^{\pm}\pi^{\mp}$, $B^0 \to D^{*\pm}\pi^{\mp}$, and $B^0 \to D^{\pm}\rho^{\mp}$ events in the signal box. All tagging categories are shown together. The solid curves are fit projections.*

Chapter 9

Evaluation of systematic uncertainties

Potential sources of systematic uncertainties in the measured *CP* asymmetries can be roughly grouped into several categories:

1. the signal parametrization and assumptions in the analysis technique (section 9.1),
2. the background description (section 9.2),
3. uncertainties in determination of the decay-time difference (section 9.3),
4. externally fixed parameters (section 9.4), and
5. Monte Carlo corrections (section 9.5).

All contributions are summarized in Section 9.6.

Systematic uncertainties are determined from data or from samples of simulated events.

9.1 Signal parametrization

The parametrization of the signal Δt distribution is discussed in Chapter 6. In this Section the description of the Δt signal resolution model is varied. Next, the analysis technique assumes common Δt resolution functions and a similar performance of the flavor-tagging algorithm between the $D\pi$, $D^*\pi$, and $D\rho$ samples, and equal tagging and reconstruction efficiencies for B^0 and $\overline{B}^0$ decays. The systematic effects due to these assumptions are estimated in this Section.

9.1.1 Common Δt resolution function

The triple-Gaussian Δt resolution model and its parameters have been described in Section 4.3.3. In the nominal fit, the same set of Δt resolution function parameters is used to fit the $D\pi$, $D^*\pi$, and $D\rho$ samples. The assumption of a common Δt resolution function has been tested using fully-simulated Monte Carlo events (section 3.5), on which we perform the fit with a single set and with three separate sets of resolution function parameters. The shifts in the *CP* parameters are listed in Table 9.1.

Variation	$\delta a^{D\pi}$	$\delta a^{D^*\pi}$	$\delta a^{D\rho}$	$\delta c_{\rm lep}^{D\pi}$	$\delta c_{\rm lep}^{D^*\pi}$	$\delta c_{\rm lep}^{D\rho}$
Different reso.	-0.0004	$+0.0002$	-0.0001	$+0.0001$	$+0.0002$	0
Syst. Error	0.0004	0.0002	0.0001	0.0001	0.0002	0

Table 9.1: *Shifts in the a and $c_{\rm lep}$ parameters observed when using separate sets of resolution function parameters in $D\pi$, $D^*\pi$, and $D\rho$ simulated events.*

9.1.2 Fixed Δt signal resolution function parameters

All resolution function parameters, discussed in Section 4.3.3, are left free in the fit to data, except for the mean and width of the outlier resolution component. The systematic contributions of the fixed outlier component are obtained by separately varying these parameters and repeating the fit. The width (bias) of the outlier Gaussian is conservatively varied by 4.0 (2.0) ps around is nominal values of 8.0 (0.0) ps. These values and variations are large compared with the B^0 lifetime (≈ 1.5 ps) and the maximum $\sigma_{\Delta t}$ value allowed (2.5 ps). The observed differences are shown in Table 9.2. The two variations are considered uncorrelated, and the biggest shifts are added in quadrature to assign the final systematic uncertainties.

Width / bias (ps)	$\delta a^{D\pi}$	$\delta a^{D^*\pi}$	$\delta a^{D\rho}$	$\delta c_{\rm lep}^{D\pi}$	$\delta c_{\rm lep}^{D^*\pi}$	$\delta c_{\rm lep}^{D\rho}$
4.0/0.0	$+0.0005$	$+0.0003$	$+0.0011$	$+0.0016$	$+0.0037$	$+0.0039$
12.0/0.0	$+0.0002$	0	0	0	$+0.0006$	$+0.0001$
8.0/$-$2.0	0	0	-0.0004	$+0.0015$	$+0.0017$	$+0.0009$
8.0/$+$2.0	$+0.0003$	0	$+0.0003$	-0.0011	-0.0008	-0.0004
Syst. Error	0.0006	0.0003	0.0013	0.0022	0.0041	0.0040

Table 9.2: *Systematic uncertainties in the a and $c_{\rm lep}$ parameters due to the fixed parameters used in the triple Gaussian resolution function. The largest contributions have been added in quadrature to obtain the assigned systematic uncertainties.*

9.1.3 Signal Δt resolution model

By default, the common Δt resolution function used to describe the signal components of the data sample is the triple-Gaussian model, as discussed in Section 4.3.3. To evaluate the sensitivity to the choice of this description, the data fit is repeated with an alternative model called `GExp` [68]

$$\texttt{GExp}(\delta_t;\mu,\sigma,\tau,f_t,f_o) = (1-f_t-f_o)\,G(\mu,\sigma) + f_t\,G(0\,\text{ps},\sigma)\otimes e^{\delta_t/\tau} + f_o\,G(0\,\text{ps},8\,\text{ps})\,, \quad (9.1)$$

with $\delta_t \equiv \Delta t_{\rm meas} - \Delta t_{\rm true}$, and $G(\mu,\sigma)$ is a Gaussian with mean μ and width σ.

Like the triple-Gaussian model, the `GExp` model consists of a core and outlier Gaussian. To account for biases from charm decays, the tail Gaussian is convoluted with a one-sided exponential, having an effective lifetime τ. The tail fraction f_t is taken to be different for each tagging category.

The shifts in *CP* parameters between the nominal triple-Gaussian and `GExp` models are shown in Table 9.3, and are assigned as systematic uncertainties.

Variation	$\delta a^{D\pi}$	$\delta a^{D^*\pi}$	$\delta a^{D\rho}$	$\delta c_{\rm lep}^{D\pi}$	$\delta c_{\rm lep}^{D^*\pi}$	$\delta c_{\rm lep}^{D\rho}$
`GExp`	$+0.0005$	$+0.0003$	-0.0004	-0.0017	-0.0014	-0.0020
Syst. Error	0.0005	0.0003	0.0004	0.0017	0.0014	0.0020

Table 9.3: *Systematic uncertainties in a and $c_{\rm lep}$ parameters due to model dependency of the Δt signal resolution. Differences in CP asymmetries are listed when using the `GExp` model instead of the triple-Gaussian.*

Variation	$\delta a^{D\pi}$	$\delta a^{D^*\pi}$	$\delta a^{D\rho}$	$\delta c_{\rm lep}^{D\pi}$	$\delta c_{\rm lep}^{D^*\pi}$	$\delta c_{\rm lep}^{D\rho}$
Art Effect	$+0.0004$	-0.0011	-0.0002	$+0.0011$	$+0.0012$	-0.0010
Syst. Error	0.0004	0.0011	0.0002	0.0011	0.0012	0.0010

Table 9.4: *Systematic uncertainties in the a and $c_{\rm lep}$ parameters due to Δt resolution differences for true-tag and mis-tag events.*

9.1.4 Δt resolution functions for correctly and incorrectly tagged events

In the analysis a common Δt resolution function has been applied for all signal events. Different resolution functions can apply to correctly (true-tag) and incorrectly (mis-tag) tagged events, the so-called 'Art-effect'. For example, B decays in the lepton tagging category may have a larger bias in Δt when tagged by secondary leptons (with opposite charge) from cascade charm decays. The effect of resolution differences between the two subsets has been estimated using simulated events.

To do so, the available signal Monta Carlo sample (section 3.5) has been split into true-tag and mis-tag events using Monte Carlo truth information, and the Δt resolution function parameters of the entire sample and both sub-samples have been determined by fitting the appropriate residual $\delta_t \equiv \Delta t_{\rm meas} - \Delta t_{\rm true}$ distributions.

Next, a toy Monte Carlo study has been performed with 600 toy Monte Carlo samples, having the generated *CP* parameters $a = 0.04$ and $b, c = 0.00$. Of these, 300 samples are generated with the common resolution parameter set for all the events, as obtained from the fully simulated events, and the other 300 samples have been generated with the different resolution parameter sets for correctly and incorrectly tagged events. All samples have been fitted using a common Δt resolution function. Table 9.4 shows the average differences in the a and $c_{\rm lep}$ parameters obtained in the two cases. The observed differences in Table 9.4 have been assigned as systematic uncertainties.

9.1.5 Common dilutions and dilution differences

In the fit to data, the same set of dilution, dilution difference, and dilution slope parameters (see Section 6.2.2) has been used to fit the $D\pi$, $D^*\pi$, and $D\rho$ samples. A source of systematic uncertainties comes from possible differences in these parameter sets between the three data samples. The effect of assuming common dilutions, dilution differences, and dilution slopes has been evaluated on the sample of fully-simulated Monte Carlo events, presented in Section 3.5, performing the fit with a single set of dilutions and with three separate sets of dilutions. The

Variation	$\delta a^{D\pi}$	$\delta a^{D^*\pi}$	$\delta a^{D\rho}$	$\delta c_{\rm lep}^{D\pi}$	$\delta c_{\rm lep}^{D^*\pi}$	$\delta c_{\rm lep}^{D\rho}$
Diff. dilutions	+0.0001	+0.0001	−0.0005	+0.0006	+0.0002	+0.0005
Syst. Error	0.0001	0.0001	0.0005	0.0006	0.0002	0.0005

Table 9.5: *Systematic uncertainties in a and $c_{\rm lep}$ from the assumption of common dilutions, dilution differences, and dilution slopes as obtained from $D\pi$, $D^*\pi$, and $D\rho$ simulated events.*

Variation	$\delta a^{D\pi}$	$\delta a^{D^*\pi}$	$\delta a^{D\rho}$	$\delta c_{\rm lep}^{D\pi}$	$\delta c_{\rm lep}^{D^*\pi}$	$\delta c_{\rm lep}^{D\rho}$
$\epsilon_{\rm rec}(B^0) > \epsilon_{\rm rec}(\overline{B}^0)$	+0.0002	+0.0001	−0.0002	+0.0004	+0.0001	−0.0002
$\epsilon_{\rm rec}(B^0) < \epsilon_{\rm rec}(\overline{B}^0)$	0	0	+0.0002	−0.0001	+0.0001	0
$\epsilon_{\rm tag}(B^0) > \epsilon_{\rm tag}(\overline{B}^0)$	−0.0006	−0.0003	−0.0001	−0.0009	−0.0007	−0.0004
$\epsilon_{\rm tag}(B^0) < \epsilon_{\rm tag}(\overline{B}^0)$	−0.0001	−0.0001	+0.0002	+0.0002	−0.0003	0
Syst. Error	0.0006	0.0003	0.0003	0.0010	0.0007	0.0004

Table 9.6: *Systematic uncertainties in the a and $c_{\rm lep}$ parameters due to the assumption of equal tagging and reconstruction efficiencies between B^0 and $\overline{B}^0$ decays. The largest contributions have been added in quadrature to obtain the assigned systematic uncertainties.*

observed shifts in *CP* parameters are shown in Table 9.5 and have been assigned as systematic uncertainties.

9.1.6 Different reconstruction and tagging efficiencies for B^0 and $\overline{B}^0$ decays

The nominal fit configuration ignores possible differences in reconstruction and tagging efficiency between B^0 and $\overline{B}^0$ decays, see Section 6.4. Two toy Monte Carlo studies have been performed to test the assumption of equal efficiencies.

First the tagging efficiency ($\epsilon_{\rm tag}$) difference, an estimate of which, 1.3%, is taken from Ref. [76]. A total of 900 Monte Carlo samples have been generated with no *CP* asymmetries, with consecutively: 300 samples having $\epsilon_{\rm tag}(B^0) > \epsilon_{\rm tag}(\bar{B}^0)$ by 1.3%, 300 samples with $\epsilon_{\rm tag}(B^0) < \epsilon_{\rm tag}(\bar{B}^0)$ by 1.3%, and 300 samples with equal tagging efficiencies. The efficiency corrections are applied to both signal and background events.

Second, we perform a similar study for the reconstruction efficiency ($\epsilon_{\rm rec}$) difference. We use a difference of 0.7% [76]. Again, a total of 900 toy Monte Carlo samples have been generated with no *CP* asymmetries, with: 300 samples having $\epsilon_{\rm reco}(B^0) > \epsilon_{\rm reco}(\bar{B}^0)$ by 0.7%, 300 samples with $\epsilon_{\rm reco}(B^0) < \epsilon_{\rm reco}(\bar{B}^0)$ by 0.7%, and 300 samples with equal reconstruction efficiencies. Again, the efficiency difference is applied equally to signal and background events.

All toy samples have been fit with the nominal fit configuration.

For both studies, Table 9.6 shows the average shifts in the a and $c_{\rm lep}$ parameters compared to the equal efficiency cases. The tagging and reconstruction efficiency differences are considered uncorrelated, and the largest shifts observed are added in quadrature to obtain the final systematic uncertainties on the a and $c_{\rm lep}$ parameters.

Variation	$\delta a^{D\pi}$	$\delta a^{D^*\pi}$	$\delta a^{D\rho}$	$\delta c_{\rm lep}^{D\pi}$	$\delta c_{\rm lep}^{D^*\pi}$	$\delta c_{\rm lep}^{D\rho}$
Simultaneous $m_{ES}\otimes\Delta t$ fit	$+0.0002$	$+0.0002$	$+0.0001$	$+0.0004$	$+0.0005$	-0.0003
Syst. Error	0.0002	0.0002	0.0001	0.0004	0.0005	0.0003

Table 9.7: *Systematic uncertainties related to signal probability fluctuations, obtained from running a simultaneous $m_{ES}\otimes\Delta t$ fit.*

Variation	$\delta a^{D\pi}$	$\delta a^{D^*\pi}$	$\delta a^{D\rho}$	$\delta c_{\rm lep}^{D\pi}$	$\delta c_{\rm lep}^{D^*\pi}$	$\delta c_{\rm lep}^{D\rho}$
Floating $E_{\rm beam}$	0	0	-0.0001	0	-0.0002	$+0.0002$
Syst. Error	–	–	0.0001	–	0.0002	0.0002

Table 9.8: *Systematic uncertainties on the a and $c_{\rm lep}$ parameters from the fixed end point $E_{\rm beam}$ in the description of the m_{ES} spectrum.*

9.2 Background description

The choice of the emperical description of the Δt distribution of background events, discussed in Chapter 6, is a possible source of systematic effects. In addition, certain background parameters have been fixed in the fit to data, either because they are extracted from independent fits, for example fits to the m_{ES} distribution, or they have been evaluated from simulated events. We consider background parameter variations and their impact on the measured *CP* asymmetries.

9.2.1 Signal probability

For reasons of speed the nominal fit has been split in two parts. First the fit to the m_{ES} distributions is performed; its parameters are fixed, and subsequentially the tagged Δt distributions are fitted. Events in the signal region, contributing to the Δt fit, get assigned (non-zero) signal probabilities based on the measured values of m_{ES} and the outcome of the m_{ES} fit. The uncertainty on the m_{ES} fit results, leading to variations in the event-by-event signal probabilities, can affect the observed values for the *CP* asymmetries.

The size of this effect is determined by fitting m_{ES} and Δt simultaneously. The observed shifts in the a and $c_{\rm lep}$ parameters compared with the nominal fit configuration are shown in Table 9.7, and are assigned as systematical uncertainties on the signal probability.

9.2.2 Beam energy $E_{\rm beam}$ in m_{ES} fits

In the m_{ES} fits used to acquire event-by-event signal probabilities, see Section 4.1.3, the center-of-mass beam energy $E_{\rm beam}$ is fixed to 5.291 GeV/c^2, see Eq. (4.11). The $E^*_{\rm beam}$ parameter is known with an uncertainty of about 0.002 GeV/c^2 [36]. Variatons in $E_{\rm beam}$ can change the signal probability and the fitted *CP* amplitudes. The systematic uncertainties on a and $c_{\rm lep}$ are evaluated by floating the beam energy parameter and redoing the m_{ES} fit. Table 9.8 shows the corresponding contributions.

Variation	$\delta a^{D\pi}$	$\delta a^{D^*\pi}$	$\delta a^{D\rho}$	$\delta c_{\rm lep}^{D\pi}$	$\delta c_{\rm lep}^{D^*\pi}$	$\delta c_{\rm lep}^{D\rho}$
Bkg. tail	-0.0001	0	-0.0001	0	0	-0.0001
Syst. Error	0.0001	–	0.0001	–	–	0.0001

Table 9.9: *Shifts observed in the a and $c_{\rm lep}$ parameters when including a tail Gaussian in the background Δt resolution model.*

Variation	$\delta a^{D\pi}$	$\delta a^{D^*\pi}$	$\delta a^{D\rho}$	$\delta c_{\rm lep}^{D\pi}$	$\delta c_{\rm lep}^{D^*\pi}$	$\delta c_{\rm lep}^{D\rho}$
total fraction	0	±0.0002	±0.0001	±0.0001	±0.0004	±0.0006
relative fraction B^+/B^0	0	±0.0001	0	±0.0002	0	±0.0002
Syst. Error	–	0.0002	0.0001	0.0002	0.0004	0.0006

Table 9.10: *Variations in a and $c_{\rm lep}$ from uncertainties in the amount and composition of the peaking background. The shifts been added in quadrature to obtain the systematic uncertainties.*

9.2.3 Background Δt resolution model

The background Δt resolution function employed in the nominal fit is modeled by a double-Gaussian, see Section 6.3.1. Compared to the signal Δt resolution model in Eq. (4.18), it has a core and outlier component, but no tail. As a systematic check, we include a tail Gaussian for the background events and redo the fit. The systematic differences are given in Table 9.9.

9.2.4 Fraction and composition of peaking background

In the fit to data, the fractions of peaking background for the $D^{(*)}\pi$ and $D\rho$ samples have been fixed to the values found in Section 4.1.4 (see Table 4.4). The relative fractions of B^+ and B^0 decays in the peaking background are fixed as well, also estimated from simulated events. To account for the uncertainties in these values, in the nominal fit the total peaking background fractions have been varied conservatively by 1%, and the relative fractions are varied by 10%. The largest contributions are shown in Table 9.10. The shifts been added in quadrature to obtain the assigned systematic uncertainties on a and $c_{\rm lep}$.

9.2.5 *CP* content of combinatorial background

The emperical description of the Δt distribution for the background has been discussed in Section 6.3. In the nominal parametrization, there are no *CP*-violating effects in the combinatorial background. To evaluate the validity of this assumption, the background model is modified to include sine mixing terms, with the same a, b, c parametrization as used in the Δt distribution for signal events (Eq. (6.4)).

We vary the corresponding a, b, and c parameters of the combinatorial background with the values 0.06, 0.03, and 0.06 respectively – approximately twice the expected asymmetries in the $D^{(*)}\pi$ samples. The corresponding variations in a and $c_{\rm lep}$ are shown in Table 9.11. To calculate the assigned systematic uncertainties, we add in quadrature the largest deviations for the three sets of variations.

Variation	$\delta a^{D\pi}$	$\delta a^{D^*\pi}$	$\delta a^{D\rho}$	$\delta c_{\rm lep}^{D\pi}$	$\delta c_{\rm lep}^{D^*\pi}$	$\delta c_{\rm lep}^{D\rho}$
CP Argus a	± 0.0009	± 0.0007	± 0.0029	± 0.0001	± 0.0002	± 0.0006
CP Argus b	0	± 0.0001	± 0.0004	0	± 0.0001	± 0.0003
CP Argus c	0	± 0.0001	± 0.0002	± 0.0002	± 0.0001	± 0.0026
Syst. Error	0.0009	0.0007	0.0029	0.0002	0.0002	0.0027

Table 9.11: *Systematic uncertainties on the a and $c_{\rm lep}$ parameters from the assumption of no CP violation in the combinatorial background.*

Variation	$\delta a^{D\pi}$	$\delta a^{D^*\pi}$	$\delta a^{D\rho}$	$\delta c_{\rm lep}^{D\pi}$	$\delta c_{\rm lep}^{D^*\pi}$	$\delta c_{\rm lep}^{D\rho}$
CP Peak a	± 0.0009	± 0.0006	± 0.0007	0	0	0
CP Peak b	± 0.0001	0	± 0.0001	0	0	0
CP Peak c	0	0	0	± 0.0009	± 0.0006	± 0.0007
Syst. Error	0.0009	0.0006	0.0007	0.0009	0.0006	0.0007

Table 9.12: *Systematic uncertainties on the a and $c_{\rm lep}$ parameters from the assumption of no CP violation in the B^0 component of the peaking background.*

9.2.6 *CP* content of peaking background

In the nominal model, no *CP* violation in the B^0 peaking background is assumed, discussed in Section 6.3.2. The effect of potential *CP* content of this background component is estimated with the same *CP*-violating model as used to describe signal events (Eq. (6.4)). We vary the peaking background's a, b, and c parameters with the values 0.06, 0.03, and 0.06, like in Section 9.2.5, and, to calculate the systematical uncertainties, add the largest shift in quadrature for the three sets of variations. The deviations observed in the a and $c_{\rm lep}$ parameters are listed in Table 9.11.

9.2.7 $B \to D^{\mp}\rho'^{\pm}$ and non-resonant $B \to D^{\mp}\pi^{\pm}\pi^0$ background

For the $B \to D^{\mp}\rho^{\pm}$ mode we consider additional sources of background with the same final state $D^{\mp}\pi^{\pm}\pi^0$, where the $\pi^{\pm}\pi^0$ system is not produced through the $\rho^{\pm}$ resonance. Interfering sources of background can introduce a dependence of the $\lambda_{\pm}^{D\rho}$ parameters of Eq. (2.59) on $m_{\pi\pi^0}$. We have studied the dependency using the distribution of $m_{\pi\pi^0}$ in Ref. [81].

The possible background contributions have been evaluated with a data sample of 130273 $B^0 \to D^-\pi^+\pi^0$ candidates, on which the requirements on the ρ helicity and on $m_{\pi\pi^0}$ have been removed. Three interfering components are considered: $B^0 \to D^-\rho^+$ (the signal), $B^0 \to D^-\rho^+(1450)$ with a pole mass of $(1465\pm25)\,\mathrm{MeV}/c^2$ and a width of $(400\pm60)\,\mathrm{MeV}/c^2$ [17] for the ρ^+, both described with P-wave relativistic Breit-Wigner functions [82, 83], and a non-resonant component, $B^0 \to D^-(\pi^+\pi^0)_{nr}$. Contributions from the decay modes $B^0 \to D^{*-}\pi^+$ ($D^{*-} \to D^-\pi^0$) and $B^0 \to \bar{D}^{**0}\pi^0$ ($\bar{D}^{**0} \to D^-\pi^+$) are negligible due to the kinematic constraints imposed on the ρ daughter particles.

We perform a fit to the binned $m_{\pi\pi^0}$ distribution to extract the amplitudes of the three components, where for each bin the combinatorial background has been subtracted, as es-

timated from the corresponding m_{ES} distribution, and the number of peaking background events has been estimated using fully simulated Monte Carlo events. The result of the fit is shown in Fig. 9.1. The fraction of $B^0 \to D^- \rho^+(1450)$ and $B^0 \to D^-(\pi^+\pi^0)_{nr}$ events in the mass window $620 < m_{\pi\pi^0} < 920$ MeV/c^2 is found to be smaller than 0.02 at 90% confidence level (C.L.). This limit is obtained performing 1000 toy Monte Carlo studies, where the measured amplitudes of the three components are varied over their statistical and systematical errors.

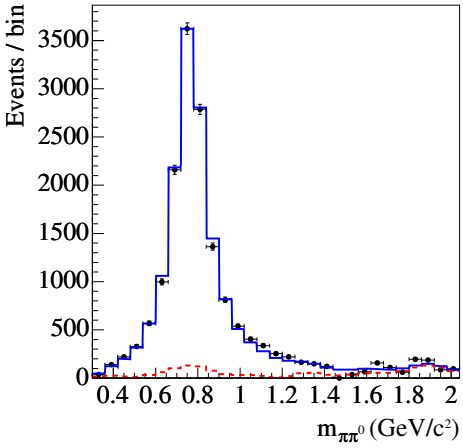

Figure 9.1: *$m_{\pi\pi^0}$ distribution for the combinatorial-background subtracted $B \to D^{\mp}\pi^{\pm}\pi^0$ sample, containing 16214 events. The solid curve is the fit projection, consisting of the three interfering components described in the text and an m_{ES} peaking background contribution, indicated with the dashed line.*

Ignoring higher-order terms, using the notation of Ref. [81] we have

$$\left| \frac{|A_{D\rho'}|^2 + |A_{D\pi\pi^0}|^2 + 2\mathrm{Re}(A_{D\rho}A^*_{D\rho'}) + 2\mathrm{Re}(A_{D\rho}A^*_{D\pi\pi^0}) + 2\mathrm{Re}(A_{D\rho'}A^*_{D\pi\pi^0})}{|A_{D\rho}|^2} \right| < 0.02\,, \quad (9.2)$$

where each CKM-favored amplitude $A_i = a_i e^{i\delta_i}\, L_{\rho\, i}\, g_i(\Omega)$ consists of a complex constant $a_i e^{i\delta_i}$, a Breit-Wigner propagator $L_{\rho\, i}$, and an angular function $g_i(\Omega)$. We integrate over the helicity angles Ω, and in each term the angular cross-product is replaced with an 'integrated angular efficiency'

$$\Phi_{ij} \equiv \int 2\,\varepsilon(\Omega)\,\mathrm{Re}(g_i g_j^*)\,d\Omega\,, \quad (9.3)$$

with the angular efficiency defined as $\varepsilon(\Omega)$. (The factor of 2 is absent for diagonal terms.) In practice the $m_{\pi\pi^0}$ distribution is fit for the constants $a_{D\rho'}$ and $a_{D\pi\pi^0}\cos(\delta_{D\pi\pi^0})$, $a_{D\pi\pi^0}\sin(\delta_{D\pi\pi^0})$. The constant $a_{D\rho}e^{i\delta_i}$ is normalized to one, and the phase difference $\delta_{D\rho'}$ is fixed to π.

Eq. (9.2) is similar to the correction to the amplitude S of the sine mixing term in Eq. (2.58) (again ignoring higher order terms)

$$\Delta S = \frac{2\mathrm{Im}(\frac{q}{p}A'A^*)}{|A|^2}\,, \quad (9.4)$$

	$a^{D\rho}$	$c_{\rm lep}^{D\rho}$
Non-resonant $D\pi\pi^0$	0.0016	0.0016
Syst. Error	0.0016	0.0016

Table 9.13: *Systematic uncertainties due to possible $B \to D^{\mp}\rho'^{\pm}$ and non-resonant $B \to D^{\mp}\pi^{\pm}\pi^0$ background picked up in the $B \to D^{\mp}\rho^{\pm}$ selection.*

as induced by the presence of $B \to D^{\mp}\rho'^{\pm}(1450)$ and non-resonant $B \to D^{\mp}\pi^{\pm}\pi^0$. Here A is the CKM-favored amplitude sum $A_{D\rho} + A_{D\rho'} + A_{D\pi\pi^0}$, where again each term has a lineshape and angular contribution, and A' is the CKM-suppressed amplitude $A'_{D\rho} + A'_{D\rho'} + A'_{D\pi\pi^0}$ with, similarly, $A'_i = a'_i e^{i\delta'_i} L_{\rho\, i}\, g_i(\Omega)$. Note that A_i and A'_i share the same lineshape and angular contributions. Again, angular cross-terms get replaced with the angular efficiencies Φ_{ij} after the angular integration.

Writing a'_i as $r_i \times a_i$, where r_i is the ratio parameter r introduced in Section 2.6 (measured to be < 0.01, but conservatively taken to be 0.02), one sees that Eq. (9.4) is approximately (50/2) times smaller than Eq. (9.2), *i.e.* at the level of 0.0008. This assumes no 'conspiracy' between the the strong phases δ_i, resulting in an unnaturally small limit[1] in Eq. (9.2). Given the uncertainty in r_i, we multiply the limit with a factor of two, and copy the result for both $a^{D\rho}$ and $c_{\rm lep}^{D\rho}$. The biases are found to be at most 0.0016, and are summarized in Table 9.13.

9.3 Uncertainties in determination of the decay-time difference

The decay-time difference Δt is calculated from the boost factor of the $\Upsilon(4S)$ and the spatial distance Δz between the two B decay vertices in an event. Hence, systematic sources in the reconstruction of the decay vertices and the knowledge of the $\Upsilon(4S)$ boost translate to systematic effects on Δt, which result in systematic uncertainties on the measured *CP* asymmetries.

Detector-related sources, not accounted for by the measurement technique, include no perfect knowledge of: the z-scale of the detector, the internal alignment of the SVT wafers, and the position of the interaction point used to constrain vertex fits. Also, we consider quality cuts on Δt and $\sigma_{\Delta t}$ in the evaluation of the systematic uncertainties in the decay-time difference.

9.3.1 Quality cuts on Δt and $\sigma_{\Delta t}$

In the final data sample we only include events with $\Delta t \in [-20, 20]$ ps, as mentioned in Section 4.1.2. This is a very loose requirement considering the B^0 lifetime of ≈ 1.5 ps. Furthermore, we require the uncertainty $\sigma_{\Delta t}$ to be less than 2.5 ps.

These cuts have been varied in the fit to data. The Δt cut has been set to 30 ps and to 10 ps, and the cut on $\sigma_{\Delta t}$ has been set at 2 ps and 3 ps. Table 9.14 summarizes the variations observed in the a and $c_{\rm lep}$ parameters. To obtain the assigned systematic uncertainties, the largest contributions have been added in quadrature.

[1] Any such cancellation should be (largely) undone since the measured coefficients a_i and δ_i are varied to obtain the upper limit on the fraction of interfering background.

Variation	$\delta a^{D\pi}$	$\delta a^{D^*\pi}$	$\delta a^{D\rho}$	$\delta c_{\rm lep}^{D\pi}$	$\delta c_{\rm lep}^{D^*\pi}$	$\delta c_{\rm lep}^{D\rho}$
$\lvert\Delta t\rvert < 30$ ps	0	+0.0005	+0.0005	+0.0023	+0.0023	+0.0016
$\lvert\Delta t\rvert < 10$ ps	−0.0017	+0.0005	+0.0009	+0.0010	+0.0009	+0.0009
$\sigma(\Delta t) < 3$ ps	0	−0.0001	0	0	+0.0001	0
$\sigma(\Delta t) < 2$ ps	−0.0004	−0.0005	−0.0013	0.0001	+0.0007	−0.0014
Syst. Error	0.0017	0.0007	0.0016	0.0023	0.0024	0.0021

Table 9.14: *Changes in a and $c_{\rm lep}$ when varying the cuts on Δt and $\sigma_{\Delta t}$.*

9.3.2 Beam spot position

For each run of data, the average position of the luminous region (beam spot) is computed every 10 minutes, using $e^+e^- \to e^+e^-$ and $e^+e^- \to \mu^+\mu^-$ events (see Section 3.2). The Δt vertex algorithm uses the position of the beam spot as a geometrical constraint in reconstructing the $B_{\rm rec}$ and $B_{\rm tag}$ decay vertices. The strongest constraint comes from the vertical position of the beam spot, the determination of which has a precision better than 1 μm. The actual beam spot size in y is 4 μm, and the amount of random walk in consecutive beam spot measurements is approximately 8 μm [39]. As a result, the production vertex is constrained to average y position, assuming a size of 10 μm.

Two effects have been considered to evaluate the sensitivity of our measurement to the beam spot position.

1. In the computation of Δt on data, the measured y position has been varied by 20 μm.

2. The assumed width of the beam spot in y is doubled to 20 μm, and is set to the actual tracking resolution of (typically) 35μm.

The processing of the data sample is redone for each of these configurations. To avoid changes in a and $c_{\rm lep}$ due to events entering or leaving the sample, we restrict the analysis to the overlapping events in all reprocessed sets, including the nominal data set.

For each reprocessed sample we perform the nominal fit. The resulting differences with the nominal beam spot scenario are shown in Table 9.15. Note that the largest shifts are seen in the *CP* asymmetries of the $D^*\pi$ sample, where the beam spot position is also used as an additional geometric contraint on the origin of the soft pion in the computation of the D^{*-} vertex, as explained in Section 4.1.2.

As systematic uncertainties on the a and $c_{\rm lep}$ parameters due to the uncertainty in the y position of the interaction point, we take the average of the +20 μm and −20 μm variations, and add that in quadrature to the average of the variations in width.

9.3.3 SVT alignment and boost uncertainty

Reconstruction of the B-decay vertices, and so the distance Δz, relies on accurate tracking of charges particles. For particles originating from the beam spot, the measurements of trajectory parameters are heavily dependent on the silicon vertex tracker (see Section 3.3.1), and in particular on the relative positions of its silicon strips and wafers – referred to as the SVT local alignment. So-called 'misalignment' occurs when the particle hits and tracks are reconstructed using incorrect positions and/or orientations of the sensors.

Variation	$\delta a^{D\pi}$	$\delta a^{D^*\pi}$	$\delta a^{D\rho}$	$\delta c_{\rm lep}^{D\pi}$	$\delta c_{\rm lep}^{D^*\pi}$	$\delta c_{\rm lep}^{D\rho}$
$y + 20\,\mu$m	-0.0038	-0.0058	-0.0074	-0.0019	-0.0028	$+0.0030$
$y - 20\,\mu$m	-0.0013	-0.0055	-0.0001	-0.0032	$+0.0124$	$+0.0098$
absolute average	0.0026	0.0058	0.0038	0.0026	0.0076	0.0064
$\sigma(y) = 20\ \mu$m	-0.0011	-0.0064	0	-0.0048	$+0.0116$	$+0.0113$
$\sigma(y) =$ tracking reso.	$+0.0018$	-0.0045	-0.0029	-0.0034	$+0.0002$	-0.0048
absolute average	0.0015	0.0055	0.0015	0.0041	0.0059	0.0081
Syst. Error	0.0029	0.0079	0.0040	0.0049	0.0096	0.0103

Table 9.15: *Systematic uncertainties in a and $c_{\rm lep}$ from the uncertainty in the position of the beam spot. The systematic error comes from the variation of the y position, and from increasing $\sigma(y)$ to $20\,\mu$m and to the tracking resolution (about $35\,\mu$m), all compared with the nominal beam spot measurement.*

The local alignment of the SVT is determined amongst others from $e^+e^- \to \mu^+\mu^-$ events by studying the tracks' impact parameters d_0 and z_0 (see Table 3.5) as a function of azimuthal angle ϕ_0 [84]. The actual positions of wafers are expressed in terms of rotations and translations with respect to the 'perfect' alignment set, where all wafers are at their nominal positions.

The effect of systematic uncertainties in the local alignment has been modeled using the simulated signal events, by default reconstructed using the perfect alignment set. Four realistic deformation scenarios of the SVT have been tested to evaluate the systematical errors from the uncertainty of the positions of the SVT wafers [84]. The simulated events are reprocessed for each of these misalignment scenarios, and for each we perform the nominal fit.

A boost misalignment SVT scenario is also tested, like in the paragraph above, to estimate the uncertainty in the knowledge of the boost on the measured *CP* asymmetries. Uncertainty in the boost affects the measurement of Δt direclty throught the relation $\Delta z = \beta\gamma\, c\Delta t$. At *BABAR*, the $\Upsilon(4S)$ boost is known with a relative uncertainty of 0.1%, based on the PEP-II knowledge of the beam energies [36].

In the reprocessing a small number of events ($< 1\%$) come into or fall out of the analysis sample due to the changes in the alignment or the boost. To avoid statistical changes in a and $c_{\rm lep}$, we restrict the analysis to overlapping events that pass all cuts in all of the sets, including the perfect alignment. About 325k of signal Monte Carlo events remain, or $\approx 18 times$ the amount of data.

The results of the misaligned samples are compared with the results for a and $c_{\rm lep}$ with no misalignment reconstruction. The misalignment model that gives the largest shift determines the final systematic error. These numbers we add in quadrature to the 'boost' misalignment. Fit results are summarized in Table 9.16.

9.3.4 Uncertainty in the z-scale

Uncertainties in the z-scale directly affect measurements of Δt through the (approximate) relation $\Delta z = \beta\gamma\, c\Delta t$. The z-scale in *BABAR* is quantified by reconstructing the beam pipe length with positrons and electrons interacting with the beam pipe wall; a relative uncertainty of 0.6% is assigned to the evaluation of this measurement [85]. The effect of the uncertainty on the boost has been evaluated in data through scaling the measured values of Δt and $\sigma_{\Delta t}$

Variation	$\delta a^{D\pi}$	$\delta a^{D^*\pi}$	$\delta a^{D\rho}$	$\delta c_{\rm lep}^{D\pi}$	$\delta c_{\rm lep}^{D^*\pi}$	$\delta c_{\rm lep}^{D\rho}$
Misalignment 'SVT1-4'	+0.0011	−0.0007	−0.0010	+0.0018	−0.0035	−0.0009
Boost	+0.0004	+0.0006	−0.0005	−0.0007	+0.0004	−0.0005
Syst. Error	0.0013	0.0009	0.0011	0.0019	0.0035	0.0010

Table 9.16: *Systematic uncertainties in a and $c_{\rm lep}$ as determined from recommended SVT misalignment and boost scenarios.*

Variation	$\delta a^{D\pi}$	$\delta a^{D^*\pi}$	$\delta a^{D\rho}$	$\delta c_{\rm lep}^{D\pi}$	$\delta c_{\rm lep}^{D^*\pi}$	$\delta c_{\rm lep}^{D\rho}$
z scale +0.6%	+0.0003	−0.0001	0	−0.0003	−0.0004	−0.0004
z scale −0.6%	−0.0003	+0.0003	+0.0001	+0.0004	+0.0003	+0.0005
Syst. Error	0.0003	0.0003	0.0001	0.0004	0.0004	0.0005

Table 9.17: *Systematic uncertainties on a and $c_{\rm lep}$ from uncertainties in the z-scale.*

up and down by 0.6%, and repeating the nominal fit.

The variations seen in a and $c_{\rm lep}$ are shown in Table 9.17. The largest shifts are taken as the final systematic uncertainties.

9.4 External parameters

In the nominal fit to data the mixing frequency Δm_d and the B^0 lifetime τ_{B^0} have been fixed to the world average values of $\Delta m_d = 0.502 \pm 0.007$ ps^{-1} and $\tau_B^0 = 1.536 \pm 0.014$ ps [17]. The fit to data is repeated varying these parameters with 1σ, and also by leaving the parameters free, seperately. The latter fit scenarios have been discussed in Section 7.7. The variations in a and $c_{\rm lep}$ are summarized in Table 9.18. For both parameter variations, the systematic uncertainties are conservatively assigned to come from the 'floating' fit cases on data.

As discussed in Section 9.18, we have floated the mixing frequency Δm_d and the B^0 lifetime τ_{B^0} simultaneously on the sample of simulated events, which has generated values of 0.489 ps^{-1} and 1.541 ps respectively. The observed differences in a and $c_{\rm lep}$ compared with the non-floating case are also shown in Table 9.18. The correlations of Δm_d and τ_{B^0} with the a and $c_{\rm lep}$ parameters are found to be small, as already shown in Table 7.8, and thus have little to no impact on the measured CP parameters.

9.5 Fit biases and Monte Carlo uncertainty

As systematic uncertainties coming from the $B \to D^{(*)}\pi$ and $B \to D\rho$ selection criteria and reconstruction chain, we assign the statistical errors on the a and $c_{\rm lep}$ coefficients as obtained in the validation fit to the sample of simulated events (performed in Section 7.2). See Table 9.19 for the numbers.

Secondly, we account for the fit biases observed in the pseudo Monte Carlo experiments performed in Section 7.3. The biases and errors given in Table 7.6 have been added quadratically. The results are shown in Table 9.19.

Variation Δm_d	$\delta a^{D\pi}$	$\delta a^{D^*\pi}$	$\delta a^{D\rho}$	$\delta c_{\rm lep}^{D\pi}$	$\delta c_{\rm lep}^{D^*\pi}$	$\delta c_{\rm lep}^{D\rho}$
$+1\sigma$	$+0.0009$	-0.0003	0	0	0	-0.0005
-1σ	-0.0009	$+0.0004$	$+0.0001$	$+0.0001$	$+0.0006$	-0.0004
τ_B^0						
$+1\sigma$	$+0.0002$	$+0.0002$	$+0.0001$	$+0.0005$	$+0.0002$	$+0.0010$
-1σ	-0.0002	-0.0002	0	-0.0005	-0.0001	-0.0010
Δm_d and τ_B^0 floating	$+0.0012$	-0.0012	-0.0001	-0.0013	-0.0013	-0.0018
Δm_d and τ_B^0 floating (MC)	-0.0003	0	0	-0.0005	-0.0005	-0.0003
Syst. Error	0.0012	0.0012	0.0001	0.0013	0.0013	0.0018

Table 9.18: *Systematic uncertainties on a and $c_{\rm lep}$ from the uncertainties in the world average values of Δm_d and τ_{B^0}.*

Variation	$\delta a^{D\pi}$	$\delta a^{D^*\pi}$	$\delta a^{D\rho}$	$\delta c_{\rm lep}^{D\pi}$	$\delta c_{\rm lep}^{D^*\pi}$	$\delta c_{\rm lep}^{D\rho}$
MC uncertainty	± 0.0051	± 0.0052	± 0.0075	± 0.0088	± 0.0093	± 0.0129
Fit bias	± 0.0005	± 0.0004	± 0.0006	± 0.0035	± 0.0035	± 0.0038
Syst. Error	0.0051	0.0052	0.0075	0.0095	0.0099	0.0134

Table 9.19: *Monte Carlo statistical uncertainties on the a and $c_{\rm lep}$ coefficients.*

9.6 Summary of systematic uncertainties

The systematic errors on a and $c_{\rm lep}$ are summarized in Tables 9.20 and 9.21. Notice that the total systematic uncertainties are dominated by detector-related effects and the Monte Carlo uncertainties. The systematic uncertainties on a and $c_{\rm lep}$ are approximately three times smaller than the statistical errors.

Source	Coefficient		
	$a^{D\pi}$	$a^{D^*\pi}$	$a^{D\rho}$
Signal parametrization			
Common Δt signal resolution [9.1.1]	± 0.0004	± 0.0002	± 0.0001
Fixed signal resolution parameters [9.1.2]	± 0.0006	± 0.0003	± 0.0013
Signal resolution model [9.1.3]	± 0.0005	± 0.0003	± 0.0004
Art effect [9.1.4]	± 0.0004	± 0.0011	± 0.0002
Common dilutions [9.1.5]	± 0.0001	± 0.0001	± 0.0005
Tagging and Reconstruction efficiency [9.1.6]	± 0.0006	± 0.0003	± 0.0003
Background description			
Signal probability: $D^{(*)}\pi/\rho$ samples [9.2.1]	± 0.0002	± 0.0002	± 0.0001
m_{ES} endpoint [9.2.2]	0	0	± 0.0001
Background resolution model [9.2.3]	± 0.0001	0	± 0.0001
Fraction and composition of peak. bkg. [9.2.4]	0	± 0.0001	± 0.0001
CP content comb. background [9.2.5]	± 0.0009	± 0.0007	± 0.0027
CP content peak. background [9.2.6]	± 0.0009	± 0.0006	± 0.0006
Non-resonant $B \to D^{\mp}\pi^{\pm}\pi^0$ background [9.2.7]	–	–	± 0.0016
Uncertainty in decay-time difference			
Cuts on Δt and on $\sigma(\Delta t)$ [9.3.1]	± 0.0017	± 0.0007	± 0.0016
Beam spot [9.3.2]	± 0.0029	± 0.0079	± 0.0040
SVT alignment and Boost [9.3.3]	± 0.0013	± 0.0009	± 0.0011
Uncertainty on z-scale [9.3.4]	± 0.0003	± 0.0003	± 0.0001
Δm_d and B^0 lifetime [9.4]	± 0.0012	± 0.0012	± 0.0001
Fit biases and Monte Carlo uncertainty [9.5]	± 0.0051	± 0.0052	± 0.0075
Total systematic error	± 0.0066	± 0.0097	± 0.0094
Statistical error	± 0.0225	± 0.0225	± 0.0313

Table 9.20: *Summary of systematic uncertainties on $a^{D\pi}$, $a^{D^*\pi}$, and $a^{D\rho}$ due to the different effects described in the text.*

Source	Coefficient		
	$c_{\rm lep}^{D\pi}$	$c_{\rm lep}^{D^*\pi}$	$c_{\rm lep}^{D\rho}$
Signal parametrization			
Common Δt signal resolution [9.1.1]	± 0.0001	± 0.0001	0
Fixed signal resolution parameters [9.1.2]	± 0.0022	± 0.0041	± 0.0040
Signal resolution model [9.1.3]	± 0.0017	± 0.0014	± 0.0020
Art effect [9.1.4]	± 0.0011	± 0.0012	± 0.0010
Common dilutions [9.1.5]	± 0.0006	± 0.0002	± 0.0005
Tagging and Reconstruction efficiency [9.1.6]	± 0.0010	± 0.0007	± 0.0004
Background description			
Signal probability: $D^{(*)}\pi/\rho$ samples [9.2.1]	± 0.0004	± 0.0005	± 0.0003
m_{ES} endpoint [9.2.2]	0	± 0.0002	± 0.0002
Background resolution model [9.2.3]	0	0	± 0.0001
Fraction and composition of peak. bkg. [9.2.4]	± 0.0002	± 0.0004	± 0.0006
CP content comb. background [9.2.5]	± 0.0002	± 0.0002	± 0.0027
CP content peak. background [9.2.6]	± 0.0009	± 0.0006	± 0.0007
Non-resonant $B \to D^{\mp}\pi^{\pm}\pi^0$ background [9.2.7]	–	–	± 0.0016
Uncertainty in decay-time difference			
Cuts on Δt and on $\sigma(\Delta t)$ [9.3.1]	± 0.0023	± 0.0024	± 0.0021
Beam spot [9.3.2]	± 0.0049	± 0.0097	± 0.0103
SVT alignment and Boost [9.3.3]	± 0.0019	± 0.0035	± 0.0010
Uncertainty on z-scale [9.3.4]	± 0.0004	± 0.0004	± 0.0005
Δm_d and B^0 lifetime [9.4]	± 0.0013	± 0.0013	± 0.0018
Fit biases and Monte Carlo uncertainty [9.5]	± 0.0095	± 0.0099	± 0.0134
Total systematic error	± 0.0117	± 0.0153	± 0.0186
Statistical error	± 0.0424	± 0.0420	± 0.0548

Table 9.21: *Summary of systematic uncertainties on $c_{\rm lep}^{D\pi}$, $c_{\rm lep}^{D^*\pi}$, and $c_{\rm lep}^{D\rho}$ due to the various effects described in this Chapter.*

Chapter 10

Determination of amplitude ratios

The measurement of γ using $B \to D^{(*)\mp} h^{\pm}$ decays ($h = \pi, \rho$) requires knowledge of the ratio of decay amplitudes $r^{D^{(*)}h} = |A(B^0 \to D^{(*)+}h^-)/A(\overline{B}^0 \to D^{(*)+}h^-)|$. In this chapter these ratios, and the errors on them, are determined using the measured branching fractions $\mathcal{B}(B^0 \to D_s^{(*)+}h^-)$.

10.1 Introduction

In the ratio of decay amplitudes $r^{D^{(*)}h} = |A(B^0 \to D^{(*)+}h^-)/A(\overline{B}^0 \to D^{(*)+}h^-)|$, the B^0 amplitude is doubly-CKM-suppressed relative to the CKM-favored amplitude $\overline{B}^0$ decay amplitude ($b \to c\overline{u}d$) with a factor of roughly $|(V_{ub}^* V_{cd})/(V_{cb} V_{ud}^*)| \approx 0.02$. The leading Feynman diagrams of both amplitudes have been shown in Fig. 2.9. Given the initial and final state quark content, there are no penguin contributions.

Unfortunately, the direct measurement of the branching fractions $\mathcal{B}(B^0 \to D^{(*)+}h^-)$ is not possible due to overwhelming background from the favored decay $\overline{B}^0 \to D^{(*)+}h^-$. Neither is it possible to measure the isospin related decays $B^+ \to D^{(*)+}h^0$ with the currently available statistics. As a result, each amplitude ratio $r^{D^{(*)}h}$ is required as external input in the extraction of the CKM-angle γ. In principle, these ratios can be obtained in two other ways.

First, their sizes can be predicted from theory. As the branching fractions of the favored decays $\mathcal{B}(B^0 \to D^{(*)-}h^+)$ are well-known [17], only the CKM-suppressed amplitudes $A(B^0 \to D^{(*)+}h^-)$ need to be estimated, such that

$$r^{D^{(*)}h} = \sqrt{\frac{\tau_{B^0} p}{8\pi m_B^2}} \frac{|A(B^0 \to D^{(*)+}h^-)|}{\sqrt{\mathcal{B}(B^0 \to D^{(*)-}h^+)}}, \tag{10.1}$$

where p is the momentum of the $D^{(*)}$ in the B rest frame. Examples of predictions for $r^{D^{(*)}\pi}$ exist using various form factor models [86], but most are outdated. Their values have been summarized in Table 10.1. We do not use these for three reasons.

1. No errors are given on the ratios.
2. Each calculation needs a form factor model $F^{B\to\pi}(q^2)$ and values for $f_{D^{(*)}}$ and V_{ub}. A lot of progress has been made on these over the last few years (as will become clear). For all estimates, their values were quite uncertain at the time.
3. The estimates do not include rescattering effects.

Model	$r^{D\pi}/0.02$	$r^{D^*\pi}/0.02$
Light Front	0.72	0.81
BSW II	1.11	1.33
NS	0.72	0.88
LCSR	0.87	1.01
MS	0.82	0.92
Average	0.85	0.99

Table 10.1: *The amplitude ratio $r^{D^{(*)}\pi}$ evaluated in various models [86], divided by* 0.02.

Second, as proposed by Dunietz [11], one can utilize $SU(3)$ flavor symmetry to relate $r^{D^{(*)}h}$ to the branching fraction of the decay $B^0 \to D_s^{(*)+}h^-$, using

$$r^{D^{(*)}h} = (\tan\theta_c)\frac{f_{D^{(*)}}F(m^2_{D^{(*)}})}{f_{D_s^{(*)}}F(m^2_{D_s^{(*)}})}\sqrt{\frac{\mathcal{B}(B^0 \to D_s^{(*)+}h^-)}{\mathcal{B}(B^0 \to D^{(*)-}h^+)}}\,, \tag{10.2}$$

where θ_c is the Cabibbo angle, $F(q^2)$ is the $B \to \pi$ form factor, and $f_{D^{(*)}}/f_{D_s^{(*)}}$ is the ratio of $D^{(*)}$ to $D_s^{(*)}$ decay constants [115, 136]. This relation is can be seen with help of the diagrams in Fig. 10.1. Both diagrams involve $b \to u$ transitions, so the B^0 decays into a W^+ and a π^- or ρ^-. In one case the virtual W^+ hadronizes into a $D^{(*)+}$, with decay constant $f_{D^{(*)}}$ and CKM-element V_{cd}, and in the other it forms a $D_s^{(*)+}$, with decay constant $f_{D_s^{(*)}}$ and CKM-element V_{cs}.

Both methods assume factorization. Although factorization has been demonstrated to work successfully in $b \to c$ transitions, no such experimental evidence exists (yet) for the $b \to u$ decays. One theoretical model of factorization, soft-collinear effective theory (SCET), sofar fails in the $b \to u$ regime [87]. However, another, N_c-QCD, does not, as will become clear shortly.

Also, for the second method, strictly speaking, in Eq. (10.1) the decays $B^0 \to D^{(*)+}h^-$ and $B^0 \to D_s^{(*)+}h^-$ are not related by $SU(3)$ symmetry. Namely, the $SU(3)$-transformed decay $B^0 \to D^{(*)+}\pi^-$ is $B_s^0 \to D_s^{(*)+}K^-$. However, the effective Hamiltonians describing $B^0 \to D^{(*)+}h^-$ and $B^0 \to D_s^{(*)+}h^-$, provided by heavy quark effective theory (HQET), are related by $SU(3)$, as here the spectator d quark is not transformed between the two decays. This argument demonstrates that decays involving the spectator quark are not related by $SU(3)$.

Two diagrams contribute to $B^0 \to D^{(*)+}h^-$: a) the color-allowed tree amplitude T in Fig. 10.1a, *i.e.* the 'effective' $SU(3)$ equivalent of Fig. 10.1b, and b) the color-suppressed W-exchange amplitude E with the spectator quark (see Fig. 10.6b). Only a single tree amplitude contributes to $B^0 \to D_s^{(*)+}h^-$, since the decay has four different quarks in the final state. Still, as long a E is small, one can relate the two decays by $SU(3)$ symmetry. Conversely, in Eq. (10.2) the W-exchange contribution to $B^0 \to D^{(*)+}h^-$ is assumed to be negligible.

The quality of these assumptions is discussed in the following Sections.

The concept of factorization is introduced in Section 10.2. In Section 10.2 we discuss the applicability of factorization to $B^0 \to D_s^{(*)+}h^-$ decays, and the corresponding predictions of N_c-QCD. $SU(3)$ breaking corrections due to soft final state interactions, or 'rescattering' effects, are discussed in Section 10.3. The amplitude ratios $r^{D^{(*)}h}$ are calculated in Section 10.4.

Figure 10.1: *Color-allowed tree diagram of: (a) CKM-suppressed decay $B^0 \to D^+\pi^-$, and (b) $B^0 \to D_s^+\pi^-$.*

Section 10.6 gives an estimate of the size of the W-exchange amplitude. $SU(3)$ breaking corrections from other non-factorizable corrections are treated in Section 10.7. We summarize the merits of (*i.e.* the *errors* of) both methods for obtaining $r^{D^{(*)}h}$ in Section 10.8.

10.2 Predictions from factorization

In this Section we present a brief introduction to factorization. This is followed by branching ratio predictions from naive factorization for the CKM-suppressed decays $B^0 \to h^- D_{(s)}^{(*)+}$.

The dominant weak diagram of the two body decay $B^0 \to h^- D_{(s)}^{(*)+}$ occurs through the Cabibbo-suppressed $b \to u$ transition, as shown in Fig. 10.1. Here, the virtual W^- hadronizes into either a $\bar{c}s$ or $\bar{c}d$ pair. This pair becomes the $D_{(s)}^{(*)+}$ meson, while the u pairs with the spectator $\bar{d}$ to form the h meson. The effective weak Hamiltonian describing the decay is

$$\mathcal{H}_W = \frac{G_F}{\sqrt{2}} V_{ub} V_{cq}^* \left[C_1(\mu)(\bar{q}c)_{V-A}(\bar{u}b)_{V-A} + C_2(\mu)(\bar{u}c)_{V-A}(\bar{q}b)_{V-A} \right], \tag{10.3}$$

where G_F is the Fermi coupling constant, V_{ij} are CKM matrix elements, and q is either a d or an s quark. The parameters $C_i(\mu)$ are the Wilson coefficients at the mass scale μ.

The first operator in Eq. (10.3), multiplied by the coefficient $C_1(\mu)$, comes from the W exchange. The second 'color-suppressed' piece, multiplied by $C_2(\mu)$, is induced by gluon exchange between the initial and final quarks. The Wilson coefficients can be calculated from QCD: $C_1 = 1.08$ and $C_2 = -0.18$ at LO at the m_B mass scale [137], with theoretical errors of about 0.02.

In analogy to semi-leptonic decays, Bauer, Stech, and Wirbel suggested [88] that color-allowed two body decays $B \to YX$ can be expressed theoretically as the product of two independent hadronic currents. One current describes the hadronization of the quark pair to form the X meson from the virtual W, and the other describes the formation of the Y meson from the b decay and spectator quark. The assumption that the amplitude can be expressed as the product of two hadronic currents is called 'factorization'. In terms of Eq. (10.3)

$$\langle h^- D_{(s)}^{(*)+} | \mathcal{H}_W | B^0 \rangle = \frac{G_F}{\sqrt{2}} V_{ub} V_{cq}^* \left(C_1(m_B) + \frac{C_2(m_B)}{N_c} \right) \langle D_{(s)}^{(*)+} | (\bar{q}c)_{V-A} | 0 \rangle \langle h^- | (\bar{u}b)_{V-A} | B^0 \rangle \,. \tag{10.4}$$

Factorization models the B decay only up to the hadronization of the X and Y mesons. Correspondingly, the terms in Eq. (10.3) are called 'short-distance' operators. (Long-distance 'rescattering' effects are discussed in Section 10.3.)

A non-rigorous argument to justify factorization has been made by Bjørken using color transparency [89]. The argument requires that the X meson, formed from the (colorless) virtual W, is ultra-relativistic. More quantitatively, its time dilation factor $\gamma_X = E_X/m_X = (m_B^2 + m_X^2 - m_Y^2)/(2m_B m_X)$, where E_X is the energy of X in the B rest frame, should be large. In that case, the color dipole moment of the quarks that form the X, produced together as a color singlet, grows to hadronic size only after a time-delayed hadronization time $\gamma_X t_X$, with $c\gamma_X t_X$ much larger than the size of the B meson. Put simply, X travels fast enough to leave the interaction region without interfering with the formation of Y. With little chance for the X and Y mesons to interact strongly, other short-distance 'non-factorizable corrections' are expected to be small.

For the Cabibbo-favored decay $B^0 \to D^-\pi^+$ one has $\gamma_\pi = 16.5$ in the B rest frame. The suppressed decay $B^0 \to \pi^- D^+$ results in $\gamma_D = 1.6$. (Which corresponds to $\beta_D = 0.78$, indicating that even though the D may not be ultra-relativistic, it is still relativistic.)

So-called naive factorization, which ignores any non-factorizable corrections, has been demonstrated to work quite successfully for $b \to c$ transitions in color-allowed tree decays. An example is given in Fig. 10.2, showing the measured and predicted fractions of longitudinal polarization in $B \to D^* X$ vector-vector decays, where the factorization prediction holds at the level of a few percent.

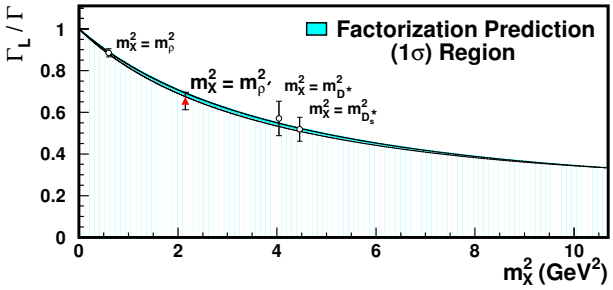

Figure 10.2: *The longitudinal polarization as a function of m_X^2, where X is a vector meson [97]. Shown (as a triangle) is the $B^0 \to D^{*-}\omega\pi^+$ polarization measurement for events with $1.1 < m_X < 1.9$ GeV ($m_X^2 = m_{\rho'}^2$, where $\rho' \equiv \rho(1450)$), as well as measurements of $B^0 \to D^{*-}\rho^+$ [90], $B^0 \to D^{*-}D^{*+}$ [91], and $B^0 \to D^{*-}D_s^{*+}$ [92]. The shaded region represents the prediction ($\pm$ one standard deviation) based on factorization and HQET, extrapolated from the semi-leptonic $\overline{B}^0 \to D^{*+}\ell^-\bar{\nu}$ form factor results [93].*

There are two limits of QCD in which factorization in $B \to D^{(*)}X$, with X a light meson, has been proven rigorously. One is the large N_c limit of QCD, where one takes the limit of infinite colors [94]. All non-factorizable corrections can be shown to be suppressed by[1] $O(1/N_c^2)$.

[1]The exchange diagrams in Figs. 10.6, ignored in HQET, are in fact suppressed by $1/N_c$ relative to the factorizable tree amplitude. These contributions are suppressed by additional effects and will be constrained

This conclusion also holds when X is heavy. The other line of approach builds on the color transparency phenomenon [89]. In the small velocity (SV) limit of the $D^{(*)}$, factorization has been proven using soft-collinear effective theory (SCET) [95]. In this case the corrections to factorization are of the order m_X/Q, where Q is a sufficiently large energy scale such as m_B or E_X. For the SV approach, the agreement of naive factorization has been demonstrated to extend well beyond its rigorously proven limits of validity.

A study of the invariant mass spectrum of the $X = \omega\pi^+$ system in the decay $B^0 \to D^{*-}\omega\pi^+$, with X coming from the virtual W, is in good agreement with expectations based on factorization and the measured spectrum in $\tau^+ \to W^+\bar{\nu}_\tau \to \omega\pi^+\bar{\nu}_\tau$ [96, 97]. The mass m_X runs from 0.8–2.7 GeV. This factorization test can only be carried out where the τ data is available, *i.e.* for $m_X < 1.7$ GeV. Also, the fraction of longitudinal polarization of the D^{*-}, as shown in Fig. 10.2, is in agreement with the expectation from factorization and heavy quark effective theory, assuming that the decay proceeds as $B^0 \to D^{*-}\rho(1450)^+$, $\rho(1450)^+ \to \omega\pi^+$. If solely the SV limit was responsible for explaining factorization in this decay, one would expect the deviations from naive factorization to grow as m_X/E_X. However, no indication of such corrections is observed.

Factorization has also been used to study $B^0 \to D^{(*)-}\bar{D}^{(*)+}_{(s)}$ decays [98], with $m_X = 2$ GeV, and $B \to D^{(*)}\bar{D}^{(*)}K$ [99]. Again it has been found that branching fractions (and polarization measurements) agree with the naive factorization predictions. Since in the latter cases the color singlet quark-anti-quark emerging from the short distance interaction forms a heavy meson, the proof of factorization in the SV limit is not applicable. However, in the large N_c limit factorization is still realized. The authors of Ref. [96] therefore suggest that factorization in $B \to D^{(*)}X$ $(b \to c)$, at least in the regime where X is heavy, should be explained by means of N_c-QCD.

We now switch back to $b \to u$ decays, such as $B^0 \to h^- D^{(*)+}_{(s)}$. Few measurements exist yet to indicate whether factorization applies in this regime. However, also here – for the same reason as discussed above – the proof of factorization in SV limit cannot be used. In fact, in the $b \to u$ regime SCET sofar has not made any prediction concerning the size of non-factorizable corrections [87]. In the large N_c limit factorization still applies, with non-factorizable corrections appearing at $O(1/N_c^2)$.

There are cases where the predictions from N_c-QCD are known to fail. For example, the so-called OZI rule[2] in decay channels with zero isospin. However, there are no known a-priori reasons to indicate that N_c-QCD does not apply to $B^0 \to h^- D^{(*)+}_{(s)}$ decays [100].

Several tests of the factorization hypothesis of $b \to u$ can be made by comparing semileptonic $B^0 \to h^- l^+ \nu$ with hadronic $B^0 \to h^+ D^{(*)-}_{(s)}$ decays, as discussed in the following Section.

10.2.1 Branching fractions

Within the framework of factorization, the decay rates of $B^0 \to h^- D_s^{(*)+}$, where h is either a π or ρ meson, can be related to the decays of $B^0 \to h^- l^+ \nu$, just like the spectra of $B^0 \to D^{(*)-} l^+ \nu$

separately, as discussed in Section 10.6. Rescattering effects, discussed in Section 10.3, are long-distance effects also of $O(1/N_c)$, but are identical for CKM-allowed and CKM-suppressed decays.

[2] The OZI rule is an empirical rule, which forbids meson decays where none of the quarks in the initial state are found in the final state mesons. For example, this rule forbids decays of non-strange mesons (*e.g.* ω or J/ψ) into $K\bar{K}$. This rule is sometimes violated, but is not likely to be relevant in $B^0 \to h^- D^{(*)+}_{(s)}$ decays.

can be used to predict the rates for $B^0 \to D^{(*)-} h^+$ [101] and $B^0 \to D^{(*)-} D_{(s)}^{(*)+}$ decays [98]

$$\Gamma(B^0 \to \pi^- D_s^+) = \frac{G_F^2 p_\pi}{16\pi\, m_B^2} |V_{cs}|^2 f_{D_s}^2 |a_1|^2 (m_B^2 - m_\pi^2)^2 |V_{ub}|^2 |f_0(m_{D_s}^2)|^2, \tag{10.5}$$

$$\begin{aligned}\Gamma(B^0 \to \pi^- D_s^{*+}) &= \frac{G_F^2 p_\pi}{16\pi\, m_B^2} |V_{cs}|^2 f_{D_s^*}^2 |a_1|^2 (2 m_B p_\pi)^2 |V_{ub}|^2 |f_+(m_{D_s^*}^2)|^2 \\ &= 6\pi^2 |V_{cs}|^2 f_{D_s^*}^2 |a_1|^2 \left.\frac{d\Gamma(B^0 \to \pi^- l^+ \nu)}{dq^2}\right|_{q^2 = m_{D_s^*}^2},\end{aligned} \tag{10.6}$$

$$\Gamma(B^0 \to \rho^- D_s^+) = \frac{G_F^2 p_\rho}{16\pi\, m_B^2} |V_{cs}|^2 f_{D_s}^2 |a_1|^2 (2 m_B p_\rho)^2 |V_{ub}|^2 |A_0(m_{D_s}^2)|^2 \tag{10.7}$$

$$\Gamma(B^0 \to \rho^- D_s^{*+}) = 6\pi^2 |V_{cs}|^2 f_{D_s^*}^2 |a_1|^2 \left.\frac{d\Gamma(B^0 \to \rho^- l^+ \nu)}{dq^2}\right|_{q^2 = m_{D_s^*}^2}, \tag{10.8}$$

where $f_+(q^2)$ and $f_0(q^2)$ are the two form factors involved in the $b \to u$ transition of $B \to \pi$. They are related at $q^2 = 0$, where $f_+(0) \equiv f_0(0)$. Only $f_+(q^2)$ is involved in the decay $B^0 \to \pi^- l^+ \nu$, so the latter can only be related directly to the decay $B^0 \to \pi^- D_s^{*+}$. Similarly, $B^0 \to \rho^- l^+ \nu$ can be related directly to $B^0 \to \rho^- D_s^{*+}$.

The form factor $A_0(q^2)$ involved in the decay $B^0 \to \rho^- D_s^+$ cannot be extracted directly from semi-leptonic $B^0 \to \rho^- l^+ \nu$ decays, since it is suppressed by the spin-flip factor $(m_l^2/2q^2)$ [102]. However, from Ref. [104, 105], Eq. (1.2), it follows that $A_0(q^2)$ can be related to the zero helicity amplitude of $B^0 \to \rho^- D_s^{*+}$ by the relation

$$H_0(q^2) \approx 2 m_B p_\rho A_0(q^2)\,. \tag{10.9}$$

The relation is exact in the limit of $q^2 \to 0$. Assuming that the form factor relation between H_0 and A_0 remains approximately valid away from zero, this gives for Eq. (10.7)

$$\Gamma(B^0 \to \rho^- D_s^+) \approx f_L\, \Gamma(B^0 \to \rho^- D_s^{*+})\,, \tag{10.10}$$

where f_L is the fraction of longitudinal polarization in $B^0 \to \rho^- D_s^+$. This corresponds to the argument used in Ref. [106] to relate $B^0 \to D^{*-} \pi^+$ to $B^0 \to D^{*-} l^+ \nu$.

To obtain the corresponding decay rate predictions for $B^0 \to h^- D^{(*)+}$, simply replace $V_{cs} \to V_{cd}$, $f_{D_s^{(*)}} \to f_{D^{(*)}}$, and evaluate the form factors at $q^2 = m_{D^{(*)}}^2$.

Calculation of the decay rates for $B^0 \to h^- D_s^{*+}$ in Eq. (10.5) requires knowledge of the $d\Gamma(B^0 \to h^- l^+ \nu)/dq^2$ spectra, which are also needed in the extraction of $|V_{ub}|$. In the past, these spectra have been calculated using $B \to h$ form factor models, leading to significant model dependence. Examples of $d\Gamma(B^0 \to h^- l^+ \nu)/dq^2$ for various form factor models are shown in Fig. 10.3. However, since last year several differential $B^0 \to h^- l^+ \nu$ decay rates have been measured [107]–[110], and results from precise lattice simulations with dynamical light quarks have become available [111, 112]. From these, we can make predictions for $d\Gamma(B^0 \to h^- l^+ \nu)/dq^2$ at $q^2 = m_{D_s^*}^2$ to the point where only little shape information is required from theory.

The relevant partial branching fractions of $B^0 \to h^- l^+ \nu$, $\Delta\mathcal{B} \equiv \Delta\Gamma \cdot \tau_{B^0}$, have been summarized in Tables 10.2 and 10.3. For $B^0 \to \pi^- l^+ \nu$ these are quite precise. The errors on the partial branching fraction measurements are dominated by statistical errors for $B^0 \to \pi^- l^+ \nu$, and (mostly) by systematical errors for $B^0 \to \rho^- l^+ \nu$. For both decays the errors from form

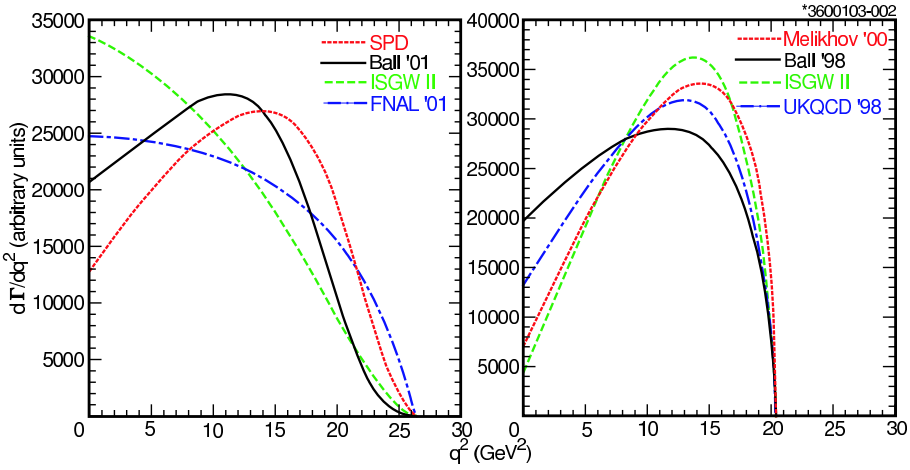

Figure 10.3: *Examples of (outdated) predictions for $d\Gamma(B^0 \to \pi^- l^+ \nu)/dq^2$ (left) and $d\Gamma(B^0 \to \rho^- l^+ \nu)/dq^2$ (right) for a variety of form factor calculations. The figure has been taken from Ref. [107].*

factor calculations are relatively small, at the level of 10% or smaller for $B^0 \to \rho^- l^+ \nu$, and at the level of a few % for $B^0 \to \pi^- l^+ \nu$.

The average value of $\tau_{B^0} \cdot \Delta\Gamma/\Delta q^2$ for $B^0 \to \pi^- l^+ \nu$ for q^2 over the range $[0, 8]$ GeV^2 is thus found to be $(6.3 \pm 0.9) \times 10^{-4}$ GeV^{-2}. For $B^0 \to \rho^- l^+ \nu$, motivated by the spectra shown in Fig. 10.3, the partial branching fraction measurement of $(0.73 \pm 0.28) \times 10^{-4}$ of Ref. [107] has been corrected to the q^2 range of $[0, 8]$ GeV^2 by subtracting $2/5^{\text{th}}$ of the adjacent bin. The correction has been added in quadrature to the error on the first bin. The average value of $\tau_{B^0} \cdot \Delta\Gamma/\Delta q^2$ for $B^0 \to \rho^- l^+ \nu$ is then found to be $(4.5 \pm 2.7) \times 10^{-4}$ GeV^{-2}.

$\Delta\mathcal{B}$ ($\times 10^{-4}$)	q^2 Range (GeV)^2	$\tau_{B^0} \cdot \Delta\Gamma/\Delta q^2$ ($\times 10^{-6}$ GeV^{-2})	Ref.
0.30 ± 0.08	$0 - 5$	6.0 ± 1.5	[107]
0.32 ± 0.06	$5 - 10$	–	[107]
0.71 ± 0.17	$0 - 8$	8.9 ± 2.1	[108]
0.43 ± 0.12	$0 - 8$	5.4 ± 1.5	[109]
0.48 ± 0.18	$0 - 8$	6.0 ± 2.2	[110]
Average	$0 - 8$	6.3 ± 0.9	

Table 10.2: *Partial branching fraction measurements, $\Delta\mathcal{B}$, for $B^0 \to \pi^- l^+ \nu$ decays by various experiments.*

Since all $d\Gamma/dq^2$ models show linear behavior over the range $q^2 \in [0, 8]$ GeV^2, to good approximation one can use the averages as $d\Gamma/dq^2$ values at $q^2 = m^2_{D_s^*} \approx 4$ GeV^2. As a cross check, the value of $(6.3 \pm 0.9) \times 10^{-4}$ GeV^{-2} at $q^2 = m^2_{D_s^*}$ is in exact agreement with that of

$\Delta\mathcal{B}$ ($\times 10^{-4}$)	q^2 Range $(\mathrm{GeV})^2$	$\tau_{B^0} \cdot \Delta\Gamma/\Delta q^2$ ($\times 10^{-6}$ GeV^{-2})	Ref.
0.82 ± 0.20	$10 - 15$	–	[107]
0.73 ± 0.28	$0 - 10$	5.0 ± 5.5 (*)	[107]
0.21 ± 0.41	$0 - 8$	2.6 ± 5.1	[108]
0.43 ± 0.32	$0 - 8$	5.4 ± 4.0	[109]
Average	$0 - 8$	4.5 ± 2.7	

Table 10.3: *Partial branching fraction measurements, $\Delta\mathcal{B}$, for $B^0 \to \rho^- l^+ \nu$ decays by various experiments. The (*) indicates that the corresponding value has been adjusted to a q^2 range of $[0, 8]$ GeV^2, as described in the text.*

the form factor model fit in Ref. [113], shown in Fig. 10.4, performed to all $B^0 \to \pi^- l^+ \nu$ partial branching fraction measurements of Refs. [107, 108, 109, 110].

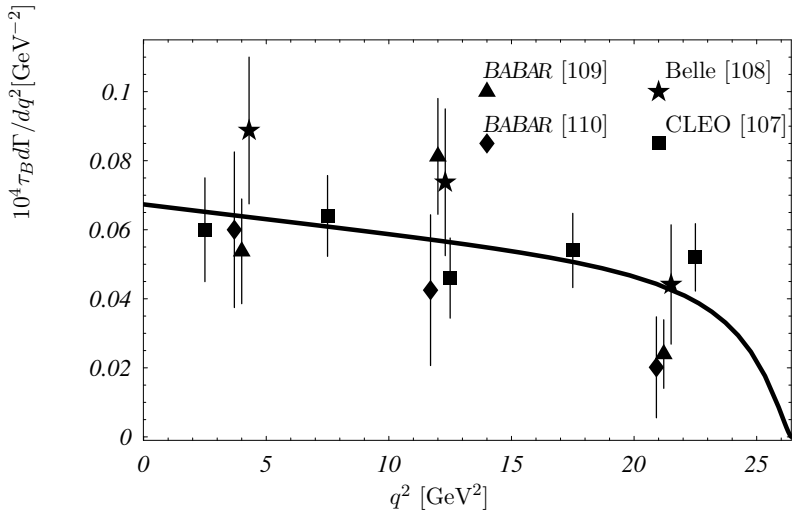

Figure 10.4: *Shown are the current data for the partial ratios of $B^0 \to \pi^- l^+ \nu$ – also given in Table 10.2 – and fit results to the $d\Gamma/dq^2$ spectrum [113]. The fit has been performed both using an analytically constrained shape [113] and the BK parametrization [114], with indistinguishable results.*

Ref. [113] also extrapolates $f_+(q^2)$ to $q^2 = 0$ and finds $V_{ub}\, f_+(0) = (0.92 \pm 0.11 \pm 0.03) \times 10^{-3}$, where the first error is experimental and the second is due to the uncertainty in the form factor shape used. From lattice calculations [111, 112] the form factor $f_0(q^2)$ is found to be well modeled by the BK parametrization [114],

$$f_0(q^2) = \frac{f_+(0)}{1 - \frac{q^2}{m_*^2}}\,, \tag{10.11}$$

where the effective pole mass m_*^2 is determined to be 33.4 ± 1.4 GeV^2. We thus have

$$|V_{ub}\, f_0(m_{D_s}^2)|^2 = (1.08 \pm 0.26\,(\text{exp.}) \pm 0.07\,(\text{ff.}) \pm 0.10\,(\text{lat.})) \times 10^{-6}\,. \tag{10.12}$$

For later use we note that

$$|V_{ub}\, f_0(m_D^2)| = (1.03 \pm 0.12\,(\text{exp.}) \pm 0.03\,(\text{ff.}) \pm 0.05\,(\text{lat.})) \times 10^{-3}\,, \tag{10.13}$$

$$|V_{ub}\, f_+(m_{D^*}^2)| = (1.13 \pm 0.08\,(\text{exp.})) \times 10^{-3}\,, \tag{10.14}$$

and, from Ref. [113]

$$f_0(0) = 0.25 \pm 0.04\,(\text{exp.}) \pm 0.01\,(\text{ff.}) \pm 0.03\,(\text{lat.})\,. \tag{10.15}$$

The form factor models in Refs. [104, 121] predict $f_0(m_{D_s}^2)/f_1(m_{D_s}^2) \approx 0.85 \pm 0.19$. Using Eq. (10.14) one can make the second extrapolation

$$|V_{ub}\, f_0(m_{D_s}^2)|^2 = (0.92 \pm 0.13\,(\text{exp.}) \pm 0.41\,(\text{ff.})) \times 10^{-6}\,, \tag{10.16}$$

which is lower than Eq. (10.12), but has a significantly larger error.

With these values, we predict the branching ratios $\mathcal{B}(B^0 \to h^- D_s^{*+})$ listed in Table 10.4. To calculate these we have used[3]: $|V_{cs}| = 0.9735$, $f_{D_s^{(*)}} = 274 \pm 20$ MeV, and $|a_1| = 1.02$ [137]. The errors on these predictions come mostly from the errors on $d\Gamma/dq^2$ and the error on $f_{D_s^{(*)}}$. The error on $\mathcal{B}(B^0 \to \pi^- D_s^+)$ receives additional contributions and is larger than $\mathcal{B}(B^0 \to \pi^- D_s^{*+})$ because, to calculate $V_{ub}\, f_0(m_{D_s}^2)$, f_+ has to be extrapolated to zero and f_0 has to be extrapolated back to $q^2 = m_{D_s}^2$.

Decay	Predicted $\mathcal{B}$ ($\times 10^{-5}$)	Eq.
$B^0 \to \pi^- D_s^+$	$3.3 \pm 0.8\,(\text{exp.}) \pm 0.2\,(\text{ff.}) \pm 0.3\,(\text{lat.}) \pm 0.5\,(f_{D_s})$	10.12
	$2.9 \pm 0.3\,(\text{exp.}) \pm 1.1\,(\text{ff.}) \pm 0.4\,(f_{D_s^*})$	10.16
$B^0 \to \pi^- D_s^{*+}$	$2.8 \pm 0.4\,(\text{exp.}) \pm 0.4\,(f_{D_s^*})$	
$B^0 \to \rho^- D_s^+$	$1.2 \pm 0.8\,(\text{exp.}) \pm 0.2\,(f_{D_s})$ (*)	
$B^0 \to \rho^- D_s^{*+}$	$2.0 \pm 1.2\,(\text{exp.}) \pm 0.3\,(f_{D_s^*})$	

Table 10.4: *Predicted branching ratios $\mathcal{B}$ for $B^0 \to h^- D_s^{(*)+}$, based on N_c-QCD factorization, before rescattering (discussed in Section 10.3). (*) We have guesstimated the fraction of longitudinal polarization in $B^0 \to \rho^- D_s^{*+}$ to be* 0.6.

The corresponding measured branching fractions $\mathcal{B}(B \to h D_s^{(*)+})$ are shown in Table 10.5. Here we have applied the isospin relation $\mathcal{B}(B^0 \to \pi^- D_s^+) = 2(\tau_B^0/\tau_B^+)\,\mathcal{B}(B^+ \to \pi^0 D_s^+)$. To find the quoted average value for $\mathcal{B}(B^0 \to \pi^- D_s^+)$, the value for $\mathcal{B}(B^0 \to \pi^- D_s^{*+})$, and the upper limit on $B^0 \to \rho^- D_s^+$, we use [4] $\mathcal{B}(D_s^+ \to \phi\pi^+) = 0.044 \pm 0.005$

Before the estimates in Table 10.4 can be compared with data, the effects of rescattering should be included. This is done in Section 10.3, Table 10.10.

[3] The PDG quotes $f_{D_s^{(*)}} = 266 \pm 32$ MeV [17], and BaBar found the new value of $279 \pm 17 \pm 6 \pm 19$ MeV [115].

[4] Calculated as the average of the *BABAR* measurement 0.0481 ± 0.0064 [120] and the PDG 2004 value of 0.036 ± 0.009 [17].

Branching fraction $\mathcal{B}$	Measured value	90% UL	Ref.
$\mathcal{B}(B^0 \to \pi^- D_s^+)\,\mathcal{B}(D_s^+ \to \phi\pi^+)$	$(0.63 \pm 0.16) \times 10^{-6}$	–	[116]
$\mathcal{B}(B^0 \to \pi^- D_s^+)\,\mathcal{B}(D_s^+ \to \phi\pi^+)$	$(0.86^{+0.39}_{-0.32}) \times 10^{-6}$	–	[117]
$2(\tau_{B^0}/\tau_{B^+})\,\mathcal{B}(B^+ \to \pi^0 D_s^+)\,\mathcal{B}(D_s^+ \to \phi\pi^+)$	$(1.34^{+0.56}_{-0.47}) \times 10^{-6}$	–	[118]
WA $\mathcal{B}(B^0 \to \pi^- D_s^+)\,\mathcal{B}(D_s^+ \to \phi\pi^+)$	$(0.73 \pm 0.14) \times 10^{-6}$	–	
WA $\mathcal{B}(B^0 \to \pi^- D_s^+)$	$(1.7 \pm 0.4) \times 10^{-5}$	–	
$\mathcal{B}(B^0 \to \pi^- D_s^{*+})\,\mathcal{B}(D_s^+ \to \phi\pi^+)$	$(1.32 \pm 0.31) \times 10^{-6}$	–	[116]
$\mathcal{B}(B^0 \to \pi^- D_s^{*+})$	$(3.0 \pm 0.8) \times 10^{-5}$	–	[116]
$B^0 \to \rho^- D_s^+$	$(0.2 \pm 0.8) \times 10^{-5}$	2.1×10^{-5}	[119]
$B^0 \to \rho^- D_s^{*+}$	–	8×10^{-4}	[17]

Table 10.5: *Measured branching ratios $\mathcal{B}$ for $B^0 \to h^- D_s^{(*)+}$, sorted by experiment. The quoted errors correspond to the quadratic sum of statistical and systematic errors.*

Notice in Fig. 10.3 that, generally speaking, $d\Gamma(B^0 \to \rho^- l^+ \nu)/dq^2$ drops off more steeply towards lower values of q^2, suggesting that $\mathcal{B}(B^0 \to \rho^- D_s^{*+})$ is smaller then $\mathcal{B}(B^0 \to \pi^- D_s^{*+})$. In Ref. [102] this is called the 'time-like form factor effect' – the ρ prefers to be produced at low momentum where q^2 is largest. It implies small sensitivity to $\sin(2\beta+\gamma)$ from *CP* asymmetries in $B^0 \to D^{*\mp}\rho^\pm$ decays, making the measurement extremely challenging. This also explains the upper limit observed for $\mathcal{B}(B^0 \to \rho^- D_s^+)$. It is consistent with the predicted value for $\mathcal{B}(B^0 \to \rho^- D_s^{*+})$, multiplied with any possible fraction of longitudinal polarization. Naive factorization then predicts that the decays $B^0 \to \rho^- D_s^{(*)+}$ are now measurable at the B-factories.

The measurements of $\Delta\mathcal{B}(B^0 \to \rho^- l^+ \nu)$ (and the upper limit on $\mathcal{B}(B^0 \to \rho^- D_s^+)$) roughly imply $A_0(m_{D_s}^2) \approx 0.1 - 0.3$. This value is smaller than the predictions in Refs. [104, 121], which are between $0.3 - 0.4$, but is still compatible within the theoretical uncertainties on these numbers (≈ 0.07). (This is clearly seen when comparing the predicted and measured $\Delta\mathcal{B}(B^0 \to \rho^- l^+ \nu)$ for $q^2 \in [0, 8]$ GeV^2 in Refs. [107]–[109], with predicted values that are consistently too large.)

Another conclusion comes from Eqs. (10.5) and (10.6), where it is seen that the decays $B^0 \to \pi^- D_s^+$ and $B^0 \to \pi^- D_s^{*+}$ relate to different form factors. For this reason, the measured branching fraction of $\mathcal{B}(B^0 \to \pi^- D_s^+)$ should not be used to calculate the amplitude ratio $r^{D^*\pi}$.

10.3 Final state rescattering

In this Section we evaluate the level of $SU(3)$ breaking due to final state rescattering effects.

First, we introduce the topic of final state rescattering. Rescattering effects are 'long-distance' final state interactions, and hence independent of the initial meson formation process of the weak B meson decay. This means, for example, that the final state rescattering amplitudes involved after the CKM-favored decay $B^0 \to D^- \pi^+$ are the same as after the CKM-suppressed decay $B^0 \to D^+ \pi^-$.

To that end, we update the analysis performed in Ref. [125] to obtain the sizes and errors of the final state rescattering amplitudes, which appear after the CKM-favored decays $B^0 \to$

$D^{(*)-}\pi^+/K^+$ and $B^0 \to D^-\rho^+/K^{*+}$. Then, for the effects of $SU(3)$ breaking due to final state rescattering, these amplitudes are used to correct the amplitude ratios $r^{D^{(*)}h}$ of Eq. (10.2).

10.3.1 Quasi-elastic rescattering

The branching ratios of the color-suppressed decay modes $\overline{B}^0 \to D^{(*)0}h^0$ ($h^0 = \pi^0, \omega, \eta, \rho^0$) [141] are considerable larger than the estimates from naive factorization. This suggests the presence of final state interactions (FSI) by strong interactions, or 'soft rescattering', such as $D^{(*)+}\pi^- \to D^{(*)0}\pi^0$, happening after the color-allowed decays $\overline{B}^0 \to D^{(*)+}\pi^-$ or $\overline{B}^0 \to D^+\rho^-$.

Soft rescattering is a non-perturbative effect, and thus is very hard to calculate. Three types of soft rescattering, shown in Fig. 10.5, can be identified. One has two 'Regge' amplitudes, denoted as a) charge-exchange; b) annihilation, and in c) 'Pomeron' rescattering between identical final states, also known as singlet exchange. These amplitudes are called r_e, r_a, and r_0 respectively. Useful introductions to soft rescattering in B decays are Refs. [123, 124].

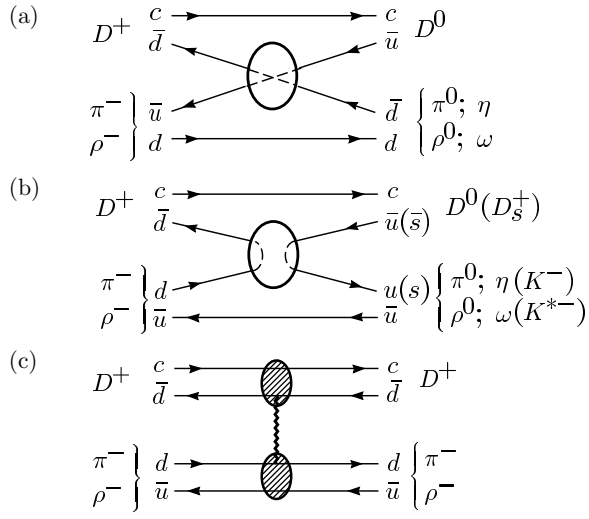

Figure 10.5: *Final state rescattering effects [125]. From top to bottom: (a) charge exchange (r_e), (b) annihilation (r_a), and (c) singlet exchange (r_0).*

Final state interactions such as $D_1\pi_1 \to D_2\pi_2$, where D_i and π_i remain within the isospin doublet $D = (D^+, D^0)$ and triplet $\pi = (\pi^+, \pi^0, \pi^-)$, are called elastic rescattering. The same name is given to the case where D is replaced by D^*, or π by ρ. Rescattering such as $D^{(*)+}\pi^- \to D^{(*)0}\eta$ and $D^+\rho^- \to D^0\omega$, where η and ω are isosinglets, is known as inelastic rescattering.

As rescattering occurs at the scale $m_B \gg m_q$, with m_q the mass of the up, down, or strange quark, the strong rescattering amplitudes should respect $SU(3)$ symmetry to a good degree[5]. This has been demonstrated by Chua, Hou, and Yang in Ref. [125].

[5] $SU(3)$ breaking in the formation of the initial mesons from the B decay is taken into account in decay constants and Wilson coefficients at the Hamiltonian level, as in Eq. (10.3).

Therefore, it is reasonable to extend isospin symmetry to $SU(3)$ for final state rescattering. Like in Ref. [125], we extend elastic rescattering $D\pi \to D\pi$ to 'quasi-elastic' rescattering $\mathcal{D}\Pi \to \mathcal{D}\Pi$, with the $SU(3)$ triplet $\mathcal{D}^{(*)} = (D^{(*)+}, D^{(*)0}, D_s^{(*)+})$, with quantum numbers 0^{-+} (1^{--}), and the pseudo-scalar octet Π including the three pions, four kaons, and the η ($\approx \eta_8$), with quantum numbers 0^{-+}. Rescattering to $D^{(*)0}\eta'$ is expected to be smaller for various reasons [125] – the η' ($\approx \eta_1$) is quite heavy, for one thing –, so the η' is excluded from Π. The vector mesons are grouped into the nonet $\mathcal{P}$, which includes the three ρ mesons, four K^* mesons, and the ω and ϕ, with quantum numbers 1^{--}. We denote the pseudo-scalar mesons in Π as P, and the vector mesons in $\mathcal{P}$ as V.

It turns out that for the vector nonet, one can have charge exchange or annihilation FSI, but not both [125]. A good fit can be obtained without annihilation rescattering. (The other solution gives branching fractions already ruled out by experiment.) Thus, in what follows, we use the assumption that $r_a = 0$ for the vector mesons.

Last, the subset of two-body final states that include a charm quark, reached via quasi-elastic rescattering, can be shown to stand out compared with other, inelastic channels. Unlike the case for quasi-elastic rescattering, inelastic channels, such as $D^*P \to DV$, need to transfer (or) spin, and/or parity, and/or charge parity from the $D^{(*)}$ to the V meson. The standard 'statistical' or 'duality' suppression arguments tell that inelastic FSI amplitudes tend to cancel each other, leading to small FSI phases [126, 127]. For example, an explicit calculation in Ref. [128] of the inelastic rescattering amplitude of $D^*\pi \to D\rho$ is at the level of only 1% compared with the elastic transition. We therefore ignore inelastic rescattering effects in the next Sections.

10.3.2 Rescattering in $D^{(*)}P \to D^{(*)}P$ and $DV \to DV$

In this Section we improve upon an analysis first performed in Ref. [125] to obtain the various final state rescattering amplitudes following the CKM-favored decays $\overline{B}^0 \to D^{(*)+}\pi^-/K^-$ and $\overline{B}^0 \to D^+\rho^-/K^{*-}$. Compared with Ref. [125], we use updated and new branching fractions of the B decays involved. Our fit returns the errors on the rescattering amplitudes, which are utilized to constrain the size of $SU(3)$ breaking in rescattering. Also new is that the results are applied to CKM-suppressed decays, such as $\overline{B}^0 \to D^{(*)-}\pi^+/K^+$ and $\overline{B}^0 \to D^-\rho^+/K^{*+}$, done in the following Section.

Let us briefly review the scattering formalism. Let $\mathcal{O}_k$ denote a T-even weak decay operator, such as present in the the weak Hamiltonian H_W in Eq. (10.3). The weak phases corresponding to $\mathcal{O}_k$ have been factored out into separate CKM-matrix elements λ_k. From time-reversal invariance one obtains

$$\langle j;\mathrm{out}|\mathcal{O}_k|B\rangle^* = \sum_i S^*_{ji}\langle i;\mathrm{out}|\mathcal{O}_k|B\rangle\,, \tag{10.17}$$

where $S_{ji} \equiv \langle j;\mathrm{out}|i;\mathrm{in}\rangle$ is the strong interaction S-matrix element, and one applies $\langle j;\mathrm{out}| = T|j;\mathrm{in}\rangle$. Time reversal invariance of the strong interactions requires that S is a symmetric matrix.

Using Watson's theorem [129], Eq. (10.17) can be formally solved as

$$\langle j;\mathrm{out}|\mathcal{O}_k|B\rangle^* = \sum_i S^{1/2}_{ji} A^f_i\,, \tag{10.18}$$

with A^f_i being a real amplitude. Ignoring the constants λ_k, we may consider the amplitudes A^f to represent 'bare' decay amplitudes, in the absence of a final state phases from strong

interactions. In our analysis, these decay amplitudes are taken to be those predicted by naive factorization. Since $S^{1/2}$ is unitary, it holds that

$$\sum_i |\langle i;\mathrm{out}|\mathcal{O}_k|B\rangle|^2 = \sum_i |A_i^f|^2\,, \tag{10.19}$$

so the probability of B decay through the operator $\mathcal{O}_k$ is invariant under rescattering – as expected. In the following, we decompose the scattering matrix as $S = 1 + i\mathcal{T}$.

It is useful to show the $SU(3)$ structures of the non-trivial neutral mesons used in this analysis. We have the pseudo-scalar mesons

$$\begin{aligned} \pi^0 &= \frac{u\bar{u} - d\bar{d}}{\sqrt{2}}\,, \\ \eta_8 &= \frac{u\bar{u} + d\bar{d} - 2s\bar{s}}{\sqrt{6}}\,. \end{aligned} \tag{10.20}$$

The physical η, η' mesons are defined through

$$\begin{pmatrix} \eta \\ \eta' \end{pmatrix} = \begin{pmatrix} \cos\vartheta & -\sin\vartheta \\ \sin\vartheta & \cos\vartheta \end{pmatrix} \begin{pmatrix} \eta_8 \\ \eta_1 \end{pmatrix}, \tag{10.21}$$

with the mixing angle $\vartheta \approx -15^\circ$ [17]. Since the mixing angle is small, we approximate η by η_8. As argued in Section 10.3.1, the η' ($\approx \eta_1$) is not used in the rescattering analysis.

The corresponding vector mesons are

$$\begin{aligned} \rho^0 &= \frac{u\bar{u} - d\bar{d}}{\sqrt{2}}\,, \\ \omega &= \frac{u\bar{u} + d\bar{d}}{\sqrt{2}}\,, \\ \phi &= s\bar{s}\,. \end{aligned} \tag{10.22}$$

For the neutral and charged decays $B \to DP$, one has the factorization amplitudes

$$\begin{aligned} A^f_{D^0\pi^-} &= T + C\,, \\ A^f_{D^+\pi^-} &= T + E\,, \\ A^f_{D^0\pi^0} &= (E - C)/\sqrt{2}\,, \\ A^f_{D^0\eta} &= (E + C)/\sqrt{6}\,, \\ A^f_{D_s^+K^-} &= E\,, \end{aligned} \tag{10.23}$$

where T, C, and E are the color-allowed tree diagram, the color-suppressed internal W-emission, and the W-exchange amplitudes, such as discussed in Eqs. (10.36–10.38). They are decay dependent. We use naive factorization predictions for the unscattered, color-suppressed decay amplitudes. More about this below[6]. The kaon modes are fit simultaneously, for which

$$\begin{aligned} A^f_{D^0K^-} &= T' + C'\,, \\ A^f_{D^+K^-} &= T'\,, \\ A^f_{D^0\bar{K}^0} &= C'\,. \end{aligned} \tag{10.24}$$

[6]Using SCET, factorization relations for the color-suppressed, unscattered decay amplitudes of $B \to D^{(*)}P$ have been derived in Ref. [130]. These results could be very different from the corresponding expectations of naive factorization. Unfortunately, however, it is very hard to make quantitative predictions from these factorization relations. Its most useful applications are to ratios of decay amplitudes.

For the $B\to D^*P$ system, simply replace $T\to T_*$, etc. For $B\to DV$ the difference with respect to the $D^0\eta$ mode is given by

$$\begin{aligned} A^f_{D^0\omega} &= (E_V+C_V)/\sqrt{2}\,, \\ A^f_{D^0\phi} &= 0\,, \end{aligned} \tag{10.25}$$

with the replacement $T\to T_V$, etc.

As it turns out, the rescattering fit works very well when the assumption is made that the same rescattering amplitudes apply to both DP and D^*P. The rescattering matrix $\mathcal{T}$ for the $D^{(*)}P$ modes is

$$\mathcal{T} = r_0\mathbf{1} + \begin{pmatrix} r_e & 0 & 0 & 0 & 0 \\ 0 & r_a & \frac{r_a-r_e}{\sqrt{2}} & \frac{r_a+r_e}{\sqrt{6}} & r_a \\ 0 & \frac{r_a-r_e}{\sqrt{2}} & \frac{r_a+r_e}{2} & \frac{r_a+r_e}{2\sqrt{3}} & \frac{r_a}{\sqrt{2}} \\ 0 & \frac{r_a+r_e}{\sqrt{6}} & \frac{r_a+r_e}{2\sqrt{3}} & \frac{r_a+r_e}{6} & \frac{r_a-2r_e}{\sqrt{6}} \\ 0 & r_a & \frac{r_a}{\sqrt{2}} & \frac{r_a-2r_e}{\sqrt{6}} & r_a \end{pmatrix} \tag{10.26}$$

where the basis $[D^{(*)0}\pi^-, D^{(*)+}\pi^-, D^{(*)0}\pi^0, D^{(*)0}\eta, D_s^{(*)+}K^-]$ is used. For $D^{(*)}K$ one has

$$\mathcal{T} = \begin{pmatrix} r_0+r_e & 0 & 0 \\ 0 & r_0 & r_e \\ 0 & r_e & r_0 \end{pmatrix} \tag{10.27}$$

with the basis $[D^{(*)0}K^-, D^{(*)+}K^-, D^{(*)0}\bar{K}^0]$.

The matrix elements can be interpreted as follows. The charged modes $D^{(*)0}\pi^-$ and $D^{(*)0}K^-$ only rescatter amongst themselves. That means $(1{+}ir_0{+}ir_e)$ has amplitude 1 and only gives a phase change. Using Fig. 10.5, this can happen through singlet exchange and by charge exchanging the $\bar{u}$ quarks between the mesons. The mode $D^{(*)+}\pi^-$ can rescatter to $D^{(*)0}\pi^0$ by annihilating the d and $\bar{d}$ quarks into $u\bar{u}$, or charge exchanging the $\bar{u}$ and $\bar{d}$. The minus sign and factor of $1/\sqrt{2}$ account for the creation a π^0 through a $(+)$ $u\bar{u}$ or $(-)$ $d\bar{d}$ quark pair, as in Eq. (10.20).

To obtain the $S^{1/2}$ matrix the following substitutions are performed

$$\begin{aligned} 1+ir_0 &= \frac{1}{2}(1+e^{i2\delta'}) \\ ir_e &= \frac{1}{2}(1-e^{i2\delta'}) \\ ir_a &= \frac{1}{8}(-1-2e^{i2\delta'}+3e^{i2\theta})\,. \end{aligned} \tag{10.28}$$

The angles δ' and θ are the two rescattering phases in the $D^{(*)}P$ system that we fit for. The matrix $S^{1/2}$ is obtained by dividing the phases in S by two; we do not show it here.

The scattering matrix of the DV system is taken to be of the form [125]

$$\mathcal{T}_V = r_0\mathbf{1} + \begin{pmatrix} r_e & 0 & 0 & 0 & 0 & 0 \\ 0 & r_a & \frac{r_a-r_e}{\sqrt{2}} & \frac{r_a+r_e}{\sqrt{2}} & r_a & 0 \\ 0 & \frac{r_a-r_e}{\sqrt{2}} & \frac{r_a+r_e}{2} & \frac{r_a+r_e}{2} & \frac{r_a}{\sqrt{2}} & 0 \\ 0 & \frac{r_a+r_e}{\sqrt{2}} & \frac{r_a+r_e}{2} & \frac{r_a+r_e}{2} & \frac{r_a}{\sqrt{2}} & 0 \\ 0 & r_a & \frac{r_a}{\sqrt{2}} & \frac{r_a}{\sqrt{2}} & r_a & r_e \\ 0 & 0 & 0 & 0 & r_e & 0 \end{pmatrix}, \tag{10.29}$$

using the basis $[D^0\rho^-, D^+\rho^-, D^0\rho^0, D^0\omega, D_s^+K^{*-}, D^0\phi]$. The $\mathcal{T}_V$ matrix for DK^* is the same as in Eq. (10.27). As already mentioned in Section 10.3.1, for the DV modes the annihilation amplitude is zero. As a result, one obtains

$$\begin{aligned} 1 + ir_0 &= \frac{1}{2}(1 + e^{i2\delta'_V}) \\ ir_e &= \frac{1}{2}(1 - e^{i2\delta'_V}) \\ ir_a &= 0\,, \end{aligned} \tag{10.30}$$

with the sole free fit parameter δ'_V.

In our study all branching fractions, masses, lifetimes, CKM-matrix elements, and decay constants are taken from the PDG [17], except where indicated below. The (average) form factor estimates are copied from Table 1 in Ref. [125], except that, inspired by our observations at the end of Section 10.2.1, we lower $A_0^{B\to\rho}(m_D^2)$ from 0.33 to 0.26. From the CLEO measurement of $B^0 \to D^- l^+ \nu$ [131] we derive (and fix) $V_{cb}F_{0,1}^{B\to D}(m^2_{\pi,K,\rho}) = 0.0250 \pm 0.0035$. Similarly, from the *BABAR* measurement of $B^0 \to D^{*-} l^+ \nu$ we find $V_{cb}A_0^{B\to D^*}(m^2_{\pi,K}) = 0.0258 \pm 0.0008$ [132]. The decay constants are set to $f_B = 185$ MeV [122], $f_\eta = 182$ MeV [121], $f_\omega = 195$ MeV [104], $f_{K^*} = 217$ MeV [104]. $f_{D_s^{(*)}} = 274$ MeV as in Eq. (10.2.1), and finally $f_{D^{(*)}} = 223$ MeV [135]. The branching fractions of $\overline{B}^0 \to D^{(*)0}\bar{K}^{(*)0}$ are taken from Refs. [133, 134]. The branching fractions of $B^0 \to D_s^{(*)-}K^+$ are averaged in Table 10.15 [116, 117]. As in Section 10.2, we take 1.02 for the Wilson coefficient a_1.

The rescattering fit involves 25 CKM-favored decays of $B \to D^{(*)}P$ (2×8) and $B \to DV$ (9). The decay $\mathcal{B}(\overline{B}^0 \to D^0\phi)$ has not been measured, which leaves 24 branching fractions measurements. Some of the measurements have been carried out on larger datasets than others. One of these, $\mathcal{B}(B^0 \to D_s^- K^{*+})$, measured by CLEO, is only a (loose) limit, and contributes little weight to fit.

The three rescattering phases δ', θ, and δ'_V are determined in the fit. We also float the exchange amplitudes E, E_*, and E_V. Last, we fit for the Wilson coefficient a_2, effectively floating the size of all color-suppressed decay amplitudes C. This gives a total of 7 fit parameters, and 17 d.o.f.

The results of our study are shown in Tables 10.6 and 10.7. The rescattering phases found are consistent with those in Ref. [125], with χ^2/d.o.f. $= 15.0/17$. The correlation of δ' to θ is +68%. As seen in Table 10.6, the rescattering model describes all branching fractions remarkably well. All color-suppressed modes are dominated by rescattering effects from the color-allowed decays. Retroactively, this justifies the use of naive factorization predictions for unscattered, color-suppressed decay amplitudes. (For example, setting $a_2 = 0$ still gives reasonable branching fractions for the color-suppressed B-decays.)

Interestingly, at the time of writing of Ref. [125], $\mathcal{B}(B^0 \to D_s^{(*)-}K^+)$ and $\mathcal{B}(B^0 \to \bar{D}^{(*)0}K^{(*)0})$ had not yet been measured. By now, these have been found to agree well with the predictions from the rescattering model.

We find $a_2 = 0.20 \pm 0.03$, consistent with the value of 0.18 in Section 10.2 from naive factorization. The fit prefers W-exchange amplitudes consistent with zero, where for all three modes $B^0 \to D^-\pi^+$, $B^0 \to D^{*-}\pi^+$, and $B^0 \to D^-\rho^+$ one has $|E_i/T_i| < 2.9\%$ at 68% C.L., consistent with (and smaller than) the error estimate in Section 10.6.

Decay mode	Factorized $\mathcal{B}$	Rescattered $\mathcal{B}$	Measured $\mathcal{B}$
$B^+ \to \bar{D}^0 \pi^+$	48.2	48.2	49.8 ± 2.9
$B^0 \to D^- \pi^+$	32.3	28.3	27.6 ± 2.5
$B^0 \to \bar{D}^0 \pi^0$	0.46	2.71	2.91 ± 0.28
$B^0 \to \bar{D}^0 \eta$	0.0	1.6	2.2 ± 0.5
$B^0 \to D_s^- K^+$	0.00	0.25	0.27 ± 0.05
$B^+ \to \bar{D}^0 K^+$	3.7	3.7	3.7 ± 0.6
$B^0 \to D^- K^+$	2.5	2.0	2.0 ± 0.6
$B^0 \to \bar{D}^0 K^0$	0.06	0.57	0.52 ± 0.07
$B^+ \to \bar{D}^{*0} \pi^+$	49.7	49.7	46 ± 4
$B^0 \to D^{*-} \pi^+$	31.4	27.4	27.6 ± 2.1
$B^0 \to \bar{D}^{*0} \pi^0$	0.7	2.9	2.7 ± 0.5
$B^0 \to \bar{D}^{*0} \eta$	0.0	1.5	2.6 ± 0.6
$B^0 \to D_s^{*-} K^+$	0.02	0.21	0.18 ± 0.06
$B^+ \to \bar{D}^{*0} K^+$	3.6	3.6	3.6 ± 1.0
$B^0 \to D^{*-} K^+$	2.4	1.9	2.0 ± 0.5
$B^0 \to \bar{D}^{*0} K^0$	0.07	0.56	0.36 ± 0.12
$B^+ \to \bar{D}^0 \rho^+$	101	101	134 ± 18
$B^0 \to D^- \rho^+$	75.9	70.4	77 ± 13
$B^0 \to \bar{D}^0 \rho^0$	0.4	3.3	2.9 ± 1.1
$B^0 \to \bar{D}^0 \omega$	0.1	2.7	2.5 ± 0.6
$B^0 \to D_s^- K^{*+}$	0.00	0.00	0.0 ± 6.6
$B^0 \to \bar{D}^0 \phi$	0.00	0.00	–
$B^+ \to \bar{D}^0 K^{*+}$	5.6	5.6	6.1 ± 2.3
$B^0 \to D^- K^{*+}$	4.0	3.8	3.7 ± 1.8
$B^0 \to \bar{D}^0 K^{*0}$	0.06	0.35	0.40 ± 0.08

Table 10.6: *Fit results from the $SU(3)$ rescattering fit to the neutral and charged decays $B \to D^{(*)} P$ and $B \to DV$. Shown are the factorized, rescattered, and measured branching fractions $\mathcal{B}$. All quoted branching fractions are to be multiplied with 10^{-4}.*

Parameter	Fit value
χ^2/d.o.f.	15.0/17
δ'	0.95 ± 0.04
θ	0.34 ± 0.06
δ'_V	0.54 ± 0.05
a_2	0.20 ± 0.03
$\lvert E \rvert$	$(1.0 \pm 3.0) \times 10^{-3}$ GeV
$\lvert E_* \rvert$	$(1.9 \pm 2.2) \times 10^{-3}$ GeV
$\lvert E_V \rvert$	$(1.5 \pm 5.0) \times 10^{-3}$ GeV

Table 10.7: *Fit results from the $SU(3)$ rescattering fit to the decays $B \to D^{(*)} P$ and $B \to DV$.*

10.3.3 Rescattering after $B^0 \to D_{(s)}^{(*)+}\pi^-$ and $B^0 \to D_{(s)}^{+}\rho^-$

Rescattering is independent of the formation process of the initial mesons produced by the B decay. Therefore, one can take rescattering results from CKM-favored decays, obtained in the previous Section, and apply these to the corresponding CKM-suppressed decay modes, such as $B^0 \to D_{(s)}^{(*)+}\pi^-$ and $B^0 \to D_{(s)}^{+}\rho^-$. In this Section we determine the $SU(3)$ breaking from final state rescattering to be applied to the amplitude ratios of Eq. (10.2).

As the final state $D_s^{(*)+}\pi^-$ has four flavors of quarks, whereas $D^{(*)+}\pi^-$ has only three, one can expect different rescattering effects to happen between both combinations of mesons. Indeed, from Fig. 10.5 it is seen that for $D_s^{(*)+}\pi^-$ annihilation rescattering is not possible. By exchanging the u and s quark, it can only rescatter into $D^{(*)0}K^0$, and vice versa[7]. In comparison, $D^{(*)+}\pi^-$ can rescatter into the modes $D^{(*)0}\pi^0$, $D^{(*)0}\eta$, $D_s^{(*)+}K^-$, and vice versa. The same holds for $D_s^+\rho^-$ versus $D^+\rho^-$. For averaging purposes, we also study $D_s^+\pi^0$, which scatters quasi-elastically with D^0K^+, D^+K^0, and $D_s^+\eta$.

The rescattering matrix of $D^{(*)+}\pi^-$ is given in Eq. (10.26), with the rescattering parameters δ' and θ. For $D_s^{(*)+}\pi^-$ ($D_s^+\rho^-$) copy Eq. (10.27), with rescattering parameters δ' and θ (δ'_V), using the basis $[D_s^{(*)+}\pi^-, D^{(*)0}K^0]$ ($[D_s^+\rho^-, D^0K^{*0}]$). And similarly, for $D^+\rho^-$ use Eq. (10.29), with parameter δ'_V, only selecting the neutral block matrices. The rescattering matrix of $D_s^+\pi^0$ is given by

$$\mathcal{T} = r_0\mathbf{1} + \begin{pmatrix} 0 & \frac{r_e}{\sqrt{2}} & -\frac{r_e}{\sqrt{2}} & 0 \\ \frac{r_e}{\sqrt{2}} & r_a & r_a & \frac{r_e-2r_a}{\sqrt{6}} \\ -\frac{r_e}{\sqrt{2}} & r_a & r_a & \frac{r_e-2r_a}{\sqrt{6}} \\ 0 & \frac{r_e-2r_a}{\sqrt{6}} & \frac{r_e-2r_a}{\sqrt{6}} & \frac{2r_e+2r_a}{3} \end{pmatrix}, \tag{10.31}$$

with the basis $[D_s^+\pi^0, D^0K^+, D^+K^0, D_s^+\eta]$. Note that the elastic rescattering amplitude for $D_s^+\pi^0$ is the same as for $D_s^+\pi^-$, and this means that taking the average of $\mathcal{B}(B^+ \to D_s^+\pi^0)$ and $\mathcal{B}(B^0 \to D_s^+\pi^-)$ in Table 10.5 is justified.

An important point in Table 10.6 is that the CKM-favored, color-allowed modes $B^0 \to D^{(*)-}\pi^+$ and $B^0 \to D^-\rho^+$ hardly receive any rescattering contributions from the color-suppressed decays. In other words, for all intents and purposes, rescattering occurs in one direction only. The same holds for the CKM-suppressed decays. So, for example, to estimate the effect of rescattering on $B^0 \to D^+\pi^-$ relative to the factorized amplitude, to first order one only needs the elastic matrix element $S_{(D^+\pi^-;\, D^+\pi^-)}$, and not the (factorized) CKM-suppressed, color-suppressed decay amplitudes.

Using the same technique and constants as in the previous Section, *i.e.* Eqs. (10.14) and (10.16), combined with $V_{ub} = (3.67 \pm 0.47) \times 10^{-3}$ [17], we calculate the branching fractions of Table 10.8. Here we have used the corresponding $SU(3)$ amplitude relations of Eqs. (10.23–10.25) in Table 14. (For completeness it includes B_s decays.) In Table 14 A is the 'annihilation amplitude' in charged B decays, where the b and $\bar{u}$ quarks annihilate into a W (not related to rescattering). Like the W-exchange amplitude, it is expected to be negligible. In our computations we have set it to zero.

Rescattering reduces the factorized branching fractions of $B^0 \to D_s^{(*)+}\pi^-$ by 20%. The

[7] One might wonder if the state $D^0\bar{K}^0$, obtained from the CKM-favored decay of $\overline{B}^0$, can oscillate into D^0K^0 and from thereon rescatter into $D_s^+\pi^-$. This however implies that, before it can possibly rescatter, the D^0 and K^0 will be tens of centimeters apart in the B rest frame, at which point we assume strong rescattering effects to be negligible.

Decay mode	Factorized $\mathcal{B}$	Rescattered $\mathcal{B}$	Measured $\mathcal{B}$
$B^0 \to D_s^+ \pi^-$	2.87 [Eq. 10.16]	2.29	1.7 ± 0.4
$B^0 \to D^0 K^0$	0.10	0.68	–
$B^0 \to D_s^{*+} \pi^-$	2.75	2.19	3.0 ± 0.8
$B^0 \to D^{*0} K^0$	0.12	0.67	–
$B^0 \to D_s^+ \rho^-$	1.91	1.78	0.2 ± 0.8
$B^0 \to D^0 K^{*0}$	0.10	0.23	0.0 ± 0.6 [134]
$B^+ \to D_s^+ \pi^0$	1.56	1.25	0.9 ± 0.2
$B^+ \to D^0 K^+$	0.11	0.37	–
$B^+ \to D^+ K^0$	0	0.07	–
$B^+ \to D_s^+ \eta$	0.18	0.18	–

Table 10.8: *Factorized, rescattered, and measured branching fractions $\mathcal{B}$ predicted for $B \to D_s^{(*)+}\pi/\rho$. All branching fractions are to be multiplied with 10^{-5}.*

	Decay	Amplitude		Decay	Amplitude
$\bar{B}^- \to$	$D^- \bar{K}^0$	$-A$	$\bar{B}^- \to$	$D^- \pi^0$	$-\frac{1}{\sqrt{2}}(T+A)$
	$\bar{D}^0 K^-$	$C+A$		$\bar{D}^0 \pi^-$	$C+A$
	$\bar{D}_s^- \pi^0$	$-\frac{1}{\sqrt{2}}T$		$\bar{D}_s^- K^0$	$-A$
	$\bar{D}_s^- \eta$	$-\frac{1}{\sqrt{6}}T$		$D^- \pi^0$	$-\frac{1}{\sqrt{6}}(T+A)$
$\bar{B}^0 \to$	$\bar{D}^0 \bar{K}^0$	C	$\bar{B}^0 \to$	$\bar{D}^- \pi^+$	$T+E$
	$\bar{D}_s^- \pi^+$	T		$\bar{D}^0 \pi^0$	$\frac{1}{\sqrt{2}}(C-E)$
				$\bar{D}_s^- K^+$	E
				$\bar{D}^0 \eta$	$\frac{1}{\sqrt{6}}(C+E)$
$\bar{B}_s \to$	$D^- \pi^+$	E	$\bar{B}_s \to$	$D^- K^+$	T
	$\bar{D}^0 \pi^0$	$-\frac{1}{\sqrt{2}}E$		$\bar{D}^0 K^0$	C
	$\bar{D}_s^- K^+$	$T+E$			

Table 10.9: *SU(3) predictions for a) $\Delta S = 1$ and b) $\Delta S = 0$ non-leptonic wrong-charm $B \to D\pi$ decays, expressed in terms of quark diagram topological amplitudes.*

reduction is only 6.8% for $B^0 \to D_s^+ \rho^-$. Table 10.10 shows the corresponding branching ratios including errors. The uncertainties from rescattering are either small or negligible.

All measured branching ratios in Table 10.5 are consistent with the predictions from factorization and rescattering within the errors. We will discuss the implications in Section 10.5.

By the same procedure, the factorizable and rescattered branching fractions of the CKM-suppressed decays $B^0 \to D^{(*)+}P^-$ and $B^0 \to D^{(*)+}V^-$ are given in Table 10.11.

As a small side-step, the branching fraction of $B^+ \to D^0 K^+$ in Table 10.8 is fully dominated by rescattering effects from the color-allowed decay $B^+ \to D_s^+ \pi^0$. For this reason, it is about twice as small as $\mathcal{B}(B^0 \to D^{0(*)} K^0)$. The branching ratio $\mathcal{B}(B^0 \to D^0 K^{*0})$ is even smaller, as it cannot be reached through annihilation rescattering. Using $\mathcal{B}(B^+ \to \bar{D}^0 K^+) = (3.7 \pm 0.6) \times 10^{-4}$ from Table 10.6, we find $|A(B^+ \to D^0 K^+)/A(B^+ \to \bar{D}^0 K^+)| \approx 0.09$. (Similarly, $|A(B^+ \to D^0 \pi^+)/A(B^+ \to \bar{D}^0 \pi^+)| \approx 0.003$.)

Decay	Predicted $\mathcal{B}$ ($\times 10^{-5}$)	Eq.
$B^0 \to \pi^- D_s^+$	$2.6 \pm 0.6\,(\text{exp.}) \pm 0.2\,(\text{ff.}) \pm 0.2\,(\text{lat.}) \pm 0.4\,(f_{D_s}) \pm 0.1\,(\text{rsc.})$	10.12
	$2.3 \pm 0.3\,(\text{exp.}) \pm 1.0\,(\text{ff.}) \pm 0.3\,(f_{D_s^*})$	10.16
$B^0 \to \pi^- D_s^{*+}$	$2.2 \pm 0.3\,(\text{exp.}) \pm 0.3\,(f_{D_s^*})$	
$B^0 \to \rho^- D_s^+$	$1.1 \pm 0.7\,(\text{exp.}) \pm 0.2\,(f_{D_s})$ (*)	
$B^0 \to \rho^- D_s^{*+}$	$1.9 \pm 1.1\,(\text{exp.}) \pm 0.3\,(f_{D_s^*})$	

Table 10.10: *Predicted branching ratios $\mathcal{B}$ for $B^0 \to h^- D_s^{(*)+}$, based on N_c-QCD factorization, after rescattering. See Table 10.4 for the corresponding branching ratios with errors without rescattering. (*) We have guesstimated the fraction of longitudinal polarization in $B^0 \to \rho^- D_s^{*+}$ to be* 0.6.

Decay mode	Factorized $\mathcal{B}$ ($\times 10^{-7}$)	Rescattered $\mathcal{B}$ ($\times 10^{-7}$)
$B^0 \to D^+ \pi^-$	10.10	8.88
$B^0 \to D^0 \pi^0$	0.12	0.78
$B^0 \to D^0 \eta$	0.02	0.47
$B^0 \to D_s^+ K^-$	0.00	0.10
$B^0 \to D^{*+} \pi^-$	10.13	8.92
$B^0 \to D^{*0} \pi^0$	0.15	0.81
$B^0 \to D^{*0} \eta$	0.03	0.47
$B^0 \to D_s^{*+} K^-$	0.00	0.10
$B^0 \to D^+ \rho^-$	6.88	6.40
$B^0 \to D^0 \rho^0$	0.12	0.37
$B^0 \to D^0 \omega$	0.08	0.31
$B^0 \to D_s^+ K^{*-}$	0.00	0.00

Table 10.11: *Predictions (without errors) for the factorized and rescattered branching fractions $\mathcal{B}$ of the neutral decays $B^0 \to D^{(*)+} P^-$ and $B^0 \to D^+ V^-$.*

From the substitutions in Eqs. (10.28) and (10.30) let us define the rescattering amplitudes with phases divided by two as $\bar{r}_i$. In that case, *e.g.* $|S^{1/2}_{(D^+\pi^-;\, D^+\pi^-)}| \approx |1 + i\bar{r}_0 + i\bar{r}_a|$. Recall that $\bar{r}_a = 0$ for $D^+\rho^-$. As argued, the modes $D_s^{(*)+}\pi^-$ cannot rescatter through annihilation. The rescattering effects on $\mathcal{B}(B^0 \to D^{(*)+}\pi^-)$, 12%, are smaller than on $\mathcal{B}(B^0 \to D_s^{(*)+}\pi^-)$, as the annihilation amplitude tends to cancel the singlet exchange amplitude.

For mode i, the $SU(3)$ correction factor due to final state rescattering, needed for Eq. (10.2), is written as

$$R_i = \left(\frac{p_{D^{(*)}}}{p_{D_s^{(*)}}}\right)^{\frac{2L+1}{2}} \left| \frac{A^{f;CS}_{D^{(*)+}\pi^-}(1 + i\bar{r}_0 + i\bar{r}_a) + A^{f;CS}_{D^{(*)0}\pi^0}(i\bar{r}_a - i\bar{r}_e)/\sqrt{2} + A^{f;CS}_{D^{(*)0}\eta}(i\bar{r}_a + i\bar{r}_e)/\sqrt{6}}{A^{f;CS}_{D_s^{(*)+}\pi^-}(1 + i\bar{r}_0) + A^{f;CS}_{D^{(*)0}K^0}(i\bar{r}_e)} \right|$$
$$\approx \left(\frac{p_{D^{(*)}}}{p_{D_s^{(*)}}}\right)^{\frac{2L+1}{2}} \left| \frac{1 + i\bar{r}_0 + i\bar{r}_a}{1 + i\bar{r}_0} \right|. \qquad (10.32)$$

where, in the factorized, CKM-suppressed decay amplitudes $A^{f;CS}$, we ignore all CKM-matrix

elements and decay constants, as these are already accounted for in Eq. (10.2), and $A^{f;CS}_{D_s^{(*)+}K^-} = 0$. In step two we neglect all (other) color-suppressed decay amplitudes. We have included the (small) $SU(3)$-breaking momentum factor seen in Eq. (10.5), with L the angular momentum of the B decay. The various correction factors R_i have been summarized in Table 10.12. They are larger than one, because of the effect indicated in the previous paragraph, and because the $D^{(*)}$ is lighter than the $D_s^{(*)}$.

Final state	R_i
$D^+\pi^-$	1.0750 ± 0.0046
$D^{*+}\pi^-$	1.1014 ± 0.0047
$D^+\rho^-$	1.0356

Table 10.12: *$SU(3)$ correction factor for Eq. (10.2) due to rescattering effects and momentum factors. The error comes from soft rescattering.*

10.4 Amplitude ratios

Following the techniques in Section 10.2.1, Eq. (10.1) allows us to make the predictions for the amplitude ratio $r^{D^{(*)}\pi}$ in Table 10.13, based on the combination of naive factorization followed by rescattering. We use $f_{D^{(*)}} = 223 \pm 17$ MeV [135], $V_{cd} = 0.224 \pm 0.012$, $\mathcal{B}(B^0 \to D^-\pi^+) = (2.76 \pm 0.25) \times 10^{-3}$, and $\mathcal{B}(B^0 \to D^{*-}\pi^+) = (2.76 \pm 0.21) \times 10^{-3}$ [17].

Decay	Predicted $r^{D^{(*)}\pi}$ ($\times 10^{-2}$)	Eq.
$B^0 \to D^{\mp}\pi^{\pm}$	$1.92 \pm 0.22\,(\text{exp.}) \pm 0.14\,(f_D) \pm 0.12\,(V_{cd}\text{ff.}) \pm 0.01\,(\text{rsc.}) \pm 0.09\,(\text{lat.})$	10.12
	$1.79 \pm 0.15\,(\text{exp.}) \pm 0.13\,(f_D) \pm 0.41\,(V_{cd}\text{ff.}) \pm 0.01\,(\text{rsc.})$	10.16
$B^0 \to D^{*\mp}\pi^{\pm}$	$1.80 \pm 0.13\,(\text{exp.}) \pm 0.13\,(f_D) \pm 0.09\,(V_{cd}) \pm 0.01\,(\text{rsc.})$	

Table 10.13: *Predicted amplitude ratios $r^{D^{(*)}\pi}$ for $B^0 \to D^{(*)\mp}\pi^{\pm}$, based on N_c-QCD factorization, after rescattering.*

These ratios can be compared with the corresponding predictions from Eq. (10.2), assuming $SU(3)$ flavor symmetry, as obtained from the measured branching fractions for $B^0 \to h^- D_s^{(*)+}$ in Table 10.5, and using the $SU(3)$ corrections in Table 10.12. The estimates are listed in Table 10.14. We use $\mathcal{B}(B^0 \to D^-\rho^+) = (7.7 \pm 1.3) \times 10^{-3}$ [17], $F(m^2_{D^{(*)}})/F(m^2_{D_s^{(*)}}) = 1$ (see Fig. 10.3), $\tan\theta_c = 0.225 \pm 0.018$ [17], and from lattice QCD $f_{D_s^{(*)}}/f_{D^{(*)}} = 1.24 \pm 0.07$ [136, 115].

Notice that the ratio of $f_{D^{(*)}}/f_{D_s^{(*)}}$ is far better known than the measured value of $f_{D^{(*)}}$, and that the errors from rescattering are negligible. The ratio $r^{D\pi}$ using $SU(3)$ symmetry is more precise, and both estimates of $r^{D\pi}$ are consistent within 1 sigma.

Also compare the numbers in Table 10.13 with those in Table 10.1. Notice that, in Table 10.1, one has $r^{D^*\pi} > r^{D\pi}$, whereas here that equality is reversed. It is not clear from Ref. [86] which exact numbers have been used to calculate the amplitude ratios, but the difference with Table 10.13 can be attributed to several factors.

Decay	Predicted $r^{D^{(*)}h}$ ($\times 10^{-2}$)
$B^0 \to D^{\mp}\pi^{\pm}$	$1.526 \pm 0.183\,(\mathcal{B}) \pm 0.086\,(r.f_D) \pm 0.118\,(V_{cq}) \pm 0.006\,(\text{rsc.})$
$B^0 \to D^{*\mp}\pi^{\pm}$	$2.102 \pm 0.286\,(\mathcal{B}) \pm 0.121\,(r.f_D) \pm 0.165\,(V_{cq}) \pm 0.008\,(\text{rsc.})$
$B^0 \to D^{\mp}\rho^{\pm}$	$0.313 \pm 0.590\,(\mathcal{B}) \pm 0.021\,(r.f_D) \pm 0.021\,(V_{cq})$

Table 10.14: *Predicted amplitude ratios $r^{D^{(*)}\pi}$ for $B^0 \to D^{(*)\mp}\pi^{\pm}$, based on $SU(3)$ flavor symmetry and rescattering. The errors are from the branching ratios and the error on $f_{D^{(*)}}/f_{D_s^{(*)}}$ respectively.*

1. The difference $f_+(m^2_{D^*}) - f_0(m^2_D)$ was probably bigger, since the uncertainties on the form factors were bigger at the time. This difference is model-dependent, clearly, since $r^{D^*\pi}/r^{D\pi}$ is not stable in Table 10.1.

2. In 2001 the measured branching ratio was $\mathcal{B}(B^0 \to D^-\pi^+) = (3.0 \pm 0.4) \times 10^{-3}$, larger than the current value.

3. Possibly, Ref. [86] uses a value for f_{D^*} larger than f_D.

As already made clear in Section 10.1, we will not use the amplitudes ratios in Table 10.1 for the extraction of the *CP*-angle γ.

It should be stressed that the amplitude ratios in Tables 10.13 and 10.14 (and Table 10.1) do not take into account the additional errors from neglected W-exchange diagrams, non-factorizable corrections, and/or higher-order $SU(3)$ breaking effects. These errors are discussed in Sections 10.6 and 10.7 respectively.

10.5 Non-factorizable corrections in $B^0 \to \pi^- D_s^{*+}$

The measured and predicted branching fractions of $B^0 \to \pi^- D_s^{(*)+}$ and $B^0 \to \rho^- D_s^{(*)+}$ in Tables 10.5 and 10.10 allow us to scale the size of possible non-factorizable contributions in $b \to u$ transitions.

The measured predicted branching fractions agree well with those predicted using the factorization hypothesis. The measured $\mathcal{B}(B^0 \to \pi^- D_s^+)$ comes out a little low, whereas $\mathcal{B}(B^0 \to \pi^- D_s^{*+})$ is somewhat high. The most precise prediction from factorization can be made for $\mathcal{B}(B^0 \to \pi^- D_s^{*+})$, as it relates directly to $B^0 \to \pi^- l^+ \nu$. The other predicted branching fractions are less precise, as they have large(r) theoretical and/or systematic uncertainties.

Given the additional uncertainties, the most powerful constraint on the size of non-factorizable contributions – now and in the future – is derived using $B^0 \to \pi^- D_s^{*+}$, for which the branching fraction prediction is most precise. The change in the decay amplitude by non-factorizable contributions, relative to a_1, is defined as $\tilde{a}_s^{\text{corr}}$. Using $\tilde{a}_s^{\text{corr}}$, the ratio of the measured over predicted amplitude ratio for $\mathcal{B}(B^0 \to \pi^- D_s^{*+})$ can be written as

$$\frac{\mathcal{B}_{\text{meas}}(B^0 \to \pi^- D_s^{*+})}{\mathcal{B}_{\text{resc}}(B^0 \to \pi^- D_s^{*+})} = |1 + \tilde{a}_s^{\text{corr}}|^2 = 1.370 \pm 0.376\,(\text{exp.}) \pm 0.200\,(f_{D_s^*}) \pm 0.028\,(\text{rsc.})\,,$$

which results in

$$|1 + \tilde{a}_s^{\text{corr}}| = 1.170 \pm 0.181\,. \tag{10.33}$$

In the factorization scenario, non-factorizable terms are expected to be less than leading order, *i.e.* $|\tilde{a}_s^{\rm corr}| < 1$, instead of, for example, the solution $\tilde{a}_s^{\rm corr} \approx -2$. As a result, to first order

$$|1+\tilde{a}_s^{\rm corr}| \approx 1 + \mathcal{R}e(\tilde{a}_s^{\rm corr}) + \tfrac{1}{2}|\tilde{a}_s^{\rm corr}|^2\,, \tag{10.34}$$

so

$$\begin{aligned}\left|\frac{\mathcal{R}e(\tilde{a}_s^{\rm corr}) + \frac{1}{2}|\tilde{a}_s^{\rm corr}|^2}{|1+\tilde{a}_s^{\rm corr}|^2}\right| &\approx \left|\frac{1}{|1+\tilde{a}_s^{\rm corr}|} - \frac{1}{|1+\tilde{a}_s^{\rm corr}|^2}\right| \\ &< 0.211\ (0.317)\ @\ 68\%\ (90\%)\ {\rm CL}\,. \end{aligned} \tag{10.35}$$

The limit should improve with improved measurements of $B^0 \to \pi^- D_s^{*+}$ and $B^0 \to \pi^- l^+ \nu$. We use this limit on the relative size of non-factorizable contributions in Section 10.7.

10.6 The W-exchange amplitude

The W-exchange amplitude (E) in Fig. 10.6 involves an interaction of the b quark with the spectator quark. As argued in Refs. [138, 139], for a decay like this to happen, the two quarks in the meson must 'find' each other, and hence the decay amplitude contains a factor of $f_B/m_B \approx 0.036$, where $f_B \approx 0.19$ GeV is the B decay constant [122]. Also, the diagram is color-suppressed. Color suppression happens because a $d\bar{d}$ quark pair is produced from the vacuum, and only $1/N_c = 1/3^{\rm rd}$ of the possibilities of producing this pair will be aligned in color with the $\bar{u}$ and c quarks. A naive estimate then gives the ratio of the exchange over color-allowed tree diagram in Fig. 10.6 to be at the level of 1% [138].

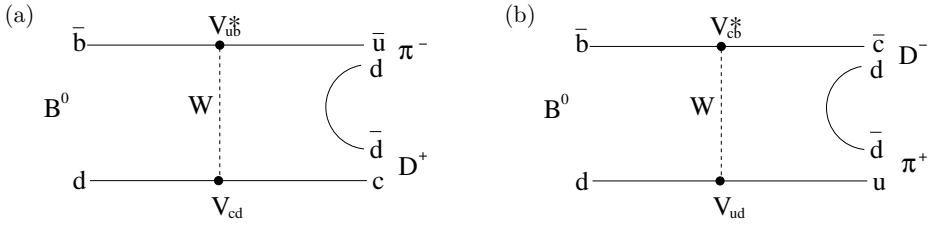

Figure 10.6: *Color-suppressed W-exchange diagram of: (a) CKM-allowed decay $B^0 \to D^-\pi^+$, and (b) doubly-CKM-suppressed decay $B^0 \to D^+\pi^-$.*

In the following Sections we discuss two methods to constrain the ratio of the W-exchange diagram E over the color-allowed tree diagram T.

10.6.1 $B^0 \to D_s^{(*)-} K^+$

In the literature it is sometimes argued [140] that the Cabibbo-favored decays $B^0 \to D_s^{(*)-} K^+$ can be used to constrain E, since, naively speaking, these decays are only possible through a pure W-exchange[8]. The measured branching ratios $\mathcal{B}(B^0 \to D_s^{(*)-} K^+)$ are given in Table 10.15. For an example of the corresponding decay, see Fig. 10.6a, and replace the $d\bar{d}$ quark pair by

[8] In Ref. [140] W-exchange is implicitly defined as the combination of pure W-exchange and rescattering.

Decay	Measured $\mathcal{B}$ ($\times 10^{-5}$)	Ref.
$B^0 \to D_s^- K^+$	$2.5 \pm 0.4 \pm 0.4$	[116]
$B^0 \to D_s^- K^+$	$4.6^{+1.2}_{-1.1} \pm 1.3$	[117]
$B^0 \to D_s^- K^+$	2.71 ± 0.54	WA
$B^0 \to D_s^{*-} K^+$	$1.8 \pm 0.5 \pm 0.3$	[116]

Table 10.15: *Measured branching ratios $\mathcal{B}$ for $B^0 \to D_s^{(*)-} K^+$.*

$s\bar{s}$. As a result, supposedly

$$|E/T|^2 = \mathcal{B}(B^0 \to D_s^{(*)-} K^+)/\mathcal{B}(B^0 \to D^{(*)-} \pi^+) \simeq 10^{-2}$$

for $b \to c$ transitions, or $|E/T| \lesssim 0.1$. A similar suppression is then assumed to hold for the Cabibbo-suppressed $b \to u$ decays.

However, as shown in Section 10.3, the higher-than-predicted rates for $B^0 \to \bar{D}^{(*)0} h^0$ ($h^0 = \pi^0, \omega, \eta, \rho^0$) [141] proof that final state interactions from $B^0 \to D^{(*)-} \pi^+$ contribute appreciably to this mode. A qualitative estimate of the pure W-exchange amplitude in Ref. [145] gives the prediction of $\mathcal{B}(B^0 \to D_s^{(*)-} K^+) = 6.5 \times 10^{-8}$, which is about 400 times smaller than observed. Hence, interpreting $\mathcal{B}(B^0 \to D_s^{(*)-} K^+)$ solely in terms of the W-exchange amplitude does not give a reliable estimate of E – any such estimate is far too conservative.

The rescattering fit to the CKM-favored decays in Section 10.3, which decouples rescattering effects from W-exchange, gives estimates of the amplitudes E consistent with zero. For all three modes $B^0 \to D^- \pi^+$, $B^0 \to D^{*-} \pi^+$, and $B^0 \to D^- \rho^+$ one has $|E/T| < 2.9\%$ at 68% C.L.

As discussed in Ref. [87], due to the unknown non-factorizable contributions, it is not clear that a correct estimate for E/T from $b \to c$ transitions can be related to the corresponding $b \to u$ ratio. For this reason, we shall not use $B^0 \to D_s^{(*)-} K^+$ decays to constrain the pure W-exchange diagram E for the CKM-suppressed decays $B^0 \to \pi^- D^{(*)+}$.

10.6.2 Other experimental modes

Other decay modes mediated by a W-exchange between the b and spectator quark are $B^0 \to D^0 \overline{D}^0$ or $B^0 \to D_s^+ D_s^-$ [144]. However, for the same reason as for $B^0 \to D_s^{(*)-} K^+$, the corresponding branching fractions should be considerably enhanced by rescattering effects from color-allowed $B^0 \to D^{(*)} D^{(*)}$ tree decays.

A recent idea from Pirjol [100] has been to study the wrong-charm decay $B^0 \to K^- D_s^{(*)+}$, through a W-exchange and $b \to u$ transition (similar to the W-exchange wrong-charm decay of $B^0 \to \pi^- D^{(*)+}$ in Fig. 10.6b), using a time-dependent analysis of $B^0 \to D_s^{(*)\mp} K^\pm$. However, this decay is dominated by rescattering from the color-allowed tree amplitude of the wrong-charm decay $B^0 \to \pi^- D^{(*)+}$ in Fig. 10.6b.

Again, any 'limit' on E – from both of the latter two methods – is actually be a limit on the size of rescattering. A qualitative estimate of the pure W-exchange contribution of $|E/T|$ is calculated in the next Section.

10.6.3 Factorization prediction

A better estimate of the W-exchange amplitude involved in the CKM-suppressed decay $B^0 \to \pi^- D^+$ can be obtained using naive factorization. We apply the effective Hamiltonian in Eq. (10.3). Assuming factorization, the CKM-suppressed, color-allowed tree amplitude of $\langle \pi^- D^+ | \mathcal{H}_W | B^0 \rangle$ is

$$\begin{aligned} T &= \frac{G_F}{\sqrt{2}} V_{ub} V_{cd}^* \left(C_1(m_B) + \frac{C_2(m_B)}{N_c} \right) \langle D^+ | (\bar{d}c)_{V-A} | 0 \rangle \langle \pi^- | (\bar{u}b)_{V-A} | B^0 \rangle \\ &= \frac{G_F}{\sqrt{2}} V_{ub} V_{cd}^* \, a_1 \, f_D \, (m_B^2 - m_\pi^2) \, F_0^{B\to\pi}[m_D^2] \,, \end{aligned} \tag{10.36}$$

and similarly for the color-suppressed exchange diagram

$$\begin{aligned} E &= \frac{G_F}{\sqrt{2}} V_{ub} V_{cd}^* \left(C_2(m_B) + \frac{C_1(m_B)}{N_c} \right) \langle \pi^- D^+ | (\bar{u}c)_{V-A} | 0 \rangle \langle 0 | (\bar{d}b)_{V-A} | B^0 \rangle \\ &= \frac{G_F}{\sqrt{2}} V_{ub} V_{cd}^* \, a_2 \, (m_D^2 - m_\pi^2) \, F_0^{0\to D\pi}[m_B^2] \, f_B \,, \end{aligned} \tag{10.37}$$

where $a_1 = [C_1 + C_2/N_c]$ and $a_2 = [C_2 + C_1/N_c]$. For later use we also give the amplitude ($\times\sqrt{2}$) of the color-suppressed decay $B^0 \to \pi^0 D^0$

$$\begin{aligned} C &= \frac{G_F}{\sqrt{2}} V_{ub} V_{cd}^* \left(C_2(m_B) + \frac{C_1(m_B)}{N_c} \right) \langle D^0 | (\bar{u}c)_{V-A} | 0 \rangle \langle \pi^0 | (\bar{d}b)_{V-A} | B^0 \rangle \\ &= \frac{G_F}{\sqrt{2}} V_{ub} V_{cd}^* \, a_2 \, f_D \, (m_B^2 - m_\pi^2) \, F_0^{B\to\pi}[m_D^2] \,, \end{aligned} \tag{10.38}$$

For the amplitude ratio we then have

$$\frac{E}{T} = \frac{a_2}{a_1} \frac{f_B}{f_D} \left(\frac{m_D^2 - m_\pi^2}{m_B^2 - m_\pi^2} \right) \frac{F_0^{0\to D\pi}[m_B^2]}{F_0^{B\to\pi}[m_D^2]} \,. \tag{10.39}$$

The value for $F_0^{B\to\pi}[m_D^2]$ is obtained using Eqs. (10.13) and (10.15), derived from $B^0 \to \pi^+ l^- \nu$ and lattice QCD calculations. We have $F_0^{B\to\pi}[m_D^2] \simeq 0.28$. We estimate $F_0^{0\to D\pi}[m_B^2]$ using the PCAC Callan-Treiman relation [103, 146], $F_0^{0\to D\pi}[m_D^2] \simeq f_D/f_\pi$. Employing p-QCD scaling [148], $F_0^{0\to D\pi} = C/q^2$, results in

$$F_0^{0\to D\pi}[m_B^2] \simeq \frac{m_D^2}{m_B^2} \frac{f_D}{f_\pi} \simeq 0.21 \,,$$

with $f_{\pi^+} = 130.7 \pm 0.4$ MeV [17] and $f_{D^+} = 223 \pm 17$ MeV [135].

The value of $|E/T|$, obtained from Eq. (10.39), is $\approx 1.3\%$, in agreement with the naive estimate of 1%, and also in good agreement with the limit $|E/T| < 2.9\%$ @ 68 % C.L. of Section 10.3.

However, there are a few points missed in this approach.

Most importantly, naive factorization does not work reliably for color-suppressed decays. It is common practice to describe non-factorizable contributions as corrections to the a_1 and a_2 coefficients. In the large N_c limit, where one takes the limit of infinite number of colors, the Wilson coefficients satisfy $a_1 \sim O(1)$ and $a_2 \sim O(1/N_c)$, and one can show that all non-factorizable corrections are at the level of $O(1/N_c^2)$. So, while non-factorizable contributions

are suppressed with $1/N_c^2$ relative to color-allowed decays (a_1), they are $O(1/N_c)$ relative to color-suppressed decays (a_2). Coming back to the color-suppressed amplitude E, the leading order terms neglected in a_2 (of order $O(1/N_c)$) might well be of the same size as those kept.

Second, the $1/q^2$ scaling in the time-like region for the form factor $F_0^{0\to D\pi}$ is not very well established [100]. In this region the form factor is in fact complex due to $D\pi$ rescattering. Not much is known about this, or about form factors in the time-like region. On the other hand, if the charm quark is treated as light, which is clearly justified at $q^2 = m_B^2$, the scaling of the form factor is the same as that of the pion form factor, which is indeed $1/q^2$ [148].

Given these issues, it does not make much sense to improve further on this estimate of E/T. We assign large systematic errors to both effects, and assume conservatively that $|E/T| < 5.0\%$. This value will be used as systematic error[9] for all modes $B^0 \to h^- D^{(*)+}$ in the extraction of the CKM-angle γ in Section 11.7.

10.7 SU(3) breaking from non-factorizable contributions

$SU(3)$ breaking relates to the perturbation parameter $2m_s/\Lambda_\chi$ [149], where m_s is the mass of the strange quark and Λ_χ is the chiral symmetry breaking scale (1 GeV), and is between 16–26%. If $SU(3)$ would be an exact symmetry, in the amplitude ratio of Eq. (10.2) and Eq. (10.32) one would have

$$\Delta = \frac{F(m^2_{D^{(*)}}) f_{D^{(*)}}}{F(m^2_{D_s^{(*)}}) f_{D_s^{(*)}}} R_i = 1\,. \tag{10.40}$$

A natural definition of $SU(3)$ breaking is then $\Delta - 1$.

Remember that Eq. (10.2) has been derived using factorization. Within factorization and rescattering, the main contribution to $SU(3)$ breaking originates from

$$\Delta_0 \equiv \frac{f_{D^{(*)}} F(m^2_{D^{(*)}})}{f_{D_s^{(*)}} F(m^2_{D_s^{(*)}})}\, R_i\,.$$

As the form factor $F(q^2)$ is smooth with no sudden changes, one can set $F(m^2_{D^{(*)}}) = F(m^2_{D_s^{(*)}})$ with negligible error. For example, in Eq. (10.11) this holds at 1% for D^+ and D_s^+. Then $SU(3)$ breaking is due to the difference between the D and D_s decay constants. This ratio has been calculated quite precisely using lattice QCD, $f_{D_s}/f_D = 1.24 \pm 0.07$ [136]. A consistent value of 1.25 ± 0.14 has recently been measured on data [115]. Note that $f_{D_s}/f_D - 1$ agrees with $2m_s/\Lambda_\chi$.

Other $SU(3)$ corrections to Eq. (10.40) may appear from (possibly complex) non-factorizable corrections. The error on the scale of $SU(3)$ breaking is therefore directly related to the uncertainty in the factorization assumption. If, using the notation of Eq. (10.4), we denote the non-factorizable corrections as

$$\langle h^- D_{(s)}^{(*)+} | \mathcal{H}_W | B^0 \rangle^{\rm corr} = \frac{G_F}{\sqrt{2}} V_{ub} V_{cq}^*\, a_q^{\rm corr}\, \langle D_{(s)}^{(*)+} | (\bar{q}c)_{V-A} | 0 \rangle \langle h^- | (\bar{u}b)_{V-A} | B^0 \rangle\,, \tag{10.41}$$

[9] In Ref. [147] – discussing a similar technique where γ is obtained from $B^0 \to D^{(*)-} D_{(s)}^{(*)+}$ – the W-exchange diagrams are entirely neglected.

then $|\Delta|$ becomes

$$
\begin{aligned}
|\Delta| &= \Delta_0 \left| \frac{a_1 + a_d^{\rm corr}}{a_1 + a_s^{\rm corr}} \right| && (10.42)\\
&= \Delta_0 \left| \frac{a_1 + a_s^{\rm corr} + a^{\rm c} \cdot 2m_s/\Lambda_\chi}{a_1 + a_s^{\rm corr}} \right| && (10.43)\\
&= \Delta_0 \left| \frac{1 + \tilde{a}_s^{\rm corr} + \tilde{a}^{\rm c} \cdot 2m_s/\Lambda_\chi}{1 + \tilde{a}_s^{\rm corr}} \right| && (10.44)\\
&= \Delta_0 \left| 1 + \bar{a}^{\rm c} \, \frac{2m_s}{\Lambda_\chi} \right| . && (10.45)
\end{aligned}
$$

Note that in Eq. (10.42) the $SU(3)$ ratio expected from factorization, f_D/f_{D_s}, has already been stripped from the non-factorizable terms $f_{D_q} a_q^{\rm corr}$ into Δ_0. However, $SU(3)$ breaking may be larger (or smaller) in the non-factorizable contributions, *i.e.* $a_d^{\rm corr} \neq a_s^{\rm corr}$. In Eq. (10.43) we relate the residual $SU(3)$ breaking to the perturbation scale $2m_s/\Lambda_\chi$, $[a_d^{\rm corr}–a_s^{\rm corr}] = a^{\rm c} \cdot 2m_s/\Lambda_\chi$, since in the $SU(3)$ limit all corrections to $\Delta-1$ should vanish. Recall that a_1 is real and equals 1.02 ± 0.01. In Eq. (10.44) $\tilde{a} = a/a_1$. In Eq. (10.45) we have substituted

$$
\begin{aligned}
\bar{a}^{\rm c} &= \frac{a^{\rm c}}{a_1 + a_s^{\rm corr}} \\
&= \frac{\tilde{a}^{\rm c}}{1 + \tilde{a}_s^{\rm corr}} \, . && (10.46)
\end{aligned}
$$

In Eq. (10.45) the residual $SU(3)$ breaking contribution to Δ_0 therefore is (smaller than) $|\bar{a}^{\rm c}| \cdot 2m_s/\Lambda_\chi$. If we assume $SU(3)$ breaking in non-factorizable terms to be about the same as within factorization, so $[a_d^{\rm corr}–a_s^{\rm corr}] \approx 0$, then, obviously, $|\bar{a}^{\rm c}| \approx 0$. If we relate the residual $SU(3)$ breaking to $2m_s/\Lambda_\chi$, for example $|a_c^{\rm c}| \approx |a_d^{\rm corr}|$ (in this scenario the non-factorizable terms have twice the 'typical' $SU(3)$ breaking), then $|\bar{a}^{\rm c}| \lesssim 1$. Obviously, this constraint becomes stronger as the non-factorizable terms become smaller.

Residual $SU(3)$ breaking then depends on the size of the non-factorizable corrections in $\bar{a}^{\rm c}$. As discussed in Section 10.2, theoretical predictions for non-factorizable contributions vary. SCET does not apply here, and so cannot make any prediction for the non-factorizable terms in $B^0 \to h^- D_{(s)}^{(*)+}$. In N_c-QCD, these are suppressed by $O(1/N_c^2)$. In the *BABAR* $\sin(2\beta+\gamma)$ publications [14, 150], a 30% estimate has been assigned to non-factorizable and higher-order $SU(3)$ breaking effects (including the uncertainty on $|E/T|$), or $|\bar{a}^{\rm c}| \approx 1$. This is equivalent to

$$
\text{Refs. [14, 150]} \quad : \quad |\bar{a}^{\rm c}| = 1 \;\leftrightarrow\; |\bar{a}^{\rm c}| \frac{2m_s}{\Lambda_\chi} \approx 25\% \, . \qquad (10.47)
$$

$$
N_c\text{-QCD} \quad : \quad |\bar{a}^{\rm c}| = O\!\left(\frac{1}{N_c^2}\right) \;\rightarrow\; |\bar{a}^{\rm c}| \frac{2m_s}{\Lambda_\chi} \approx 3\% \, . \qquad (10.48)
$$

One obtains Eq. (10.48) with the prediction from N_c-QCD.

Clearly, compared with N_c-QCD, the *BABAR* error is conservative. As an example, the *BABAR* assumption is equivalent to

1. $a_d^{\rm corr} \simeq a_1$ – the non-factorizable contributions are as large as the factorizable ones,
2. $a^{\rm c} \simeq 2a_d^{\rm corr}$ ($\sqrt{2} a_d^{\rm corr}$) – $SU(3)$ breaking in the non-factorizable terms is 3 ($\sqrt{2}+1$) times the typical size, when $a_d^{\rm corr}$ is real (imaginary).

Indications that factorization works therefore have a large impact on the size of this theoretical error.

We now make an estimate of the residual $SU(3)$ breaking from the measured and predicted branching fraction of $B^0 \to \pi^- D_s^{*+}$ – the one decay mode where a precise prediction of $\mathcal{B}$ can be made using factorization. In Eq. (10.33) it was found that the factorization hypothesis works well. In the assumption that non-factorizable corrections are therefore small ($|\tilde{a}_q^{\rm corr}| < 1$), *e.g.* such as predicted by N_c-QCD, we find the limit in Eq. (10.35).

From Eq. (10.42) we have

$$\begin{aligned}
\left| 1 + \bar{a}^{\rm c} \, \frac{2m_s}{\Lambda_\chi} \right| &= \left| \frac{1+\tilde{a}_d^{\rm corr}}{1+\tilde{a}_s^{\rm corr}} \right| && (10.49)\\
&= \sqrt{\frac{1 + 2\mathcal{R}e(\tilde{a}_d^{\rm corr}) + |\tilde{a}_d^{\rm corr}|^2}{1 + 2\mathcal{R}e(\tilde{a}_s^{\rm corr}) + |\tilde{a}_s^{\rm corr}|^2}} && (10.50)\\
&= \sqrt{1 + \frac{[2\mathcal{R}e(\tilde{a}_d^{\rm corr}) + |\tilde{a}_d^{\rm corr}|^2] - [2\mathcal{R}e(\tilde{a}_s^{\rm corr}) + |\tilde{a}_s^{\rm corr}|^2]}{|1+\tilde{a}_s^{\rm corr}|^2}} && (10.51)\\
&\approx 1 + \frac{[\mathcal{R}e(\tilde{a}_d^{\rm corr}) + \frac{1}{2}|\tilde{a}_d^{\rm corr}|^2] - [\mathcal{R}e(\tilde{a}_s^{\rm corr}) + \frac{1}{2}|\tilde{a}_s^{\rm corr}|^2]}{|1+\tilde{a}_s^{\rm corr}|^2} && (10.52)
\end{aligned}$$

where, in Eq. (10.52), the approximation is to first order. So, for any given estimate of the $SU(3)$ breaking in the non-factorizable terms, one can now take the limit from Eq. (10.35) to constrain $|\bar{a}^{\rm c}|$. If we take the residual $SU(3)$ breaking to be within $[-2 \cdot 2m_s/\Lambda_\chi, 2 \cdot 2m_s/\Lambda_\chi]$, *i.e.* $SU(3)$ breaking in the non-factorizable piece can be up to three times the typical $SU(3)$ breaking scale (around 75%), like in the *BABAR* estimate above, then[10]

$$\begin{aligned}
|\bar{a}^{\rm c}| \frac{2m_s}{\Lambda_\chi} &< 2\,\frac{2m_s}{\Lambda_\chi} \left| \frac{\mathcal{R}e(\tilde{a}_s^{\rm corr}) + \frac{1}{2}|\tilde{a}_s^{\rm corr}|^2}{|1+\tilde{a}_s^{\rm corr}|^2} \right| \\
&< 0.105 \;@\; 68\%\ {\rm CL}\,. && (10.53)
\end{aligned}$$

One of the key ingredient in the $SU(3)$ flavor method is the claim that, within factorization, the leading order $SU(3)$ breaking scale is given by $2m_s/\Lambda_\chi \simeq f_{D_s}/f_D - 1$, and is about 25%. As argued, this has been demonstrated to hold in $B \to D^{(*)} D_{(s)}^{(*)}$ decays [98]. Table 10.16 demonstrates the measured branching fractions and also the square root of the ratio of branching fractions, which should equal $\tan\theta_c \cdot f_D/f_{D_s} = 0.181 \pm 0.018$, as in Eq. (10.2). The measured ratios agree well, indicating that the $SU(3)$ breaking scale is consistent with $2m_s/\Lambda_\chi$.

One might still worry that the estimate of $SU(3)$ breaking is too small based on what happens in D decays. For example, using the above arguments, one would expect $\sin^2\theta_c\,\mathcal{B}(D^0 \to K^-\pi^+)/\mathcal{B}(D^0 \to K^-K^+) \simeq (f_\pi/f_K)^2 = 0.67$. Experimentally, this ratio is found to be 0.50 ± 0.02 [17], meaning 16% additional $SU(3)$ breaking at the amplitude level.

But, as argued by Datta and Londen [147], there are significant differences between D and B decays. (We copy their arguments here.) Factorization is badly broken in $D^0 \to K^-\pi^+/K^-K^+$, where, at lower energies, large rescattering effects are present from nearby resonances [153]. In addition, large exchange contributions are significant in many D decays [154]. At the B mass scale – above 'the resonance region' – there is less rescattering and no evidence of large exchange diagrams [101, 98]. Consequently, these effects are more sizable in D decays, which,

[10] The limit also holds using second order approximations in Eqs. (10.34) and (10.49).

Decay	$\mathcal{B}(B\to D^{(*)}D^{(*)})$ $(\times 10^{-4})$	$\mathcal{B}(B\to D^{(*)}D_s^{(*)})$ $(\times 10^{-2})$	$\sqrt{\text{ratio}}$
$B^0\to D_{(s)}^{*-}D^{*+}$	8.2 ± 0.9	1.9 ± 0.2	0.21 ± 0.02
$B^0\to D_{(s)}^{-}D^{+}$	2.3 ± 0.4	0.8 ± 0.3	0.17 ± 0.04
$B^0\to D_{(s)}^{*\pm}D_{(s)}^{\mp}$	6.1 ± 1.0	2.1 ± 0.6 (*)	0.17 ± 0.03
$B^+\to \overline{D}^{*0}D^{*+}$	8.1 ± 1.7	2.7 ± 1.0	0.17 ± 0.04
$B^+\to \overline{D}^{0}D^{*+}$	3.9 ± 0.5	0.9 ± 0.4	0.21 ± 0.05
$B^+\to \overline{D}^{*0}D^{+}$	6.3 ± 1.7	1.2 ± 0.5	0.23 ± 0.06
$B^+\to \overline{D}^{0}D^{+}$	4.2 ± 0.6	1.3 ± 0.4	0.18 ± 0.03
Average	–	–	0.194 ± 0.011

Table 10.16: *Measured branching ratios $\mathcal{B}$ for $B\to D^{(*)}D_s^{(*)}$, taken from Refs. [17, 151, 152]. The (*) indicates the sum of $\mathcal{B}(B^0\to D_s^{*-}D^{+})$ and $\mathcal{B}(B^0\to D_s^{-}D^{*+})$.*

in general, will lead to larger $SU(3)$ breaking. For these reasons, it is argued, D decays do not provide a reliable estimate of $SU(3)$ breaking in B decays.

From Eq. (10.45) another important conclusion can be drawn. In determining the amplitude ratio using $SU(3)$ flavor symmetry in Eq. (10.2), the error from non-factorizable corrections is suppressed by the $SU(3)$ breaking scale (and should vanishes in the $SU(3)$ limit). Conversely, the higher-order $SU(3)$ breaking is suppressed by the size of the non-factorizable corrections. Compare this with the amplitude ratio in Eq. (10.1) from naive factorization. Here, the non-factorizable corrections are not suppressed, making the uncertainty larger by a factor of roughly $\Lambda_\chi/2m_s$.

In Tables 10.13 and 10.14, both methods have similar experimental errors on the predicted amplitude ratios. Including the theoretical uncertainty from corrections to factorization, the amplitude ratios from $SU(3)$ flavor symmetry are clearly favored in the extraction of γ.

10.8 Discussion and summary

Within the framework of factorization, the decay rates of $B^0\to h^-l^+\nu$ can be related to the decay rates of $B^0\to h^-D_s^{(*)+}$, where h is a π or ρ meson. The branching fractions thus found need to be corrected for soft rescattering effects, which have a significant impact on the factorization predictions. Soft rescattering amplitudes can be determined precisely from the CKM-favored decays $B\to D\pi$ and $B\to D\rho$ using a quasi-elastic rescattering model. As rescattering is independent of the formation process of the initial mesons from the B decay, one can take the rescattering results from CKM-favored decays, and apply these to the corresponding CKM-suppressed decay modes, such as $B^0\to D_{(s)}^{(*)+}\pi^-$ and $B^0\to D_{(s)}^{+}\rho^-$.

All rescattering-corrected predictions are found to be consistent with the measured branching fractions. Except for $\mathcal{B}(B^0\to\pi^-D_s^{*+})$, the predicted branching fractions have large theoretical and/or systematic uncertainties. The most powerful constraint on the size of non-factorizable contributions – now and in the future – is therefore derived using $B^0\to\pi^-D_s^{*+}$. A tremendous help there is that, for $B^0\to\pi^-l^+\nu$, the partial branching fraction $\Delta\mathcal{B}$ is measured symmetrically around 4 GeV^2.

The measured and predicted branching fractions for $B^0\to\pi^-D_s^{*+}$ agree well, consistent

with the hypothesis that factorization applies to this decay. In the factorization scenario, where non-factorizable terms are expected to be less than leading order ($|\tilde{a}_q^{\rm corr}| < 1$), we find the (Gaussian) upper limit in Eq. (10.35)

$$\left|\frac{\mathcal{R}e(\tilde{a}_s^{\rm corr}) + \frac{1}{2}|\tilde{a}_s^{\rm corr}|^2}{|1+\tilde{a}_s^{\rm corr}|^2}\right| < 0.211\ (0.317)\ @\ 68\%\ (90\%)\ {\rm CL}\,. \tag{10.54}$$

If we assume that $SU(3)$ breaking in non-factorizable contributions can be up to three times the typical $SU(3)$ breaking scale (up to 75%), we find in Eq. (10.53)

$$|\bar{a}^{\rm c}|\frac{2m_s}{\Lambda_\chi} < 0.105\ (0.154)\ @\ 68\%\ (90\%)\ {\rm CL}\,. \tag{10.55}$$

Note that $\bar{a}^{\rm c} = 0$ if $SU(3)$ breaking in non-factorizable corrections is the same as in factorizable terms.

In determining the amplitude ratio using $SU(3)$ flavor symmetry in Eq. (10.2), the theoretical error from non-factorizable corrections is suppressed by the $SU(3)$ breaking scale (and vice versa). For any prediction of the amplitude ratio from naive factorization, such as in Eq. (10.1), the non-factorizable corrections are not suppressed, however, making the theoretical uncertainty larger by a factor of roughly around four to seven ($\Lambda_\chi/2m_s$). The amplitude ratios obtained from $SU(3)$ flavor symmetry are therefore clearly favored in the extraction of γ.

A qualitative estimate of the W-exchange amplitude involved in the CKM-suppressed decay $B^0 \to D^+\pi^-$ can be obtained from naive factorization. It is found to be severely suppressed, due to color-suppression and f_B/m_B, compared with the color-allowed tree amplitude, at the level of 1.3%. However, relatively large systematic errors from factorization and p-QCD scaling should be accounted for this estimate. Therefore, we assign

$$|E/T| < 5.0\%\,. \tag{10.56}$$

This is consistent with results from the rescattering fit to the CKM-favored decays in Section 10.3. For all three modes $B^0 \to D^-\pi^+$, $B^0 \to D^{*-}\pi^+$, and $B^0 \to D^-\rho^+$, the fit estimates of the W-exchange amplitude are consistent with zero. One has $|E/T| < 2.9\%$ @ 68% C.L.

For all modes $B^0 \to h^- D^{(*)+}$, in the extraction of the CKM-angle γ one can therefore take the Gaussian error of 10.5% as systematic uncertainty from residual $SU(3)$ breaking in non-factorizable corrections, and a flat error of 5.0% from neglecting W-exchange diagrams when using the $SU(3)$ flavor symmetry method to obtain the suppressed over favored amplitude ratios.

Chapter 11

Extraction of γ

This chapter deals with the extraction of γ from the results of the time-dependent fit to the $B \to D^{(*)\mp}h^{\pm}$ data samples. It describes the construction and validation of a χ^2 minimization procedure. We use a frequentist method loosely based on the Feldman-Cousins approach to set a confidence limit on γ based on the latest world average values of a^j and $c^j_{\rm lep}$.

In obtaining the *CP* angle γ from the time-dependent decays of $B \to D^{(*)\mp}h^{\pm}$, a two step analysis has been adopted. First, the *CP*-related observables a and $c_{\rm lep}$ are measured, as summarized in the previous chapters. Next we extract γ from these measurements.

The analysis has been split up for various reasons.

1. It has become clear in the validation process that the measurements of a and $c_{\rm lep}$ obey Gaussian statistics. Therefore, observables from different experiments can be averaged easily. As the mapping to γ is non-trivial, this is not the case for the *CP* angle itself.

2. A change in interpretation of the *CP* parameters can be easily accommodated, without having to redo the time-dependent analysis. An example is an update of the amplitude ratios r^j in Eq. (10.2).

3. The simulation of just the Gaussian parameters a and $c_{\rm lep}$ is straight-forward. However, the combined validation of a time-dependent analysis that includes the extraction process of γ would be extremely time-consuming.

11.1 Frequentist versus Bayesian inference

The field of probability and statistics is divided into two camps: the frequentists and Bayesians[1]. Here we do not discuss the fundamental, philosophical differences between each method of inference – see for example Ref. [17].

This Chapter follows a frequentist approach in setting a confidence region on the CKM-angle γ from the measured *CP* parameters in Table 8.5. We have tried both methods to constrain γ, and our experience with Bayesian inference is that, with the current statistical errors, the dependence on the choice of prior distribution for γ is not negligible. Others have found the same in the extraction of the CKM phase α [156]. The frequentist technique laid

[1] Put simply: 'A frequentist is a person whose long-run ambition is to be wrong 5% of the time.' And: 'A Bayesian is one who, vaguely expecting a horse, and catching a glimpse of a donkey, strongly believes he has seen a mule.' [155]

out here to constrain γ from a and $c_{\rm lep}$ has been adopted by the CKMFitter group [21]. A Bayesian limit, set by the UTFit group, can be found in Ref. [122].

11.2 Construction of χ^2

Not all of the a, b, c observables related to *CP* violation carry significant information about the angle $(2\beta+\gamma)$. In particular, all parameters related to tag-side interference are insensitive due to large theoretical uncertainties in the size of this effect, as demonstrated in Section 5.8. This implies that all b and c parameters associated with non-leptonic tagging categories can be ignored in the extraction process of $(2\beta+\gamma)$, leaving $a^{D\pi}$, $a^{D^*\pi}$, $c_{\rm lep}^{D\pi}$, and $c_{\rm lep}^{D^*\pi}$ for further consideration.

In the previous sections, the coefficients most sensitive to $(2\beta+\gamma)$ have been measured to be

$$\begin{aligned}
a^{D\pi} &= 2r^{D\pi}\sin(2\beta+\gamma)\,\cos\delta^{D\pi} &&= -0.010 \pm 0.023\,(\text{stat.}) \pm 0.007\,(\text{syst.})\,, && (11.1)\\
a^{D^*\pi} &= 2r^{D^*\pi}\sin(2\beta+\gamma)\,\cos\delta^{D^*\pi} &&= -0.040 \pm 0.023\,(\text{stat.}) \pm 0.010\,(\text{syst.})\,, && (11.2)\\
a^{D\rho} &= 2r^{D\rho}\sin(2\beta+\gamma)\,\cos\delta^{D\rho} &&= -0.024 \pm 0.031\,(\text{stat.}) \pm 0.009\,(\text{syst.})\,, && (11.3)\\
c_{\rm lep}^{D\pi} &= 2r^{D\pi}\cos(2\beta+\gamma)\,\sin\delta^{D\pi} &&= -0.033 \pm 0.042\,(\text{stat.}) \pm 0.012\,(\text{syst.})\,, && (11.4)\\
c_{\rm lep}^{D^*\pi} &= 2r^{D^*\pi}\cos(2\beta+\gamma)\,\sin\delta^{D^*\pi} &&= 0.049 \pm 0.042\,(\text{stat.}) \pm 0.015\,(\text{syst.})\,, && (11.5)\\
c_{\rm lep}^{D\rho} &= 2r^{D\rho}\cos(2\beta+\gamma)\,\sin\delta^{D\rho} &&= -0.098 \pm 0.055\,(\text{stat.}) \pm 0.018\,(\text{syst.})\,. && (11.6)
\end{aligned}$$

The latest world averages are given in Table 11.1 [31]. (The significance of the individual measurements is discussed in Section 12.2.) In Section 10.4 the amplitude ratios r^j have been determined to be

$$\begin{aligned}
r^{D\pi} &= (1.53 \pm 0.33\,(\text{exp.}) \pm 0.08\,(\text{theo.})) \times 10^{-2}\,,\\
r^{D^*\pi} &= (2.10 \pm 0.47\,(\text{exp.}) \pm 0.11\,(\text{theo.})) \times 10^{-2}\,,\\
r^{D\rho} &= (0.31 \pm 0.59\,(\text{exp.}) \pm 0.02\,(\text{theo.})) \times 10^{-2}\,. \qquad (11.7)
\end{aligned}$$

As explained in Section 2.6.1, there is a four-fold ambiguity in the extraction of $(2\beta+\gamma)$ from these parameters. Given the true solutions $(2\beta+\gamma)_0$ and $\delta(3)_0 = (\delta^{D\pi}{}_0, \delta^{D^*\pi}{}_0, \delta^{D\rho}{}_0)$, the observables are invariant under the two transformations

$$\begin{aligned}
[2\beta+\gamma, \delta(3)] &\rightarrow [-(2\beta+\gamma)_0, \pi - \delta(3)_0] \quad ; \quad \text{and}\\
&\rightarrow [\pi - (2\beta+\gamma)_0, -\delta(3)_0]\,.
\end{aligned}$$

Note that the presentation in terms of $|\sin(2\beta+\gamma)|$ is the same for all of these solutions.

Note that – physically – both a^j and $c_{\rm lep}^j \in [-2r^j, 2r^j]$, with $r^j \lesssim 0.02$. Considering the uncertainties in the parameters it is clear that: with current statistics the sensitivity to γ is limited, and the chance for fit coefficients to end up in the unphysical region not negligible.

One can determine the sensitivity to γ by minimizing a χ^2 function built from a^j and $c_{\rm lep}^j$, with $j = D\pi$, $D^*\pi$, and $D\rho$, and their corresponding relations

$$\chi^2 = v^T M^{-1} v + \left(\frac{\beta - \beta_{\rm meas}}{\sigma[\beta_{\rm meas}]}\right)^2 + \sum_j \Delta^2(r^j)\,, \qquad (11.8)$$

Parameter	*BABAR* Fully reconstructed (232M $B\overline{B}$) [14]	Belle Fully reconstructed (386M $B\overline{B}$) [158]	*BABAR* Partially reconstructed (232M $B\overline{B}$) [150]	Belle Partially reconstructed (386M $B\overline{B}$) [158]	World average	Weight of this measurement (%)
$a^{D\pi}$	-0.010 ± 0.023	-0.050 ± 0.024	–	–	-0.030 ± 0.017	52
$a^{D^*\pi}$	-0.040 ± 0.025	-0.039 ± 0.024	-0.034 ± 0.014	-0.041 ± 0.026	-0.037 ± 0.011	17
$a^{D\rho}$	-0.024 ± 0.033	–	–	–	-0.024 ± 0.033	100
$c_{\rm lep}^{D\pi}$	-0.033 ± 0.044	-0.019 ± 0.024	–	–	-0.022 ± 0.021	23
$c_{\rm lep}^{D^*\pi}$	0.049 ± 0.045	-0.011 ± 0.024	-0.019 ± 0.026	-0.007 ± 0.027	-0.006 ± 0.014	10
$c_{\rm lep}^{D\rho}$	-0.098 ± 0.058	–	–	–	-0.098 ± 0.058	100

Table 11.1: *World averages (WA) of the a and* $c_{\rm lep}$ *parameters by the BABAR and Belle experiments. The measurement described in this thesis is titled 'BABAR Fully reconstructed'.*

where v is the vector

$$v = \begin{pmatrix} a^{D\pi} & -2r^{D\pi}\sin(2\beta+\gamma)\,\cos\delta^{D\pi} \\ a^{D^*\pi} & -2r^{D^*\pi}\sin(2\beta+\gamma)\,\cos\delta^{D^*\pi} \\ a^{D\rho} & -2r^{D\rho}\sin(2\beta+\gamma)\,\cos\delta^{D\rho} \\ c_{\rm lep}^{D\pi} & -2r^{D\pi}\cos(2\beta+\gamma)\,\sin\delta^{D\pi} \\ c_{\rm lep}^{D^*\pi} & -2r^{D^*\pi}\cos(2\beta+\gamma)\,\sin\delta^{D^*\pi} \\ c_{\rm lep}^{D\rho} & -2r^{D\rho}\cos(2\beta+\gamma)\,\sin\delta^{D\rho} \end{pmatrix}, \tag{11.9}$$

and M is the measured covariance matrix, taken to be diagonal for the world average values of a^j and $c_{\rm lep}^j$. The off-diagonal terms one gets from the time-dependent fit, see Table 8.1, are sufficiently small to be safely neglected. The systematic uncertainties – see Tables. 9.20 and 9.21 – have been added in quadrature to the elements. We choose the world average value of $\beta_{\rm meas} = 0.377 \pm 0.022$ [122] consistent with the Standard Model solution. The last terms in the χ^2 function, $\Delta^2(r^j)$, take into account the Gaussian experimental errors and the 5% theoretical uncertainties on r^j of Eq. (11.7) according to the description of Ref. [21]

$$\Delta^2(r^j) = \begin{cases} \left(\frac{r^j - 1.05\, r^j_{\rm meas.}}{\sigma[r^j_{\rm exp.}]}\right)^2 & , \quad \xi_{r^j} > 0.05 \\ 0 & , \quad |\xi_{r^j}| \leq 0.05 \\ \left(\frac{r^j - 0.95\, r^j_{\rm meas.}}{\sigma[r^j_{\rm exp.}]}\right)^2 & , \quad \xi_{r^j} < -0.05 \end{cases} \tag{11.10}$$

where $\xi_{r^j} \equiv (r^j - r^j_{\rm meas})/r^j$. The result (*i.e.* the minimum observed χ^2) is determined by scanning over the free parameters $(2\beta+\gamma)$, $\delta^{D\pi}$, $\delta^{D^*\pi}$, $\delta^{D\rho}$, and $r^{D\pi}$, $r^{D^*\pi}$, and $r^{D\rho}$.

The extraction of γ with the χ^2 technique has been performed on the world average results in Table 11.1. Fig. 11.1 shows the value of χ^2 as function of $(2\beta+\gamma)$ and as a function of $\sin(2\beta+\gamma)$. The minima of the χ^2 distribution lie (ambiguously) at $\gamma = 1.37$ ($\sin(2\beta+\gamma) = 0.85$). Also shown in Fig. 11.1 is the χ^2 as a function of $\delta^{D\pi}$, $\delta^{D^*\pi}$, and $\delta^{D\rho}$. The minima for the strong phases lie (ambiguously) at 2.54, 2.91, and 2.35, respectively. There is little sensitivity to the strong phase difference $\delta^{D\rho}$. The best fit values for the ratios $r^{D\pi}$, $r^{D^*\pi}$, $r^{D\rho}$ are found to be 0.0162, 0.0216, and 0.0047 respectively.

Notice that the measured value of $|\sin(2\beta+\gamma)|$ is close to the edge of the physical region (1), resulting in asymmetric left-hand and right-hand side errors on γ. For example, for the value of γ closest to the Standard Model solution, the interval $\chi^2 - \chi^2_{\rm min} = 1$ can only be considered on the right-hand side. When setting a confidence region for the value of γ, we ask ourselves the following questions. Where lies the 68.3% confidence limit, and does is correspond to the usual Gaussian interpretation of $\chi^2 - \chi^2_{\rm min} = 1$? Second, what maximum confidence limit interval on the value of γ can we derive from the data?

The next Sections determine the sensitivity to γ and validate the coverage of the confidence limit interval.

11.3 Coverage of $\Delta\chi^2$

The question raised by Fig. 11.1 – χ^2 plotted as a function of γ using the a and $c_{\rm lep}$ coefficients from the nominal data fit – is whether the interval spanned by $\Delta\chi^2 \equiv \chi^2 - \chi^2_{\rm min} \leq 1$ covers the true value of $(2\beta+\gamma)$ with the usual Gaussian interpretation of a 68.3% confidence level.

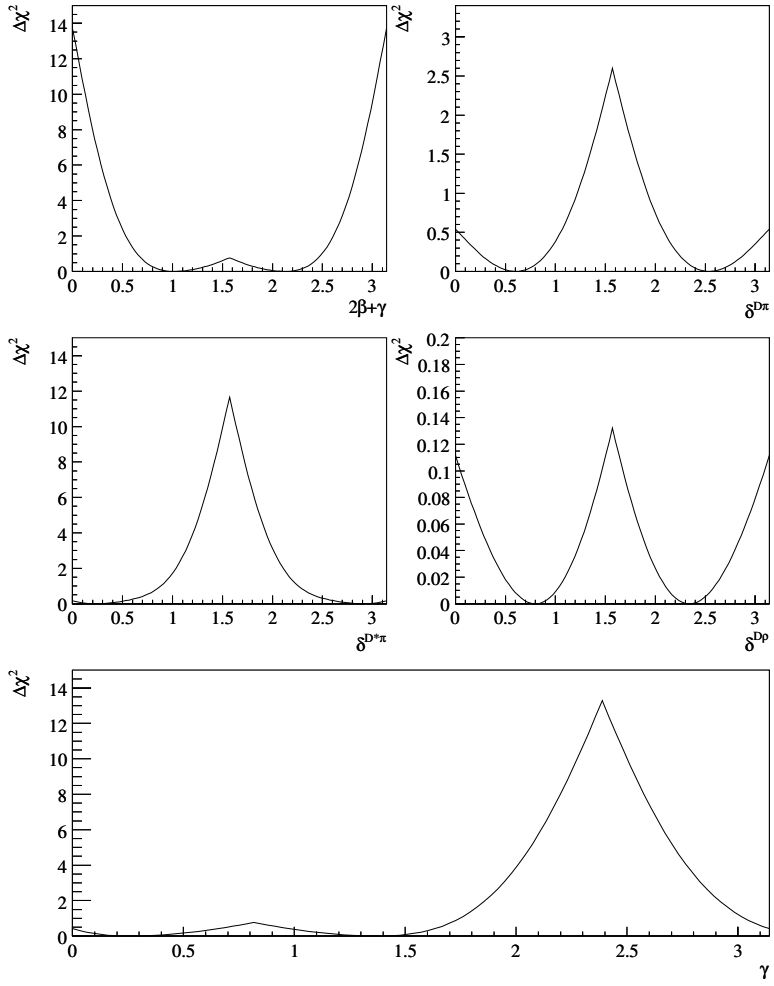

Figure 11.1: *χ^2 as a function of $2\beta+\gamma$ (top left), $\delta^{D\pi}$ (top right), $\delta^{D^*\pi}$ (middle left), $\delta^{D\rho}$ (top right), and as a function of γ (bottom) for 210 fb^{-1} of data.*

The idea behind this Section is, for world average statistics, to: a) determine the frequentist coverage of the constraint $\Delta\chi^2 = 1$ for the whole spectrum of γ, and b) to find the $\Delta\chi^2$ cut that is guaranteed to cover a specific confidence level (for example 68.3%), independent of the true value of $|\sin(2\beta+\gamma)|$.

To do so, we generate the following ensemble of pseudo-experiments.

1. Pick $\gamma_{\rm true}$ in steps of $\pi/20$ between 0 and π, and generate δ^j at zero. As it turns out, there is some dependency on what strong phases are generated, as shown later in this Chapter. The ratios $r^{D\pi}$, $r^{D^*\pi}$, and $r^{D\rho}$ are generated from flat Gaussian distributions, with the means from Eq. (11.7), generated uniformly in the theoretical error range, and with experimental (Gaussian) widths outside this range. All amplitude ratios are required to be positive. Next, $a^{D\pi}$, $a^{D^*\pi}$, $a^{D\rho}$, $c_{\rm lep}^{D\pi}$, $c_{\rm lep}^{D^*\pi}$, and $c_{\rm lep}^{D\rho}$ are calculated using Eq. (11.1).

2. Smear the coefficients with the world average errors, and insert these into the χ^2 function. The pseudo-experiments use the statistical and systematic uncertainties added in quadrature. On can simply generate a^j and $c_{\rm lep}^j$, as demonstrated in Chapter 7, since these coefficients obey Gaussian distributions with unit pulls.

3. Find the minimum χ^2, $\chi^2_{\rm min}$ (leaving γ, r^j, δ^j free), and also minimize it at $\gamma_{\rm true}$ (fixing γ), called $\chi^2_{\rm pnt}$. Define $\Delta\chi^2 \equiv \chi^2_{\rm pnt} - \chi^2_{\rm min}$.

4. Repeat the last two steps.

5. Find the fraction of pseudo-experiments for which $\Delta\chi^2 < 1$. In other words: the fraction of pseudo-experiments that cover $|\gamma_{\rm true}|$ in the interval mapped out by the constraint $\chi^2 - \chi^2_{\rm min} \leq 1$. This includes all measurements with little sensitivity to γ, *i.e.* the experiments that never reach $\Delta\chi^2 = 1$, and that naturally cover the full range $|\sin(2\beta+\gamma)_{\rm true}| \in [0,1]$.

We discuss some observations before showing the results from this study. Fig. 11.2 shows fit values of $|\sin(2\beta+\gamma)|$ obtained from pseudo-experiments generated at $\sin(2\beta+\gamma)_{\rm true} = 0.5$. The distribution is similar shaped for all values of $\sin(2\beta+\gamma)_{\rm true}$. One can always map between $\sin(2\beta+\gamma)$ and γ to get the corresponding scattering distribution for $\gamma_{\rm true} = 1.86$. The events at $|\sin(2\beta+\gamma)| = 1$ and at $|\sin(2\beta+\gamma)| = 0$ ($|\cos(2\beta+\gamma)| = 1$) come from unphysical a^j and $c_{\rm lep}^j$ coefficients, as illustrated in Fig. 11.2. The former contribute to $|\sin(2\beta+\gamma)| = 1$, and the latter end up at zero. Notice how the 'a-space' mapped by the formulas, $a^j \in [-0.04, +0.04]$, is missing in the right-hand plot.

In Fig. 11.3 one can see $\Delta\chi^2$ versus the fit value of $|\sin(2\beta+\gamma)|$, all for pseudo-experiments generated at $\sin(2\beta+\gamma)_{\rm true} = 0.5$. Generally speaking, $\Delta\chi^2$ gets larger for fit values of $|\sin(2\beta+\gamma)|$ farther away from the true value. For example, for small values of $\sin(2\beta+\gamma)_{\rm true}$ experiments with $\Delta\chi^2 > 1$ lie predominantly at $|\sin(2\beta+\gamma)| = 1$. Likewise, for large $\sin(2\beta+\gamma)_{\rm true}$ experiments with $\Delta\chi^2 > 1$ mostly lie at zero.

The coverage for $\Delta\chi^2 = 1$ versus the generated value of γ is shown in Fig. 11.4. Every point corresponds to 5k of generated pseudo-experiments. Note the non-Gaussian coverage; in a Gaussian regime the coverage would be flat at 68.3%. The minimum confidence limit lies at $\gamma_{\rm true} \approx 1$, and equals about 63%. For this point $\Delta\chi^2 = 1.20$ provides a coverage of 68.3%, so, irrespective of the true value of γ, this cut value is guaranteed to set at least the corresponding confidendence level. Clearly, however, for a larger part of the γ spectrum, interpreting $\Delta\chi^2 = 1$ as the 'normal' 68.3% CL interval is too conservative, let alone applying a cut of $\Delta\chi^2 = 1.20$. As a result, we will not use this method to set a lower limit on the value of γ in data.

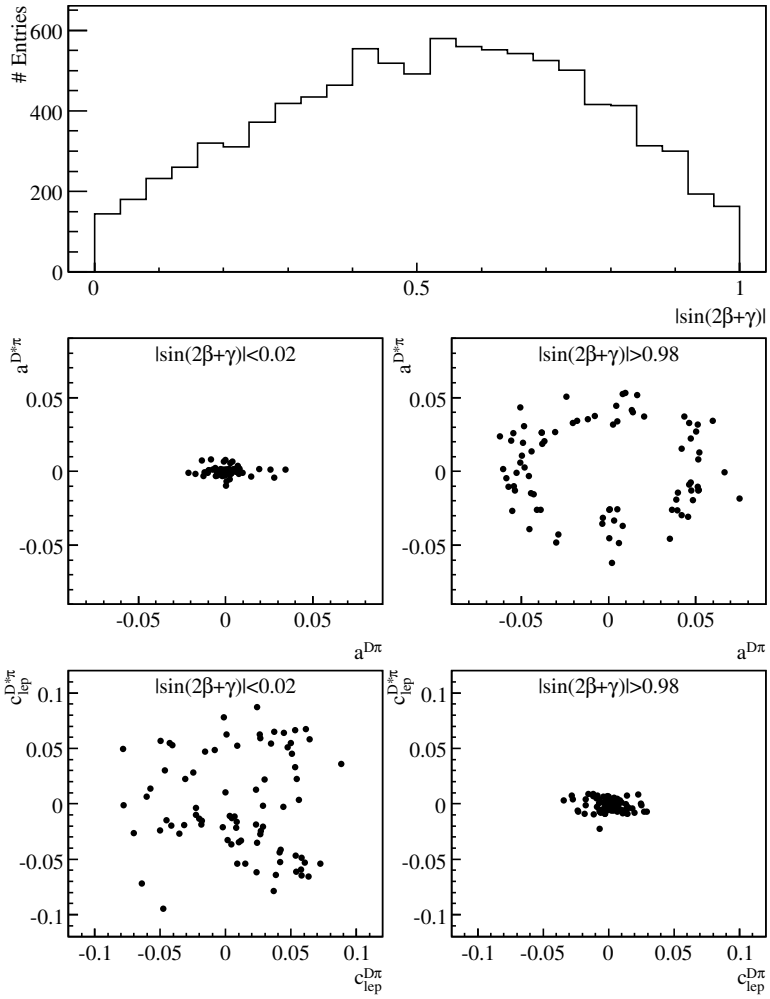

Figure 11.2: *Fit values of* $|\sin(2\beta+\gamma)|$ *obtained for* $\sin(2\beta+\gamma)_{\rm true} = 0.5$.

The next Section considers instead a ranking method for setting a confidence limit on γ that takes into account the sensitivity and the χ^2 curve obtained from our data.

11.4 Ranking approach

From the discussion in the previous Section – concerning coverage versus true value of γ – it has become clear that, for the χ^2 curve obtained from data, the interval spanned by the constraint $\Delta\chi^2 \equiv \chi^2 - \chi^2_{\rm min} \leq 1.2$ covers the true value of γ with *at least* 68.3% confidence

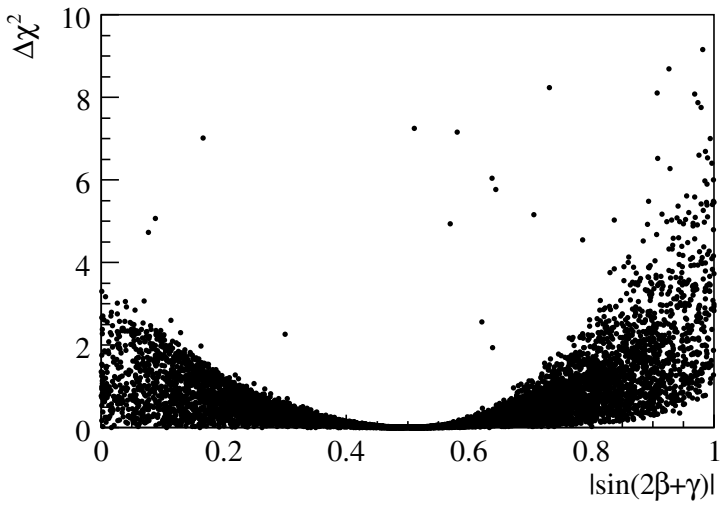

Figure 11.3: $\Delta\chi^2$ *vs fit value of* $|\sin(2\beta+\gamma)|$*, obtained for* $\sin(2\beta+\gamma)_{\rm true} = 0.5$.

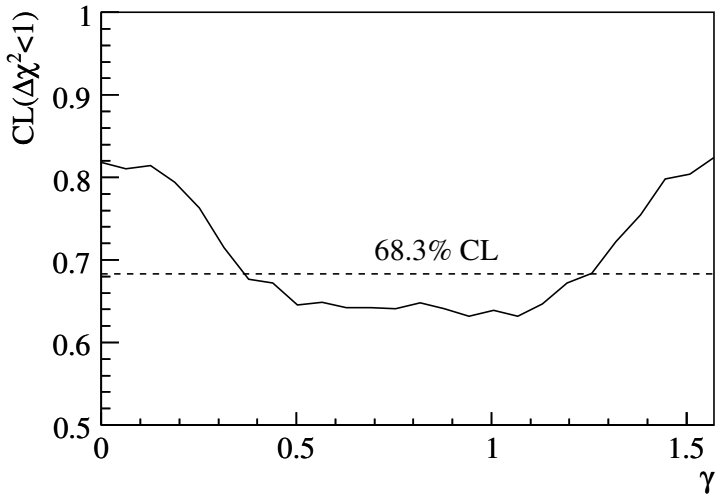

Figure 11.4: *Coverage corresponding with* $\Delta\chi^2 = 1$ *for different true values of* $\sin(2\beta+\gamma)$.

level. Also, it is evident that that $\Delta\chi^2$ cut is too conservative for most of the γ spectrum. The non-linearity in coverage induced by unphysical a^j and $c^j_{\rm lep}$ coefficients indicates we are not in a Gaussian regime, and suggests one should rank the $\Delta\chi^2$ cut at each point of the γ spectrum differently.

For each value of γ we determine the coverage for pseudo-experiments generated at this value, using as $\Delta\chi^2$ cut the corresponding point on the $\Delta\chi^2$ curve from data – a ranking method inspired by the Feldman-Cousins technique [157]. The results are shown in Fig. 11.5. Every point in Fig. 11.5 has been calculated with generated pseudo-experiments. This puts the 90.0% CL of γ at $\gamma \in [-0.28, 1.91]$, or $|\sin(2\beta+\gamma)| > 0.46$. The confidence region is dominated by the experimental errors on a^j, $c^j_{\rm lep}$, and $\mathcal{B}(B^0 \to \pi^- D_s^{(*)+})$.

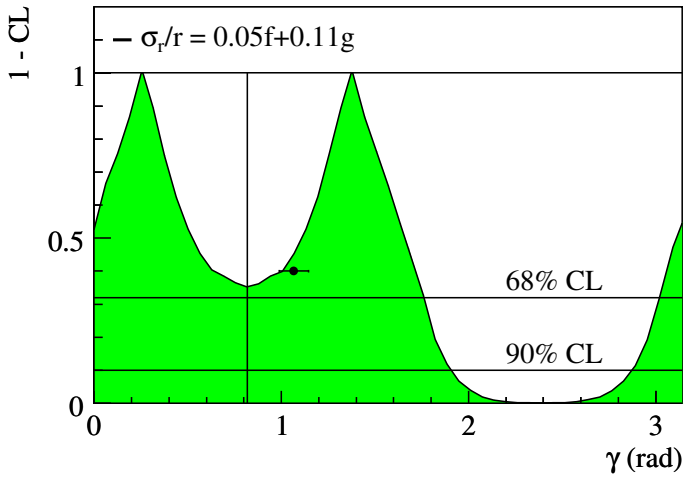

Figure 11.5: *World average confidence region for the CP angle γ, obtained from $B^0 \to D^{(*)\mp}h^{\pm}$, for various uncertainties on r^j. The black point is the indirect measurement of γ. The vertical black line indicates $2\beta+\gamma = \pi/2$. We use a flat error of 5.0% from neglecting W-exchange diagrams on the amplitude ratios $r^{D^{(*)}h}$ ('0.05f'), and a Gaussian systematic error of 10.5% for residual $SU(3)$ breaking in non-factorizable corrections ('0.11g').*

11.5 High-statistics validation

The correctness of the χ^2 minimization and ranking approach has been validated using a set of a and $c_{\rm lep}$ pseudo parameters, with

1. The parameters r^j and β are the current world average values.
2. The other input parameters are: $\gamma = 1.37$, $\delta^{D\pi} = 2.04$, $\delta^{D^*\pi} = 2.91$, and $\delta^{D\rho} = 2.35$.
3. The errors on a, $c_{\rm lep}$, and β are 10 times smaller than the world average errors.

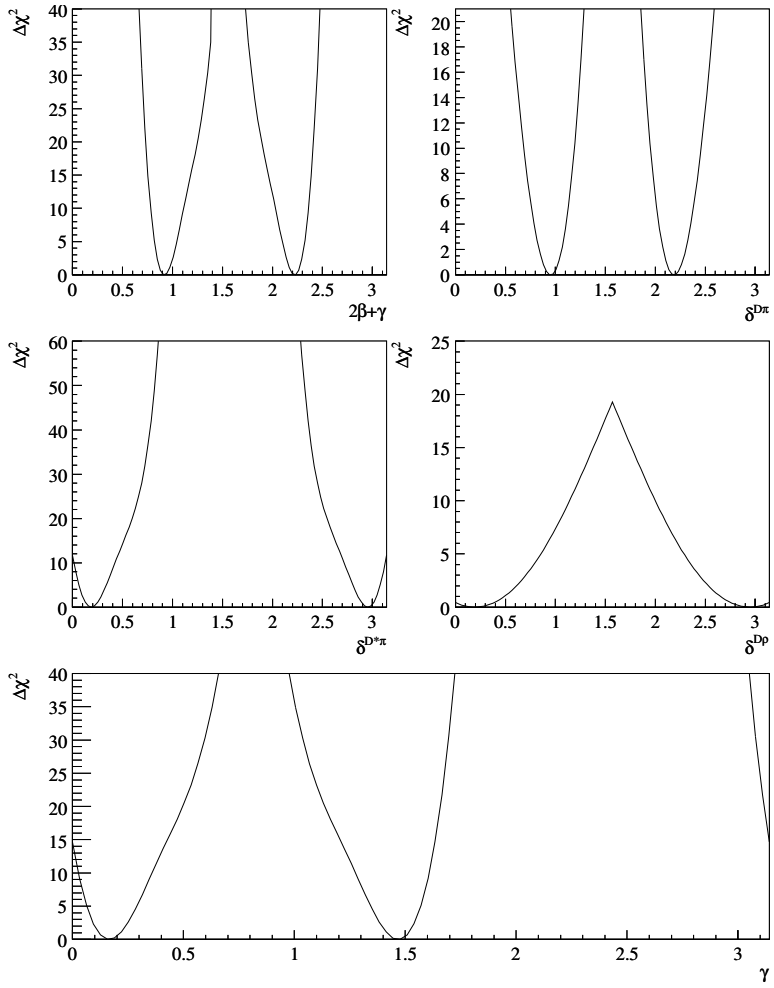

Figure 11.6: *High-statistics validation of χ^2 minimization. χ^2 as a function of $2\beta+\gamma$ (top left), $\delta^{D\pi}$ (top right), $\delta^{D^*\pi}$ (middle left), $\delta^{D\rho}$ (middle right), and as a function of γ (bottom), for the pseudo-experiment described in the text.*

The χ^2 minimization yields (modulo the noted discrete ambiguities): $\gamma = 1.369^{+0.058}_{-0.068}$, $\delta^{D\pi} = 2.042^{+0.080}_{-0.075}$, $\delta^{D^*\pi} = 2.910^{+0.070}_{-0.082}$, and $\delta^{D\rho} = 2.55^{+1.44}_{-0.71}$.

Fig. 11.6 shows the corresponding χ^2 as a function of γ, $(2\beta+\gamma)$, $\delta^{D\pi}$, $\delta^{D^*\pi}$, $\delta^{D\rho}$. Fig. 11.7 displays the χ^2 as a function of $2\beta+\gamma$ for $\chi^2 < 17$, which is close to parabolic.

The minima found with the χ^2 method agree well with the generated input values. The high-statistics χ^2 is still slightly asymmetric around the minimum in γ, explaining the difference

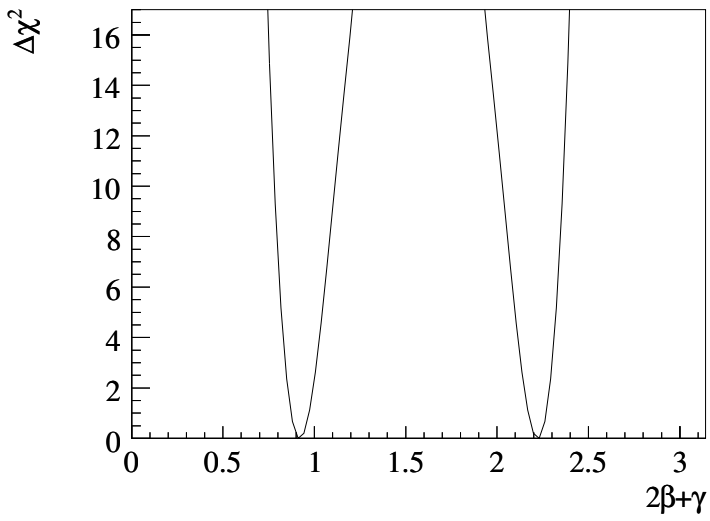

Figure 11.7: χ^2 *as a function of* $2\beta+\gamma$*, for the high-statistics pseudo-experiment described in the text.*

in left-hand and right-hand side errors.

For this set of input parameters, a test of the coverage corresponding with $\Delta\chi^2 = 1$ still results in a plot similar to Fig. 11.4, *i.e.* we do not have Gaussian coverage over the entire range of γ. Again, the ranking technique of Section 11.4 can be used to set a confidence limit on γ.

It should be noted that the ranking technique makes a relative comparison between the χ^2 curve in data and those obtained from the pseudo-experiments. Thus, for the same measured coefficients, it is not immediately clear whether an increase or decrease in statistics automatically leads to a different confidence limit. Fig. 11.8 shows the ranking technique of Section 11.4 applied to the coefficients measured in data, but under the hypotheses of 0.25, 0.5, 2.0, and 4.0 times the observed errors. Every point consists of about 2k pseudo-experiments, generated according to the recipe in Section 11.3. Clearly, for each case the obtained limit on γ moves in the desired direction, and the ranking technique behaves as desired.

11.6 Choice of generated phases δ^j

Here we return to the issue of why, for the pseudo-experiments in Fig. 11.4, the phases δ^j are set to zero. For $\gamma = 1.665$, the variation in confidence limit versus generated strong phase differences is shown in Fig. 11.9. Every point consists of 600 pseudo-experiments. We scan the confidence limit stepping uniformly through $\delta^{D\pi}$, $\delta^{D^*\pi}$, and $\delta^{D\rho}$. The confidence limit appears to behave as

$$[1-\mathrm{CL}]\,(\gamma \equiv 1.665) = a + b\,\cos^2\delta^{D\pi}\,\cos^2\delta^{D^*\pi}\,\cos^2\delta^{D\rho}\,. \tag{11.11}$$

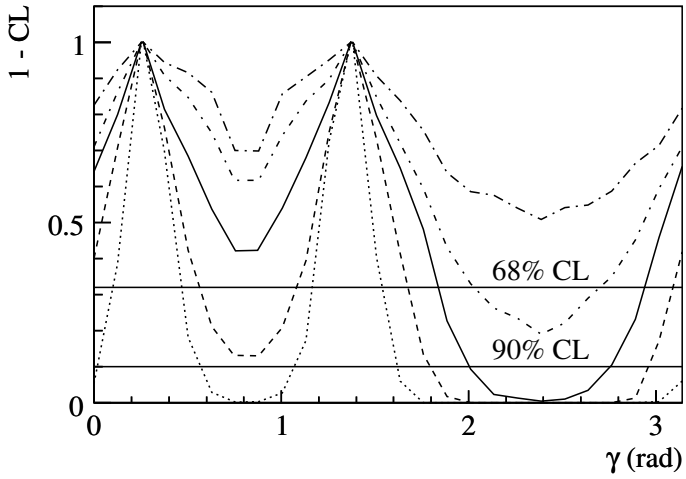

Figure 11.8: *Ranking technique applied to the world averaged a and $c_{\rm lep}$ coefficients, assuming* 0.25 *(dotted),* 0.5 *(dashed),* 1.0 *(solid),* 2 *(dashed-dotted), and* 4 *(long dashed-dotted) times the statistical plus systematical errors (added in quadrature) observed in data.*

We conclude that δ^j should be set to a multiple of π to obtain the most conservative confidence limit[2].

The confidence limit on data with δ^j generated randomly and at zero is also shown in Fig. 11.10. For randomly generated phases δ^j the 90% CL is $\gamma \in [-0.21, 1.84]$. Likewise, $\gamma \in [-0.28, 1.91]$ at 90% CL when δ^j is kept at zero.

11.7 Uncertainties on amplitude ratios r^j

Following the frequentist coverage technique described in Refs. [14, 150], we extract the CKM-angle γ using the WA values for the *CP*-related parameters a and $c_{\rm lep}$, given in Table 11.1, and obtain the confidence limit shown in Fig. 11.11. We use: a) a Gaussian systematic error of 10.5% for residual $SU(3)$ breaking in non-factorizable corrections, and a flat error of 5.0% from neglecting W-exchange diagrams on the amplitude ratios $r^{D^{(*)}h}$. The confidence limit is also obtained with: b) the flat theoretical error of 30%, as in the *BABAR* measurements, and c) with no additional error – all given in Fig. 11.11. In these plots, $2\beta+\gamma = \pi/2$ lies at the dip at $\gamma = 0.817$.

In comparing the three figures, notice that the central values of γ slightly shift. These changes can be easily understood. Because of the smaller uncertainties on $r^{D^{(*)}h}$, in the extraction of γ the fit to data prefers smaller values of the amplitude ratios, closer to the central values in Table 10.14 (as obtained using the $SU(3)$ flavor symmetry method). Making the

[2]Coincidentally, as discussed in Chapter 10, $\delta^j = n\pi$ is the prediction from factorization theory.

amplitude ratios smaller is compensated by making $\sin(2\beta+\gamma)$ larger, *i.e.* by making $2\beta+\gamma$ closer to $\pi/2$.

Compared with no error from $SU(3)$ breaking, the difference with the updated error for $SU(3)$ breaking is small. The change in central value(s) of γ is only 3°. The 90% confidence region of γ is $[-0.28, 1.91]$ rad, compared with $[-0.27, 1.90]$ rad for no $SU(3)$ breaking errors.

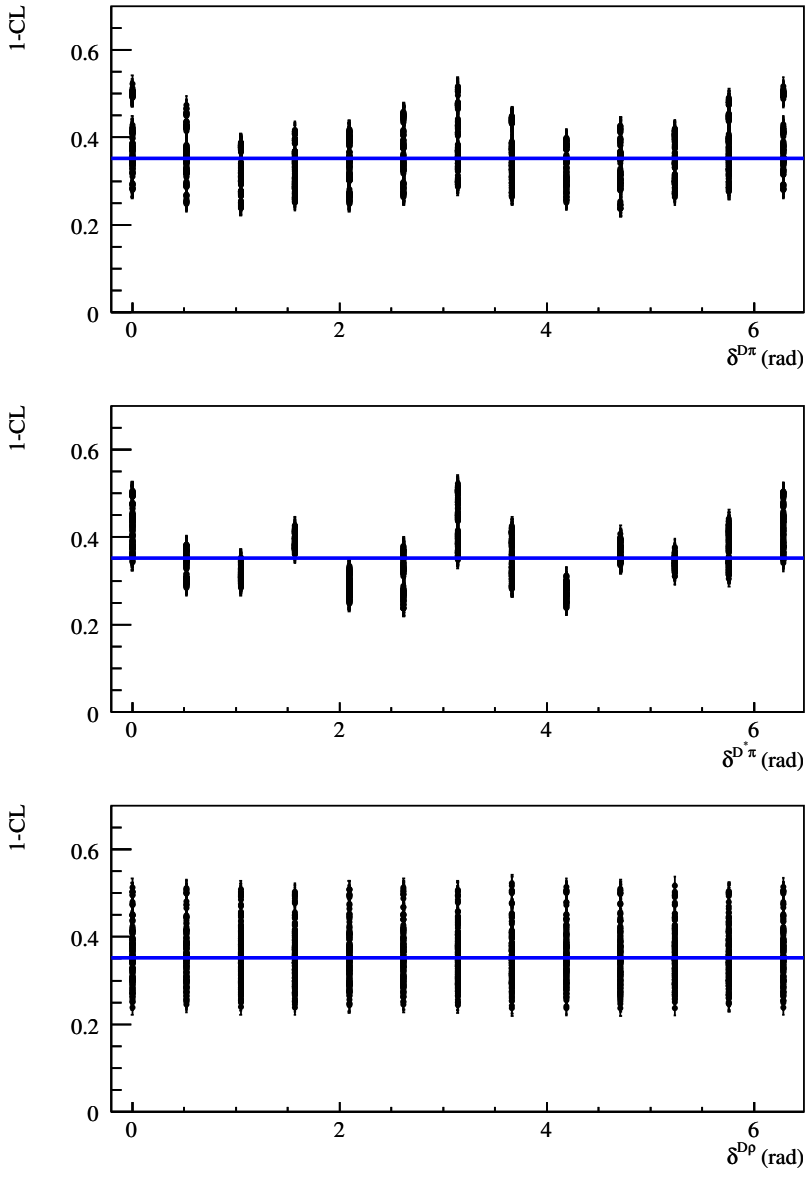

Figure 11.9: *Confidence limit versus generated strong phase difference of $\delta^{D\pi}$ (top), $\delta^{D^*\pi}$ (middle), and $\delta^{D\rho}$ (bottom). The solid horizontal line indicates the confidence limit when δ^j are generated randomly.*

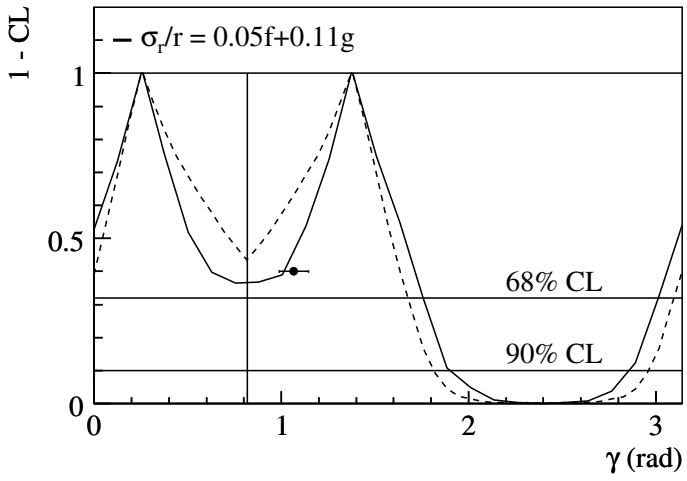

Figure 11.10: *Confidence region for the CP angle γ, obtained from $B^0 \to D^{(*)\mp}h^{\pm}$. The solid line indicates the confidence limit with the strong phase differences $\delta^j = 0$, and the dashed curve indicates the confidence limit with randomly generated phases. (The black point represents the result of the indirect measurement of γ. The vertical black line indicates $2\beta+\gamma = \pi/2$.)*

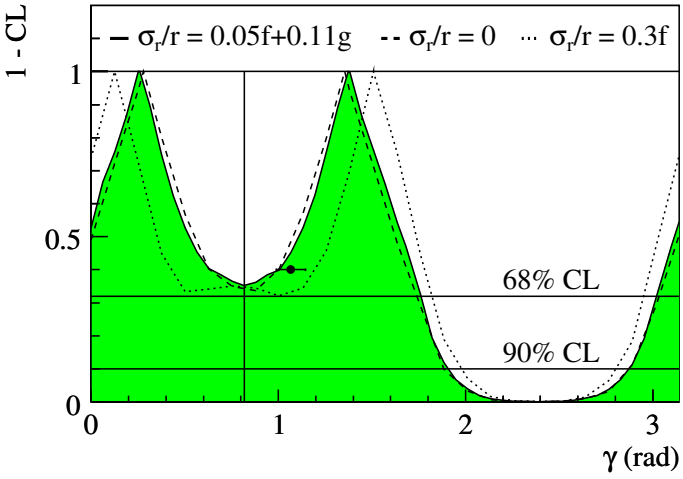

Figure 11.11: *World average confidence region for the CP angle γ, obtained from $B^0 \to D^{(*)\mp}h^{\pm}$. The black point is the indirect measurement of γ. The vertical black line indicates $2\beta+\gamma = \pi/2$.*

Chapter 12

Conclusions

The CKM-angle γ is the most difficult of the Unitarity Triangle angles to measure with B mesons. A precise, direct measurement of γ is essential for a critical test of the Standard Model flavor sector.

Here, we summarize our measurement, compare its significance, and end with a perspective for γ in the near future.

12.1 Summary of results

The coefficients most sensitive to the angle $(2\beta+\gamma)$, as obtained from the nominal fit to the Δt spectra of $B \to D^{(*)}h$ data samples have been measured to be

$$\begin{aligned}
a^{D\pi} &= 2r^{D\pi}\sin(2\beta+\gamma)\cos\delta^{D\pi} &&= -0.010 \pm 0.023\,(\text{stat.}) \pm 0.007\,(\text{syst.})\,,\\
a^{D^*\pi} &= 2r^{D^*\pi}\sin(2\beta+\gamma)\cos\delta^{D^*\pi} &&= -0.040 \pm 0.023\,(\text{stat.}) \pm 0.010\,(\text{syst.})\,,\\
a^{D\rho} &= 2r^{D\rho}\sin(2\beta+\gamma)\cos\delta^{D\rho} &&= -0.024 \pm 0.031\,(\text{stat.}) \pm 0.009\,(\text{syst.})\,,\\
c_{\text{lep}}^{D\pi} &= 2r^{D\pi}\cos(2\beta+\gamma)\sin\delta^{D\pi} &&= -0.033 \pm 0.042\,(\text{stat.}) \pm 0.012\,(\text{syst.})\,,\\
c_{\text{lep}}^{D^*\pi} &= 2r^{D^*\pi}\cos(2\beta+\gamma)\sin\delta^{D^*\pi} &&= 0.049 \pm 0.042\,(\text{stat.}) \pm 0.015\,(\text{syst.})\,,\\
c_{\text{lep}}^{D\rho} &= 2r^{D\rho}\cos(2\beta+\gamma)\sin\delta^{D\rho} &&= -0.098 \pm 0.055\,(\text{stat.}) \pm 0.018\,(\text{syst.})\,.
\end{aligned}$$

The resulting world averages are

$$\begin{aligned}
a^{D\pi} &= -0.030 \pm 0.017\,,\\
a^{D^*\pi} &= -0.037 \pm 0.011\,,\\
a^{D\rho} &= -0.024 \pm 0.033\,,\\
c_{\text{lep}}^{D\pi} &= -0.022 \pm 0.021\,,\\
c_{\text{lep}}^{D^*\pi} &= -0.006 \pm 0.014\,,\\
c_{\text{lep}}^{D\rho} &= -0.098 \pm 0.058\,.
\end{aligned}$$

The amplitude ratios r^j have been determined to be

$$\begin{aligned}
r^{D\pi} &= (1.53 \pm 0.33\,(\text{exp.}) \pm 0.08\,(\text{theo.})) \times 10^{-2}\,,\\
r^{D^*\pi} &= (2.10 \pm 0.47\,(\text{exp.}) \pm 0.11\,(\text{theo.})) \times 10^{-2}\,,\\
r^{D\rho} &= (0.31 \pm 0.59\,(\text{exp.}) \pm 0.02\,(\text{theo.})) \times 10^{-2}\,.
\end{aligned}$$

These numbers result in the following values

$$\begin{aligned} \gamma &= 1.37\ (|\sin(2\beta+\gamma)| = 0.85)\,, \\ \delta^{D\pi} &= 2.54\,, \\ \delta^{D^*\pi} &= 2.91\,, \\ \delta^{D\rho} &= 2.35\,. \end{aligned}$$

where the invariance under the discrete ambiguities noted in Eq. (2.69) should be noted. The choice for this particular ambiguity is based on the Standard Model expectation. The ranking approach described in the previous Chapter obtains the confidence limit shown in Fig. 11.5, and sets the constraint of $\gamma \in [-0.28, 1.91]$, or $|\sin(2\beta+\gamma)| > 0.46$, at a 90% confidence level using the current world average results. The confidence region is dominated by the experimental errors on a^j, $c^j_{\rm lep}$, and $\mathcal{B}(B^0 \to \pi^- D_s^{(*)+})$.

12.2 Significance of the result

Here, we compare our results with other $B \to D^{(*)\mp} h^\pm$ ($h = \pi, \rho$) analyses, and with a class of $B^\pm \to D^{(*)} K^\pm$ decays employed to measure γ.

Comparison with $B \to D^{(*)\mp} h^\pm$ ($h = \pi, \rho$) measurements

The measured *CP* asymmetries of the various time-dependent analyses of $B \to D^{(*)\mp} h^\pm$ ($h = \pi, \rho$) have been summarized in Table 11.1. Though not shown in Table 11.1, the errors on all a and $c_{\rm lep}$ observables are statistics limited. The relative weights of this measurement in the current world averages are given in the right-most column, and vary between 10% and 100%.

The 'partially reconstructed' analyses by *BABAR* and Belle can only reconstruct the decay mode $B \to D^{*\mp}\pi^\pm$. The D^* decay is recognized through its soft, charged pion, and the D^0 is reconstructed inclusively by combining all particles within a cone of its estimated direction. These measurements have high background levels, with signal purities between 30% and 50%, but enjoy high statistics ($\approx$ 90k signal events [150], compared with about 37k in this measurement). Hence, the small error on $a^{D^*\pi}$ by the partial reconstruction measurement of *BABAR*. The corresponding Belle measurement uses lepton tags only to reduce background levels and to avoid tag-side interference effects, resulting in a significantly larger error.

The 'full reconstruction' analyses have comparatively low efficiencies, $\mathcal{O}(10^{-3})$, but much smaller background levels (signal purities between 80% and 90%). The Belle full reconstruction analysis employs in addition a data sample of inclusively reconstructed $B^0 \to D^{*-} l^+ \nu$ decays. These final states can only be reached through a Cabibbo-favored transition, and, by themselves, do not induce time-dependent sine mixing terms. As such, these B decays provide an excellent handle on the sine mixing terms from tag-side interference effects of the other B in the event. Where *BABAR* only uses c observables of the `Lepton` tagging category – not affected by tag-side interference – Belle uses the c observables of all its tagging categories, resulting in smaller errors in its quoted '$c_{\rm lep}$' observables. Smaller errors on $c_{\rm lep}$ are useful, since, in the extraction of γ, the a and $c_{\rm lep}$ observables are equally important.

The Belle full reconstruction analysis does not reconstruct $B \to D^\mp \rho^\pm$ decays. Interestingly enough, though this analysis has about 66% more $B\overline{B}$ events available, and find roughly the same percentage of $B \to D^{*\mp}\pi^\pm$ signal events, the total errors on the measured $a^{D\pi}$ and $a^{D^*\pi}$ observables are almost identical.

Together, the four measurements of $a^{D^*\pi}$ indicate *CP* violation in the $B \to D^{*\mp}\pi^{\pm}$ system with 3.4σ significance.

The conversion of the measured a and $c_{\rm lep}$ observables into γ is non-trivial. For example, one set of measurements of a and $c_{\rm lep}$ does not necessarily contribute the same weight in the confidence limit on γ as in the corresponding world averages. The limit itself depends, among others, on the measured values of a and $c_{\rm lep}$ observables, their errors, the values and errors on the input amplitude ratios, and on the possible unphysicality of the measured observables (see for example $c_{\rm lep}^{D\rho}$). As described in Chapter 11, the three B decay modes result in a four-fold ambiguity in γ, whereas the a and $c_{\rm lep}$ observables from just one decay mode result in an eight-fold ambiguity. That said, even though the partially reconstructed decay mode $B \to D^{*\mp}\pi^{\pm}$ gives the most precise observables, for the extraction of γ it helps to add the decays $B \to D^{\mp}\pi^{\pm}$ and (to a lesser extend) $B \to D^{\mp}\rho^{\pm}$. Along the same line of reasoning, the extend to which γ can be resolved further through the addition of $B \to D^{\mp}h^{\pm}$ depends also on how much $\delta^{D\pi}$, $\delta^{D^*\pi}$, and $\delta^{D\rho}$ differ.

Comparison with $B^+ \to D^{(*)}K^+$ measurements

Next, we discuss the class of measurements that uses $B^+ \to D^{(*)}K^+$ decays, which determine γ with measurements of direct *CP* violation. The neutral $D^{(*)}$ meson can be both a $D^{(*)0}$ and a $\overline{D}^{(*)0}$. The final state $\overline{D}^{(*)0}K^+$ corresponds to the color-allowed, Cabibbo-favored $\bar{b} \to \bar{c}$ transition, whereas $D^{(*)0}K^+$ corresponds to the color-suppressed, doubly Cabibbo-suppressed $\bar{b} \to \bar{u}$ transition. The CKM-angle γ is the relative weak phase between the two B decay amplitudes. If $D^{(*)0}$ and $\overline{D}^{(*)0}$ decay to the same final state, the two decay amplitudes interfere. The resulting decay rates are sensitive to γ.

Three types of measurements are typically mentioned.

1. The GLW method [159], where the neutral $D^{(*)}$ is reconstructed in a *CP* eigenstate such as K^+K^- or $\pi^+\pi^-$;

2. The ADS method [160], with the $D^{(*)}$ reconstructed in another common final state, such as $K^{\pm}\pi^{\mp}$ for D^0 and $\overline{D}^0$; and

3. The GGSZ method, also known as the D Dalitz method [161], using the self-conjugate three-body final state $K^0_S\pi^+\pi^-$.

All variations are sensitive to the same B decay parameters, and we have

$$\mathcal{A}_{CP} \equiv \frac{\Gamma(B^- \to D^{(*)}K^-) - \Gamma(B^- \to D^{(*)}K^+)}{\Gamma(B^- \to D^{(*)}K^-) + \Gamma(B^- \to D^{(*)}K^+)} \propto 2r_B^{(*)} \sin\delta_B^{(*)} \sin\gamma\,, \qquad (12.1)$$

where $\delta_B^{(*)}$ is the *CP*-even, relative strong phase between the interfering amplitudes, and $r_B^{(*)} = |A(B^+ \to D^{(*)0}K^+)/A(B^+ \to \overline{D}^{(*)0}K^+)|$ is the ratio of decay amplitudes. For the ADS analysis the $D^{(*)}$ mesons do not decay to *CP* eigenstates, and two more parameters appear (another unknown amplitude ratio and phase). Eq. (12.1) shows that the sensitivity of these measurements to γ is inversely proportional the size of $r_B^{(*)}$ (expected to be about 0.1, see Section 10.3.3). The advantage of the $B^+ \to D^{(*)}K^+$ channels is that $r_B^{(*)}$ can be extracted from the measurements themselves, and do not need to be obtained through other means. Compared with $B \to D^{(*)\mp}h^{\pm}$ ($h = \pi, \rho$) decays, no theoretical uncertainty is assigned to the amplitude ratios.

The GLW and ADS analyses combined result in a four-fold ambiguity in γ. The GGSZ analysis exploits the three-body Dalitz plot of the D decay, which enhances the sensitivity to γ and $r_B^{(*)}$ compared with the former methods. It has a two-fold ambiguity in γ.

An up-to-date summary of all available GLW, ADS, and GGSZ measurements can by found at Ref. [31]. Their confidence levels for γ, including the combined constraint, are shown in the left-hand side of Fig. 12.1, and are determined with a frequentist approach [21]. Their combined average is $\gamma = (62^{+35}_{-25})^\circ$ [21], and is dominated by the D Dalitz approach. The errors are statistics limited. The systematic uncertainty (about $\pm 14^\circ$) is dominated by the D Dalitz model used (about $\pm 10^\circ$).

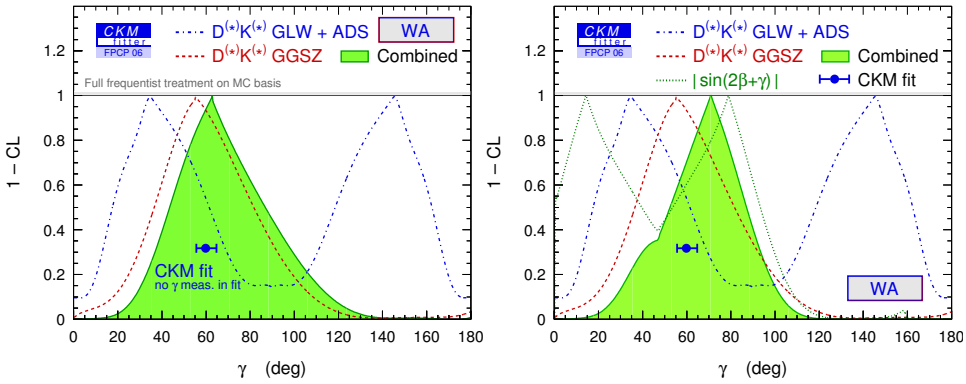

Figure 12.1: *Left: confidence level for γ from the direct CP violation measurements in $B^\pm \to D^{(*)}K^{(*)\pm}$ decays. Right: including the measurement of γ from $B \to D^{(*)\mp}h^\pm$ decays. A theoretical error of 15% has been added to account for $SU(3)$ breaking in the determination of the amplitude ratios r^j. The frequentist approach uses to set the confidence level assumes uniform prior distributions for the strong phase differences δ^j [21].*

Combined results

The combined confidence level for γ from the *CP* violation measurements in $B^\pm \to D^{(*)}K^{(*)\pm}$ and $B \to D^{(*)\mp}h^\pm$ decays is shown on the right-hand side of Fig. 12.1. The frequentist approach of Ref. [21] uses a theoretical error of 15% to account for $SU(3)$ breaking in the determination of the amplitude ratios r^j, and assumes uniform prior distributions for δ^j to set the confidence level for γ. The current, overall γ average is found to be $\gamma = (71^{+22}_{-30})^\circ$ [21]. Effectively, the direct measurements of γ prefer a value in the first quadrant of the $(\bar{\rho}, \bar{\eta})$ plane. The value found is fully consistent with the γ estimate from all indirect measurements $\gamma = (60^{+5}_{-4})^\circ$.

The world average of the direct measurements of γ is not dominated by any individual measurement, although the GLW and ADS analyses contribute the least. A large weight in the γ average comes from the GGSZ analysis, which has a single solution to $\gamma \in [0, \pi]$. The γ measurement of $B \to D^{(*)\mp}h^\pm$ decays excludes large values of γ. The left-hand side error on γ is dominated by the GGSZ analyses. The right-hand side error is dominated by the $B \to D^{(*)\mp}h^\pm$

decays.

12.3 Retrospective and prospects for γ

Over the last few years, the hunt for the CKM-angle γ at the B factories has been like searching for a needle in a haystack. Many B decay channels have been pursued to measure γ, and many, unfortunately, turned out to be irrelevant. To name a few: $B \to K\pi$ in combination with $B \to \pi\pi$, $B \to D^{(*)0}K^0_S$, the ADS method, $B^0 \to DK\pi$, and $B \to D^{(*)}_{(s)}D^{(*)}$ [16]. On the other hand, the D Dalitz analysis of $B^+ \to D^{(*)}K^+$, currently an important decay channel, was only introduced in late 2003, and was completely overlooked when the *BABAR* and Belle experiments started.

No single measurement has (yet) been found to dominate the direct measurements of γ. The lessons learned have been that, at least presently, the combination of many methods and decay modes is crucial to break ambiguities and constrain γ. Second, and most importantly, the measurement of γ requires large amounts of statistics.

The *BABAR* and Belle experiments intend to record 1 ab^{-1} of data each 2008, meaning a quintupling of the available dataset compared with this analysis.

For that dataset, the combined GLW, ADS, and Dalitz analyses of *BABAR* predict a total error on γ of 15° [162]. In this estimate, the systematic error is dominated by uncertainty on D Dalitz model assumptions. The prediction assumes a value of $r^{(*)}_B = 0.1$.

Initial expectations of $r^{(*)}_B$ varied between 0.1 and as much as 0.3, using naive factorization and color suppression. The Belle experiment published a value of $r_B = 0.21 \pm 0.08 \pm 0.03 \pm 0.04$ in 2004 [163], but this has dropped with the latest ADS measurement to $r_B < 0.18$ at 90% C.L. [164]. The current world averages are $r_B = 0.077 \pm 0.028$ and $r^*_B = 0.085 \pm 0.046$ [122]. This drop in the value of r_B has *increased* the uncertainty on the world average of the latest direct γ measurements from 2005 to 2006, and – until the doubly CKM-suppressed decay $B^+ \to D^0K^+$ has been actually observed – this may happen again in the future.

For the time-dependent analysis of $B \to D^{(*)\mp}h^\pm$ ($h = \pi, \rho$) described in this thesis, it is expected that the uncertainties on *CP*-related observables will remain statistics dominated, and scale with the inverse square-root of the integrated luminosity, or better with possible improvements in analysis, vertexing, and B tagging algorithms. Simultaneous updates of the branching fractions $\mathcal{B}(B^0 \to h^- l^+ \nu)$ and $\mathcal{B}(B^0 \to h^- D^{(*)+})$ are required to reduce the experimental and theoretical uncertainties in the amplitude ratios r^j. A most useful addition to this particular analysis would be the measurement of tag-side interference effects with inclusively reconstructed $B^0 \to D^{*-} l^+ \nu$ decays, thereby reducing the uncertainties in the $c^j_{\rm lep}$ observables with a factor of two, and doubling their sensitivity to γ. Another recommendation, easier to implement, is to split the measured c^j_i observables (18 in total) into B-mode dependent parts, $c^j_{\rm lep}$ (3), and tag-side interference related observables (5, one per tagging category). This also reduces the errors on the $c^j_{\rm lep}$ observables.

Combining the *BABAR* analyses of $B \to D^{(*)\mp}h^\pm$, it may be possible at the end of the *BABAR* era to set individual 90% confidence levels for the ambiguous solutions of γ (as in Fig. 11.8), corresponding to an error on γ of about 15°. What will certainly happen, perhaps already in the next round of analyses updates, is the (combined) observation of *CP* violation in $B \to D^{*\mp}\pi^\pm$, *i.e.* $a^{D^*\pi}$ inconsistent with zero, which is currently at the level of 3.4σ.

In conclusion, the enlarged *BABAR* data sample available in the near future and the im-

proved measurements of γ-related observables will lead to a more accurate determination of γ, up to 12–15° by the year 2008. Similar results are expected for the Belle experiment.

With physics data-taking of the LHCb experiment expected to start in 2008, the availability of B_s mesons allows a new set of possible measurements of γ. An example is $SU(3)$ equivalent of this measurement, namely the time-dependent measurement of the decays $B_s \to D_s^{(*)\mp} K^{\pm}$. The first results for γ using B_s mesons are likely produced by 2010. The most promising decay channel is $B_s \to K^+K^-$, combined with $B_d \to \pi^+\pi^-$. With an estimated error as small as 5° after one year of data taking [165], we may finally balance out the error-scale between the direct and indirect measurements of γ and make a powerful comparison.

References

[1] J. H. Christenson, J. W. Cronin, V. L. Fitch, and R. Turlay, Phys. Rev. Lett. **13** 138 (1964).

[2] A. D. Sakharov, ZhETF Pis. Red. 5, 32 (1967); JETP Lett. 5, 24 (1956).

[3] M. Kobayashi and T. Maskawa, Prog. Theor. Phys. **49**, 652 (1973).

[4] S.L. Glashow, Nucl. Phys. **22**, 579 (1961); S. Weinberg, Phys. Rev. Lett. **19**, 1264 (1967); A. Salam, in *Proc. 8th Nobel Symp.*, ed. N. Swartholm, Almquist and Wiksells, Stockholm (1968).

[5] N. Cabibbo, Phys. Rev. Lett. **10**, 531 (1963).

[6] *BABAR* Collaboration, B. Aubert *et al.*, Phys. Rev. Lett. **94**, 161803 (2005).

[7] Belle Collaboration, K. Abe *et al.*, BELLE-CONF-0569, LP2005-204 (2005) [hep-ex/0507037].

[8] *BABAR* Collaboration, B. Aubert *et al.*, Phys. Rev. Lett. **95**, 041805 (2005).

[9] Belle Collaboration, A. Somov, A. J. Schwartz *et al.*, Phys. Rev. Lett. **96**, 171801 (2006).

[10] R.G. Sachs, Enrico Fermi Institute Report, EFI-85-22 (1985) (unpublished); I. Dunietz and R.G. Sachs, Phys. Rev. D **37**, 3186 (1988) [E: Phys. Rev. D **39**, 3515 (1989)]; R. Aleksan, I. Dunietz and B. Kayser, Z. Phys. **C54**, 653 (1992); I. Dunietz, Phys. Lett. B **427**, 179 (1998); D. London, N. Sinha, and R. Sinha, Phys. Rev. Lett. **85**, 1807 (2000).

[11] I. Dunietz, Phys. Lett. B **427**, 179 (1998;)I. Dunietz, R.G. Sachs, Phys. Rev. D **37**, 3186 (1988.)

[12] N. Cabibbo, Phys. Rev. Lett. **10**, 531 (1963); M. Kobayashi and T. Maskawa, Prog. Theor. Phys. **49**, 652 (1973).

[13] Charge conjugation is implied in this thesis, unless otherwise stated. The superscript $(*)$ indicates that a symbol must be considered both with and without the $*$ suffix.

[14] *BABAR* Collaboration, B. Aubert *et al.*, Phys. Rev. D **73**, 111101 (2006).

[15] I. I. Bigi and A. I. Sanda, Nucl. Phys. B **193**, 85 (1981); Nucl. Phys. B **281**, 41 (1987).

[16] P.F. Harrison and H.R. Quinn (editors),"The *BABAR* Physics Book", SLAC-R-504 (1998).

[17] Particle Data Group, S. Eidelman *et al.*, Phys. Lett. B **592**, 1 (2004).

[18] C. Jarlskog, Phys. Rev. Lett. **55**, 1039 (1985).

[19] See, for example, L. Wolfenstein, Phys. Rev. D **66**, 010001-118 (2002).

[20] A.J. Buras and R. Fleischer, Adv. Ser. Direct. High Energy Phys. **15**, 65 (1998).

[21] CKMfitter Group, J. Charles *et al.*, Eur. Phys. Jour. **C41**, 1 (2005).

[22] A. J. Buras, M.E. Lautenbacher and G. Ostermaier, Phys. Rev. **D50**, 3433 (1994).

[23] S. W. Herb *et al.*, Phys. Rev. Lett. **39**, 252 (1977); W. R. Innes *et al.*, Phys. Rev. Lett. **39**, 1240 (1977).

[24] E. Fernandez *et al.*, Phys. Rev. Lett. **51**, 1022 (1983); N. Lockyer *et al.*, Phys. Rev. Lett. **51**, 1316 (1983).

[25] G.C. Branco, L. Lavoura, and J.P. Silva, "*CP* violation International series of monographs on physics", Oxford Science Publications (1999).

[26] UA1 Collaboration, C. Albajar *et al.*, Phys. Lett. **B186**, 247 (1987).

[27] ARGUS Collaboration, H. Albrecht *et al.*, Phys. Lett. **B192**, 245 (1987).

[28] S. Laplace, Z. Ligeti, Y. Nir and G. Perez, Phys. Rev. **D65**, 094040 (2002).

[29] *BABAR* Collaboration, B. Aubert *et al.*, Phys. Rev. Lett. **88**, 221803 (2002).

[30] H. Boos, T. Mannel, and J. Reuter, Phys. Rev. **D70**, 036006 (2004).

[31] Heavy Flavor Averaging Group, E. Barberio *et al.*, hep-ex/0603003.

[32] *BABAR* Collaboration, B. Aubert *et al.*, Phys. Rev. Lett. **93**, 131801 (2004).

[33] R. Fleischer, Nucl. Phys. B 671, 459 (2003).

[34] J. Seeman *et al.*, "The PEP-II Storage Rings", SLAC-PUB-8786 (2001), submitted to Nucl. Instr. and Methods **.**

[35] J. Seeman *et al.*, "Status Report on PEP-II Performance", *Proceedings of the 7th European Particle Accelerator Conference(EPAC 2000)*, Vienna, Austria (2000).

[36] *BABAR* Collaboration, B. Aubert *et al.*, The *BABAR* Detector, Nucl. Instr. and Methods **A479**, 1-116 (2002).

[37] P. Oddone, "An Asymmetric B Factory Based on PEP", published in *Santa Monica 1989, The fourth family of quarks and leptons*, 237 (1989).

[38] A. Foland and K. Bloom, "Introduction to CLEO" (1998).

[39] M. Baak and G. Raven,
`http://www.slac.stanford.edu/~mbaak/MY_TALKS/bbdynamics.pdf.gz`

[40] G. Lynch, S. Schaffner, S. Wagner, G, Raven, and F. Wilson, "*BABAR* Drift Chamber Tracking Conventions", *BABAR* Note #488, TNDC-NOTE-99-95 (1999).

[41] M. Sullivan, "B-Factory Interaction Region Design", *Proceedings of the IEEE Particle Accelerator Conference (PAC97)*, Vancouver, BC, Canada (1997), SLAC-PUB-7563.

[42] Up-to-date information about the PEP-II integrated luminosity can be found at
`http://www.slac.stanford.edu/grp/cd/soft/images/lum.gif`

[43] GEANT4 Collaboration, S. Agostinelli *et al.*, Nucl. Instrum. Meth. A **506**, 250 (2003).

[44] A. Ryd and D. Lange *et al.*, "The EvtGen particle decay simulation package", Nucl. Instr. and Methods A **462**, 152 (2001).
`http://www.slac.stanford.edu/~lange/EvtGen/`

[45] T.Sjöstrand, Comput. Phys. Commun. **82**, 74 (1994); T.Sjöstrand and M.Bengston *ibid.* **43**, 367 (1987); T.Sjöstrand, *ibid.* **39**, 347 (1986)

[46] D. N. Brown, E. A. Charles, and D. A. Roberts, "The *BABAR* Track Fitting Algorighm", *Proceedings of CHEP 2000*, Padova, Italy (2000).

[47] P. Billoir, Nucl. Instr. and Methods **A255**, 225 (1984).

[48] B. Brabson *et al.*, Nucl. Instr. and Methods A **332**, 419 (1993).

[49] S. Menke *et al.*, "Calibration of the *BABAR* Electromagnetic Calorimeter with π^0 s", *BABAR* Note #528 (2000).

[50] A. Drescher *et al.*, Nucl. Instr. and Methods **A237**, 464 (1985).

[51] S. Spanier and G. Mancinelli, "Kaon Selection at *BABAR*", *BABAR* Analysis Document #116 (2001).

[52] G. Mancinelli and. S. Yellin, "An Event Likelihood Algorithm for DIRC-Based Particle Identification", *BABAR* Analysis Document #165 (2001).

[53] R. Sinkus and T. Voss, Nucl. Instr. and Methods A **391**, 360 (1997).

[54] U. Langenegger, "Cut-based Electron Identification", *BABAR* Analysis Document #90 (2001).

[55] L. Lista and F. Fabozzi, "Muon Identification in the *BABAR* Experiment", *BABAR* Analysis Document #60 (2000).

[56] *BABAR* Collaboration, B. Aubert *et al.*, Phys. Rev.**D66**, 032003 (2002).

[57] F. Martinez-Vidal *et al.*, "The Babar vertexing", *BABAR* Analysis Document #102 (2001); "Vertexing performances and systematic checks with fully reconstructed B events", *BABAR* Analysis Document #130 (2001); "Vertexing supporting document for summer 2001 conferencs", *BABAR* Analysis Document #254 (2001).

[58] M. Bruinsma, D.J. Lange, G. Sciolla, and M.C. Simani, "A B flavor tagging algorithm for CP violation measurements with the *BABAR* experiment", BAD 1025 (2005).

[59] G.C. Fox and S. Wolfram, Phys. Rev. Lett. **41**, 1581 (1978).

[60] S. Brandt *et al.*, *Phys. Lett.* **12** (1964) 57; E. Fahri, Phys. Rev. Lett. **39**, 1587 (1977.)

[61] W.T. Ford, "Choice of Kinematic Variables in B Meson Reconstruction – Take 3", *BABAR* Analysis Document #53 (2000).

[62] A general description of kinematic- and vertex-fitting techniques and their benefits falls outside the scope of this report. See for example:
Paul Avery, "Applied Fitting Theory", CLEO Note CBX 91-72 (1991).
`http://www.phys.ufl.edu/~avery/fitting.html`

[63] ARGUS Collaboration, H. Albrecht *et al.*, Phys. Lett. **B 241** 278 (1990).

[64] W. Hulsbergen *et al.*, "Measurement of the Branching Ratio and the Time-Dependent CP-asymmetries for $B^0 \to K_S\pi^0$ decays on Run $1-4$ data", *BABAR* Analysis Document #904 (2005).

[65] *BABAR* Collaboration, B. Aubert *et al.*, Phys. Rev. Lett. **92**, 251801 (2004.)

[66] ARGUS collaboration, Z. Phys. **C62**, 371 (1994).

[67] F. Le Diberder, "*CP* Violation as seen from the Δz Distribution", *BABAR* Note #42 (1990).

[68] J. Stark *et al.*, "Measurements of the charged and neutral B meson lifetimes using fully reconstructed B decays", *BABAR* Analysis Document #144 (2001).

[69] C.-H. Cheng and P. Burchat, "Correlation between mistag of kaon tag and calculated error on Δt", *BABAR* Analysis Document #349 (2002).

[70] A. Snyder, "Dilution vs. Error explained?",
`http://www.slac.stanford.edu/~snyder/BaBar/dilerrIII.ps`

[71] M. Baak *et al.*, "Measurement of the wrong-flavor to right-flavor Amplitude Ratio in $\overline{B}^0/B^0 \to J/\psi K^{*0}\,(K^{*0} \to K^+\pi^-)$", *BABAR* Analysis Document #423.

[72] O. Long and S. Prell *et al.*, "Supporting document for the summer 2002 sin2beta measurement using charmonium decay modes.", *BABAR* Analysis Document #442.

[73] O. Long, M. Baak, R.N. Cahn, and D. Kirkby, Phys. Rev. **D68**, 034010 (2003).

[74] *BABAR* Collaboration, B. Aubert *et al.*, Phys. Rev. Lett. **87**, 201803 (2001).

[75] W. Verkerke and D. Kirkby,
`http://roofit.sourceforge.net`

[76] M. Bruinsma, D.J. Lange, O. Long, M.C. Simani, "Summer 2004 update of sin2beta using $B \to (c\bar{c})K$ decays", *BABAR* Analysis Document #929 (2004).

[77] Sh. Rahatlou and S. Prell, "Determination of Difference in Reconstruction and Tagging Efficiencies with a Time-Dependent Method", *BABAR* Analysis Document #467 (2003).

[78] T. Skwarnicki, DESY F31-86-02, Ph.D. thesis (1986).

[79] Particle Data Group, K. Hagiwara *et al.*, Phys.Rev. **D66**, 010001 (2002).

[80] *BABAR* Collaboration, B. Aubert *et al.*, Phys. Rev. Lett. **87**, 201803 (2001).

[81] M. Baak, G. Raven, and L. Wilden, "The ρ Lineshape Decomposition and Measurement of the Angular Decay Amplitudes of $B \to D^{(*)\mp}\rho^{\pm}$", *BABAR* Analysis Document #1101 (2005).

[82] J.H. Kühn and A. Santamaria, Z. Phys. **C48**, 445 (1990).

[83] J. Blatt and V. Weisskopf, "Theoretical Nuclear Physics", John Wiley & Sons, New York, 362 (1956).

[84] D. Brown *et al.*, "Local Alignment of the SVT", *BABAR* Analysis Document #486 (2002). http://www.slac.stanford.edu/BFROOT/www/Detector/SVT/LocalAlignment/

[85] B. Dunwoodie *et al.*, "Radial and longitudinal length scale from beampipe structure", presented at the *BABAR* collaboration meeting, December 2000. http://www.slac.stanford.edu/~wmd/beampipe/dec00.talk

[86] D.A. Suprun, C. Chiang, and J.L. Rosner, Phys. Rev. D **65**, 054025 (2002).

[87] D. Pirjol, Proc. of the Beauty Workshop on B physics at hadron machines, June 2005, Assisi, Italy, to be published in Nucl. Instrum. Methods A. http://www.slac.stanford.edu/~mbaak/pirjol_beauty05.pdf

[88] M. Bauer, B. Stech, and M. Wirbel, Zeit. Phys. **C34**, 103 (1987).

[89] J.D. Bjørken, Nucl. Phys. Proc. Suppl. **11**, 325 (1989). http://lls.fnal.gov/archive/1988/conf/Conf-88-134-T.pdf

[90] CLEO Collaboration, S. E. Csorna *et al.*, Phys. Rev. **D67**, 112002 (2003).

[91] Belle Collaboration, H. Miyake *et al.*, Phys. Lett. **B618**, 34 (2005).

[92] *BABAR* Collaboration, B. Aubert *et al.*, Phys. Rev. **D67**, 092003 (2003).

[93] *BABAR* Collaboration, B. Aubert *et al.*, submitted to Phys. Rev. **D**, hep-ex/0602023.

[94] A.J. Buras, J.-M. Gérard, and R. Rückl, Nucl. Phys. B268, 16 (1986).

[95] H.D. Politzer, and M.B. Wise, Phys. Lett. B257, 399 (1991); M. Beneke, G. Buchalla, M. Neubert, and C.T. Sachrajda, Phys. Rev. Lett. **83**, 1914 (1999); C.W. Bauer, D. Pirjol, and I.W. Stewart, Phys. Rev. Lett. **87**, 201806 (2001).

[96] Z. Ligeti, M. Luke, and M.B. Wise, Phys. Lett. **B507**, 142 (2001).

[97] *BABAR* Collaboration, B. Aubert *et al.*, submitted to Phys. Rev. **D**, hep-ex/0604009.

[98] Z. Luo and J.L. Rosner, Phys. Rev. **D64**, 094001 (2001).

[99] C.W. Bauer, B. Grindstein, D. Pirjol, and I.W. Stewart, Phys. Rev. D **67**, 014010 (2003); M. Zito, Phys. Lett. **B507**, 586 (2004).

[100] D. Pirjol, private communications.

[101] J.L. Rosner, Phys. Rev. **D42**, 3732 (1990).

[102] J.G. Körner and G.A. Schuler, Phys. Lett. **B231**, 306 (1989).

[103] C.A. Dominguez, J.G. Körner, and K. Schilder, Phys. Lett. **B248**, 399 (1990).

[104] P. Ball and R. Zwicky, Phys. Rev. **D71**, 014029 (2005).

[105] CLEO Collaboration, J.E. Duboscq *et al.*, Phys. Rev. **D76**, 3898 (1996).

[106] D. Bortoletto and S. Stone, Phys. Rev. Lett. **65**, 2951 (1990).

[107] CLEO Collaboration, S.B. Athar *et al.*, Phys. Rev. **D68**, 072003 (2003).

[108] Belle Collaboration, K. Abe *et al.*, hep-ex/0408145.

[109] *BABAR* Collaboration, B. Aubert *et al.*, Phys. Rev. **D72**, 051102 (2005).

[110] *BABAR* Collaboration, B. Aubert *et al.*, hep-ex/0506064.

[111] M. Okamoto *et al.*, Nucl. Phys. Proc. Suppl. **140**, 461 (2005).

[112] J. Shigemitsu *et al.*, Nucl. Phys. Proc. Suppl. **140**, 464 (2005).

[113] T. Becher and R.J. Hill, Phys. Lett. **B633**, 61 (2006).

[114] D. Becirevic and A.B. Kaidalov, Phys. Lett. **B478**, 417 (2000).

[115] *BABAR* Collaboration, B. Aubert *et al.*, *BABAR* Analysis Document #1394, to be submitted to Phys. Rev. Lett.

[116] *BABAR* Collaboration, B. Aubert *et al.*, submitted to Phys. Rev. Lett., hep-ex/0604012.

[117] Belle Collaboration, P. Krokovny *et al.*, Phys. Rev. Lett. **89**, 231804 (2002).

[118] *BABAR* Collaboration, B. Aubert *et al.*, *BABAR* Analysis Document #1329, to be submitted to Phys. Rev. Lett.

[119] *BABAR* Collaboration, B. Aubert *et al.*, hep-ex/0408029.

[120] *BABAR* Collaboration, B. Aubert *et al.*, Phys. Rev. **D71**, 091104 (2005).

[121] D. Scora and N. Isgur, Phys. Rev. **D52**, 2783 (1995); D. Melikhov and B. Stech, Phys. Rev. **D62**, 014006 (2000); H.-Y. Cheng, C.-Y. Cheung, and C.-W. Hwang, Phys. Rev. **D55**, 1559 (1997);

[122] UTFit Collaboration, M. Bona *et al.*, `http://www.utfit.org`.

[123] J.F. Donoghue, E. Golowich, A.A. Petrov, and J.M. Soares, Phys. Rev. Lett. **77**, 2178 (1996).

[124] B. Blok, I.E. Halperin, Phys. Lett. **B385**, 324 (1996).

[125] C.-K. Chua, W.-S. Hou, and K.-C. Yang, Phys. Rev. **D65**, 096007 (2002).

[126] M. Suzuki and L. Wolfenstein, Phys. Rev. **D60**, 074019 (1999).

[127] J.-M. Gérard and W.S. Hou, Phys. Rev. **D43**, 2909 (1991).

[128] G. Nardulli and T.N. Pham, Phys. Lett. **B391**, 165 (1997).

[129] K.M. Watson, Phys. Rev. **88**, 1163 (1952).

[130] S. Mantry, D. Pirjol, I.W. Stewart, Phys. Rev. **D68**, 114009 (2003).

[131] CLEO Collaboration, J. Bartelt *et al.*, Phys. Rev. Lett. **82**, 3746 (1999).

[132] *BABAR* Collaboration, B. Aubert *et al.*, Phys. Rev. **D71**, 051502 (2004).

[133] Belle Collaboration, P. Krokovny *et al.*, Phys. Rev. Lett. **90**, 141802 (2003).

[134] *BABAR* Collaboration, B. Aubert *et al.*, submitted to Phys. Rev. **D**, hep-ex/0604016 (2006).

[135] CLEO Collaboration, M. Artuso *et al.*, Phys. Rev. Lett. **95**, 251801, (2005).

[136] C. Aubin *et al.*, Phys. Rev. Lett. **95**, 122002, (2005).

[137] G. Buchalla, A. Buras, and M. Lautenbacher, Rev. Mod. Phys. **68**, 1125 (1996).

[138] B. Blok, M. Gronau, and J.L. Rosner, Phys. Rev. Lett. **78**, 3999 (1997).

[139] M. Gronau, O.F. Hernández, D. London, and J.L. Rosner, Phys. Rev. **D52**, 6356 (1995).

[140] C.W. Chiang and J.L. Rosner, Phys. Rev. **D67**, 074013 (2003); C.S. Kim, S. Oh, and C. Yu, Phys. Lett. **B621**, 259 (2005).

[141] Belle Collaboration, K. Abe *et al.*, Phys. Rev. Lett. **88**, 052002 (2002); CLEO Collaboration, T.E. Coan *et al.*, Phys. Rev. Lett. **88**, 062001 (2002); *BABAR* Collaboration, B. Aubert *et al.*, Phys. Rev. **D69**, 032004 (2004).

[142] C.-K. Chua, W.-S. Hou, and K.-C. Yang, Phys. Rev. **D65**, 096007 (2002).

[143] D. Du, L.-B. Guo, and D.-X. Zhang, Phys. Lett. **B406**, 110 (1997); K. Ukai, Proc. of the BCP4 Workshop on B physics and CP violation, February 2001, Ise-Shima, Japan, p. 287.

[144] J.O. Eeg, S. Fajfer, and A. Hiorth, Phys. Lett. **B570**, 46 (2003).

[145] Z.-Z. Xing, Phys. Rev. **D53**, 2847 (1996).

[146] C.G. Callan and S.B. Treiman, Phys. Rev. Lett. **16**, 153 (1966); C.A. Dominguez, Phys. Lett. **B86**, 171 (1979).

[147] A. Datta, D. London, Phys. Lett. **B584**, 81 (2004).

[148] G. P. Lepage and S. J. Brodsky, Phys. Rev. **D22**, 2157 (1980).

[149] J.L. Goity, Phys. Rev. **D46**, 3929 (1992); M. Hayakana, T. Kurimoto, and A.I. Sanda, Prog. Theor. Phys. **92**, 377 (1994).

[150] *BABAR* Collaboration, B. Aubert *et al.*, Phys. Rev. **D71**, 112003 (2005).

[151] *BABAR* Collaboration, B. Aubert *et al.*, submitted to Phys. Rev. **D**, hep-ex/0604037.

[152] *BABAR* Collaboration, B. Aubert *et al.*, Phys. Rev. **D71**, 091104 (2005).

[153] F. Buccella, M. Lusignoli, G. Miele, and A. Pugliese, Zeit. Phys. **C55**, 243 (1992); A.N. Kamal, Q.P. Xu, and A. Czarnecki, Phys. Rev. **D49**, 1330 (1994); F. Buccella, M. Lusignoli, G. Miele, A. Pugliese, and P. Santorelli, Phys. Rev. **D51**, 3478 (1995);

[154] F.E. Close and H.J. Lipkin, Phys. Lett. **B405**, 157 (1997).

[155] Unknown.

[156] J. Charles *et al.*, " Bayesian statistics at work: The Troublesome extraction of the CKM phase alpha.", hep-ex/0607246.

[157] G.J. Feldman and R.D. Cousins, Phys. Rev. **D57**, 3873 (1998).

[158] Belle Collaboration, F.J. Ronga *et al.*, Phys. Rev. **D73**, 092003 (2006).

[159] M. Gronau and D. London, Phys. Lett. **B253**, 483 (1991); M. Gronau and D. Wyler, Phys. Lett. **265**, 172 (1991).

[160] D. Atwood, I. Dunietz, and A. Soni, Phys. Rev. Lett. **78**, 3257 (1997); Phys. Rev. **D63**, 036005 (2001).

[161] A. Giri, Y. Grossman, A. Soffer, and J. Zupan, Phys. Rev. **D68**, 054018 (2003); Belle Collaboration, A. Poluektov *et al.*, Phys. Rev. **D70**, 072003 (2004).

[162] Nicola Neri, private communications.

[163] Belle Collaboration, K. Abe *et al.*, BELLE-CONF-0476 (2004) [hep-ex/0411049].

[164] Belle Collaboration, K. Abe *et al.*, BELLE-CONF-0552 (2005) [hep-ex/0508048].

[165] LHCb Collaboration, R. Antunes Nobrega *et al.*, "LHCb Reoptimized detector design and performance", CERN/LHCC 2003-030.

Summary

This thesis reports measurements of the time-dependent *CP* asymmetries in fully reconstructed $B^0 \to D^{(*)\mp}\pi^{\pm}$ and $B^0 \to D^{\mp}\rho^{\pm}$ decays in approximately 232 million $\Upsilon(4S)\to B\overline{B}$ events, collected with the *BABAR* detector at the PEP-II asymmetric-energy B factory at the Stanford Linear Accelerator Center in California, as published in Ref. [14].

The phenomenon of *CP* violation allows one to distinguish between matter and antimatter, and, as such, is one of the essential ingredients needed to explain the apparent abundance of matter over antimatter in the universe. The Standard Model describes the observed elementary particles in terms of three generations of quarks and leptons, as well as the weak, electromagnetic, and strong interactions between them. In the Standard Model, *CP* violation is incorporated in the Cabibbo-Kobayashi-Maskawa (CKM) matrix, which describes the weak interactions between the quarks. The weak interactions between quarks are described by coupling constants that are functions of three real parameters and one irreducible complex phase. The magnitude of all *CP* violating effects in the Standard Model is related to this complex phase.

The measurement of the *CP* violating phase of the CKM matrix is an important part of the present scientific program in particle physics. Violation of the *CP* symmetry manifests itself as a non-zero area of the Unitarity Triangle. The Unitarity Triangle needs to be overconstrained by experimental measurements in order to demonstrate that the CKM mechanism is the correct explanation of this phenomenon. No stringent measurement of the CKM-angle γ is yet available.

The B meson is an excellent probe of the Unitarity Triangle. The time evolution of $B \to D^{(*)\mp}h^{\pm}$ decays, where h is a pion or ρ meson, is sensitive to the CKM-angle γ, because the CKM-favored decay amplitude $\overline{B}^0 \to D^{(*)+}h^-$ and the doubly-CKM-suppressed decay amplitude $B^0 \to D^{(*)+}h^-$ interfere due to $B^0\overline{B}^0$ mixing. The relative weak phase between these two amplitudes is γ. With $B^0\overline{B}^0$ mixing, the total weak phase difference between the interfering amplitudes is $2\beta+\gamma$.

The *BABAR* experiment consists of the PEP-II asymmetric-energy e^+e^- collider and the *BABAR* detector. The design of the *BABAR* experiment has been optimized for the study of *CP* violation in the decays of neutral B mesons. The PEP-II collider operates at the $\Upsilon(4S)$ resonance, which is a clean source of B mesons and decays to a $B^0\overline{B}^0$ pair half of the time. PEP-II provides abundant samples of B mesons, and makes it possible to perform a direct test of Kobayashi-Maskawa model of *CP* violation.

One of the B^0 mesons produced by the $\Upsilon(4S)$ resonance is fully reconstructed in the desired final state $D^{(*)\mp}h^{\pm}$. The measurement of time-dependent *CP* violation requires knowledge of Δt, the time difference between the decays of the two B mesons. This is computed from the distance between their decay vertices. Another requirement for time-dependent measurements is the determination of the flavor of one of the two decaying B mesons. This is done by

using the B decay products like leptons, kaons and other flavor-sensitive features such as low momentum pions from D^* decays. Since the efficiency for full reconstruction of B mesons is small, an inclusive method is used to infer the flavor and decay vertex from the decay products of the other B meson.

Interference between CKM-favored $b \to c\overline{u}d$ and doubly-CKM-suppressed $\overline{b} \to \overline{u}c\overline{d}$ amplitudes in final states used for B flavor tagging gives deviations from the standard time evolution assumed in CP-violation measurements at B factories producing coherent $B^0\overline{B}^0$ pairs. The time-dependent analysis of $B \to D^{(*)\mp}h^{\pm}$ decays incorporates this possible effect of tag-side interference, which could produce asymmetries as large as the expected signal asymmetry.

From a time-dependent maximum likelihood fit we obtain for the parameters related to the CP violation angle γ:

$$\begin{aligned}
a^{D\pi} &= -0.010 \pm 0.023 \pm 0.007 \quad , \quad c_{\rm lep}^{D\pi} = -0.033 \pm 0.042 \pm 0.012 \ , \\
a^{D^*\pi} &= -0.040 \pm 0.023 \pm 0.010 \quad , \quad c_{\rm lep}^{D^*\pi} = 0.049 \pm 0.042 \pm 0.015 \ , \\
a^{D\rho} &= -0.024 \pm 0.031 \pm 0.009 \quad , \quad c_{\rm lep}^{D\rho} = -0.098 \pm 0.055 \pm 0.018 \ ,
\end{aligned}$$

where the first error is statistical and the second is systematic. To extract γ from the CP-violating observables, some theoretical input parameters are needed. These parameters are obtained from the decay rates of $B^0 \to \pi^- D_s^{(*)+}$ and $B^0 \to \rho^- D_s^+$. By using data from other measurements and some theoretical assumptions, we interpret the results in terms of the angles of the Unitarity Triangle. We use a frequentistic method to set a constraint on γ, and find $\gamma \in [-0.28, 1.91]$, or $|\sin(2\beta+\gamma)| > 0.46$, at 90% confidence level.

Populaire samenvatting

Speurtocht naar een verstoorde natuursymmetrie

Al zeven jaar zoeken honderden deeltjesfysici van over de hele wereld met het *BABAR* experiment bij Stanford in Californië naar iets ogenschijnlijk onbenullig: subtiele variaties in de vervaltijd van een deeltje, het zogenaamde B-meson. Toch is dit wellicht de sleutel tot één van de grootste mysteries van de natuur ...

De aanwezigheid van materie in het heelal vormt één van de belangrijkste problemen uit de kosmologie. Sterren, planeten en het leven op aarde, ze bestaan er allemaal uit. En dat is merkwaardig, want uit experimenten met deeltjesversnellers volgt dat het universum helemaal geen materie zou moeten bevatten. We verwachten dat bij de oerknal gelijke hoeveelheden materie en antimaterie zijn ontstaan. De twee zijn toen gerecombineerd en zouden allemaal moeten zijn omgezet in licht. Een klein beetje materie, zo'n één op de miljard deeltjes, heeft deze slachting vreemd genoeg wél overleefd. De vraag is: waarom?

Niemand kent de precieze verklaring voor dit overschot, maar natuurkundigen hebben wel een vermoeden. In 1967 wees de Russische theoreticus Andrei Sakharov op de voorwaarden die nodig zijn om in het jonge universum een voorkeur voor materie te doen ontstaan. De belangrijkste is dat deeltjes en antideeltjes zich niet hetzelfde gedragen. Het verschijnsel dat ze zich verschillend gedragen heet '*CP*-schending'. Materie en antimaterie lijken volkomen gelijkwaardig, alleen zijn hun eigenschappen zoals lading precies tegenovergesteld. Maar door een klein verschil in gedrag hebben ze soms een verschillende vervaltijd, zodat een overschot aan materie kan ontstaan. Hoe groter de *CP*-schending, hoe meer materie uiteindelijk kan zijn overgebleven.

Gebroken symmetrieën

Het concept *CP*-schending heeft alles te maken met symmetrieën. Symmetrie is een van de meest krachtige begrippen in de moderne natuurkunde. Niet alleen zorgt het voor een elegante wiskundige beschrijving van het gedrag van materie, nog nuttiger is dat een symmetrie altijd leidt tot een behoudswet. Zo volgt bijvoorbeeld uit de symmetrie in tijd, ofwel het feit dat de natuurwetten niet in de tijd veranderen, de wet van behoud van energie.

Er bestaan ook meer abstracte symmetrieën. Stel dat in het hele universum alle deeltjes worden omgewisseld met antideeltjes, een zogenaamde C-transformatie (C van het Engelse 'lading'). Zou je het verschil merken? Of wat als we alle ruimte-coördinaten zouden spiegelen. Zou deze P-transformatie (naar 'pariteit') waarneembaar zijn? Vroeger dacht men van niet, en dat C en P dus echte symmetrieën waren.

Eind jaren vijftig toonden experimenten aan dat in één van de vier fundamentele natu-

urkrachten, de zwakke wisselwerking, verantwoordelijk voor radioactief verval, beide symmetrieën geschonden zijn. Zo vinden we in de natuur linksom draaiende neutrino's, deeltjes die in grote hoeveelheden door de zon worden geproduceerd. Als je een C-transformatie toe zou passen op een neutrino, zou je een linksom draaiend anti-neutrino moeten krijgen. Maar deze deeltjes komen in de natuur niet voor. Hetzelfde geldt voor pariteitomkeer, waarbij het neutrino rechtsom zou gaan draaien. Ook deze deeltjes worden nergens teruggevonden. Het neutrino is net een vampier, het heeft geen reflectie in de C- of P-spiegel.

Bij toepassing van beide spiegelingen op een neutrino, een 'CP-transformatie', ontstaat er een deeltje dat wél wordt waargenomen: het rechtsom draaiende anti-neutrino. De gecombineerde CP-symmetrie is hier dus niet geschonden.

Natuurkundigen waren behoorlijk verbaasd toen in 1964 CP-schending werd waargenomen bij zogenaamde kaon deeltjes. Men vond dat een type kaon genaamd K_L^0 – een langlevend neutraal 'meson' deeltje, bestaand uit een quantummechanisch mengsel van een strange en anti-down quark en hun antideeltjes – af en toe vervalt naar twee pionen. Als de natuurwetten aan de CP-symmetrie zouden voldoen, dan zou dit verval niet mogelijk zijn.

De waargenomen CP-schending in kaonen is heel klein, slechts 0.3%, en duidt op een kleine voorkeur voor materie boven antimaterie. Maar kan deze ook de waargenomen asymmetrie tussen materie en antimaterie verklaren in het universum?

Barsten in het Standaard Model

Al onze kennis over de elementaire eigenschappen van deeltjes is samengevat in het zogenaamde 'Standaard Model' (zie Fig. 12.2). Het beschrijft alle waargenomen subatomaire deeltjes en hun interacties in termen van slechts enkele fundamentele bouwstenen. In de afgelopen dertig jaar is het Standaard Model nauwelijks gewijzigd, maar om het overwicht aan materie in het heelal te verklaren moet het waarschijnlijk worden uitgebreid.

Het Standaard Model staat een beetje CP-schending toe, in het gedeelte dat de zwakke wisselwerking tussen de quarks beschrijft. De wisselwerking tussen quarks worden beschreven met 'koppelings-constanten'. Hoe groter een koppelings-constante, hoe sterker de kracht tussen twee deeltjes. CP-schending blijkt alleen mogelijk als de koppelingsconstante van een interactie geen reëel getal is, maar imaginair. (Een imaginair getal bevat de wortel uit -1.)

De 'Unitariteitsdriehoek' (zie Fig. 12.3) verbeeldt de imaginaire getallen die de zwakke wisselwerking beschrijven tussen de quarks. De zwakke koppelingen tussen de lichte (up en down) en zware quarks (bottom en top) zijn evenredig met de lengtes van de zijden van de Unitariteitsdriehoek. De driehoek zou niet bestaan als de CP-symmetrie in de zwakke wisselwerking behouden was. In het Standaard Model zijn alle waarneembare CP-schendende asymmetrieën in de natuur functies van de hoeken van deze driehoek.

Het Standaard Model kan grofweg voorspellen hoeveel materie bij het ontstaan van het heelal is overgebleven als gevolg van CP-schending, maar dit blijkt niet genoeg om de samenstelling van het huidige universum te verklaren. En dat verschilt niet een factor twee of drie, het model voorspelt 10^{15} maal minder protonen dan we zien. Dit gebrek suggereert dat het Standaard Model incompleet is, en er andere manieren zijn waarop de CP-symmetrie wordt geschonden.

CP-schending in B-mesonen

Een ideale plaats om te zoeken naar CP-schending is bij het verval van B-mesonen. Het in 1980 ontdekte B-meson, B^0, is de grote broer van het kaon en gedraagt zich in veel opzichten

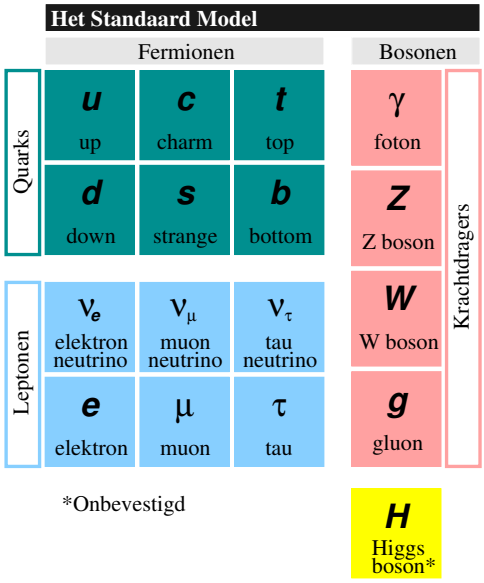

Figure 12.2: *Het Standaard Model beschrijft alle bekende elementaire deeltjes en de krachten daartussen. Er zijn zes leptonen (elektron, muon, tau en drie bijbehorende neutrino's) en zes quarks (up, down, charm, strange, top, bottom). Elk van deze deeltjes heeft een antideeltje. Ook beschrijft het Standaard Model drie krachten tussen deze deeltjes. De elektromagnetische kracht wordt uitgewisseld door het foton (γ). De zwakke wisselwerking heeft drie krachtdragers (twee W bosonen en het Z boson). De sterke kernkracht wordt uitgewisseld door acht gluonen (g). Verder voorspelt de theorie nog een zeer zwaar deeltje, het Higgs boson (H), die zorgt voor massa.*

hetzelfde. In plaats van een strange quark bevat deze het veel zwaardere bottom quark. Hierdoor kan het B-meson op veel meer manieren vervallen dan een kaon. Men vindt er een significant grotere CP-asymmetrie, soms wel in de orde van 70%, die het mogelijk maakt de Unitariteitsdriehoek precies vast te leggen. Ook hopen natuurkundigen dat de vele soorten B-vervallen op andere plaatsen dan alleen in de zwakke wisselwerking CP-schending aan het licht zullen brengen.

In vervalskanalen waarbij het B^0 meson en zijn antideeltje, het $\overline{B}^0$ meson, naar dezelfde deeltjes vervallen, zorgen CP-schending en quantummechanische processen die B^0 en $\overline{B}^0$ mesonen in elkaar om kunnen zetten ervoor dat de gemiddelde levensduur van de twee mesonen verschillend is. Een B-meson leeft gemiddeld ongeveer een picoseconde lang ($10^{-12}s$). De CP-asymmetrie tussen B^0 en $\overline{B}^0$ vervallen is een functie van de levensduur van het B-meson.

Met B-meson vervallen zijn twee hoeken van de Unitariteitsdriehoek, α en β, de afgelopen jaren vrij nauwkeurig gemeten. Maar het meten van twee van de drie hoeken is niet genoeg om CP-schending in het Standaard Model echt te testen. Daarvoor moeten alledrie de hoeken worden bepaald, om vast te leggen of ze optellen tot 180°, zoals verwacht bij een driehoek.

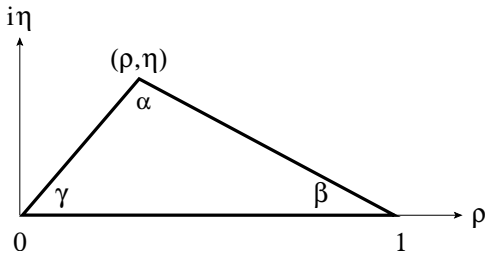

Figure 12.3: *Het Standaard Model beschrijft alle waarneembare CP-schending met slechts één parameter η. Dit is het imaginaire gedeelte van het complexe getal $\rho + i\eta$, dat de zwakke wisselwerking beschrijft tussen de lichte (up en down) en zware quarks (bottom en top). In het complexe vlak wordt dit afgebeeld met het punt (ρ, η). Samen met de oorsprong en het punt $(1, 0)$ legt het de Unitariteitsdriehoek vast. De hoeken van de driehoek, α, β en γ, bepalen de grootten van de CP-asymmetrieën in B-vervallen.*

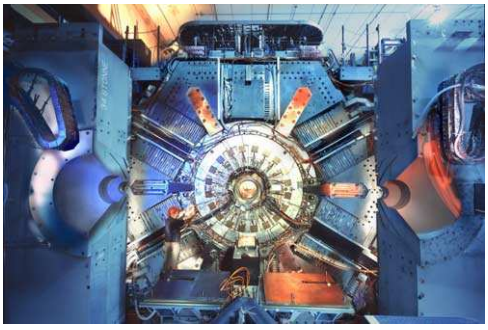

Figure 12.4: *Vooraanzicht van de BABAR deeltjesdetector bij het Stanford Linear Accelerator Center in Californië.*

Tijdens mijn promotieonderzoek bij het *BABAR* experiment heb ik gewerkt aan de eerste directe meting van de overgebleven hoek γ. Zo'n meting is belangrijk om uit te wijzen of we wel of niet te maken hebben met een ingewikkelder model van *CP*-schending.

Het *BABAR* experiment

Om te kunnen experimenteren heb je natuurlijk wel B-mesonen nodig. En veel ook, want *CP*-schendende B-vervallen zijn zeldzaam. Natuurkundigen bij het *BABAR* experiment in Californië schieten met deeltjesversnellers elektronen en positronen (antideeltjes van elektronen) op elkaar met een totale energie van ongeveer 12 GeV. Dat is de optimale energie voor het produceren van B^0-$\overline{B}^0$ meson paren. Deze 'B-fabriek' produceert zo miljoenen B-mesonen per jaar. Die worden waargenomen met de *BABAR* deeltjesdetector (zie Fig. 12.4) door het meten van de posities, impulsen en ladingen van hun vervalsdeeltjes. De laatste twee worden bijvoorbeeld

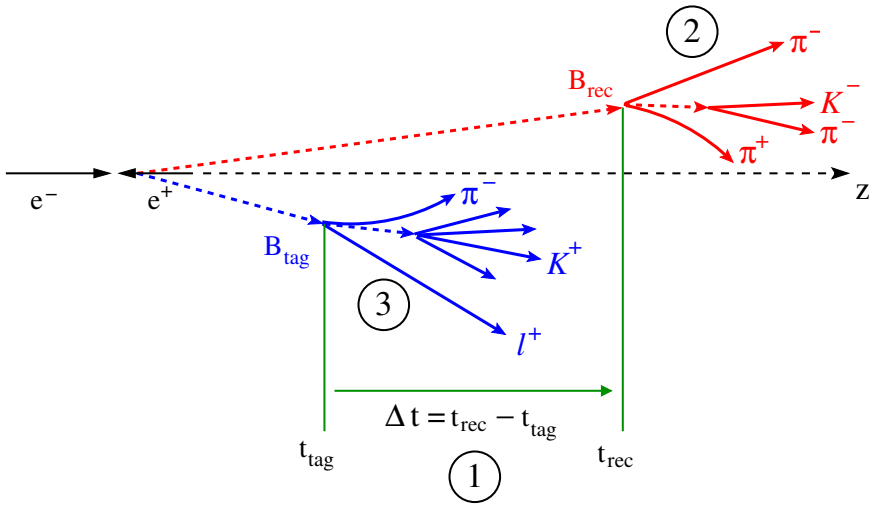

Figure 12.5: *Bij de botsing tussen het elektron en positron ontstaan twee B-mesonen. In het voorbeeld vervalt $B_{\rm rec}$ naar een pion en een aangeslagen D-meson. De vervalsproducten van het andere B-meson, $B_{\rm tag}$, wordt gebruikt om zijn begintoestand te bepalen. De tijdsduur tussen de twee vervallen, $\Delta t = t_{\rm rec} - t_{\rm tag}$, is evenredig met het verschil in vervalafstand.*

bepaald uit de kromming van het spoor van een deeltje in het magnetisch veld binnen de detector.

Drie stappen zijn nodig om *CP*-asymmetrieën te meten met met B^0 vervallen (zie Fig. 12.5).

1. De elektronen en positronen worden tot verschillende energieën versneld voordat ze met elkaar botsen. De mesonen uit een geproduceerd B-meson paar vliegen in bijna dezelfde richting met ongeveer de halve lichtsnelheid. Dit maakt het mogelijk de twee B-mesonen te onderscheiden. Ze vervallen onafhankelijk, en met behulp van hun vervalsdeeltjes kunnen de vervalsposities worden gereconstrueerd. De afstand daartussen is gemiddeld maar 260 micrometer, en is evenredig met de tijdsduur tussen de twee vervallen.

2. Een van de mesonen in een paar wordt gereconstrueerd in het verval naar een geladen pion of rho meson plus de grondtoestand of eerste aangeslagen toestand van het tegengesteld-geladen $D^{(*)}$-meson, bestaand uit een charm en anti-down quark. (De ster geeft de aangeslagen toestand aan.) Deze vervallen komen minder dan één in de honderd keer voor. De *CP*-asymmetrieën in de B-vervallen zijn evenredig met $\sin(2\beta+\gamma)$. De meting is uitdagend, want de voorspelde asymmetrieën zijn maar 4% groot.

3. Vervolgens wordt achterhaald of het pion (of ρ meson) en $D^{(*)}$-meson paar komt van een B^0 of $\overline{B}^0$ meson. Dit gebeurt met een techniek genaamd 'flavor tagging'. Als een van de B-mesonen is vervallen, vervalt de ander naar een tweede groep deeltjes. Door de typen van deze deeltjes te bestuderen is het mogelijk te bepalen of het eerste verval van een B^0 of $\overline{B}^0$ meson kwam.

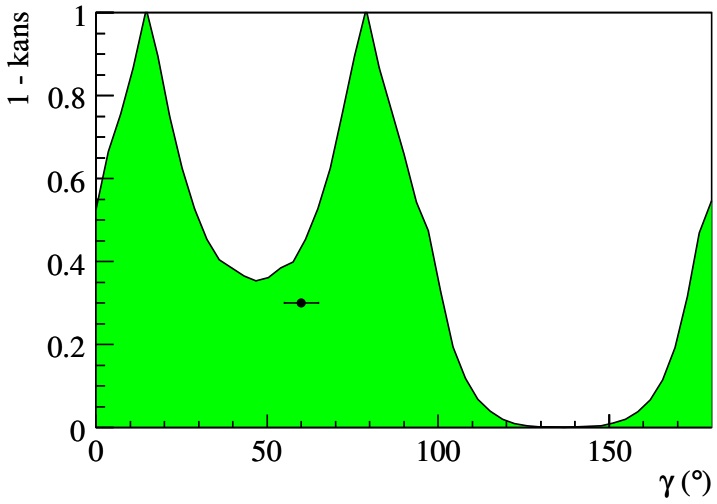

Figure 12.6: *Verdeling voor de hoek γ van de Unitariteitsdriehoek zoals volgend uit de meting. Eén oplossing ligt bij $\gamma = 78°$. Een tweede oplossing is $\gamma = 15°$. Met 90% waarschijnlijkheid ligt γ in het gebied $[-16°, 109°]$. Het zwarte punt toont de indirecte bepaling van $\gamma = 60 \pm 5°$.*

Bij dit onderzoek zijn 116 miljoen B^0-$\overline{B}^0$ meson paren bestudeerd. De beperkte efficiënties van deze techniek en de *BABAR* detector zorgen ervoor dat slechts 37 duizend gereconstrueerde en 'flavor-tagged' B-mesonen overblijven om CP-schending mee te meten.

Blinde verwerking

De verwerking van de resultaten gebeurt volkomen 'blind'. Door het optellen van geheime getallen weet niemand de gemeten CP-asymmetrieën totdat de meeting is afgerond en goedgekeurd. Zo is iedere kans op toewerken naar een gewenst eindresultaat, bewust of onbewust, uitgesloten.

Uit de gemeten vervaltijd distributies van het B-meson naar het pion-D^*-meson paar vindt het *BABAR* experiment een totale CP-asymmetrie van $3.5 \pm 1.2\%$. Het Belle experiment in Japan, een bijna exacte kopie van het *BABAR* experiment, meet een consistente CP-asymmetrie van $4.0 \pm 1.8\%$. De kans dat de combinatie van deze metingen consistent is met de hypothese dat er geen CP-schending is in dit verval is slechts 0.038%. De gevonden CP-asymmetrieën in het pion-D-meson en ρ-D-meson systeem zijn minder nauwkeurig en consistent met nul.

Uit de gevonden CP-asymmetrieën kan een meting worden afgeleid voor de hoek γ. Met 90% waarschijnlijkheid bevindt deze zich tussen $-16°$ en $109°$ (zie Fig. 12.6). Deze vinding is consistent met de bestaande Standaard Model voorspelling van $\gamma = 60 \pm 5°$. De waarden zijn niet even precies, maar vormen toch een belangrijke test van het Standaard Model. De voorspelde waarde van γ is namelijk indirect bepaald, uit de lengtes van de zijden van de Unitariteitsdriehoek. Als de directe hoekmeting niet overeenkomt, klopt het Standaard Model niet.

Nieuwe natuurkunde?

De hoop is dat deze en toekomstige experimenten de weg zullen wijzen naar een nieuwe, sterkere bron van *CP*-schending, die van invloed is geweest in het vroege universum en tot de bestaande verdeling van materie en antimaterie heeft geleid. In de tussentijd is een oerwoud van aanvullingen op het Standaard Model verzonnen, die elk nieuwe vormen van *CP*-schending kunnen bevatten. Een voorbeeld is *CP*-schending in neutrinos. Ook denkt men aan zogenaamde 'supersymmetrieën' waarbij alle deeltjes 'superpartners' hebben. Mogelijk worden die ontdekt als de Large Hadron Collider in 2008 van start gaat op het CERN in Genève. Tot die tijd blijft het bestaan van materie in het heelal een mysterie, en gaat de speurtocht naar *CP*-schending door.

Acknowledgements

Over the last five years many people have contributed to the work presented here. I'm indebted to everyone who has helped me over the years.

Ik wil Jo van den Brand graag bedanken voor de gelegenheid te promoveren in dit vakgebied, en verder voor het zijn van mijn promotor. De tweede persoon die ik wil bedanken is mijn copromotor Gerhard Raven. Beste Gerhard, hoewel we lang een halve aardbol gescheiden van elkaar hebben gewerkt kon ik altijd rekenen op je hulp. Ik vermoed dat je erg vaak je maaltijd moest opwarmen, want meestal vielen onze transatlantische gesprekken samen met je avondeten. Bedankt voor de samenwerking over de afgelopen vijf jaar! Je enthousiasme werkt aanstekelijk en is zeker sterker dan $1/r^2$.

Thanks a million to Vivek Sharma for adopting me as his student into the UC San Diego group at *BABAR*, and for extending my stay at SLAC to three years. Whilst in the UCSD group, I've had the fortune and the pleasure of working with some of the best people in the experiment: Sören Prell and Shahram Rahatlou. Thanks for showing me the ropes in *BABAR* land. And Sören, thanks for a pleasant trip to Iowa!

Hats off to Riccardo Faccini and in particular to Cecilia Voena for all our hard work on this measurement. Leif Wilden, although we've mostly worked together on the $B \to D^* \rho$ analysis, your contributions to this analysis, from your experience with ROOT to the ρ lineshape analysis, have been extremely helpful. And thanks for having been an pleasant officemate.

Owen Long, thanks for our collaboration on the tag-side interference puzzle. Much of Chapter 5 is based on your work. (Please don't tell anyone.) Thanks also to Dan Pirjol for answering all my questions on factorization, rescattering, and $SU(3)$ breaking. Apart from the people listed above, this measurements relies on the work of many people in the *BABAR* collaboration. Thanks to you all.

A special thanks to many people at SLAC for making my time there so nice: Carsten, Donna, Maarten, Chiara, Owen, Philip, Olya, Wouter H., Wouter V., Paola, Leif, Haleh, Amir, Shahram, Ed, David, Sylvie, Niels, Lideke, and everyone I forgot. Cheers!

Ook aan het werken op NIKHEF heb ik veel plezier beleefd. Bij mijn terugkomst bleek snel dat de meeste Hollandse collega's beter slap kunnen ouwehoeren dan Amerikaanse.

De leden van mijn leescommissie, Nicolo de Groot, Frank Linde, Eric Laenen en Piet Mulders, wil ik bedanken voor het lezen van mijn proefschrift en voor hun tips en suggesties.

Ben and Levien, bedankt dat jullie me als paranimfen terzijde willen staan, en bedankt voor het leesbaar maken van mijn samenvatting. Surya, bedankt voor de leuke kaft! Verder wil ik mijn ouders, familie en vrienden hartelijk bedanken voor hun niet aflatende steun, mogelijkheden tot ontspanning en voor hun geduld bij het aanhoren van al mijn verhalen de afgelopen jaren.

En last but not least: Hella. Bedankt voor al je hulp en steun! De volgende mooie zin is speciaal voor jou: "De vlammen *likken* aan het hout." Zo, staat 'ie er toch nog in.

					B^0	e^-	π	
	e^+			e^-			β	γ
	π							ρ
			e^-			π		β
	D^*		β	e^+	$\overline{B}^0$		e^-	
β		e^+			γ			
e^-							D^*	
π	γ			ρ			B^0	
	ρ	B^0	π					

Voor de lezer: één Sudoku puzzel. De symbolen zijn: e^+, e^-, B^0, $\overline{B}^0$, D^*, π, ρ, β en γ.
A Sudoku puzzle for the reader. The symbols are: e^+, e^-, B^0, $\overline{B}^0$, D^*, π, ρ, β, and γ.